

Brushes and Soap

**Grafted polymers and their interactions with
nanocolloids**

promotoren: dr. M. A. Cohen Stuart,
hoogleraar fysische chemie, met bijzondere aandacht voor de
kolloïdchemie
dr. G. J. FLeer,
persoonlijk hoogleraar bij het Laboratorium voor Fysische Chemie
en Kolloïdkunde

NN08201, 2770

Brushes and Soap

Grafted polymers and their interactions with nanocolloids

Edwin P.K. Currie

Proefschrift

ter verkrijging van de graad van doktor

op gezag van de rector magnificus

van Wageningen Universiteit,

dr. C. M. Karssen,

in het openbaar te verdedigen

op vrijdag 7 april 2000

des namiddags te 13.30 in de Aula.

van 975701

Nederlandse titel: Polymeer borstels en zeep; verankerde polymeren en hun interacties met nanokolloïden

ISBN 90-803470-6-X

Subject headings: brushes/colloids/complexation/surfactants.



Dit proefschrift is tot stand gekomen met steun van de Stichting Scheikundig Onderzoek in Nederland (SON) met een subsidie van de Nederlandse Organisatie voor Wetenschappelijk Onderzoek (NWO).

BIBLIOTHEEK
LANDBOUWUNIVERSITEIT
WAGENINGEN

This thesis is based on the following papers:

- Currie, E.P.K.; Leermakers, F.A.M.; Cohen Stuart, M.A.; Fleer, G.J. *Macromolecules* **1999**, 32, 487 (Chapter 2).
- Currie, E.P.K.; Wagemaker, M.; Cohen Stuart, M.A.; van Well, A.A. *Macromolecules* **1999**, 32, 9041 (Chapter 3).
- Currie, E.P.K.; Sieval, A.B.; Avena, M.; Zuilhof, H.; Sudhölter, E.J.R.; Cohen Stuart, M.A. *Langmuir*, **1999**, 15, 7116 (Chapter 4).
- Currie, E.P.K.; Sieval, A.B.; Fleer, G.J.; Cohen Stuart, M.A. *submitted to Langmuir* (Chapter 4).
- Currie, E.P.K.; Van der Gucht, J.; Borisov, O.V.; Cohen Stuart, M.A. *Langmuir* **1998**, 14, 5740 (Chapter 5).
- Currie, E.P.K.; Cohen Stuart, M.A.; Fleer, G.J.; Borisov, O.V. *Europhys. Lett.* **2000**, 49, 438 (Chapter 6).
- Currie, E.P.K.; Cohen Stuart, M.A.; Fleer, G.J.; Borisov, O.V. *submitted to Macromolecules* (Chapter 6).
- Currie, E.P.K.; Cohen Stuart, M.A.; Fleer, G.J.; Borisov, O.V. *Europ.Phys.J. E* **2000**, 1, 27 (Chapter 7).
- Currie, E.P.K.; Van der Gucht, J.; Borisov, O.V.; Cohen Stuart, M.A. *Pure & Appl. Chem.*, **1999**, 71, 1227 (Chapter 8).

Stellingen

behorend bij het proefschrift
'Brushes and Soap' van Edwin Currie

1. In tegenstelling tot de conclusies van vele onderzoeken volgen neutrale borstels in een goed oplosmiddel de voorspelde gemiddeld-veld schalingswetten, mits de ketenlengte enkele honderden monomeren beslaat en mogelijke oppervlakteactiviteit in beschouwing wordt genomen. *Dit proefschrift, hoofdstuk 2.*
2. De afwijkende theoretische resultaten van Carignano & Szleifer voor de oppervlaktedruk van verankerde ketens zijn het gevolg van een foute uitdrukking voor de oppervlaktedruk van verankerde polymeren in een roostermodel. *Carignano, M.A.; Szleifer, I. J.Chem.Phys. 1994, 100, 3210.*
3. De dikte van zwak-zure borstels vertoont experimenteel een maximum als functie van de ionensterkte, zoals theoretisch voorspeld. *Israëls, R. et al., Macromolecules 1994, 27, 3087; Zhulina, E.B. et al., Macromolecules 1995, 28, 1491 en Lyatskaya Y.V. et al., Macromolecules 1995, 28, 3562.*
4. De orde van de keten-complex fase-overgang in polymeeroplossingen met complexerende nanokolloïden wordt voornamelijk bepaald door de osmotische interacties in het systeem. *Dit proefschrift, hoofdstuk 6 en 9.*
5. De geadsorbeerde hoeveelheid nanokolloïden per oppervlakte-eenheid op oppervlaktes bekleed met polymeer borstels kan een maximum vertonen als functie van de verankeringsdichtheid, in tegenstelling tot vele conclusies in de literatuur. *Dit proefschrift, hoofdstuk 7 en 8.*
6. Er is een groot verschil tussen co-auteurs en mede-auteurs van een artikel.
7. Hardlopen loopt niet hard.
8. Het feit dat de fractie 'gamma'-studenten in Nederland spontaan toeneemt ten opzichte van de fractie 'beta'-studenten impliceert volgens de thermodynamica dat gamma-studenten minder arbeid verrichten.
9. De opkomst van particuliere beveiligingsdiensten kan samengevat worden als 'je betaalt je blauw'.
10. Het afgelopen eeuw zijn we van een credo- naar een credit-maatschappij gegaan.

Contents

Chapter 1. Introduction	1
1.1. General Introduction	1
1.2. Brushes	5
1.2.1. Neutral brushes	5
1.2.2. Charged brushes	8
1.2.3. Preparation of brushes	11
1.3. Outline of the Thesis	13
Chapter 2. Grafted Adsorbing Polymers	15
2.1. Introduction	15
2.2. Self-consistent Field Model	19
2.3. Scaling laws	22
2.4. Pancake-Brush Transition	29
2.5. Conclusions	35
Acknowledgement	36
Appendix	37
Chapter 3. Structure of Monodisperse and Bimodal Brushes	41
3.1. Introduction	41
3.2. Materials and Method	44
3.3. Monodisperse Brushes	46
3.4. Bimodal Brushes	53
3.5. Discussion and Conclusions	59
Acknowledgements	61
Chapter 4. Annealed Brushes	63
4.1. Introduction	63
4.2. Surface Pressure Isotherms	64
4.2.1. Materials & Method	64
4.2.2. Results	65
4.2.3. Discussion	68
4.3. Reflectometry	73
4.3.1. Materials & Method	73
4.3.2. Results	74
4.3.3. Discussion	76
4.4. Ellipsometry	77
4.4.1. Materials & Method	77

4.4.2. Results	78
4.4.3. Discussion	83
4.5. Conclusions	85
Acknowledgements	86
Appendix	87
Chapter 5. Polymers with Surfactants	89
5.1. Introduction	89
5.2. Model	91
5.3. Estimation of Parameters	96
5.4. Results	98
5.5. Conclusions	104
Acknowledgements	105
Appendix	106
Chapter 6. Phase Separation in Polymer-Surfactant Solutions	109
6.1. Introduction	109
6.2. General Formalism	110
6.3. Phase Behaviour	114
6.3.1. Good solvent	114
6.3.2. Bad solvent	117
6.4. The Coil-Globule Transition	124
6.4.1. The volume approximation	124
6.4.2. Finite size corrections	127
6.5. Discussion and Conclusions	131
Chapter 7. Brushes with Annealed Excluded-volume Interactions	133
7.1. Introduction	133
7.2. General aSCF Formalism	134
7.3. Intrinsic Structure of the Brush	139
7.3.1. Continuous distributions: one-phase brush	140
7.3.2. Microphase separation	144
7.4. Large-scale Properties	148
7.5. Discussion and Conclusions	151
Chapter 8. Interactions of PEO Brushes with BSA	155
8.1. Introduction	155
8.2. Materials and Methods	156
8.3. Results	157
8.4. Discussion and Conclusions	159
Acknowledgements	161
Chapter 9. Complexation of Polyelectrolytes with Nanocolloids	163
9.1. Introduction	163
9.2. Model	165

9.3. Results	174
9.3.1. Separate parameters	174
9.3.2. Phase behaviour	178
9.3.3. Comparison with experiments	180
9.4. Discussion and Conclusions	183
Summary & Outlook	187
Samenvatting	193
Glossary	197
Bibliography	201
Dankwoord	207
Curriculum Vitae	209

CHAPTER 1

Introduction

ABSTRACT

In this chapter a general introduction is given to grafted polymers and interactions between small colloidal particles and polymers. To start with, some general aspects of such systems are reviewed, with the emphasis placed upon practical applications. We continue with a more detailed discussion of simple theoretical models for polymer brushes and of the problems associated with their experimental preparation. The chapter closes with a brief outline of the thesis.

1.1. GENERAL INTRODUCTION

Polymers play an all-important role in biological systems. For example, our DNA consists of polymers with four different monomers, the sequence of which determines the coding of our genes. Also, the supply of readily available energy in animals is regulated through production and degradation of glycogen, a polysaccharide made up of glucose monomers. When such glucose monomers are linked in a slightly different way the result is cellulose, the polymer responsible for the tensile strength of plant fibres. The protecting exoskeleton of insects is formed by chitin, a polymer resembling cellulose. In a sense, proteins are nothing more than polymers with twenty different monomers, the amino acids, and their sequence determines the specific conformations and functions of proteins. One can therefore say that nature has used the structural and functional properties of polymers to their full extent. [1]

Besides natural polymers, products consisting of synthetically produced polymers surround us in our daily life. Plastic bags are made of polyethylene, water-based latex paints contain polystyrene sulfonate. Clothing, nylons, the interior of a car and the exterior of computers are all made from synthetic polymers in one form or another. The progress made in polymer chemistry since polymers were first synthetically produced around 1930 is immense. [2]

Most of the above examples refer to polymers in a bulk phase, whereas this thesis generally concerns polymers at interfaces. More specifically, we will largely restrict ourselves to end-grafted polymers, i.e. polymers with the first monomer fixed to a grafting plane. An important application of polymers at interfaces is that of colloidal stabilisation. Colloids are particles that are at least an order of magnitude larger than a single solvent molecule, but they are small enough to be invisible to the bare eye. The radius of particles in the colloidal domain generally ranges from a few nanometers to a micrometer. Colloidal systems consist of colloids dispersed in a continuous phase, which can be either a liquid or a gas. Examples of colloidal systems are fat droplets in milk, pigment particles in paint, proteins in blood, but also mist. [3]

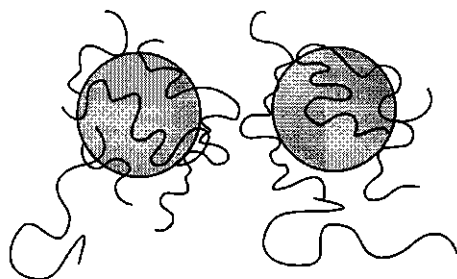


FIGURE 1.1. *Colloidal stabilisation through polymer adsorption*

Colloids in a continuous phase, be it water, an organic solvent or air, attract each other as a result of van der Waals interactions. These interactions originate from the electronic structure of the atoms that constitute the colloid and the continuous phase, and can be summed up as 'like attracts like'. Without any kind of stabilisation colloids in solution aggregate and form a separate, aggregated phase. Colloids in water are often stabilised by an electrical surface charge, as two particles of equal charge repel each other. The theory for colloidal stabilisation through electrostatic interactions (DLVO theory) was developed by Deryagin, Landau, Verwey and Overbeek around 1940. [4]

In some cases stabilisation of colloids via surface charges is not an option, for instance in the case of organic solvents or water-based solutions with a high salt concentration. Polymers adsorbed on colloids can also stabilize a colloidal solution against aggregation. The stabilisation is now the result of *steric* interactions. If polymers are adsorbed on the particle surfaces the resulting polymer layers have to be compressed for the particles to aggregate, see Figure 1.1. This compression of the polymeric layers is unfavourable for entropic reasons, and leads to an effective repulsive force. When the amount of adsorbed polymer is sufficiently high the steric repulsion is strong enough to prevent aggregation. A classic example of steric stabilisation is the production of ink in ancient Egypt and China. In those days ink consisted of soot (carbon particles) in water mixed with natural, water-soluble polymers, such as casein from milk, egg albumine or gum arabic. Without the added polymer the soot aggregates and separates from the water phase, which is not desirable when one is writing a letter.

Besides adsorption of polymers from a bulk phase, the end-grafting of polymers to a surface also may prevent colloidal aggregation, and this trick is applied by nature in milk. A major constituent of milk is casein, a particle (micelle) consisting of several kinds of proteins. In milk, casein is covered with long end-grafted proteins, κ -casein, which prevent aggregation. Upon adding a particular enzyme (chymosin) the enzyme cuts the κ -casein hairs and the casein micelles aggregate. [5,6] The result of this aggregation is a separate phase, also known as cheese. [7,8]

If the number of end-grafted polymers per unit area is high, and the solvent quality is good, the chains are forced to stretch normal to the particle surface due to steric interactions between monomers. The result is a thick polymer layer surrounding the particle, a so-called *brush*. The thickness of the brush depends on the chain length and

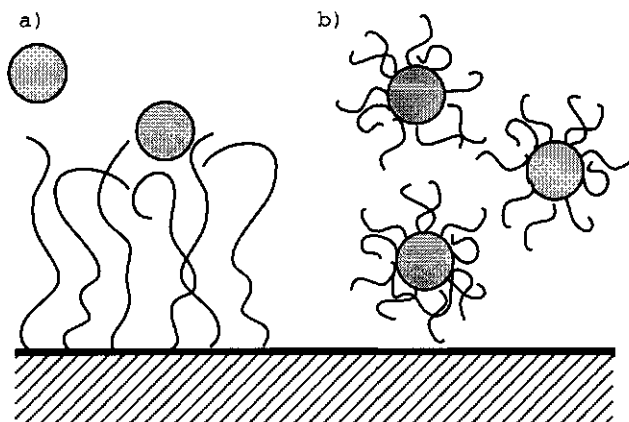


FIGURE 1.2. *Prevention of adsorption of a) particles on a grafted surface, and b) grafted particles on a bare surface*

the number of chains grafted per unit area. As a brush is relatively thick it may offer excellent protection against colloidal aggregation.

It was soon recognised that a polymer brush does not only prevent aggregation of identical colloidal particles. One can prevent the adsorption of bare particles from solution by grafting polymers onto a surface, as shown in Figure 1.2a. An example of this is medical glassware that is inserted in a body for a prolonged period, for instance catheters. A bare glass surface is vulnerable for adsorption of bacteria. [9] After a period of time the result of such bacterial adsorption and subsequent multiplication can be an infection. Densely grafted polymers may prevent adsorption of bacteria on the glass, and therefore reduce the risk of an infection during a prolonged period of insertion. [10, 11]

In a similar vein, coating a particle with polymers can prevent its adsorption on a bare surface, provided the polymers themselves do not adsorb on the surface, see Figure 1.2b. A good example of this is liposomes, the surface of which is covered by end-grafted polymers. Liposomes are small containers made up of surfactant molecules in which a drug molecule can be placed. When inserted in the blood stream the liposomes eventually adsorb on the surface of arteries, change their conformation and release the encapsulated drugs. The grafting of water-soluble polymers to the liposome surfaces can increase the period of circulation in the blood stream significantly. The kinetics of drug release can thus be controlled via the grafting density of polymers on the liposomes. [12, 13]

So far, we did not pay explicit attention to brushes consisting of polymers with charged monomers, so-called polyelectrolytes. Natural or synthetic polymers are often charged, and these charges greatly influence the behaviour of the polymers. When a brush consists of charged polymers, its properties not only depend on the number of monomers per chain and the chain length, but also on the fraction of charged monomers and the salt concentration. If the charges on the monomers have the same sign, charged monomers repel each other strongly at low salt concentrations. However, with increasing salt concentration the range of the electrostatic interactions between charged monomers lessens,

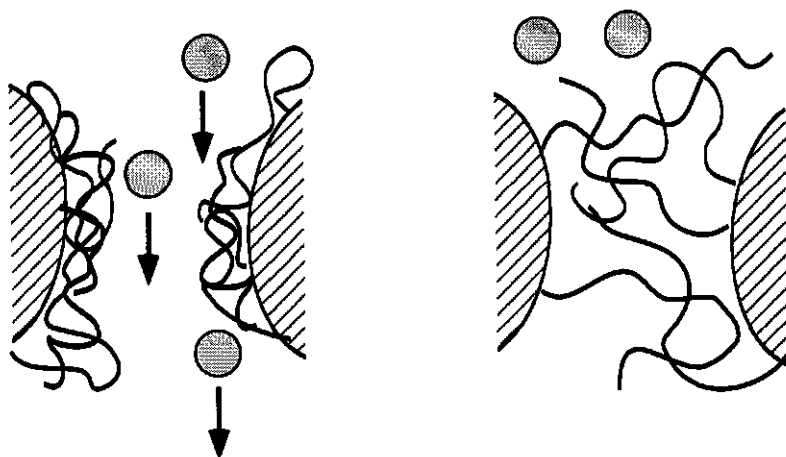


FIGURE 1.3. *Grafted polyacids in a pore at low pH, and high pH*

that is, the repulsive interactions become weaker. This results in a decrease in the height of a polyelectrolyte brush with increasing salt concentration. The grafted polymers can also consist of weak-acidic or weak-basic groups. In this case the fraction of charged monomers, and thus the average strength of the monomeric repulsion, also depends on the pH and the grafting density.

An application of charged brushes is the control of the width of pores through the grafting of polyacids, see Figure 1.3. At low pH the polymers are uncharged, the brushes are weakly stretched and the pores are wide open. At a high pH, however, the monomers are charged and the brush stretches. This feature is used in the field of membrane technology, where the permeability of membranes to, for instance, insulin is regulated by the pH via the grafting of polyacrylic acid. [14]

A different, but equally important field in polymer research are attractive interactions between polymers or polyelectrolytes and colloidal particles. In this thesis we concentrate on colloidal particles which are considerably smaller than the overall size of the polymers. We refer to such particles as 'nanocolloids', as their size is in the range of a few nanometers. A good example of nanocolloids is surfactants that form micelles (aggregates of a limited number of surfactant molecules) above a *critical micelle concentration* (CMC). In the presence of a hydrophilic, neutral polymer, the polymer and surfactants may form complexes at a *critical aggregation concentration* (CAC), which is generally below the CMC. The result is a polymer chain covered with micelles, a *necklace*, see Figure 1.4. At high enough polymer concentrations a visco-elastic network of such complexes may be formed. Due to the combination of a visco-elastic polymer network and the detergent action of surfactants, polymer-surfactant complexes are a basic ingredient in cosmetic products, such as shaving creams and shampoos. [15]

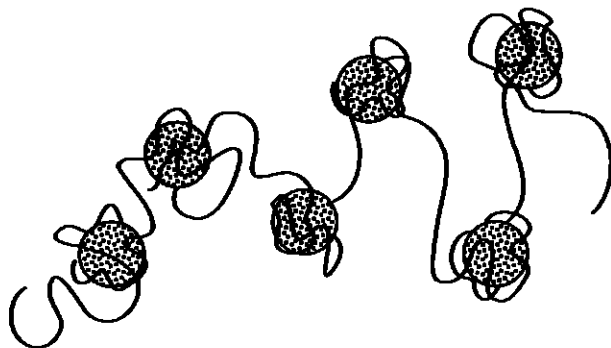


FIGURE 1.4. A 'necklace'

The interactions between neutral polymers and micelles, however, are weak compared to those between polyelectrolytes and oppositely charged nanocolloids. In the former case the attraction arises from relatively weak hydrophobic interactions, in the latter case from relatively strong electrostatic interactions. If a complex between a polyelectrolyte and small, oppositely charged particles is formed, the resulting complex may be electrostatically neutral or close to neutral. As mentioned, colloidal solutions are stabilised against aggregation by the charges on the colloidal particles. Therefore, upon complexation a separate aggregated phase of collapsed polyelectrolyte chains with complexed particles may form. This process depends sensitively on the salt concentration of the solution, as this determines the strength of the (attractive) electrostatic interactions. Generally speaking, at high salt concentrations no complexation occurs whereas at low salt concentrations the particles bind strongly to the polyelectrolyte.

A practical application of such complexation is selective complex coacervation. In a solution containing a mix of proteins the charge of the various proteins varies, due to the different characteristics of each protein species. By controlling the salt concentration and pH of a protein mixture, complex coacervation between polyelectrolytes and a selected protein can be induced, whilst the other proteins do not form complexes and remain solvated. After phase separation of the complex coacervate one can regain the separated protein simply by increasing the salt concentration and dissolving the complex coacervate. [16]

1.2. BRUSHES

1.2.1. Neutral brushes

In this section we take a closer look at some simple theoretical descriptions of both neutral and charged polymer brushes. Two important classes of brush models are discussed, namely scaling theories and analytical self-consistent-field models. In the final section we comment upon the experimental preparation of brushes.

The concept of brushes (strongly stretched polymer chains, densely grafted onto an interface) was first introduced by Alexander in 1977, although the phrase *brush* was introduced later. [17] In this seminal paper polymer chains with a strongly adsorbing end-group at high densities were described as cigar-like conformations. In 1980 de Gennes modelled such end-adsorbed polymers using a blob or scaling model. [18] At low grafting densities the conformation of the grafted polymer is a coil conformation (for non-adsorbing chains) or a flat conformation (when the interactions between the grafting surface and chain are attractive). If the distance between grafted chains is much smaller than the unperturbed coil size the chains are forced to stretch normal to the surface due to steric interactions, and form a brush.

In the scaling models of Alexander and de Gennes (AdG) the monomer density is assumed to be constant throughout the brush, the so-called *box-model*. This implies that the polymers are uniformly stretched and that all chain ends are located at the edge of the brush. The confinement of chains results in the formation of a number of blobs per chain. The definition of a blob is a string of monomers, the conformation of which is unperturbed by intermolecular interactions. [19] The increase in free energy upon formation of a blob is of order $k_B T$, where k_B is the Boltzmann constant and T the temperature. The size ξ of blobs in a brush is equal to the spacing between two adjacent grafted chains $\sigma^{-1/2}$, where σ is the grafting density, defined as the number of chains per unit area. In a good solvent the number of monomers per blob is $g \approx (\xi/l)^{5/3}$, with the monomer length denoted by l and where, in the spirit of scaling theory, numerical prefactors are neglected. The thickness of the brush H (often also referred to as the brush height) is simply the total number of blobs per grafted chain (N/g) multiplied by their size ξ where N denotes the number of monomers in a grafted chain. This yields the simple scaling law for the brush thickness

$$(1.1) \quad H \sim N \sigma^{1/3} l^{5/3}$$

The surface pressure π of the brush is proportional to the number of blobs per unit area ($N\sigma/g$) and, as the formation of each blob requires an energy of order $k_B T$, π is proportional to

$$(1.2) \quad \pi \sim N \sigma^{11/6} l^{5/3}$$

The main assumption in the AdG box-model, namely all polymers in a brush are equally stretched with their chain ends positioned at a distance H from the grafting surface, is a serious oversimplification. At the end of the 1980's analytical self-consistent field (aSCF) models were introduced in which the chain ends are allowed to distribute themselves throughout the brush. [20–23] In the aSCF model the assumption is made that the grafting density is high enough for the brush to be laterally homogeneous. This implies that the monomer density and chain end density are solely functions of the distance to the grafting surface. If a chain end is positioned at a certain distance, then only the most probable chain conformation is considered in the aSCF models. It turns out that this implies that no back-folding of chains is taken into account. With increasing

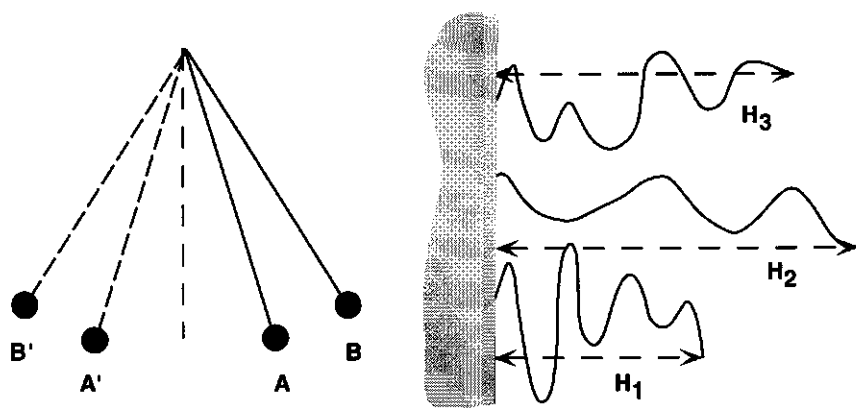


FIGURE 1.5. *Analogy between a harmonic oscillator and grafted chains in a brush.*

monomer number s (s is zero for the grafted monomer and N for the free end) the polymer monotonously 'moves' away from the grafting surface.

Furthermore, an analogy is made between a harmonic oscillator, for instance a pendulum in a gravitational field, and a grafted polymer chain, as shown in Figure 1.5. As the period of a harmonic oscillator is independent of the amplitude, its potential field is a so-called *equal-time potential*. Effectively, this means that when a pendulum is released from position A , the same time period is required to reach A' as is the case when it is released from position B and travels to B' . Likewise, a grafted chain requires N 'time-steps' to reach its chain end, irrespective of its amplitude (the position of the chain end of the grafted chain, denoted by H_1 , H_2 and H_3 in Figure 1.5). The general form of an equal-time potential field is $A - Bx^2$. [24] Noting that B is equal to $2\pi^2/\tau^2$ according to classical mechanics, and that the chain length Nl corresponds to $1/4$ of a full period τ , it follows that B is simply $\pi^2/8N^2l^2$.¹

Finally, a harmonic oscillator 'reacts' to a potential field, in the case of a pendulum this field is simply the gravitational field. In the case of grafted chains in a brush the corresponding field arises from intermolecular osmotic interactions. In the aSCF model a mean-field approach for good solvent conditions is used, in which only binary osmotic interactions between monomers are considered. The monomeric potential field $u(x)$ is equal to $v_0 \rho(x)$, where $\rho(x)$ is the monomer density. The second virial coefficient v_0 may be interpreted as the volume one monomer effectively excludes another from. Therefore, in a good solvent (repulsive monomer-monomer interactions) v_0 is approximately the volume occupied by a monomer, l^3 . If we combine both expressions for the potential field $u(x)$, the monomer density is given as

¹In the literature the exact value of the numerical prefactor B varies. In some papers the prefactor equals $3\pi^2/8N^2l^2$, as the grafted chain is considered a 3D object. [23, 25] In this chapter we follow the convention of MWC, in which the chains effectively are 1D objects. [20]

$$(1.3) \quad \rho(x) = v_0^{-1} \left(A - \frac{\pi^2 x^2}{8N^2 l^2} \right)$$

and it is evident that the aSCF model predicts a parabolic density profile in the brush. The constant A is determined by the normalisation condition $N\sigma = \int_0^H \rho(x) dx$ (conservation of mass) and equals

$$(1.4) \quad A = \frac{N\sigma v_0}{H} + \frac{\pi^2 H^2}{24N^2 l^2}$$

We may characterise the brush height H in the aSCF model by $\rho(H) = 0$. Inserting this in the above equation it follows that the aSCF model yields the same scaling expression for the brush height as the AdG scaling model, $H \sim N\sigma^{1/3}$. The surface pressure in the aSCF model is found by integrating the local osmotic pressure in the brush, $\frac{1}{2}v_0\rho(x)^2$, over the total height. This gives

$$(1.5) \quad \begin{aligned} \pi &= \frac{v_0}{2} \int_0^H \rho(x)^2 dx \\ &\approx \frac{1}{2} N\sigma^{5/3} v_0^{2/3} l^{-2/3} \end{aligned}$$

We thus find that the surface pressure of the brush scales as $N\sigma^{5/3}$ in the aSCF model. The power law exponent of π as a function of σ differs slightly from that of the AdG model (10/6 vs. 11/6). It must be remarked that the expression for the monomer potential field is only valid for relatively low monomer densities and good solvent conditions. If these conditions are not met the complete viral expansion for the potential field in terms of the monomer density $\rho(x)$ must be taken into account, and the above scaling relationships are not valid.

As is the case with all elegant physical models, the aSCF model for brushes has its flaws. The most serious simplification is that the grafted chain in the aSCF model assumes its most probable conformation; fluctuations around this conformation are not taken into account. Such fluctuations, however, may be of importance for the brush structure, especially at small grafting densities. Numerical self-consistent field (nSCF) studies have shown that such fluctuations may result in an extended tail region, in which the monomer density smoothly decreases to zero. [26–30] We return to this point in Chapter 3.

1.2.2. Charged brushes

The number of possible structures of neutral brushes is limited. For instance, in a good solvent the brush is swollen, and as the solvent quality decreases the brush thickness continuously decreases, as the chains collapse towards the grafting surface. [25] A charged brush has a larger variety of possible configurations, as the number of parameters is larger and the range of interactions (electrostatic, steric) varies. Numerous papers have examined various properties of charged brushes theoretically and several configurational regimes have been characterised. [31–35] In the following some experimentally relevant

regimes for charged brushes in good solvent conditions are discussed.

We distinguish between brushes consisting of grafted polyelectrolytes with a fixed fraction of charged monomers (*quenched*), and polyelectrolytes with a varying fraction of charged monomers (*annealed*). An example of the former is sodium-polystyrenesulfonate (NaPSS), an example of the latter is polyacrylic acid (PAA), the charge density of which depends on the pH and the salt concentration, but also the grafting density and the distance from the grafting plane. [34–36]

The configuration of *quenched* polyelectrolytes at a high grafting density depends upon the salt concentration. At high salt concentrations the range of electrostatic interactions (characterised by the Debye length κ^{-1}) is small compared to the brush height, $\kappa^{-1} \ll H$. As the range of electrostatic interactions between two charged monomers is of order of magnitude of the Debye length, and thus limited, the electrostatic interactions are comparable to the excluded-volume interactions between two neutral monomers. In this *Salted Brush regime* (SB) the scaling behaviour of the brush height and surface pressure is therefore predicted to be similar to that of neutral brushes, as given in Eqs.(1.1) and (1.2). The excluded-volume parameter of neutral monomers v_0 in Eqs.(1.3) and (1.4) is replaced by an effective excluded-volume parameter v_{eff} , defined as

$$(1.6) \quad v_{eff} \approx v_0 + \frac{\alpha^2 l_B}{\kappa^2}$$

where α denotes the fraction of charged monomers and l_B denotes the Bjerrum length. [25] For reasonable values of α and κ the contribution of the neutral monomers v_0 is negligible with respect to the electrostatic interactions. Thus, the brush height in the SB-regime scales as

$$(1.7) \quad H \sim N (\sigma v_{eff})^{1/3} \sim N \left(\frac{\sigma \alpha^2}{\rho_s} \right)^{1/3}$$

where ρ_s denotes the salt concentration and is proportional to κ^2 . Note that in this model the brush height again scales as $H \sim N \sigma^{1/3}$ and the surface pressure as $\pi \sim N \sigma^{5/3}$, similar to neutral brushes.

In the limit of zero salt concentration the range of electrostatic interactions between charged monomers is large ($\kappa^{-1} \sim H$). In this regime the chains are strongly stretched by osmotic interactions of the counterions of the dissociated monomers in the brush. At low grafting densities the counterion density in the brush is low and the osmotic pressure is proportional to the counterion density. In this *Osmotic Brush regime* (OsB) the equilibrium conformation of the chains is obtained when the elastic force acting on a monomer ($\sim H \sigma / N l^2$) equals the osmotic pressure of the counterions in the brush ($\sim N \alpha \sigma / H$), under the condition of local electroneutrality throughout the brush. The resulting scaling expressions are

$$(1.8) \quad H \sim N l \alpha$$

and

$$(1.9) \quad \pi \sim N\alpha\sigma$$

Note that in the OsB-regime the brush thickness is independent of the grafting density. Moreover, the surface pressure resulting from the $N\alpha\sigma$ counterions per unit area is ideal, each counterion contributes an amount of energy of order $k_B T$.

The situation is more complicated in the case of *annealed* brushes, as the fraction of charged monomers α is not constant, but varies with varying conditions. Thus, the excluded-volume parameter v_{eff} in Eq.(1.6), which characterises the (average) strength of osmotic interactions between monomers, can be expected to vary as a function of the grafting density and distance to the grafting plane. We consider weak polyacids for which a degree of dissociation α_b in the bulk is defined. This is the average degree of dissociation a monomer would have in the bulk solution:

$$(1.10) \quad \frac{1 - \alpha_b}{\alpha_b} = \frac{K_a}{\rho_{H^+}}$$

where K_a is the monomer dissociation constant and ρ_{H^+} the proton concentration in the bulk solution. Note that α_b is fully determined by the pH of the solution and varies between 0 and 1. It is important to realise that in the case of annealed brushes consisting of polyacid chains a clear distinction is made between (indifferent) salt ions, that solely screen electrostatic interactions, and protons, that both screen electrostatic interactions and may associate with the dissociated monomers. In the case of quenched brushes the role of protons is limited to the screening of electrostatic interactions, and no distinction between protons and other ions is necessary.

At high salt concentrations in the bulk, i.e. $\rho_s \gg \rho_{H^+}$, the proton concentration in the brush is approximately equal to that in the bulk, as the dissociated protons in the brush are exchanged with salt ions from the bulk whilst maintaining electroneutrality in the brush. As the conditions are similar to those in the SB-regime of quenched brushes, the scaling relationships for the height and surface pressure of annealed brushes are therefore equal to those for quenched brushes in the SB-regime (Eq.(1.7)), with α in Eq.(1.6) replaced by α_b .²

In the limit of zero salt concentration the proton concentration in the brush is significantly higher than in the bulk phase, as the exchange of dissociated protons with indifferent counterions is negligible. As a result, the degree of dissociation in the brush is lower than that of the bulk. This regime is referred to as the *annealed Osmotic Brush regime* ($\bar{O}SB$). The average degree of dissociation in the brush has been derived to be [34]

$$(1.11) \quad \alpha \approx \left(\frac{\alpha_b}{1 - \alpha_b} \sigma^{-1} (\rho_{H^+} + \rho_s) \right)^{2/3}$$

²We remark that in the case of the scaling law for H of annealed brushes in the SB-regime, formally the total ionic strength must be considered in Eq.(1.7), i.e. the sum of the salt and proton concentrations. As the salt concentration is magnitudes larger than that of protons, the latter contribution to the Debye length may be neglected.

where only an average or overall value of α is considered. In more detailed models the variation of α throughout the brush, i.e. $\alpha(x)$, can be taken into account. [35] From the above expression it follows that for a given pH, i.e. a fixed α_b , α decreases with increasing grafting densities. At high grafting densities α may become low enough for the brush to effectively resemble a neutral brush.

In the NB and SB brush regimes the chains are stretched as a result of osmotic interactions, be it between neutral or charged monomers. As the grafting density increases these osmotic interactions result in an increase in average stretching of the chains. The above expression for α , however, demonstrates that in the $\tilde{O}S$ B-regime the fraction of charged monomers, and therefore v_{eff} , decreases with increasing grafting density. If we use the same expression for the brush height, i.e. Eq.(1.7), and insert Eq.(1.11) into Eq.(1.6), the following scaling expression for the brush height in the $\tilde{O}S$ B-regime is found:

$$(1.12) \quad H \sim N (\sigma \alpha^2 \rho_s^{-1})^{1/3} \sim N \sigma^{-1/3} \left(\frac{\alpha_b}{1 - \alpha_b} \right)^{2/3} (\rho_{H^+} + \rho_s)^{1/3}$$

To conclude, using a simple scaling model the paradoxical result is obtained that the brush height in the $\tilde{O}S$ B-regime may *decrease* with increasing grafting density or *increase* with increasing salt concentration. The underlying reason is that the decrease in osmotic interactions between charged monomers due to a decrease in α (Eq.(1.11)) is not compensated by the increase in total monomer density with increasing grafting density. The interplay of the pH, salt concentration and grafting density thus yields interesting theoretical predictions for annealed brushes, most of which await experimental verification.

1.2.3. Preparation of brushes

Brushes under various conditions have been investigated theoretically with several models. For instance, brushes in good, bad and polymeric solvents have been studied [25, 28, 28–30, 32, 33, 36–41], they have been examined under various kinds of deformation [42–45], liquid crystalline brushes have been discussed [46, 47], polyelectrolyte brushes in good and bad solvents, with or without salt have been examined [35, 36, 48–51], and the list goes on. However, the experimental preparation of a homodisperse brush of controlled length and grafting density on a given grafting surface is not a simple issue. In the following a brief survey is given of the various techniques found in the literature for the preparation of brushes, together with their (dis)advantages.

One of the common techniques applied in the literature is adsorption of polymers from solution on a surface and subsequent chemical grafting to the surface. To this end polymers containing a reactive end-group form a chemical bond with the grafting surface. The chain length of the chemically grafted brushes prepared with this method is well known. The grafting density, however, can not be controlled beforehand, and has to be determined after preparation via optical techniques. Accurate measurement of the amount of grafted chains is difficult, especially at low grafting densities. In general, the grafting density increases with increasing polymer concentration, but it also depends on the time of annealing and on washing procedures. [52–56]

A similar technique is irreversible adsorption of block copolymers, polymers consisting of two (or more) blocks of monomers with different characteristics. If one block is soluble in the bulk solution and the other block is not, the non-soluble block collapses towards the interface and a brush may be formed. Again, the grafting density obtained with this method is not well controlled and must be determined after preparation. [57-61]

Graft polymerisation is another way to prepare brushes. In this technique polymerisation sites on a surface are exposed to a solution containing reactive monomers. In the ensuing polymerisation reaction polymers 'grow' from the surface, and, provided the density of polymerisation sites is high enough, a brush is formed. This method, however, has several disadvantages. The chain length is not well defined and needs to be inferred from additional measurements. Moreover, the polydispersity of the grafted chains is large. The grafting density is not controlled either, as it cannot be assumed beforehand that on all grafting sites a chain successfully polymerises. [62]

A widely applied method is the spreading of diblock copolymers, dissolved in a volatile solvent, on an air/liquid interface. After spreading the solvent, which does not dissolve in the bulk phase, evaporates and the block copolymer is anchored to the interface by an insoluble anchoring block. This procedure has two major advantages: the chain length is well determined and the deposited polymer density at the interface is known, and can be easily followed via measurement of the surface pressure. A brush with a chosen grafting density is formed by compressing the polymeric monolayer in a Langmuir trough. It is evident that no loss of polymers into the bulk phase may occur in order for the grafting density to be known accurately. This can be checked by examination of the reproducibility of the surface pressure isotherms. Most papers, however, report a loss of polymer, either during spreading or during compression. In such cases the surface density must again be determined indirectly via optical measurements. [63-70]

The preparation of charged brushes is even more complex than that of neutral brushes. As polyelectrolytes generally do not dissolve in organic solvents, spreading of block copolymers with a polyelectrolyte block is difficult. Adsorption of polyelectrolytes with an anchoring block is possible, but the grafting density attained can be limited, due to the strong osmotic pressure in the adsorbed layer. Moreover, a decrease in ionic strength of the bulk solution enhances the osmotic pressure in the adsorbed layer, so that the adsorbed polymers may desorb. One way to circumvent these problems is to prepare end-grafted neutral brushes and subsequently chemically ionize the chains. However, the degree of ionisation is not known exactly, nor the profile of ionised monomers in the brush. In the literature it is generally assumed that after ionisation the distribution of charges on the chains is homogeneous, but no hard evidence is provided. Also, the process of chemical ionisation is very aggressive, and can degraft ('break') the polymer chains. [71-73]

We can thus conclude that the preparation of brushes of controlled chain length and grafting density is not straightforward. In Chapters 4 and 8 we introduce a novel way of preparing neutral and charged brushes on solid substrates from block copolymers deposited on the air/water interface. These are transferred to coated Si-wafers, after

which an annealing step follows in which the chains are firmly implanted by incorporating the apolar moiety of the block copolymer into the apolar coating on the wafer. Using this manner of preparation, we are able to avoid most of the discussed problems.

1.3. OUTLINE OF THE THESIS

This thesis can be divided, roughly speaking, into two parts. The first part, consisting of Chapters 2, 3 and 4, examines the thermodynamic and structural properties of neutral and charged brushes. The second part, Chapters 5 to 9, concentrates on the interactions of (grafted) polymers with nanocolloids.

In Chapter 2 neutral, adsorbing polymers grafted to a surface are investigated with the Scheutjens-Fleer numerical SCF model (nSCF). The results are compared to experimental results for polystyrene-polyethyleneoxide (PS-PEO) block copolymers irreversibly adsorbed at the air/water interface. The scaling behaviour of the experimental and numerical surface pressure and the experimental brush height is compared to the predictions of the aSCF model. The thermodynamic classification of the adsorption/desorption transition of the grafted chains with increasing grafting density is examined numerically and compared to various theoretical predictions.

The structure of PS-PEO at the air/water interface is studied in Chapter 3. The density profile of a neutral brush of monodisperse PS-PEO chains is determined with neutron reflectivity and compared to the profiles predicted by the nSCF model. The mixing of two PEO block lengths results in a bimodal chain length distribution. Such bimodal brushes are also investigated with NR and the experimental density profiles are compared to nSCF profiles.

In Chapter 4 we focus on annealed polyelectrolyte brushes, consisting of polystyrene-polyacrylic acid (PS-PAA), both at the air/water interface and grafted to a solid substrate. The SB- and \tilde{O} B-regime are investigated via analysis of surface pressure isotherms. The titration of such brushes and the dependence of the titration curves on the grafting density is measured with reflectometry. Using ellipsometry we investigate the thickness of such PAA brushes as a function of the pH, salt concentration and grafting density.

The remaining chapters deal with an analytical mean-field model for polymers interacting with nanocolloids. A Flory-like approach for the description of single, complexed chains in a good solvent is presented in Chapter 5, in which the size of the complexes is predicted as a function of density of adsorbed aggregates. This mimics the change in the necklace size as a function of the surfactant concentration. The model results are compared to recent experimental results for PEO-gels complexed with an anionic surfactant.

The phase behaviour of complexed systems with a high (local) polymer density is investigated in the following chapter. We first consider polymer-nanocolloid complexes in semi-dilute solutions. In contrast to single coils in a good solvent, osmotic interactions play an important role in such systems. Possible phase separation upon complex formation of polymers in a good solvent is discussed. The behaviour of polymer-nanocolloid

complexes in solvents that are below the Θ -temperature, i.e. bad solvents for the polymer, is examined as well. The transition from a collapsed, bare globule to a swollen, complexed chain is discussed. The effect of finite chain lengths upon the nature of this transition is also considered.

Polymer brushes may be regarded as localised semi-dilute solutions. In Chapter 7 the analysis of Chapter 6 is extended to polymer brushes in a good solvent interacting with nanocolloids. An aSCF model for complexing polymer brushes is presented. The density profiles of both the chain monomers and adsorbed colloids are analysed, as well as general quantities such as the brush height and the overall adsorbed amount. The possibility of microphase separation within the brush is also discussed.

In Chapter 8 both lines of research are combined as we investigate experimentally PEO-brushes interacting with nanocolloids. The adsorption of bovine serum albumine (BSA) proteins on a hydrophobic surface with grafted PEO chains is measured as a function of the chain length and grafting density. The results of adsorption are discussed and compared to previous suggested theoretical models and our aSCF model.

We finally extend our model to complex formation between polyelectrolytes and charged nanocolloids in Chapter 9. The analysis is limited to the complexation of quenched polyelectrolytes and oppositely charged nanocolloids through electrostatic interactions. The phase behaviour of such systems is analysed, and compared to existing experimental data.

The thesis is concluded with a summary of the present work, and an outlook to possible research in the future.

Grafted Adsorbing Polymers

ABSTRACT

Grafted adsorbing polymers are investigated with the Scheutjens-Fleer self-consistent-field model. The surface pressure of such systems is calculated numerically and semi-quantitative agreement is found with experimental surface pressure isotherms of PS-PEO diblock copolymers at the air/water interface. Scaling relationships of aSCF models for brushes predict the surface pressure π and the height H of neutral brushes to scale with the grafting density σ as $\pi \sim \sigma^{5/3}$ and $H \sim \sigma^{1/3}$, respectively. These scaling relationships are corroborated experimentally for long PEO-chains, provided contributions to π arising from PEO adsorption at the air/water interface are taken into account. Analysis of the $\pi(\sigma)$ -isotherms is shown to be an excellent way of investigating the scaling behaviour of brushes. In the nSCF model the pancake-brush transition in a good solvent is found to be continuous, irrespective of the chain length and adsorption energy. With increasing adsorption energy the pancake-brush transition of the grafted chains is increasingly abrupt and resembles a continuous phase transition close to a critical point, a so-called λ -transition.

2.1. INTRODUCTION

The conformation of linear polymers end-grafted at low densities depends on the interactions between the monomers, the solvent and the grafting surface. If the monomer-surface interaction is non-attractive, a so-called mushroom structure is found. The grafted polymer has a deformed coil conformation with a radius of gyration similar to its dimensions in solution. At increasing grafting densities steric interactions between the grafted polymer chains result in an anisotropic stretching of the polymers normal to the surface, leading to a brush conformation. In a good solvent the brush conformation is determined by a balance between monomer-monomer excluded-volume interactions, and the entropic cost of stretching a chain. As demonstrated in Chapter 1, the height H of the brush in the scaling approach of Alexander and de Gennes scales as $H \sim N\sigma^{1/3}$. [17, 18] The same model predicts the surface pressure π to scale as $\pi \sim N\sigma^{11/5}$. Mean-field aSCF models predict a similar scaling relationship for the brush height, that for π is $\pi \sim N\sigma^{5/3}$. [20–23] Under Θ -conditions the second-order virial coefficient of monomer-monomer interactions is zero and the aSCF scaling relationships are $H \sim N\sigma^{1/2}$ and $\pi \sim N\sigma^2$, respectively.

In subsequent theoretical studies the behaviour of the brush thickness in a good solvent under non-adsorbing conditions was investigated as a function of the grafting density and chain length with nSCF models [26, 28–30], Monte Carlo simulations [37] and MD-simulations. [76] The results for the brush height generally agree with the above aSCF scaling relationship. A more stringent test, however, is the behaviour of the surface

pressure as a function of σ . In two studies (nSCF and MD) the surface pressure of the brush was found to deviate from the predicted 5/3 power law. [30, 76] In both studies higher exponents were reported for narrow regimes with constant scaling behaviour. The chain lengths used in these studies were between 25 and 200 monomers. Martin and Wang found a large regime exhibiting the predicted scaling of the surface pressure using a nSCF model with chains up to 1000 monomers. [28] They concluded that aSCF scaling relationships, which take only second virial interactions into account, are indeed valid for long chains, whereas for short chains a more extended virial treatment is necessary. The good agreement between aSCF scaling relationships and numerical models for the brush height of short chains is explained by the relatively weak dependence of the brush thickness on the grafting density. The numerical results therefore indicate that scaling laws for brushes should be tested experimentally using sufficiently long chains.

A number of experimental studies on brushes have examined the predicted scaling laws. In particular, the power law for the brush thickness $H \sim N\sigma^{1/3}$ has been investigated in several papers. One of the techniques used is measurement of the repulsive force between mica plates on which diblock copolymers with a strongly adsorbing block are deposited. Patel and Tirrell investigated polystyrene (PS) brushes in toluene in this manner, with N ranging from 600 to 1500, and their results compared favourably with the predicted power law. [77] Poly(*t*-butylstyrene) brushes in toluene of length $N = 30, 120$ and 240 were investigated in a similar fashion, and a weaker scaling dependence on the degree of polymerisation was found, $H \sim N^{0.7}$, although this exponent was found with only three data points. [57] In another study of PS-brushes in toluene ($N = 850$ and 2400) it was concluded that the thickness scaled more than linear with N . [58] As pointed out by Whitmore and Noolandi, the scaling behaviour of the disjoining pressure as a function of the chain length is not equivalent to the scaling of the brush height. [78] The disjoining pressure between brushes is measured as a function of the distance of separation between the plates coated with polymer. Under the assumption that the brush height scales as $H \sim N$, the height estimated from the disjoining pressure was found to scale approximately as $H \sim N^{1.2}$. Moreover, the applied model to analyse the data of the disjoining pressure contains four adjustable parameters. Therefore, comparison of surface force results and scaling models for brush height is not straightforward.

The height of a brush layer of diblock copolymers adsorbed on a substrate or at an air/solvent interface can also be measured by neutron reflectivity (NR) or small-angle neutron scattering (SANS). In one study polystyrene-polyethylene oxide (PS-PEO) diblock copolymer was deposited from a toluene bulk solution onto quartz, on which PEO strongly adsorbs. [80] The thickness of the PS-layer as a function of N was concluded to agree with the scaling models. As Baranowski and Whitmore pointed out, this agreement is based upon the assumption that $H \sim \sigma^{1/3}$. [81] The experimental data yield a less than linear dependence on N if no assumptions are made a priori. Bijsterbosch *et al.* measured the thickness and surface pressure of PS-PEO diblock copolymers at the air/water interface for various lengths of the PEO-block. [69] The height of the PEO-brush averaged over all chain lengths was found to scale as $H \sim N^{0.8}\sigma^{0.41}$. Kent *et al.* used poly(dimethyl-siloxane)-polystyrene (PDMS-PS) diblock copolymers with ethyl

benzoate as the solvent. [66–68] In this case the PS-block is solvated and the PDMS-block anchors the block copolymer to the interface. They concluded that the thickness of the layer does not scale as $H \sim N\sigma^{1/3}$, but approximately as $H \sim N^{0.86}\sigma^{0.22}$. [68] In the same paper the behaviour of the surface pressure of the PS brushes was investigated and compared with the predicted scaling law. It was concluded that the scaling exponent of the surface pressure as a function of the grafting density ranges from approximately 4.2 to 6.6, and increases slightly with N . In an elegant study Auroy *et al.* used SANS to investigate PDMS end-grafted onto silica. [52, 53] The brush height was observed to obey the scaling law. In this study however the grafting density could not be varied independently from the chain length.

It follows that a thorough experimental investigation of the scaling behaviour of the thickness and surface pressure of neutral brushes is lacking. One of the problems is that block copolymers adsorbing from a solvent onto a surface are commonly used to obtain grafted polymer layers. The grafting density depends on the length and characteristics of the adsorbing and non-adsorbing block, and on the solvent quality. A problem associated with adsorption from solution is that the polymeric surface density is not known during the experiment and has to be inferred from the experimental data. In the case of NR of NS this is done by fitting a model density profile to the reflectivity curve. This results in relative high uncertainties in the surface density, especially at low coverage. [65] Such uncertainties can greatly influence the outcome of a power law fit, from which scaling exponents follow.¹ Furthermore, it is uncertain whether in practice the density of the adsorbed block copolymers is high enough to enter the asymptotic brush regime.

In the case of *attractive* surface-monomer interactions the situation is even more complex. In this case a pancake structure is found at low grafting densities; the polymer optimises its monomer-surface contacts by assuming a relatively flat conformation. With increasing grafting densities steric interactions force the chain to protrude into the solution, and a brush gradually forms as the extent of displacement increases. Alexander investigated this 'pancake-cigar' transition of grafted adsorbing chains using a simple scaling model. In this model the monomer density profile of both states is taken to be a step function. [17] The model predicts the pancake-brush transition to be first-order, which is inferred from the observation that the chemical potential μ of the grafted polymer chains is not a monotonically increasing function of σ . A van der Waals loop in $\mu(\sigma)$ is obtained, corresponding with the coexistence of two phases. The transition from a cigar-like to a brush-like conformation is reported to occur at a grafting density $\sigma \cong R_G^{-2}$.

A more refined scaling model, in which the constraint of an uniform monomer density is released, was used by Ligoure to analyse a similar system of grafted, adsorbing polymers. [82] In this model the adsorbed polymer is represented as a distribution of loops, trains, and tails, and constitutes a so-called self-similar adsorbed layer (SSAL). A loop distribution is assumed beforehand, in which small loops and tails are neglected. The

¹We return to this point in detail in section 3.3

chemical potential is analysed in a similar fashion as in the paper of Alexander. It is concluded that the conformation transition from a SSAL to a quasi-brush upon increasing σ is first-order under certain conditions. The density at which this transition is found is higher than the overlap density, i.e. $\sigma^* > 1$. The relative coverage σ^* is defined as $4\pi R_G^2 \sigma$, where R_G is the three-dimensional radius of gyration of the coil. The width of the phase coexistence regime is predicted to depend on the length of the chain and on the monomeric adsorption energy.

In a recent paper Aubouy *et al.* investigated grafted adsorbing chains with the same model as Ligoure, but they included small loops and tails in the loop distribution. They concluded that the transition between the SSAL and a quasi-brush is continuous. [83] At grafting densities $\sigma^* > 1$ the polymer layer consists of a SSAL close to the surface, and a polydisperse brush layer stretched outwards from the surface. The grafting density at which the layer structure progressively changes is of order of an adsorbed monolayer, i.e. $\sigma \sim (Nl^2)^{-1}$. Scaling relationships are given for several quantities in this continuous transition as a function of σ , such as μ , H and the loop distribution. Clearly, the character of the pancake-brush transition varies with the assumptions made in the various analytical models. By postulating a functional form for the loop distribution Ligoure concludes that the brush is formed through gradual enlargement of the loops close to the surface (the proximal region). [82] If no loop distribution is assumed beforehand, the brush develops in the distal region by a gradual extension of the polymer tails and, simultaneously, a gradual diminishment of the SSAL. [83]

Experimentally, a first-order adsorption-desorption transition of tethered polymers was reported for the adsorption on PS spheres of PEO triblock copolymers with a hydrophobic center block adsorbed. [84] The transition was concluded to be first-order on the basis of the occurrence of a plateau in the measured hydrodynamic radius of the coated spheres. However, the nature of a conformational transition is defined by the behaviour of thermodynamic quantities of a system, not by the behaviour of structural ones. A more correct manner to determine the nature of the adsorption-desorption transition of either grafted chains or chains with strongly adsorbing end-groups is measurement of π as σ is increased. The surface pressure is inversely proportional to the compressibility of the grafted polymeric monolayer. Therefore, a plateau of constant surface pressure corresponds to an infinite compressibility of the grafted layer, and thus indicates a first-order transition between two polymeric phases. This is comparable to the constant surface pressure of a surfactant monolayer during the (first-order) liquid expanded - liquid condensed phase transition.

The nature of the pancake-brush transition can be investigated experimentally by compressing block copolymers adsorbed at an air/solvent interface in a Langmuir trough. The surface pressure resulting from both the solvated and non-solvated blocks is measured as a function of the continuously changing grafting density. Bijsterbosch *et al.* investigated the properties of diblock PS-PEO at the air/water interface with this technique. [69] The short PS-blocks act as inert anchors and do not contribute to the surface pressure at the grafting densities involved. The long PEO-chains are water-soluble, but also adsorb at the air/water interface. [85] A grafting density regime is reported in which the surface

pressure of the polymer layer slowly increases with increasing σ . The observed density at which this semi-plateau is found corresponds roughly to that of an adsorbed polymeric monolayer. This semi-plateau is attributed to the gradual desorption of the PEO- chains from the air/water interface. No density regime corresponding with an infinite compressibility of the monolayer is reported, nor any other property characteristic of a first-order phase transition.

In this chapter the properties of grafted polymers with and without surface affinity in a good solvent are examined theoretically using the Scheutjens-Fleer nSCF model. In this model all possible polymer conformations are taken into account. In this respect the approach differs from a scaling or aSCF model, in which solely the most probable configurations are considered. The results of the surface pressure measurements of the PS-PEO system by Bijsterbosch *et al.* are used to verify the validity of the numerical results. Taking the adsorption of the PEO-chains to the interface into account, the results of Bijsterbosch *et al.* are re-examined. The scaling behaviour of π and H as a function of σ is investigated both experimentally and numerically. We also consider the transformation of the layer from an adsorbed to a partially desorbed structure with increasing σ numerically. As phase transitions are characterised by the behaviour of thermodynamic quantities, such as the chemical potential μ and its derivatives, special attention is given to these quantities. This approach yields information on the mechanism of the adsorption-desorption transition of the grafted chains and the classification of this transition. The results are compared to mean-field theories for phase transitions, in particular scaling relationships for thermodynamic parameters near a critical point.

2.2. SELF-CONSISTENT FIELD MODEL

The properties of neutral, linear polymers end-grafted to a surface are investigated using the nSCF model of Scheutjens and Fleer. [86,87] The equilibrium distribution of the polymers is calculated taking all possible conformations into account, weighted by their respective Boltzmann probability factors. In this section a short review of the underlying principles is given; a more extensive treatment can be found in the literature. [26]

A cubic lattice is considered, consisting of M layers, numbered $z = 1, 2, \dots, M$, where z is the distance to the surface measured in units of the thickness of a lattice layer l (note that the monomer length and lattice cell length are intentionally given the same symbol). Each lattice layer consists of L sites of volume l^3 , and each site is occupied by either a polymer monomer or a solvent entity. The system is incompressible, which implies that the sum of the densities of all monomer species is unity in each layer. As we consider end-grafted chains immersed in pure solvent, the solvent density in the bulk is unity. The polymer chains are N monomers long and are end-grafted with a grafting density σ , defined as the number of grafted chains per unit area. End-grafted in this case simply defines the probability of the first monomer to reside in the first layer to be unity. We stress that the chemical potential μ of the grafted polymer chains is not coupled to a

bulk concentration as (i) the polymer bulk density is zero, and (ii) there is no exchange of polymers between the grafting plane and the bulk.

In the mean-field approximation the monomer density in each layer is considered to be laterally uniform, and the dimensionless polymer monomer density $\rho(z)$ is solely a function of the distance to the surface. Flory-Huggins parameters χ_{ij} account for nearest-neighbour interactions between monomers of species i and j . The potential energy of a solvent monomer, in units of $k_B T$, is given as

$$(2.1) \quad u_0 = -\ln(1 - \rho(z))$$

whereas that of a polymeric monomer is

$$(2.2) \quad u'(z) = -\ln(1 - \rho(z)) - 2\chi\langle\rho(z)\rangle + \delta(z, 1)(\chi_{sur} - \lambda_1\chi)$$

Note that in the above equation the translational entropy of the grafted chains along the grafting surface has been accounted for. The angular brackets $\langle \dots \rangle$ denote the weighted average of nearest-neighbour contacts in the layers $z-1$, z and $z+1$, i.e. $\langle\rho(z)\rangle = \lambda_1\rho(z-1) + \lambda_0\rho(z) + \lambda_1\rho(z+1)$. For a cubic lattice λ_0 and λ_1 equal $4/6$ and $1/6$, respectively. The χ parameter accounts for the polymer-solvent interactions, χ_{sur} accounts for those of the polymer monomers with the surface. In the definition of χ_{sur} it is taken into account that the number of contacts between the surface and the monomer is a factor λ_1 smaller than the number of contacts between the monomer and the solvent. Thus, the definition of χ_{sur} is similar to that of Silberberg, besides a difference in sign. [88] The χ for solvent-surface interactions is default zero in our calculations. The logarithmic term in Eqs.(2.1) and (2.2) is the mixing entropy of the solvent; the conformational entropy of the polymer chain is taken into account in the following chain statistics.

The conformations of the grafted polymer chains in the local field $u'(z)$ are expressed in terms of a two-point correlation (or Green) function $G(z, z'; s)$, which is the joint probability of a chain of s steps having monomer $s' = 1$ in layer z and monomer $s' = s$ in layer z' , taking all possible configurations into account. To this end the monomer weighting factor $G(z)$ is defined as the Boltzmann factor of a single detached monomer in layer z :

$$(2.3) \quad G(z) = \exp(-u'(z))$$

Due to the connectivity of the chain monomers, the distribution of a given monomer depends on that of its neighbours; in the case of a monomer s located in layer z , monomer $s-1$ must be located in the layers $z-1$, z or $z+1$. This results in a recurrence relationship, in which $G(z, z'; s)$ is expressed in terms of Green functions of a chain which is one monomer shorter in length,

$$(2.4) \quad G(z, z'; s) = \langle G(z, z'; s-1) \rangle G(z')$$

where $\langle G(z, z'; s-1) \rangle$ denotes a weighted average as defined above. In the case of grafted chains the grafting gives a restriction for the first monomer in the form of a Dirac function.

The probability of monomer s residing in layer z' is furthermore recognised as the joint probability of the end-monomer of a chain of length s and that of a chain of length

$(N - s + 1)$ residing in layer z' , corrected for a double counting of $G(z')$. In the case of grafted chains the grafting restriction applies to one of the chain parts. The density of monomer s of a chain of length N in layer z' is therefore

$$(2.5) \quad \rho(z', s) = C \frac{G(1, z'; s) \sum_z G(z', z; N - s + 1)}{G(z')}$$

The normalisation constant C is determined using the fact that the grafting density is fixed. The average density of each monomer summed over all layers must equal the initial grafting density, and thus

$$(2.6) \quad C = \frac{\sigma}{\sum_z G(1, z; N)}$$

The total polymer density in layer z , for a given field $u'(z)$, is given by summation of $\rho(z, s)$ over all chain monomers, $s = 1, 2 \dots N$. The resulting density must be *consistent* with the potential fields expressed by Eqs.(2.1) (2.2) for all z . The solution is generated by numerical iteration.

Besides in structural properties of the grafted polymers, we are interested in the thermodynamic properties of the system. In order to examine the behaviour of the surface pressure of the grafted polymers as a function of σ , it is necessary to determine the excess free energy of the layer. This quantity, denoted by Δ , consists of two terms; an entropic contribution, which takes all polymer configurations with the corresponding probabilities into account, and an enthalpic contribution, which is a function of the (averaged) densities in combination with the χ -parameters. In general, Δ is given as (per unit area, in units $k_B T$) [89]

$$(2.7) \quad \Delta = G - \sum_b n_b \mu_b$$

$$= \sigma \ln \left(\frac{\sigma N}{\sum_z G(1, z; N)} \right) - \sum_{z,i} \rho_i(z) u_i(z) + \frac{1}{2} \sum_{z,i,j} \rho_i(z) \chi_{ij} \langle \rho_j(z) \rangle$$

where G is the total Gibbs free energy of the system, and \sum_b denotes the sum over all components that are in equilibrium with the bulk solution. In the case of a grafted polymer in pure solvent this reduces to

$$(2.8) \quad \Delta = \sigma \ln \left(\frac{\sigma N}{\sum_z G(1, z; N)} \right) + \sum_z \ln(1 - \rho(z))$$

$$+ \sum_z \left(\chi \rho(z) \langle \rho(z) \rangle - \frac{1}{2} \chi \lambda_1 \rho(z) \delta(z, 1) \right)$$

In the derivation of this equation, we make use of the fact that $\sum_z \frac{1}{2} \chi (\rho(z) - \langle \rho(z) \rangle)$ is simply $\frac{1}{2} \chi \lambda_1 \rho(z) \delta(z, 1)$, as the sum is taken over all layers. It is evident that, if all

χ -parameters are set zero, Eq.(2.8) reduces to a similar expression derived by Martin and Wang. [28]

$$(2.9) \quad \Delta = \sigma \ln \left(\frac{\sigma N}{\sum_z G(1, z; N)} \right) - \sum_z u_0(z)$$

Both the chemical potential of the grafted chains and the surface pressure of the system contribute to Δ . The surface pressure is defined as ($k_B T$ per unit area)

$$(2.10) \quad \pi \equiv \left(\frac{\partial G}{\partial A} \right)_{T, n_p, n_s}$$

where G is the total free energy and A is the total area. In a lattice model, however, the grafting density is varied, whereas the total volume and area are constant. This entails that Eq.(2.10) cannot be applied.

We can replace the Gibbs energy in Eq.(2.10) by the excess free energy Δ , as the bulk contribution of pure solvent is zero. This excess free energy consists of a contribution of the chemical potential of the grafted chains, and a contribution of the surface pressure due to the grafted chains. The first term is equal to $\sigma(\partial\Delta/\partial\sigma)$. The surface pressure of grafted chains in pure solvent in a lattice model is therefore²

$$(2.11) \quad \pi = \sigma \left(\frac{\partial \Delta}{\partial \sigma} \right)_{T, A, \mu_i} - \Delta$$

Carignano and Szleifer reported an analytical expression for π , using a similar nSCF model. [29] According to these authors, the surface pressure at a given σ can be explicitly calculated from the monomer density profiles and the interaction parameters. Their method is believed incorrect, as is demonstrated in the Appendix. In our view it is necessary to take the derivative of the excess free energy with respect to the grafting density by numerical central differentiation to obtain π , as was done previously by Martin and Wang. [28]

2.3. SCALING LAWS

In this section the nSCF results for the surface pressure of grafted chains are presented and compared with experimental results. In Figure 2.1 the surface pressure isotherm of grafted, *non-adsorbing* chains consisting of 700 monomers is presented in a double logarithmic plot for a good ($\chi = 0$) and a Θ -solvent ($\chi = 1/2$). The length of a lattice cell l is set 0.35 nm. This is equal to the PEO monomeric length and facilitates comparison with experimental data. [90] The χ_{sur} is set zero for both solvent qualities. At low densities the surface pressure scales linearly with the grafting density, and is independent of the solvent quality. This is the expected ideal gas behaviour for non-interacting coils. Carignano and Szleifer found a quadratic dependence of the surface pressure on the grafting density at very low densities. This is physically unrealistic, and must be attributed to

²In ref. 69 the contribution of the chemical potential of the grafted chains is not subtracted from Δ in the nSCF calculations. This leads to erroneous surface pressure isotherms.

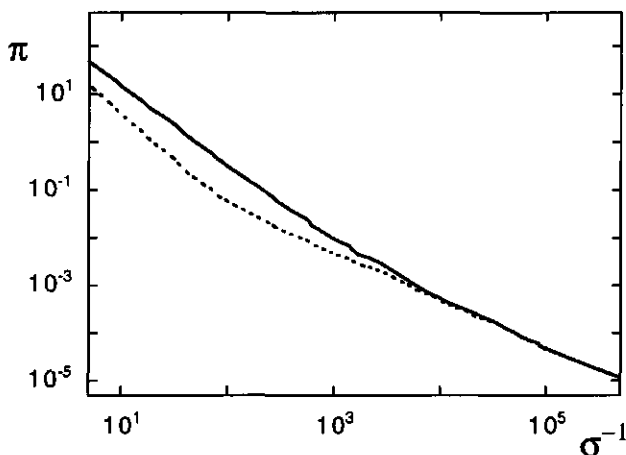


FIGURE 2.1. Lateral pressure π (in mNm^{-1}) in the $n\text{SCF}$ model of grafted non-adsorbing polymers as a function of σ^{-1} (in nm^2) on a double logarithmic scale. Two solvent conditions are shown: $\chi = 0$ (solid curve) and $\chi = 1/2$ (dashed curve). The scaling exponents at high σ are $5/3$ and 2 , respectively, $N = 700$, $l = 0.35$ nm.

their incorrect expression for the surface pressure. [29] For a good solvent ($\chi = 0$) the power law exponent at high densities is $5/3$, as predicted by the $a\text{SCF}$ model. The crossover between the mushroom and the brush regime is found at relatively low densities. As the solvent quality decreases the cross-over between the coil and brush regime is found at higher densities, and the power law exponent at high densities increases. This is in accordance with the fact that as the solvent quality decreases the polymers are less stretched. As a result, the monomer density in the brush is higher and higher-order virial interactions between monomers are increasingly important. In a Θ -solvent ($\chi = 0.5$) the linear scaling of the surface pressure is found up to relatively high grafting densities. At high densities the power law exponent equals 2 . This is the expected exponent in the case that the brush properties are predominantly determined by third virial interactions, as predicted by $a\text{SCF}$ models. [20,23]

The surface pressure isotherms of grafted *adsorbing* polymers are given for several chain lengths in Figure 2.2. The polymers have an attractive adsorption energy of $1 k_B T$ per monomer, $T = 298$ K, l is again 0.35 nm and χ is set zero. This parameter set represents a grafted polymeric system in a good solvent with an appreciable surface affinity. Density distributions of such brushes were calculated by Bijsterbosch *et al.* and presented the following picture. [69] At low σ the polymers have a pancake conformation due to attractive interactions with the surface, nearly all monomers are close to the surface. At sufficiently high σ the monolayer at the surface is filled, and excess monomers are forced into the solvent by steric interactions. The grafting density at which this transition takes place corresponds roughly with a filled monolayer, $\sigma \sim (Nl^2)^{-1}$. At higher densities an increasing fraction of monomers is in the solvent phase and gradually

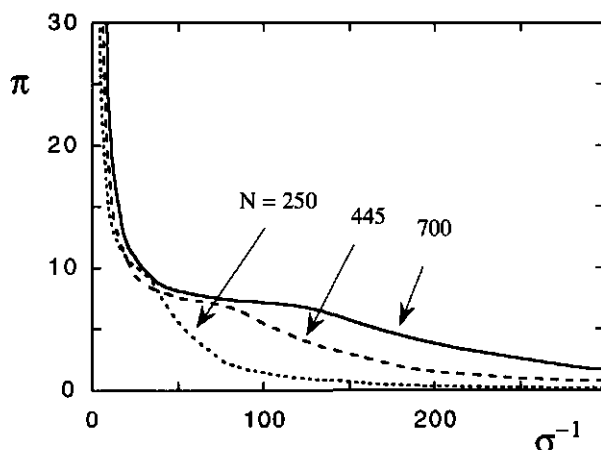


FIGURE 2.2. *nSCF* surface pressure isotherms (in mNm^{-1}) of grafted adsorbing chains as a function of σ^{-1} (in nm^2). Chain lengths are $N = 250$, 445 and 700, $l = 0.35 \text{ nm}$, $\chi = 0$ and $\chi_{\text{sur}} = -1$.

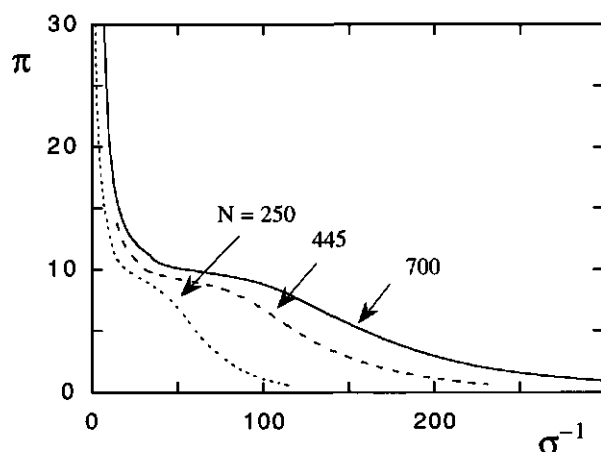


FIGURE 2.3. Experimental surface pressure as a function of σ^{-1} for PS-PEO block copolymers at the air/water interface from ref. 69. PEO-lengths are 250, 445 and 700.

a brush is formed. We note that in the brush regime the density in the monolayer at the surface remains close to unity.

The density distributions are found to correlate with the numerical surface pressure isotherms in Figure 2.2. At low grafting densities the surface pressure increases strongly, due to the filling of the monolayer next to the surface. When $\sigma \sim (Nl^2)^{-1}$ (the pancake-brush transition) a semi-plateau is found, in which the surface pressure increases slowly but continuously with increasing σ . At high grafting densities the surface pressure again

increases strongly with increasing σ , as a result of strongly interacting chains in the brush. The adsorption-desorption transition is continuous in the numerical calculations for this set of parameters. This is also evident from the fact that μ is a monotonically increasing function of σ (not shown).

In Figure 2.3 the experimental isotherms of PS-PEO block copolymers at the air/water interface, measured by Bijsterbosch *et al.*, are presented. [69] The block copolymers consist of short PS-blocks which act as inert anchors, and PEO-tails of lengths identical to those used in Figure 2.2. The polymers are deposited on the air/water interface from a volatile apolar solvent. The surface pressure of the block copolymers is measured continuously at room temperature as the layer is compressed in a Langmuir trough. The Θ -temperatures of PEO in water are reported as $\Theta_- = -12^\circ\text{C}$ (UCST) and $\Theta_+ = 96^\circ\text{C}$ (LCST), indicating that water at room temperature is a good solvent. [91,92] From the height of the adsorption-desorption plateau ($9.6\text{--}9.8\text{ mNm}^{-1}$ for $N = 700$) the adsorption energy per PEO-monomer is deduced. This is the sum of the effective adsorption energy per monomer ($\pm 0.4 k_B T$) and the critical adsorption energy per monomer ($\pm 0.2 k_B T$). As the air/water interface is not perfectly sharp, an additional entropic contribution must be taken into account. The effective adsorption energy is therefore estimated to be somewhat more than $0.6 k_B T$ per monomer.

Comparison of Figures 2.2 and 2.3 shows that the nSCF model is in semi-quantitative agreement with the experimental data, especially at high densities. The shape of the numerical isotherm, in particular that of the adsorption-desorption plateau occurring at a surface pressure of approximately 8 mNm^{-1} , corresponds well with that of the experimental isotherm. Both the numerical and the experimental isotherms show a continuous increase in π with decreasing area per molecule, i.e. increasing σ . This indicates that the continuous adsorption-desorption transition is modelled in a correct manner. A slightly smaller value for l could be used to match the experimental and numerical isotherms more accurately. Nevertheless, the value for the PEO monomer length as reported in the literature gives a very satisfying agreement. At low densities the behaviour is qualitatively correct but the quantitative agreement is less satisfactory. This is characteristic in general for mean-field models, which cannot cope with lateral inhomogeneities.

At densities above the adsorption-desorption transition density the surface pressure is considered to consist of two contributions: a constant pressure π_{pla} , resulting from a saturated monolayer of adsorbed monomers, and an increasing surface pressure π_b , due to formation of a brush. The plateau value π_{pla} corresponds with the saturated pressure of the adsorbed homopolymer. Experimentally, the saturated surface pressure of a solution of long PEO-chains is reported to be equal to 9.8 mNm^{-1} , indicating that the additional surface pressure upon compression is indeed due to brush formation. [85] For the nSCF isotherm the value of the semi-plateau is estimated to be 8.2 mNm^{-1} .

In Figure 2.4 the surface pressure of the brush, $\pi_b = \pi - \pi_{pla}$, is plotted double-logarithmically against the area per chain of $N = 700$, both for the experimental PEO data and for the nSCF data. A line corresponding with a power law exponent $5/3$ is drawn for comparison. The power law exponent of π_b obtained at high densities approximately

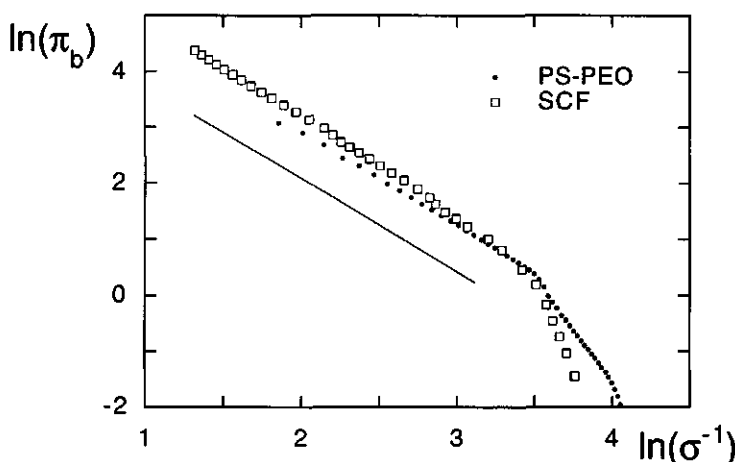


FIGURE 2.4. *Experimental and nSCF π_b vs. σ^{-1} on a double-logarithmic scale for $N = 700$. A line corresponding with a scaling exponent $5/3$ is drawn as an illustration.*

equals the value predicted by scaling relationships of aSCF models. The exact value of the exponent obtained from the PEO data depends slightly on the choice of the plateau value; π_{pla} taken to be 9.6 mNm^{-1} gives 1.58 as an exponent, 9.8 gives 1.67 and subtracting 10 mNm^{-1} results in 1.78. Nevertheless, the experimentally measured surface pressure of the PEO-brush at high densities corresponds with the scaling predictions of aSCF models, and can be reproduced successfully with the nSCF theory.

We note that surface pressure π_b of the PEO brush increases strongly in the double-logarithmic plot at low densities (see Figure 2.4). This is an artifact resulting from the necessary subtraction of π_{pla} . At total surface pressures slightly larger than π_{pla} , the value of π_b is close to zero. In a double-logarithmic plot a small increase in π_b with increasing σ results in a large increase. Physically, this merely signifies that the grafting density, with respect to the pancake-brush transition density, is not high enough for a brush to be formed.

A comment should also be made concerning the value of the scaling exponent. As discussed in Chapter 1, the AdG blob model predicts an exponent $11/6 \approx 1.83$, whereas the aSCF model predicts an exponent $5/3 \approx 1.67$. This last value is exactly the value obtained when π_{pla} is set equal to 9.8 mNm^{-1} in the experimental PEO data. The exponent of the blob model is significantly higher than the values obtained from the experimental data. This may indicate that the aSCF model gives a qualitative better description of the thermodynamic features of the PEO-brush than the blob model.

It is of interest to examine whether this scaling behaviour is reproduced by all PEO chain lengths. In Figure 2.5 the surface pressure for chain lengths 90, 148, 250 and 700 is plotted in a similar fashion as Figure 2.4. It is found that a regime with a constant power law exponent, as observed both experimentally as numerically for $N = 700$, is not present in the experimental isotherms of short PEO chains. A regime with a constant exponent

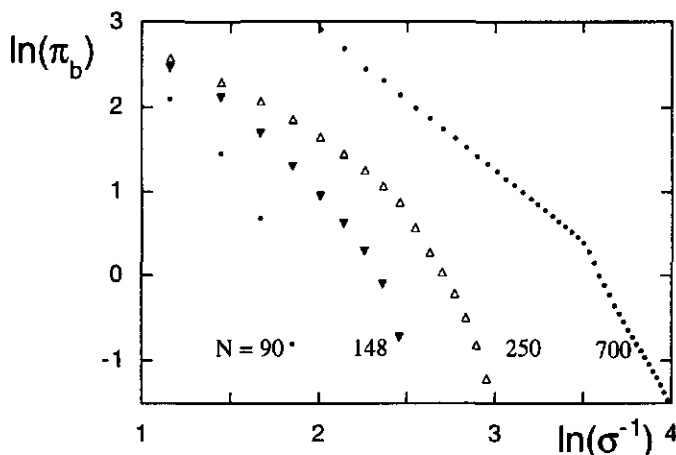


FIGURE 2.5. π_b vs. σ^{-1} for various PEO chain lengths ($N = 90, 148, 250$ and 700). The value of π_b is the same as in Figure 2.4.

is found for PEO chains of 445 monomers, if the plateau value is taken to be slightly lower, $\pi_{pla} = 9.2 \text{ mN m}^{-1}$ (not shown). This observation agrees with the experimental observation of Cao and Kim that in this molecular weight regime the saturated surface pressure of PEO homopolymer increases with increasing molecular weight. [85] The extent of the regime of constant exponent for $N = 445$ is less than that of $N = 700$. These results demonstrate that scaling relationships should be verified experimentally with sufficiently long chains. In the light of this, it is questionable whether MC- and MD-simulations are suitable to examine polymer properties in the brush regime. [37, 76] The chain length used in these studies is often not more than 50 monomers. Figure 2.5 clearly demonstrates that such limited chain lengths lead to higher power law exponents with rather narrow regimes of constant scaling exponents.

With the above results in mind, we re-examine the data for the thickness of the PS-PEO brushes measured by NR. Bijsterbosch *et al.* combined the NR results for the thickness of the PEO layer at high densities in one plot, regardless of the chain length. [69] The fitted power law for H/N vs. σ yielded an exponent 0.41, which is somewhat higher than the predicted $1/3$. The analysis of the surface pressure isotherms, however, demonstrates that only the long PEO chains are expected to be truly in the asymptotic brush regime. In Figure 2.6 the measured thickness for PEO chains of 445 and 700 monomers is plotted double-logarithmically as a function of the number of chains per unit area. Fitting these results to a power law yields an exponent 0.33 for $N = 700$ and 0.35 for $N = 445$. Again, the aSCF model correctly predicts the behaviour of the polymer brush, provided long chains at high grafting densities are examined.

The question now arises why the results from the nSCF model and the experimental PS-PEO system are in good agreement with aSCF models, whereas in the literature it is reported by several authors that such agreement does not exist. [57, 66–68] From our analysis it is evident that the grafting density and surface affinity of the grafted chains

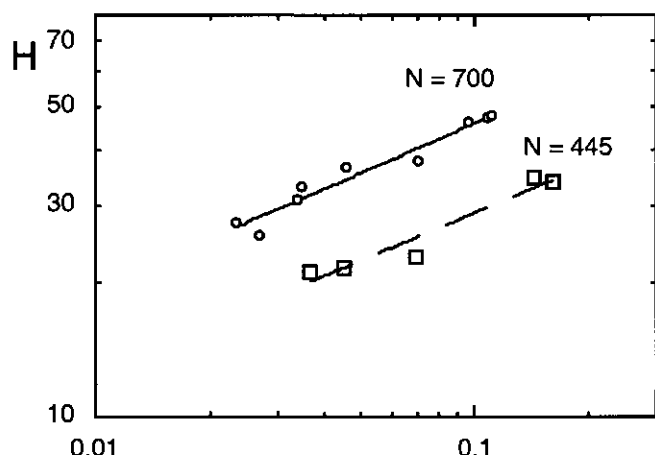


FIGURE 2.6. The experimental brush height H (in nm) vs. σ (in nm^{-2}) for $N = 445$ and 700 on a double-logarithmic scale. The corresponding scaling exponents of the fitted lines are 0.35 and 0.33 , respectively.

must be dealt with in a proper manner to investigate power law dependencies of the surface pressure and brush height. As the subtraction of the saturated surface pressure of PEO demonstrates, it is necessary to know the adsorption behaviour of the bouy block and the contribution of the anchoring block to interpret the total surface pressure. We remark that the small polystyrene blocks used by Bijsterbosch *et al.* are known not to wet the surface; their contribution to the surface pressure has been checked to be zero at the examined surface densities. The measured surface pressure can therefore be completely ascribed to the PEO-chain, and at high σ safely separated into a contribution due to adsorption and a contribution due to brush formation. In the case of block copolymers with anchoring blocks that wet the surface, or blocks that are large compared to the bouy block, the interaction between the anchoring block, solvent interface and solvated block is not known. The assumption is usually made that such activity is a negligible factor. As demonstrated, the surface pressure of the brush is the net difference between total surface pressure and the surface contributions of the anchoring block and the bouy block combined. It is clear that the scaling of the surface pressure of a brush cannot be examined in a reasonable manner without correcting for adsorption effects.

Another problem is the determination of the amount of polymer on the surface. Bijsterbosch *et al.* deposited the PS-PEO block copolymer on the air/water interface using chloroform as a solute. Both chloroform and PS are highly hydrophobic and, when carefully deposited from the air, do not mix with water. The deposited amount is therefore known within a reasonable accuracy. In contrast, Kent *et al.* used either a polymer solution of higher density than the organic bulk phase or dry block copolymer. [67,68,93] Due to loss of polymer during deposition the polymeric density is not known during the experiment and is determined via integration of the neutron reflectivity curves. This

is inaccurate, in particular at low polymeric densities. [65] Such inaccuracy is particularly important when the surface pressure or layer thickness is measured as a function of the grafting density and fitted to a power law. Verification of the scaling law of $H(\sigma)$ is therefore difficult when both parameters are determined by neutron reflectivity and, consequently, this method is sensitive to experimental uncertainties. We return to this point in section 3.3 and 3.5.

To conclude, detailed knowledge of the adsorption properties of the block copolymers is essential for the correct interpretation of experimental results of grafted or irreversible adsorbed polymers. Surface pressure isotherms in combination with the nSCF model can be analysed for identification of the polymer conformation at a given σ . Such identification is necessary for the interpretation of NR results. Moreover, the power law of the surface pressure in the brush regime as predicted by aSCF models is only observed if three conditions are met: (i) the grafting density has to be known accurately, due to the strong dependence of π on σ ; (ii) all contributions to π arising from surface affinity of both the solvated and non-solvated block have to be known and subtracted from the total surface pressure, as these do not contribute to the surface pressure of the solvated brush; (iii) long chains at high densities are necessary to obtain the power law corresponding with the asymptotic brush regime. Especially this last condition is very important: if it is not satisfied, a regime with a constant scaling exponent can not be expected to be found.

2.4. PANCAKE-BRUSH TRANSITION

In the previous section it was shown that the nSCF model correctly models the adsorption-desorption mechanism of the PS-PEO block copolymers, also known as the pancake-brush transition. In this section we numerically investigate the adsorption-desorption transition of grafted polymers of varying adsorption energies and chain lengths in a good solvent; unless specified otherwise χ is set zero (athermal solvent). The transition is expected to become increasingly abrupt as the interaction between the monomers and the surface becomes more attractive. Also, with increasing adsorption energies the total polymer density at which the transition takes place is expected to progressively mirror an adsorbed monolayer of unity density. It is especially interesting to investigate whether the transition becomes first-order in certain regimes or whether it remains continuous throughout.

The behaviour of the surface pressure for various adsorption energies is plotted in Figure 2.7 for a constant chain length ($N = 50$). Along the abscissa axis the total grafted polymer density $\Sigma \equiv \sigma N$ is plotted. The adsorption energies are -1 , -3 and $-6 k_B T$ per monomer. For rather high adsorption energies, the surface pressure of the adsorbed, grafted chains changes abruptly around the transition density ($\Sigma \approx 1$). Below this density the surface pressure is relatively low and corresponds with that of a partially filled monolayer, above the transition density one finds a semi-plateau in $\pi(\sigma)$, corresponding to a monolayer of constant density and partially desorbed chains. The height of the plateau evidently depends on the adsorption energy. With increasing σ (not shown in

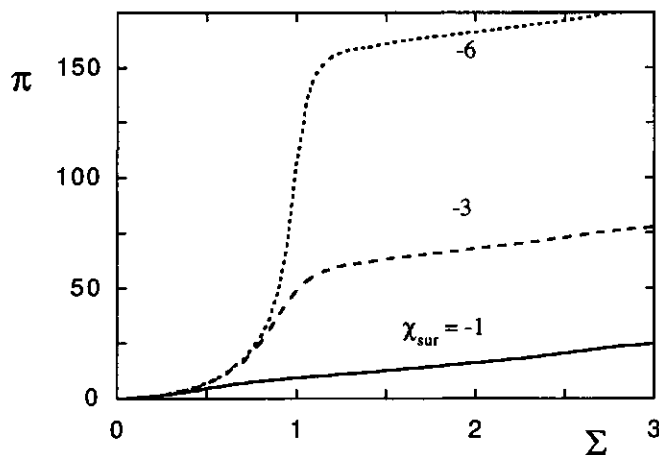


FIGURE 2.7. *nSCF* surface pressure isotherms of grafted adsorbing polymers as a function of Σ for $N = 50$. The monomeric adsorption energies χ_{sur} are -1 , -3 and -6 .

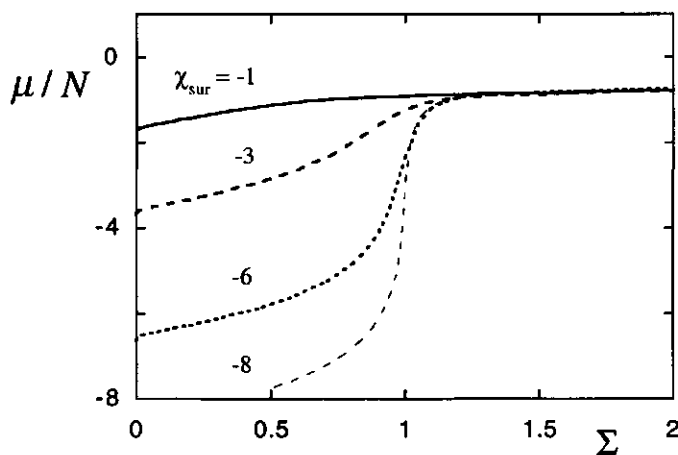


FIGURE 2.8. μ/N as a function of Σ for $N = 50$, $\chi_{sur} = -1$, -3 , -6 and -8 .

Figure 2.7) the surface pressure of the brush develops, and eventually the isotherms for different adsorption energies merge, as the pressure of the brush π_b dominates the constant contribution of the saturated monolayer π_{pla} .

A suitable quantity for examining the behaviour of the system during this transition is the chemical potential μ of the grafted chains. As mentioned in section 2.2, μ is not defined by a bulk concentration. It must be determined from the derivative of Δ with respect to σ . Therefore, μ can be characterised as a thermodynamic function of an independent field σ . In Figure 2.8 the monomeric chemical potential μ/N is plotted as a function of Σ for $N = 50$ and various adsorption energies. Below the transition density

($\Sigma \approx 1$) μ depends strongly on the adsorption energy, as the newly introduced polymer can adsorb at the surface. Above the transition density it is independent of the adsorption energy. The saturated monolayer gives a constant contribution to the free energy and in this regime μ only depends on the chain length and the solvent conditions. The increasing abruptness of the transition is illustrated by the behaviour of μ around $\Sigma = 1$ with increasing adsorption energies in Figure 2.8. The transition remains continuous, however, as is clear from the continuous increase in μ with increasing σ .

The behaviour of μ suggests that for $\Sigma \gg 1$ the development of the polymer configuration is independent of the adsorption energy. For a density as low as $\Sigma \sim 1.2$, μ is virtually equal for all adsorption energies. As μ is defined as the change in Δ with increasing σ , the adsorbed monolayer is concluded to give a constant contribution to Δ . In this regime μ is determined by the increasing polymeric density in the solvent phase. For $\Sigma \gg 1$ μ is solely determined by the entropic contribution to Δ of the desorbed polymer strands (the enthalpic part of the excess free energy is zero as χ is set zero). As in this regime μ converges for all adsorption energies in Figure 2.8, the entropic contribution of the desorbed polymer is apparently independent of the adsorption energy. This agrees with the picture of the brush formation being initiated in the distal part of the polymer layer, i.e. by the tails. This mechanism also excludes a significant role for loops in the proximal part of the adsorbed layer, as a dependence of the loop distribution on the adsorption energy would translate itself in a similar dependence of μ on χ_{sur} . This indicates that the grafted polymer layer consists of a collapsed monolayer of constant density at the surface and a number of tails sticking out into the solvent phase.

Aubouy *et al.* carefully investigated the regime above the overlap density, i.e. $\Sigma \gtrsim 1$. [83] In their model the adsorption of grafted chains is modelled with a distribution of loops, trains and tails, and the excess free energy, height and μ are evaluated with scaling arguments. It is concluded that if Σ is of order unity the polymer layer close to the surface is similar to that of a purely adsorbed layer, whereas in the distal region it resembles a polydisperse brush. They further derive that μ in this regime scales as $\mu \sim \sigma^{5/6}$. Such a power law is not found in our nSCF results. In other respects the physical picture of the scaling approach and the nSCF analysis are in good agreement. The model of Aubouy *et al.* therefore correctly predicts a continuous transition with increasing grafting density. The emphasis on the gradual disappearance of the loop distribution is, however, not observed in the nSCF model.

It is instructive to try to classify the pancake-brush transition, and to relate it to phase transitions in other well-studied systems. In the theory of phase transitions all thermodynamic parameters that are zero in a disordered phase and non-zero in an ordered can be used as an order parameter. To this extent the non-adsorbed conformation may be identified with the disordered phase, and the adsorbed (pancake) conformation with the ordered. Consequently, $\mu - \mu_0$ is recognised as a suitable order parameter, and σ as an external field parameter, where μ_0 is the chemical potential of non-adsorbed chains and μ that of the adsorbed.³ In an Ising model, for example, the analogous

³In the following not $(\mu - \mu_0)$ but $\partial(\mu - \mu_0)/\partial\sigma$ is considered. As $\partial\mu_0/\partial\sigma$ is approximately zero, we neglect this contribution.

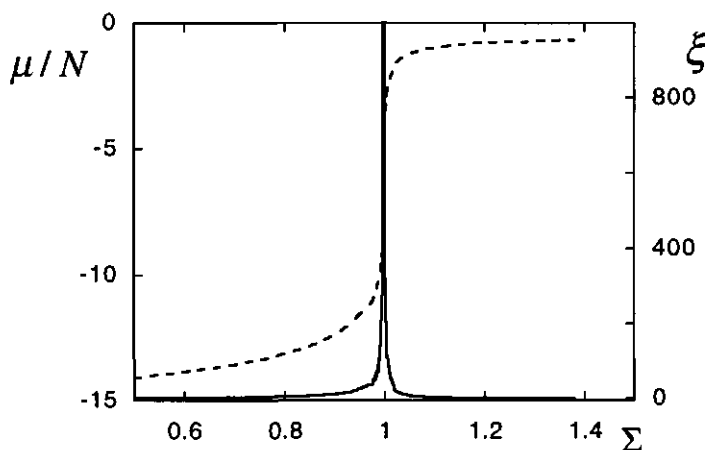


FIGURE 2.9. μ/N (dotted curve) and ξ (solid curve) as a function of Σ , $N = 50$ and $\chi_{sur} = -14.5$.

quantities are the effective magnetisation and the external magnetic field. As χ_{sur} is a temperature-dependent parameter, and the transition becomes sharper with increasing adsorption energies, the analogy between χ_{sur} and the reciprocal temperature in an Ising model is reasonable. We are interested in whether the pancake-brush transition in a good solvent remains continuous under all circumstances. In other words, is the system always found above the critical temperature, or can a set of variables (chain length, adsorption energy) be derived for which the change in μ is discontinuous? The latter behaviour is characteristic for a first-order transition, for instance the non-zero magnetisation of a ferromagnet in a zero magnetic field below its critical temperature. [94, 95]

In Figure 2.9 μ/N and its derivative with respect to the total polymer density,

$$(2.12) \quad \xi \equiv N^{-1} (\partial\mu/\partial\Sigma)$$

are plotted in the neighbourhood of the critical polymer density ($\Sigma = 1$). The length of the chain is 50 monomers, the adsorption energy $\chi_{sur} = -14.5$. In this regime μ remains a continuous increasing function of σ ; its derivative ξ with respect to the polymeric density at $\Sigma = 1$ is close to divergent. This derivative may be interpreted as a monomeric conformational susceptibility. This quantity is a measure for the change in polymer conformation with varying σ . It is evident that the near-divergence of ξ indicates a strong change in conformation around $\Sigma = 1$. This should correspond to the change from a totally flat conformation (pancake) to a partially desorbed conformation. The curve of μ is similar to that of the magnetisation M of a ferromagnet as a function of the external field \mathcal{H} (not to be confused with the brush height H) at a temperature slightly above the critical temperature. In this case the magnetisation changes strongly with small changes in \mathcal{H} around $\mathcal{H} = 0$. Consequently, the curve of ξ is similar to the so-called λ -curve of the susceptibility $\chi \equiv (\partial M/\partial\mathcal{H})$ of a ferromagnet at a temperature close

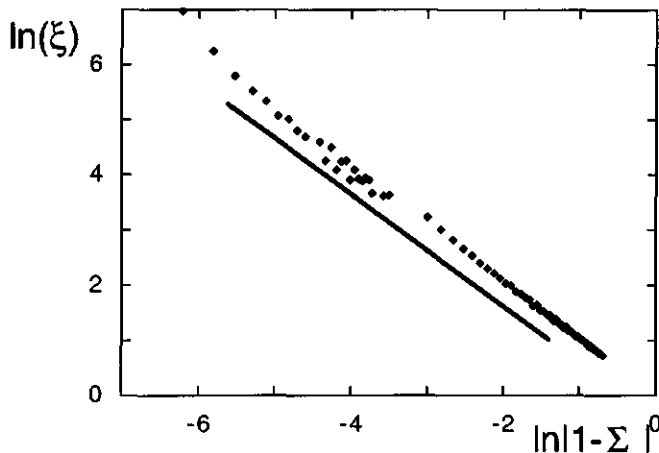


FIGURE 2.10. *Scaling behaviour of ξ as a function of $|\Sigma - 1|$ in the proximity of the critical density $\Sigma = 1$ for $N = 50$ and $\chi_{sur} = -14.5$. A line corresponding with a scaling exponent -1 is drawn as an illustration.*

to the critical temperature. Such behaviour is a fingerprint of a continuous transition approaching the critical point. [95,96]

The theory of phase transitions and the renormalisation theory of critical phenomena describe the behaviour of thermodynamic quantities in the vicinity of a critical point. The majority of the derived relationships account for the behaviour of such quantities at the critical point. An exception, however, is the derivative of the order parameter to an external field parameter at constant temperature close to the critical temperature, for example the magnetic susceptibility or, in our case, the conformational susceptibility ξ . In a magnetic system the magnetic susceptibility changes strongly around zero external field, in the pancake-brush transition ξ changes strongly around $\Sigma = 1$. According to renormalisation theory the scaling exponent of these quantities as a function of the external field parameter for small values of the external field equals -1 in a mean-field model, both above and below the critical temperature. [96] In Figure 2.10 ξ is shown as a function of the reduced density $|1 - \Sigma|$ for $\chi_{sur} = -14.5$ and $N = 50$ in a double-logarithmic plot. A line with an exponent -1 is drawn as an illustration. The increase in ξ corresponds nicely with the power law $\xi \sim |1 - \Sigma|^{-1}$. The behaviour of the strongly adsorbed, grafted polymers in the mean-field model therefore exhibits standard mean-field critical behaviour in the limit of high adsorption energies.

We now need to examine two asymptotic limits to verify that in the nSCF model the adsorption-desorption transition never reaches its critical temperature, namely the limit for finite chain length and infinite adsorption energy, and that of finite adsorption energy and infinite chain length. If ξ remains finite in both asymptotic limits the adsorption-desorption transition is continuous in the nSCF model for all parameter sets. In Figure 2.11 the maximum of ξ for $N = 50$ is logarithmically plotted as a function of χ_{sur} . It is found that at high adsorption energies ξ_{max} scales as $\xi_{max} \sim (-\chi_{sur})^\nu$ where

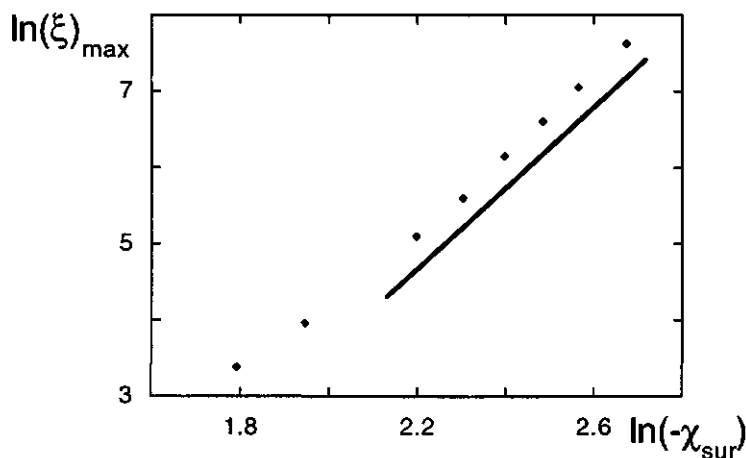


FIGURE 2.11. ξ_{max} in the proximity of $\Sigma = 1$ for various adsorption energies on a logarithmic scale. The scaling exponent of the line drawn is 5.

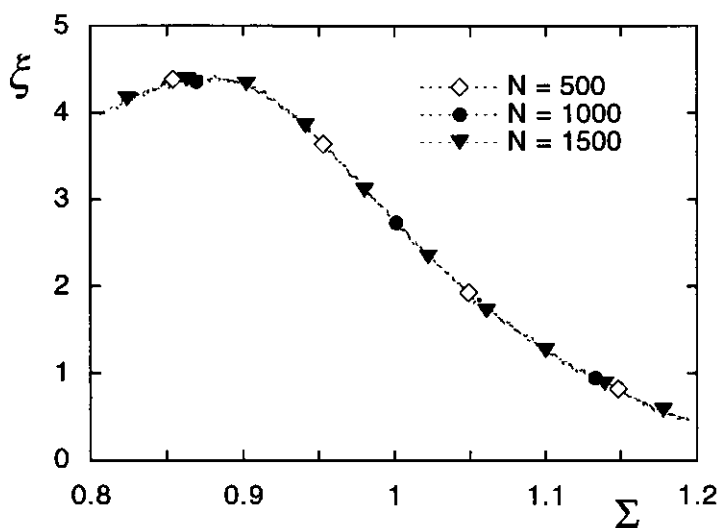


FIGURE 2.12. ξ as a function of Σ for $\chi_{sur} = -3$ and $N = 500$ (diamonds), 1000 (circles) and 1500 (triangles).

ν is approximately 5. Therefore, a true divergence of the monomeric conformational susceptibility is only found at infinite adsorption energy for a finite chain length. The pancake brush transition for finite chain lengths is therefore continuous for all adsorption energies.

The behaviour of ξ is examined for various values of N at constant χ_{sur} in Figure 2.12. Three chain lengths are used, $N = 500, 1000$ and 1500 . It is found that the change of ξ during the pancake-brush transition for a finite adsorption energy is independent of

the chain length. This agrees with the interpretation that primarily tail-ends of grafted polymers desorb during the pancake-brush transition. The entropic gain by desorption of a monomer at high surface affinity and increasing surface density is independent of the total chain length. The chain length therefore plays no significant role in this transition and the transition remains continuous for an infinite N at finite adsorption energies.

2.5. CONCLUSIONS

In this chapter we have examined grafted polymer chains with surface affinity in a good solvent from two different viewpoints. In section 2.3 it is shown that there is a semi-quantitative agreement between the isotherms calculated with the Scheutjens-Fleer nSCF model and the experimental isotherms of irreversibly adsorbed PS-PEO block copolymers at the air/water interface. It is concluded that the pancake-brush transition of the tethered PEO is reproduced in a correct manner in the numerical calculations. The experimental adsorption-desorption transition of the grafted chains is characterised by a semi-plateau in the surface pressure isotherm. This plateau is reproduced nicely by the nSCF model using experimental values for parameters as the chain length, grafting density and monomeric adsorption energy.

It is also concluded that both the experimental surface pressure isotherms of PS-PEO and the numerical isotherms obey the aSCF scaling law of $\pi(\sigma)$ for brushes. In order to verify this scaling behaviour it is important to correct for adsorption contributions of the grafted polymers to the surface pressure. The predicted scaling law of the asymptotic brush regime is found experimentally only for long chains. This entails that surface pressure isotherms can be used to identify the brush regimes. Using the isotherms to discriminate the brush regime, the scaling behaviour of the thickness of long PEO-chains at high grafting densities is found to agree nicely with the aSCF scaling law. In the case of short chains the results for the brush height do not obey this scaling law.

In section 2.4 the nature of the pancake-brush transition is investigated with the nSCF model. It is concluded that the transition is continuous for all chain lengths and adsorption energies. This contradicts the model of Ligoure [82], which predicts a first-order transition in the adsorption-desorption process. It does agree qualitatively with the more recent findings of Aubouy *et al.*, who also conclude that the transition is continuous. [83] The mechanism proposed in their paper, a gradual decrease in the loop distribution and subsequent formation of a quasi-brush from a self-similar adsorbed layer, does not agree with our results. We conclude that the pancake-brush transition from an adsorbed monolayer at low σ to a brush at high σ occurs through the gradual desorption of tail-ends; the role of loops in the transition mechanism can be neglected.

It has been shown that the chemical potential μ of grafted chains can be interpreted as a thermodynamic order parameter, which is a function of an external field, the grafting density σ . Using this, the numerical results have been analysed according to the theory of phase transitions. With increasing surface affinity the system approaches a critical point, with the corresponding critical behaviour of the thermodynamic parameters. The critical exponent for the conformational susceptibility corresponds with that of the magnetic

susceptibility of a ferromagnet in a mean-field model. The critical point, at which the character of the transition changes from continuous to first-order, is only reached at infinite adsorption energy. The chain length plays no significant part in the adsorption-desorption transition close to the critical point.

ACKNOWLEDGEMENT

We are greatly indebted to Henri Bijsterbosch for providing the experimental data used in this Chapter.

APPENDIX

In this appendix it is argued why numerical differentiation is necessary to obtain the surface pressure (or the chemical potential) of grafted chains in nSCF models. This is equivalent to demonstrating that the method of Carignano and Szleifer (CS-SCF) for calculating π is generically wrong, i.e. that there is no closed expression for π (a non-differential equation in terms of the monomer density profile and potential field profiles). [29, 30] In the following ref. 29 is denoted as CS1, ref. 30 as CS2.

Within the lattice-based nSCF theory of Scheutjens and Fleer (SF-SCF) it is possible to write the canonical partition function, and thus the free energy, in terms of the optimised set of conformations of the molecules or, equivalently and more convenient, in terms of the equilibrium density and potential profiles (see for instance Evers *et al.* [89]). To rule out possible differences on fundamental grounds, we start by proving the equivalence of the free energy functionals used in the SF-SCF and the CS-SCF approach. This is done by expressing the free energy of Evers *et al.* in the notation as used in CS1. We then point out the problems of obtaining a closed expression for the surface pressure.

A general expression for the dimensionless free energy per unit area is given by Evers *et al.*, namely:

$$(2.13) \quad F = \sum_i \sigma_i \ln \frac{\sigma_i}{q_i} - \sum_{z'} \left[\sum_{A'} \rho_{A'}(z) u_{A'}(z) - \frac{1}{2} \sum_A \sum_B \rho_A(z) \chi_{AB} \langle \rho_B(z) \rangle \right]$$

Here i is the index which refers to the molecule types. The summation over A' is over all monomer types except the surface component, the other two summations run over all monomer types in the system, including the surface component. In Eq.(2.13) σ_i refers to the number of molecules i per unit area and q_i is the corresponding single chain partition function, which is the weighted sum of all possible conformations of molecule i in the system. Finally, the contact energies are accounted for by the Flory-Huggins interaction parameters.

We can reduce Eq.(2.13) to the two-component case, where component $i = 1$ is an end-grafted polymer of length N , and molecule $i = 2$ is the monomeric solvent with a bulk density unity. The result is simply Eq.(2.8) in section 2.2, which is consistent with Eq.(13) in CS1. The exact correspondence is obvious when one realises that there is a sign difference between the χ parameter in Evers *et al.* and the $\chi|z - z'|$ function in CS1. In addition, the angular brackets $\langle \dots \rangle$ have exactly the same effect as integration over z' in the $\chi|z - z'|$ function of CS1. The short-range energetic interactions are irrelevant for the problem at hand. We can therefore discuss the athermal case ($\chi = 0$) without losing the point.

Defining n as the number of polymer chains in the system and A as the surface area, we may find the surface pressure from the function G by

$$(2.14) \quad \pi = \sigma \left(\frac{\partial F}{\partial \sigma} \right)_A - F = - \left(\frac{\partial FA}{\partial A} \right)$$

which is analogous to Eq.(2.11) The quotient within the first brackets equals μ . We note again that F is a dimensionless free energy per unit area, and that π is dimensionless as well. As all quantities are normalised per unit area, the differentiation to the surface area is not operational. Consequently, it is necessary to differentiate F with respect to σ . The problem with an analytical differentiation of F with respect to σ is that both the single chain partition function q and the Lagrange field $u_0(z)$ (see Eq.(2.1)) are a function of σ . Thus, the chemical potential of the grafted chains can only be found by 'measuring' the change in F when σ is changed slightly. We have checked that if we do this operation numerically in the limit of very low surface coverages, we find that the surface pressure approaches the ideal gas law (see Figure 2.1). Moreover, we checked that Gibb's law, which in the case of grafted polymers can be written as $\partial\pi/\partial\mu = \sigma$, is obeyed rigorously.

In CSII the $\sigma \ln \sigma$ term of Eq.(2.13), i.e. the translational entropy of the grafted chains, was dropped by arguing that this term is only necessary when there is no chemical grafting. We believe that this is not allowed; the effect is that in SCII the ideal gas limit for the surface pressure is not recovered. Following this argumentation, however, the free energy is given by: $F = -\sigma \ln q - \int_z u'(z)dz$. Inserting this in Eq.(2.14) we find for the surface pressure:

$$\begin{aligned}
 \pi &= \sigma \frac{\partial F}{\partial \sigma} - F = \sigma \left[-\ln q - \sigma \frac{\partial \ln q}{\partial \sigma} - \frac{\partial \int_z u'(z)dz}{\partial \sigma} \right] + \sigma \ln q + \int_z u'(z)dz \\
 &= -\sigma^2 \frac{\partial \ln q}{\partial \sigma} - \sigma \frac{\partial \int_z u'(z)dz}{\partial \sigma} + \int_z u'(z)dz \\
 (2.15) \quad &= \sigma^2 \int_z \rho(z) \frac{\partial u'(z)}{\partial \sigma} dz - \sigma \frac{\partial \int_z u'(z)dz}{\partial \sigma} + \int_z u'(z)dz
 \end{aligned}$$

where we have used a generic property of SCF theories that $\partial \ln q = \int_z \rho(z) \partial u'(z) dz$ in the absence of short range interactions. When subsequently σ^2 in Eq.(2.15) is **wrongly** replaced by σ , the CSII result (corresponding to Eq.(7) in this paper) is found in just a few steps:

$$(2.16) \quad \pi = \int_0^\infty u'(z)dz - \sigma N \propto (\sigma N)^2 + O(N\sigma)^3 \dots$$

On the right-hand-side of Eq.(2.16) we have used the fact that the Lagrange field can be approximated by:

$$\begin{aligned}
 u'(z) &= -\ln \frac{\rho_0(z)}{\rho_0^b} = -\ln \frac{1 - \rho(z)}{1 - \rho_p^b} \\
 (2.17) \quad &\approx \frac{1}{2} (\rho(z) - \rho_p^b)^2 + O()^3
 \end{aligned}$$

Here, ρ_p^b is the density of polymer in the bulk, which in our case of grafted chains in contact with a pure solvent is equal to zero. Clearly the result of Eq.(2.16) does not comply with the ideal gas law for low surface coverages, as was also concluded in CSII. We note again that the ideal gas contribution can be retrieved in Eq.(2.16) if in the free energy equation the term $\sigma \ln \sigma$ is kept.

It is instructive to consider the case that all molecules in the system can equilibrate with the bulk. This case has been worked out in Evers *et al.* and starts obviously at Eq.(2.13). [89] The surface pressure for a two-component polymer-solvent system can be written as (ignoring again the energetic terms for simplicity):

$$\begin{aligned}
 \pi &= - \left(1 - \frac{1}{N} \right) (\sigma N - M \rho_p^b) + \sum_z u'(z) \\
 (2.18) \quad &\approx \sigma - \frac{M \rho_p^b}{N} \approx \sigma_{ex}
 \end{aligned}$$

where σ_{ex} is the excess number of polymer molecules per unit area at the surface. The result of Eq.(2.18) is the ideal gas law for the surface pressure in dimensionless form (found for low adsorbed amounts). From the above it is clear that it is misleading to think that the Lagrange field profile and the surface pressure are directly linked. In fact, from Eq.(2.18) we find that the Lagrange field contribution cancels out in a first approximation at low excess adsorbed amounts.

It is tempting to use Eq.(2.18) for the case where the polymers are grafted by substituting $\rho_p^b = 0$ in Eq.(2.18). Interestingly, Eq.(2.15) is recovered (including the dropped term). In equilibrium, however, there is a one-to-one relation between the excess number of polymer chains at the surface and the chemical potential of the polymer, and thus with the polymer bulk concentration ρ_p^b . By setting $\rho_p^b = 0$, one needs to set $\sigma = 0$ as well, even when there is a very strong anchor group binding the polymer with one end to the surface. Indeed, for a fixed σ , the bulk density of polymer can practically approach zero when the grafting energy is increased correspondingly. However, at a fixed surface affinity of the anchor group (no matter how high this is), it is always possible to lower the bulk concentration in order to reduce the amount of adsorbed polymers. Thus, the *mathematical* point of no polymers in the bulk, $\rho_p^b = 0$, is only compatible with no polymers at the interface, that is, $\sigma = 0$. Again, we find that Eq.(2.16) is not the correct result for the surface pressure in a system where polymers are grafted to an interface.

We thus conclude that Eq.(2.15) is wrong. The error in the derivation of CS has been identified and a complimentary route to obtain Eq.(2.16) was shown to be wrong as well. Therefore, the only way to obtain the surface pressure in a system that features grafted chains is by numerical differentiation.

Structure of Monodisperse and Bimodal Brushes

ABSTRACT

The structure of monodisperse and bimodal brushes consisting of PS-PEO diblock copolymers at the air/water interface is investigated with neutron reflectivity, and the results are compared with the structure predicted by the Scheutjens-Fleer self-consistent-field lattice model. The monomer density profile of a monodisperse PEO-brush at relatively low and intermediate grafting densities is found to be block-like with an extended tail region, in which the density smoothly decays to zero. At high grafting densities, however, the profile is found to be predominantly parabolic, as predicted by analytical self-consistent-field models. Quantitative agreement is obtained between the experimental measured profiles and those predicted by the Scheutjens-Fleer model. Bimodal PEO-brushes are investigated for three chain length ratio's and mixing ratio's at various grafting densities. It is concluded that at a given grafting density the long chains are more extended in bimodal brushes than in monodisperse brushes at the same grafting density. This additional stretching increases with increasing length of the smaller block or increasing fraction of smaller blocks. The agreement between the Scheutjens-Fleer density profiles and measured density profiles is also good in the case of bimodal brushes.

3.1. INTRODUCTION

A key issue in brush models is the monomer density profile, i.e. the variation in the monomer density as a function of the distance from the grafting plane. Initially, scaling models assumed the monomer density to be constant throughout the brush, the so-called AdG box-model. [17,18] As discussed in Chapter 1, the aSCF model of Milner *et al.* and Zhulina *et al.* predicts the monomer density to decrease parabolically from a finite value at the grafting plane to zero at the edge of the brush. [20,23] The aSCF model, however, only considers the most probable conformation of quasi-infinite long chains. Fluctuations of chain ends at the brush edge and interactions of monomers with the grafting plane are not taken into account.

Studies with nSCF and molecular dynamics models demonstrated that in the case of non-adsorbing polymers a depletion zone appears close to the grafting plane, as the impermeability of the grafting plane is entropically unfavourable. [26,27,78,79] At the edge of the brush an extended tail region is found, which is the averaged result of large fluctuations in the conformation of the chain ends. These fluctuations originate from the fact that the chain ends are weakly stretched in this distal region. [27] The monomer density in the tail region is predicted to smoothly drop to zero with increasing distance from the grafting plane. In nSCF calculations the importance of such fluctuations was found to decrease with increasing chain length and increasing grafting density, as the

degree of stretching of the chains increases with increasing grafting density. The nSCF density profile of long chains at high grafting densities thus closely resembles the parabolic profile predicted by the aSCF model. [26]

Polymer brushes can be investigated experimentally with small angle neutron scattering (SANS) and neutron reflectivity (NR). The information obtained from NR is the spatial distribution of components perpendicular to the reflecting interface. The characteristic length scale on which information may be obtained is roughly 1 to 1000 nm. In NR the reflectivity is measured as a function of the wavevector component perpendicular to the interface $q = 2\pi \sin \theta / \lambda$, where λ is the neutron wavelength and θ the angle of reflection. The measured reflectivity $R(q)$ depends on the neutron refractive index profile perpendicular to the interface. [97] As the neutron refractive index is directly related to the (average) scattering length density nb (where n is the particle number density and b the sum of the scattering lengths of the specific nuclei in the particle), NR probes the number density profile $n(z)$ with high spatial resolution. Subsequently, $n(z)$ can be related to the volume fraction profile of the components in the interfacial layer. In the case of polymer brushes this corresponds with the monomer density distribution throughout the brush.

In refs. 52, 53, 67, 69, 93 and 98 the overall brush properties (the brush height H as a function of N and σ) in various systems were examined with SANS and NR. The density profile of the brush was not considered in detail in these papers. The results of Auroy *et al.* for H as a function of N and σ agreed with the aSCF scaling laws [52, 53], whereas others reported no agreement with the same scaling laws. [65, 69, 93]

Karim *et al.* observed a parabolic profile, corrected with a tail region, for PS-brushes in toluene. [56] In this study, however, a single grafting density was investigated at various solvent qualities, and the above scaling laws for H and π were not examined. Field *et al.* also considered the density profiles of PS in toluene, but had four different chain lengths at a fixed grafting density. [80] Both studies showed a parabolic profile to fit the data well, although Field *et al.* also reported a good fit with an error function.

Bijsterbosch *et al.* investigated PS-PEO diblock copolymers deposited on an air/D₂O interface using NR. [69] The aSCF scaling laws for the brush height as a function of σ were found to disagree; a power law exponent 0.41 instead of the predicted 0.33 was reported for the scaling relationship $H \sim \sigma^\nu$. Also, the measured reflectivity of the PS-PEO monolayers was not high enough to consider the density profile in detail. In the previous chapter, however, we demonstrated that the PEO brushes do corroborate the predicted aSCF scaling laws for the brush height and surface pressure, provided (i) long chains are used ($N \gtrsim 450$), (ii) the grafting density is high enough and known accurately, and (iii) the surface activity of the grafted chain (in this case the PEO block) is taken into account.

In this chapter we examine the structure of the PS-PEO brushes using NR under conditions where the aSCF scaling laws are expected to be valid, using the results of Chapter 2. The brush of a known chain length ($N = 700$) is investigated at various grafting densities. The grafting density is varied at fixed chain length via compression of the polymeric monolayer in a Langmuir trough. In order to interpret all data in a

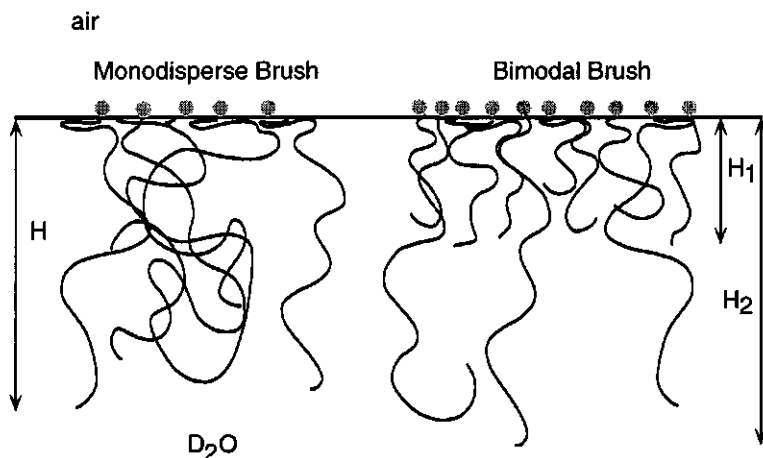


FIGURE 3.1. a graphic representation of a monodisperse and a bimodal PEO-brush at the air/water interface. The gray spheres represent the PS anchoring blocks, H_1 and H_2 the thickness of the layer of relatively short and long chains, respectively.

consistent way, the density profiles obtained from NR-fits are compared with the nSCF profiles using the same parameter set that gives good agreement between experimental and numerical surface pressure isotherms, see Chapter 2.

The brush architecture can be varied by mixing two different chain lengths at a certain mixing ratio, resulting in a so-called bimodal brush. Such brushes can be viewed upon as model systems for polydisperse brushes, which contain several different chain lengths. Analyses of bimodal brushes of chain lengths N_l and N_s with aSCF and nSCF models demonstrate that, provided the ratio N_l/N_s is large and the mixing ratio within 'reasonable' limits, the brush effectively consists of two regions: (i) a proximal region close to the grafting plane in which the shorter chains reside, and in which the longer chains are locally highly stretched, and (ii) a distal region in which the bulk of the monomers of the longer chains is found. [99–102] A schematic illustration of a monodisperse and a bimodal brush is given in Figure 3.1. Variation of the grafting density, mixing ratio's and length ratio's of the chains affects the structure of the grafted layer.

In this chapter the density profiles of bimodal PEO brushes at the air/water interface are also analysed using NR and compared with nSCF calculations. Comparison of the nSCF density profiles with those obtained by analysis of the NR-spectra may provide insight in the brush architecture.

The structure of this chapter is as follows: in section 3.2 the experimental details of the preparation of PEO brushes and the analysis of the NR-data are briefly discussed. In section 3.3 the results for monodisperse PEO brushes are examined, in section 3.4 those

of bimodal PEO brushes. Finally, in section 3.5 we discuss the results and present our conclusions.

3.2. MATERIALS AND METHOD

The PS-PEO block copolymers were synthesised in the group of Dr. G. Riess, Mulhouse, France. [103] The polymers used in this study consist of a PS block of 38 monomers and of a PEO block of 148, 250 and 700 monomers. The reported polydispersities are 1.15, 1.2 and 1.25, respectively. The block copolymers were dissolved in chloroform and deposited on an air/D₂O interface in a Langmuir trough using a Hamilton microsyringe. The D₂O (99.8 %) was purchased from Acros. The surface pressure of the interface was measured with a Wilhelmy plate during the NR measurements. All measurements of the spread layers were performed at room temperature. Due to the fact that a small fraction of the polymer sample consists of PEO homopolymer, the polymer layer was first compressed far above the saturated surface pressure of PEO, i.e. 10 mNm⁻¹, as discussed in Chapter 2 and ref. 69. This ensures that the homopolymer is forced into the water phase, and the remaining monolayer consists solely of PS-PEO block copolymer. The surface pressure of the resultant layer remained constant during measurement. This indicates that the polymeric layer is stable and that no material, other than the PEO homopolymer, is lost during measurement. More details on the preparation of PS-PEO monolayers are given in ref. 69.

The NR measurements were performed on SURF at ISIS, Rutherford Appleton Laboratory, U.K. Three reflection angles were used, 0.4°, 0.8° and 1.5°, and the period of measurement was 30, 100 and 200 minutes, respectively. The information obtained with NR is the spatial distribution of components perpendicular to the reflecting interface. As solely the specular reflectivity of the reflected beam is measured, the phase information in plane with the reflecting interface is lost. The specular reflectivity is measured as a function of the wave vector component perpendicular to the interface $q = (2\pi/\lambda) \sin \theta$, where λ is the neutron wavelength and θ the angle of reflection. The reflectivity $R(q)$ depends upon the neutron refractive index profile perpendicular to the interface, here defined as the z -direction. The neutron refractive index is directly related to the scattering length density (SLD) $\Gamma = 4\pi nb$, where n is the particle number density and b the sum of the scattering lengths of the specific nuclei in the particle.

Since the phase information is lost in the neutron detection, inversion from a certain reflectivity spectrum $R(q)$ to a SLD profile is not direct, and is usually done by fitting a chosen model to the experimental data. The model of the SLD depth profile is divided in a predetermined number of layers. The thickness, SLD and interfacial roughness of each layer can be fitted to the experimental data. Under the assumption of ideal mixing (no volume contraction upon dissolvment) the SLD profile of a polymer adsorbed or end-grafted at the air-solvent interface can be expressed in the volume fraction $\rho(z)$ of the polymer, the SLD Γ_p of pure polymer and that of pure solvent Γ_s , according to

$$(3.1) \quad \Gamma(z) = \rho(z)\Gamma_p + (1 - \rho(z))\Gamma_s$$

To summarise, the measured neutron reflectivity of the grafted polymeric layer can be related to a depth profile of the polymer volume fraction.

In this chapter the NR-spectra were interpreted using weighted least-squares fitting of the calculated reflectivity of the presupposed model to the experimental data. The NR-spectra of the monodisperse brush in D₂O were analysed using two models for the volume fraction of the tail region, namely a parabolic profile,

$$(3.2) \quad \rho(z) = \rho(0) \left(1 - \frac{z^2}{H^2}\right)$$

for $z \leq H$, and a block profile (single layer) with roughness

$$(3.3) \quad \rho(z) = \rho_b \left(1 - \operatorname{erf}((z - H)/\zeta_b \sqrt{2})\right)$$

where ρ_b is the volume fraction of the polymer block, and H is the brush thickness. The tail region of the adsorbed polymers is modelled by an error function [104], for which ζ_b is a measure for the decay length of the roughness. During fitting, the error function is cut off within the thickness of the smallest layer. Therefore, ζ_b should be smaller than the layer thickness not to give large discontinuities in $\rho(z)$. In the case of bimodal brushes $\rho(z)$ is simply the sum of either two parabolic profiles, two block profiles or a combination of both, with each parabola characterised by $\rho(0)$ and H , and each block by ρ_b , H and ζ_b .

The interface of the solution with the air was also modelled with an error function, resulting in the following model for the SLD

$$(3.4) \quad \Gamma(z) = (\rho(z)\Gamma_p + (1 - \rho(z))\Gamma_s) \operatorname{erf}(z/\zeta_{int}\sqrt{2})$$

In the PS-PEO monolayer the roughness of the interface consists of three contributions: (i) the generic roughness of an air/water interface, (ii) the monolayer of adsorbed PEO at the interface, and (iii) the collapsed PS blocks. Characterisation of these three contributions with a single parameter ζ_{int} would appear to be incomplete, as there seems to be no direct relationship between the PS blocks, the adsorbed PEO layer and ζ_{int} . There are two arguments, however, that support the choice to model the above contributions to the total SLD with a single roughness parameter. First, neutrons with a wave vector component perpendicular to the interface q probe length scales in the z -direction in the order of π/q . Because the contribution of the neutrons in a high q -range to the reflectivity is relatively small, the q -range in which relevant information is obtained is limited by the background signal. In our case this background signal was found to be the dominant contribution for values of q larger than 1.2 nm^{-1} . Thus, the information obtained from the reflectivity profile on the structure of the interface is limited. The second argument is that Γ_{PEO} and Γ_{PS} are small compared to $\Gamma_{\text{D}_2\text{O}}$ (Γ_{PEO} is $0.75 \cdot 10^{-3} \text{ nm}^{-2}$, that of PS $1.76 \cdot 10^{-3} \text{ nm}^{-2}$, whereas that of D₂O is $7.96 \cdot 10^{-3} \text{ nm}^{-2}$). It is therefore mainly solvent depletion (the second term in Eq.(3.4)) that determines the total SLD near the air/water interface. The conclusion of both arguments is that the overall contribution of the PS and PEO to the SLD at the air/water interface is small as compared to the SLD of the thick brush layer, so that the interfacial roughness can be approximated by a single roughness parameter.

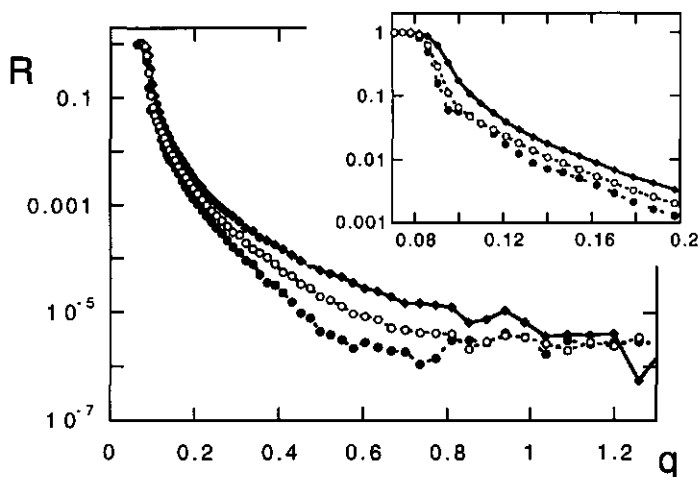


FIGURE 3.2. $R(q)$ of the PEO brushes ($N = 700$) plotted semi-logarithmically as a function of q (in nm^{-1}) for 18 nm^2 per PS-PEO molecule (open circles) and 6 nm^2 (closed circles), together with that of D_2O (diamonds).

In the experiments presented in this chapter the brush region is the subject of interest, rather than the thin adsorbed surface layer. If instead one would be interested the structure of this thin layer, then it can be highlighted by selectively substituting deuterium atoms for hydrogen atoms in the polymer groups of interest in combination with solvent contrast variation. This is already a well established technique in revealing thin layer structures. [105]

The nSCF calculations were done with the Scheutjens-Fleer self-consistent-field lattice model, as discussed in Chapter 2. The same parameter set is used as that for the modelling of the surface pressure isotherms (see Figure 2.2).

3.3. MONODISPERSE BRUSHES

The NR-spectra of monodisperse PEO brushes ($N = 700$) were measured at four grafting densities, all in the brush regime according to the surface pressure isotherms (i.e. $\pi > 10 \text{ mNm}^{-1}$, see Chapter 2). The measured reflectivities R of the PS-PEO layer are plotted semi-logarithmically in Figure 3.2 for two grafting densities as a function of q , together with the reflectivity of pure D_2O . The curve drawn through the symbols is a guide to the eye. The inset in Figure 3.2 shows a part of $R(q)$ at low values of q in more detail. It is clear that the reflectivity curve of PEO is significantly more irregular than the smooth Fresnel curve of D_2O , and that this irregularity is enhanced with increasing grafting density.

This enhanced irregularity is observed more clearly in Figure 3.3, in which the ratio of the reflectivities $R(q)$ and that of the D_2O bulk phase $R_{\text{D}_2\text{O}}(q)$ is plotted for three grafting densities. Evidently, as σ increases the ratio $R/R_{\text{D}_2\text{O}}$ is expected to decrease,

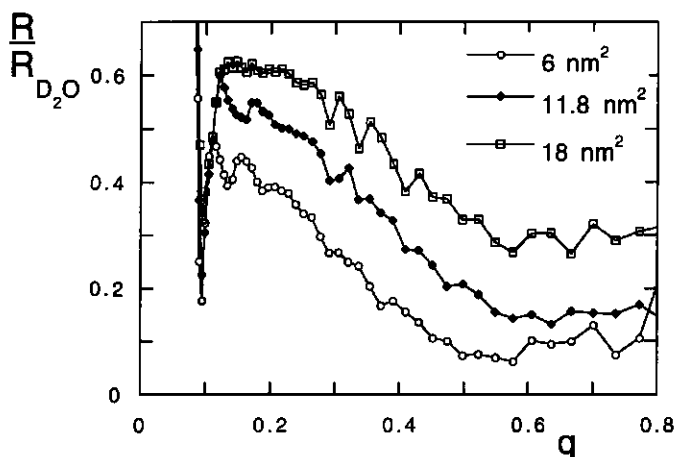


FIGURE 3.3. $R(q)$ of the PEO brushes ($N = 700$) plotted with respect to that of D_2O for three densities.

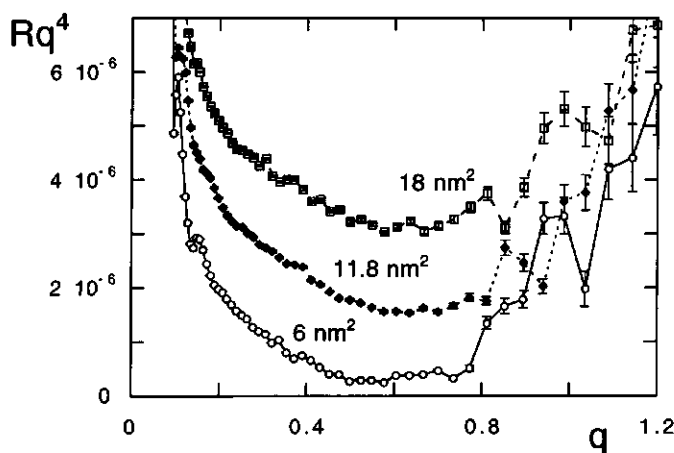


FIGURE 3.4. $R(q)$ of the PEO brushes ($N = 700$) plotted as Rq^4 , with error-bars. For clarity, the data corresponding to 11.8 nm^2 and 18 nm^2 per molecule have been shifted upwards by 10^{-6} and $2 \cdot 10^{-6}$, respectively.

as $\Gamma_{PEO} < \Gamma_{D_2O}$. This is seen in Figure 3.3, in which R/R_{D_2O} decreases strongly with decreasing area per molecule.

In Figure 3.4 $R(q)q^4$ is plotted as a function of q . We remark that for clarity $2 \cdot 10^{-6}$ has been added to the value of $R(q)q^4$ in the spectrum corresponding with 18 nm^2 per molecule, and 10^{-6} to that corresponding with 11.8 nm^2 per molecule in Figure 3.4.

Representation of the grafted PEO layer as a single block with an uniform scattering length density, i.e. a grafted layer of constant monomer density with no roughness, gave no reasonable fit of the NR-spectra for any value of σ . This implies that the decrease

area	π	fit	ζ_{int}	H	ρ	ζ_b	$\Gamma_{D_2O} \cdot 10^3$	χ^2
D ₂ O	0		0.27(2)				7.96(2)	1
18 nm ²	13.8	block	1.01(2)	26.3(8)	0.0818(3)	8(1)	7.35(2)	0.41
		parabola	0.97(2)	34(1)	0.0818(4)		7.33(2)	1.10
14.5 nm ²	15.8	block	1.16(3)	33(1)	0.12(1)	11(1)	7.44(2)	0.54
		parabola	1.12(2)	41(1)	0.0938(4)		7.38(2)	0.67
11.8 nm ²	18.5	block	1.20(2)	33.3(6)	0.121(3)	10.1(7)	7.35(2)	0.54
		parabola	1.20(2)	44.4(9)	0.106(4)		7.19(2)	0.80
6.0 nm ²	35.2	block	1.61(2)	40(1)	0.167(3)	10.1(9)	7.26(2)	1.72
		parabola	1.59(2)	52.2(6)	0.133(5)		7.07(2)	0.94

TABLE 3.1. NR-fit results for monodisperse PEO-brushes of $N = 700$, with the surface pressure π (mNm⁻¹), surface roughness ζ_{int} (nm), brush height H (nm), monomer density ρ , roughness block ζ_b (nm), scattering length density solvent (nm⁻²) and fit quality χ^2 with respect to the fit of pure D₂O. The notation 0.27(2) denotes 0.27 ± 0.02 .

in monomer density in the brush is gradual and not abrupt, in agreement with earlier results. [56,80] In Table 3.1 the values of the fit parameters that give the best fit for a parabolic profile and for a block with roughness are listed. The corresponding areas per molecule are given, together with the surface pressure of the polymeric monolayer (in mNm⁻¹). The ζ_{int} is the roughness of the interface (nm), H is the height of either the parabolic profile or the block (nm), ρ is either the (dimensionless) monomer density at the interface ($\rho(0)$ in the case of a parabolic profile, or the block density ρ_b in the case of a block profile), Γ_{D_2O} is the scattering length density of the subphase, and χ^2 is the fit quality, renormalised with respect to the χ^2 of the pure D₂O-fit. The overall best fit (parabolic or rough block) for a given grafting density, corresponding to the lowest value of χ^2 , is shown in bold face in Table 3.1.

As discussed in section 3.2, the roughness of the interface of the PS-PEO monolayer consists of three contributions: (i) the generic roughness of an air/water interface, (ii) the monolayer of adsorbed PEO at the interface, and (iii) the collapsed PS blocks. In the brush regime the first two contributions to the interface roughness remain approximately constant as σ increases, the third evidently increases with increasing σ . As these three contributions are modelled by ζ_{int} , ζ_{int} is expected to increase with increasing σ . This is confirmed in Table 3.1, where ζ_{int} is seen to increase with decreasing area per PEO chain.

It is instructive to compare the reflectivity curves of the fits of the parabolic and block profiles with the experimental measured reflectivities. In Figure 3.5 the curves of the best parabolic fits are plotted as $R(q)q^4$ vs q for three grafting densities, namely 6, 11.8 and 18 nm² per molecule in the low q -range. (In the following, low σ denotes the lowest measured grafting density and high σ the highest measured. It does not characterise the difference between the coil and brush regime.) The solid curves denote the calculated

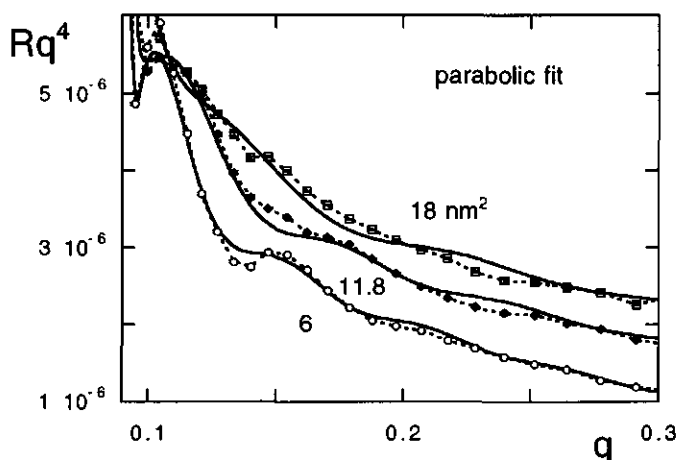


FIGURE 3.5. The measured reflectivities for three areas per molecule (symbols) and calculated reflectivities (solid curves) of the best parabolic fit.

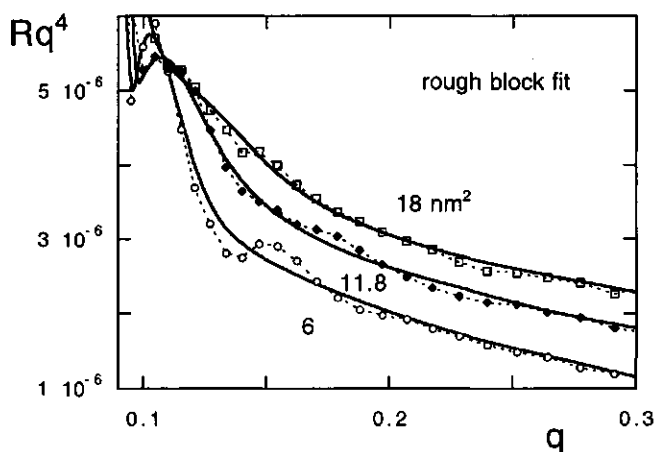


FIGURE 3.6. The measured reflectivities for three areas per molecule (symbols) and calculated reflectivities (solid curves) of the best block fit.

reflectivities of the best parabolic fits, the symbols are the measured reflectivities. In Figure 3.6 the same is done for the fits of block profiles with roughness. From Figure 3.5 it is clear that at low σ (18 nm^2) a parabolic reflectivity curve does not match the reflectivity well, whereas at the highest σ (6 nm^2) the match is quite good. In contrast, in Figure 3.6 the match between the reflectivity of the block profile and the experimental reflectivity is rather good at low grafting densities, and lessens as the grafting density increases.

From Table 3.1 and Figures 3.5 and 3.6 it can be concluded that the best fit for the three lower σ is a block with a significant degree of roughness, whereas that of the highest

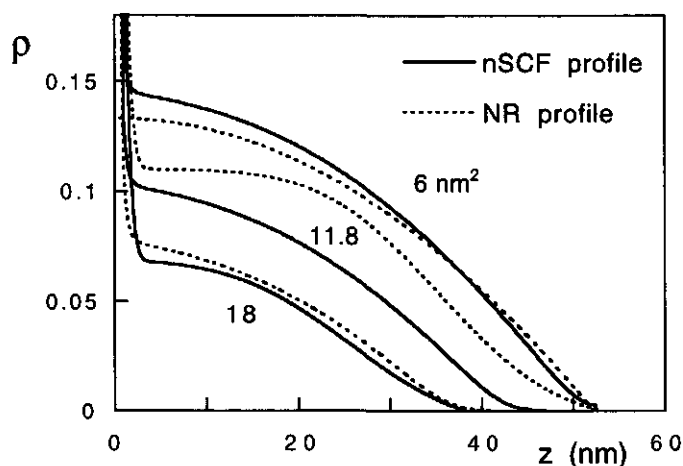


FIGURE 3.7. The *nSCF* density profiles (solid curves) and the profiles of the best NR-fits (dashed curves) for three areas per molecule.

σ is a parabolic fit. However, the difference in fit quality between a parabolic and block profile at the two intermediate values of σ is small, whereas the difference in fit quality at the highest and lowest σ between both profiles is significant. This indicates that the density decay in the PEO brush at high σ is predominantly parabolic, whereas at low σ it is block-like close to the grafting surface and decays smoothly at the brush edge. At intermediate σ the NR-data suggest that the density profile contains features of both profiles.

We can now compare the monomer density profiles obtained from the best fits of the NR-spectra (either parabolic or a rough block) with the profiles predicted by the *nSCF* model. In Figure 3.7 the profiles are plotted for same densities as those in Figures 3.5 and 3.6. The dashed curves denote the profiles obtained from the best NR-fits, the solid curves are the *nSCF* profiles for the same parameters as used in the isotherms in Figure 2.2. The distal tail region, in which the density decreases smoothly towards zero, is found to be relatively extensive in the *nSCF* profile at the lowest σ , i.e. 18 nm^2 per molecule. It can be expected that, provided that the PEO brush indeed has a tail region at this grafting density, it contributes significantly to the reflectivity spectrum. As the grafting density increases the distal region diminishes in size in the *nSCF* profiles and the density profile 'steepens'. At the highest σ (6 nm^2 per molecule) the contribution of the distal tail region to the *nSCF* density profile is negligible, and the parabolic decay of the density is the prominent feature. Therefore, in this grafting regime the parabolic decrease in density may be expected to be the dominant contribution to the reflectivity spectrum of the brush, and the contribution of the tail region may be expected to be negligible.

This corroborates the observed profiles of the best fits of the NR-data, see Table 3.1 and Figure 3.7. At low σ a block profile with a significant roughness resembles the *nSCF* profile nicely. At the highest σ the form of the parabolic profile agrees with the

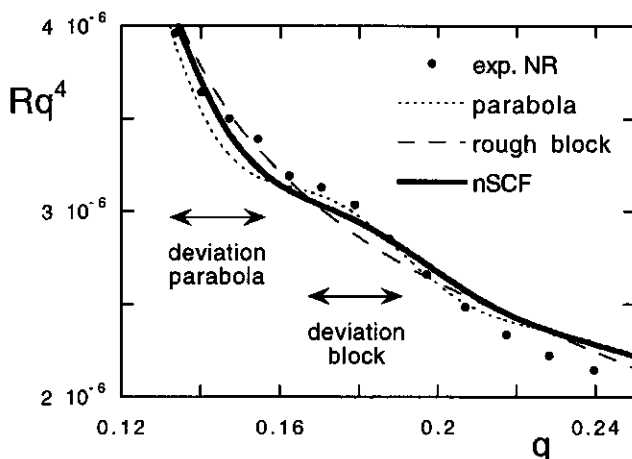


FIGURE 3.8. Rq^4 vs q for the two asymptotic models (rough block and parabola) and Rq^4 following directly from the nSCF profile.

nSCF profile, although the predicted nSCF density is somewhat higher than that of the parabolic fit. At intermediate σ the quantitative agreement between the density profiles is less satisfactory. It can be seen that in this regime the predicted nSCF profile contains features of both (asymptotic) models fitted to the NR-data. It can thus be argued that, due to this combination of features, the quantitative agreement is less than in the case where the nSCF profile corresponds closely to a fitted (asymptotic) model.

To verify this, we have calculated the $R(q)q^4$ directly from the nSCF profile at a density 11.8 nm^2 per molecule (intermediate σ). To do this, we have used values for $\Gamma_{\text{D}_2\text{O}}$ and ζ_{int} equal to those obtained in experimental fits. Again we stress that, apart from insertion of the above parameters, no nSCF parameter has been fitted. In Figure 3.8 we have plotted $R(q)q^4$ vs. q for the parabolic fit (short dashes), rough block fit (long dashes) and nSCF model (thick curve), together with the experimental data (dots). The length scale investigated in the q -range in the figure, given by π/q , corresponds to the distance from the grafting plane at which the characteristic density gradient is found (10 - 30 nm). As seen in Figure 3.8, the reflectivity of the nSCF model follows the curve of the experimental data quite nicely. The optimised fits of a parabolic and block profile, however, have a q -range in which the deviation from the experimental data is significant. These ranges are indicated in the figure by arrows. Although the effects are subtle, Figure 3.8 indicates that in the intermediate σ -regime the nSCF profile, which combines features of the asymptotic block and parabolic model, is a better representation of the experimental density profile than either asymptotic model.

We can thus conclude that a true parabolic density profile, predicted by the aSCF model, is only obtained in brushes of $N \sim 10^3$ at relatively high σ . At low and intermediate values of σ the profile is 'flattened' and the tail region, in which the density smoothly decays to zero, is relatively important. As mentioned in section 3.1, the distal tail region originates from fluctuations in the conformation of weakly stretched chain

σ_{exp}^{-1}	σ_p^{-1}	σ_b^{-1}
6.0 nm ²	5.5 nm ²	5.0 nm ²
11.9 nm ²	8.4 nm ²	8.7 nm ²
14.5 nm ²	10.3 nm ²	11.2 nm ²
18.4 nm ²	16.3 nm ²	19.9 nm ²

TABLE 3.2. The area per molecule according to NR-fits, where σ_p^{-1} is that of the parabolic model and σ_b^{-1} that of the rough block model.

ends. Our results indicate that fluctuations of the chain ends of the grafted chains contribute strongly to the structure of the grafted layer up to high grafting densities. This outcome agrees with the nSCF calculations of Wijmans *et al.* [26]

One could suggest that ζ_b is a measure for the strength of the density fluctuations in the grafted layer. However, as shown in Table 3.1, ζ_b is relatively constant as σ increases. A better measure, in our opinion, is the ratio ζ_b/H . At low σ the ratio ζ_b/H is high and the structure of the grafted layer is strongly determined by the fluctuations. As ζ_b/H decreases with increasing σ , the relative importance of the fluctuations decreases and the structure becomes increasingly parabolic. Evidently, a true parabolic structure is found in the asymptotic limit $\zeta_b/H = 0$.

We remark that the other correction to the parabolic aSCF profiles, the depletion zone near the grafting plane, does not apply to our measurements. As we have mentioned, PEO strongly adsorbs to the air/water interface. [69, 85] A depletion zone only occurs when the grafted polymer does not adsorb to the grafting plane, and is not formed in our system.

It is interesting to determine whether the total monomer density, as obtained by fitting a block and parabolic model to the NR-data, corresponds with that deposited experimentally. Such an integration is used in some studies to determine σ , as this quantity is unknown during the measurement. [93] In Table 3.2 this amount is given for both fitted models, expressed as the area per molecule. It is clear that the agreement between the deposited amount and that according to the NR-fit is reasonable for the parabolic model at the highest grafting density and for the rough block at the lowest. At intermediate densities, however, the deposited and estimated amounts differ up to 30 %. This demonstrates that simultaneous determination of the brush structure and total deposited amount from NR-data is sensitive to the applied model. Moreover, in the case that the fitted model is not suitable for the investigated density regime, the obtained values for σ via fitting of the NR-data can deviate significantly from the experimental values.

Finally, it can be checked whether the aSCF scaling law for the brush height as a function of the grafting density, $H \sim \sigma^{1/3}$, is also obeyed in these NR-measurements. In the previous chapter the aSCF scaling law was concluded to be correct for long PEO chains. If H , obtained by fitting a parabolic profile, is plotted as a function of σ an exponent of 0.36 is found. Interestingly, fitting the results of the rough block yields the

<i>sample</i>	N_l, N_s	<i>mixing ratio $l:s$</i>	<i># measured densities</i>
Bb1	700, 148	1:5	4
Bb2	700, 250	1:5	5
Bb3	700, 148	1:3	3

TABLE 3.3. *The examined bimodal brush layers*

same power law exponent. The height of the layer in the rough block model and that in the parabolic model are found to vary by a constant for the four measured densities, namely 1.3. Although the number of data points is limited, the results corroborate our previous conclusion that the aSCF scaling law of H as a function of σ is valid in the investigated regime.

3.4. BIMODAL BRUSHES

We continue with the analysis of the NR-data for bimodal PEO brushes. Three samples were measured at various grafting densities. The chain lengths, mixing ratio's and number of measurements are listed in Table 3.3. The ratio of chain lengths N_l and N_s in the series Bb1 and Bb3 is approximately 5, that in Bb2 approximately 3. According to the predictions of the aSCF and nSCF models, such ratio's should result in bimodal brush structures. [100,101]

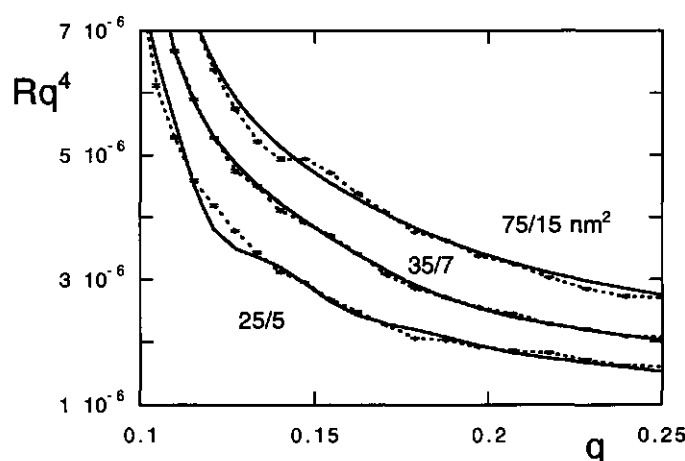
The NR-data were fitted to models consisting of a single block or two blocks with and without roughness, a single and two parabola's, and a combination of a parabola and a block. The total monomer density at a given distance z is simply the sum of the densities of both blocks in the diblock or double parabola model at that distance (or the density of the longer block if $z > H_1$, where H_1 is the height of the brush formed by the shorter chains, see Figure 3.1). In general, a single block or two blocks without roughness did not give a good fit of the NR-data, similar to the NR-fits of the monodisperse brush in section 3.3. Moreover, modelling the layer with a single block and single parabola gave fits of significant less quality than modelling it with two blocks or parabola's.

In the Bb1-series the fit quality of a model of two parabola's and two rough blocks was, roughly speaking, equivalent. The values for the biparabola fit parameters are listed in Table 3.4. In Figure 3.9 Rq^4 is plotted vs. q for a part of the q -range. The points denote the experimental reflectivities, the solid curves are the best fit of a biparabola model. The dashed curves through the experimental points are a guide to the eye. It can be seen in Figure 3.9 that the fitted reflectivities agree quite nicely with the measured ones, although at some values of q the measured reflectivities significantly differ from the fitted. The same result is obtained found when the reflectivities of a model of two blocks are compared with the experimental. This entails that representation of the grafted layer as either a biparabolic structure or the sum of two blocks with an Gaussian-like tail region is reasonable, but does not fully represent the density profiles in the grafted layer.

As can be seen in Figure 3.9, the area per chain of the long chains is quite large, whereas that of the short is relatively small. The large difference in relative grafting

	π	ρ_1	H_1	ρ_2	H_2	χ^2
15, 75 nm ²	11.0	0.063(2)	7(1)	0.0198(3)	27.8(6)	0.85
10, 50 nm ²	11.9	0.099(3)	7.1(9)	0.0470(3)	28.3(8)	1.66
7, 35 nm ²	16.0	0.105(2)	8.5(6)	0.0472(4)	32.4(6)	1.26
5, 25 nm ²	22.3	0.104(3)	12.0(4)	0.0602(3)	34.3(8)	0.75
15, 75 nm ²	12.1	0.0275(2)	11(1)	0.0468(3)	27.8(8)	0.59
12, 60 nm ²	13.0	0.0475(3)	10.2(9)	0.0535(4)	26.9(6)	0.54
10, 50 nm ²	14.2	0.048(3)	14(1)	0.0643(3)	30.0(8)	0.42
8, 40 nm ²	16.4	0.0544(2)	14.8(8)	0.0696(4)	31.9(6)	0.78
6.5, 32.5 nm ²	21.0	0.0694(3)	19.7(6)	0.080(3)	37.4(8)	0.75
10, 30 nm ²	12.1	0.274(4)	1(1)	0.0636(2)	29.0(6)	1.21
7, 21 nm ²	14.7	0.0184(4)	8(1)	0.0743(3)	31.3(5)	0.95
5, 15 nm ²	22.3	0.0629(3)	11.1(4)	0.100(2)	41.3(8)	0.69

TABLE 3.4. Results for biparabola fits for Bb1-, Bb2- and Bb3-series

FIGURE 3.9. Rq^4 vs q for the Bb1-series at three grafting densities. The points denote the experimental reflectivities connected by a dashed curve, the solid curves the reflectivities of the best fits of a biparabolic model.

density between the short and long chains, however, could result in a parabolic structure close to the interface and a more block-like structure in the distal region. This should corroborate the density profile for the monodisperse brush at low σ , discussed in the previous section. To check this, we also fitted the NR-data to a model consisting of a combination of a parabola and a rough block. For the two lowest grafting densities in the Bb1-series this combination gave a slightly better result than a double parabola, for the

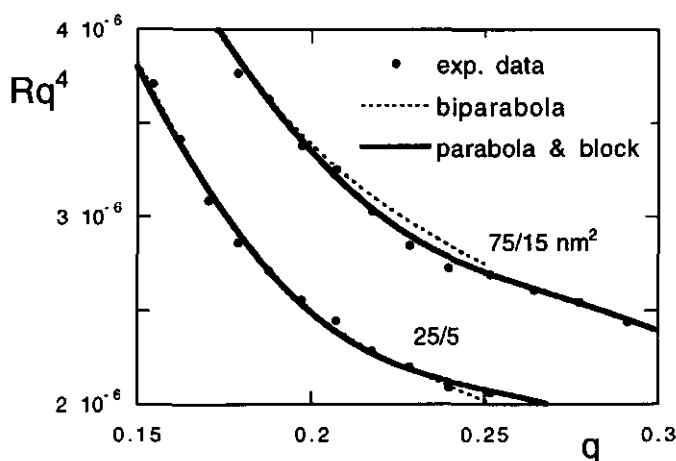


FIGURE 3.10. Rq^4 vs q for a model consisting of a combination of a parabola and a block (solid curve) and a biparabolic model (dashed curve) for two grafting densities.

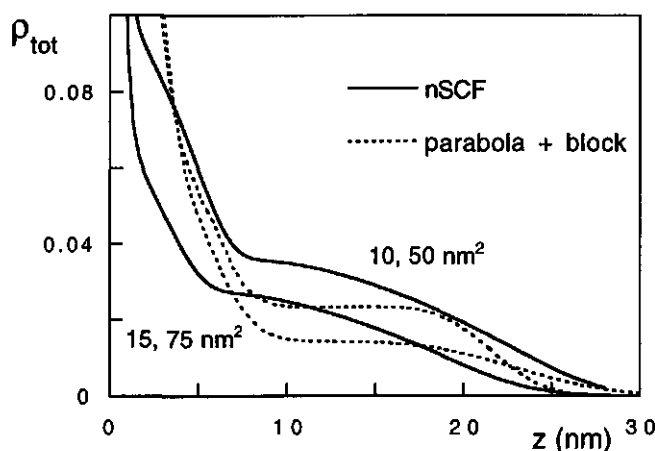


FIGURE 3.11. The nSCF density profiles (solid curves) and profiles of the best NR-fits (dashed curves) for the two low grafting densities in the Bb1-series.

two high values of σ the result was approximately equivalent. The subtle difference in the reflectivity spectra of both models is shown in Figure 3.10 for low σ and high σ . At low σ the biparabolic model has a small but significant deviation from the experimental NR-data at intermediate values of q . This deviation is located at higher values of q than the deviation found for a single parabolic model in Figure 3.8. As the grafting density of the long chains in the Bb1-series at low σ is lower than that in the monodisperse brush (75 nm² and ± 15 nm², respectively) the brushes are less stretched and the q -regime containing information on the density distribution is shifted to larger values of q .

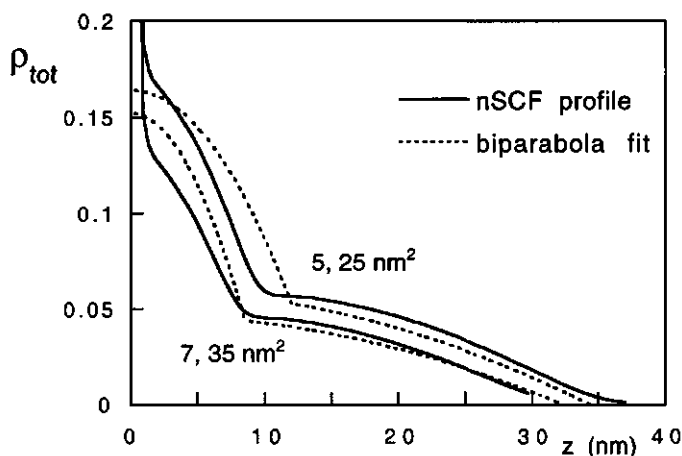


FIGURE 3.12. The nSCF density profiles (solid curves) and profiles of the best NR-fits (dashed curves) for the two high grafting densities in the Bb1-series.

In Figure 3.11 the nSCF density profiles for the two lower grafting densities of the Bb1-series are compared to the profile resulting from fitting a parabola-block model. In Figure 3.12 the nSCF profiles are compared to those of the biparabolic model for the high grafting densities. As mentioned in section 3.2, no free parameters were used to obtain the nSCF density distributions. In the nSCF profiles the monomer density decreases strongly in the inner layer of the bimodal brush, whereas the decay is more gradual in the periphery. This feature is also observed in the NR-profiles. A remarkable feature of both Figures 3.11 and 3.12 is the fact that the height of the inner and outer layers, obtained by fitting the NR-data, is in good agreement with the nSCF profiles. Although the bimodal structure in the nSCF profiles is considerably less pronounced at low values of σ than at high, the fitted thickness of the inner layer agrees well with the predicted thickness. The boundary of the inner layer, i.e. H_1 , corresponds to a sharp change in the density gradient. It appears that the NR-fits are sensitive to the position of this density gradient. The quantitative agreement of the density profiles is good at high grafting densities, but less satisfactory at lower. The reason for this may be the low overall monomer densities in the periphery in this regime, and subsequent small difference in scattering length densities of the polymer layer and subphase.

In Figure 3.13 the profiles of the best NR-fits of the Bb2-series and the concurrent nSCF density profiles are plotted for three grafting densities. The best fit at low σ is that of a parabola-block, at higher densities the best fit is obtained with 2 parabola's. As shown in Table 3.2, the mixing ratio of this series is the same as that of the Bb1-series (i.e. long : short 1:5), but the short block consists of 250 instead of 148 monomers. It is therefore expected that H_1 and H_2 differ less than in the Bb1-series. This is confirmed by the fits of the NR-data. As is the case for the Bb1-series, the agreement of H_1 and H_2 of the NR-fits and the nSCF profiles is good, whereas the quantitative agreement of the monomer density distributions is less.

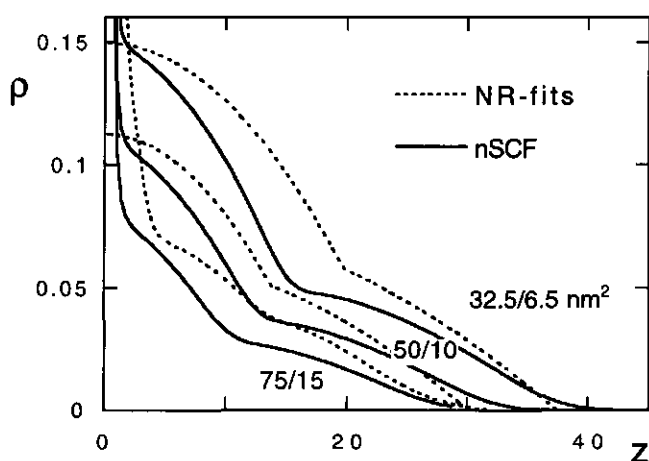


FIGURE 3.13. Same as Figure 3.12 for Bb2-series at three grafting densities.

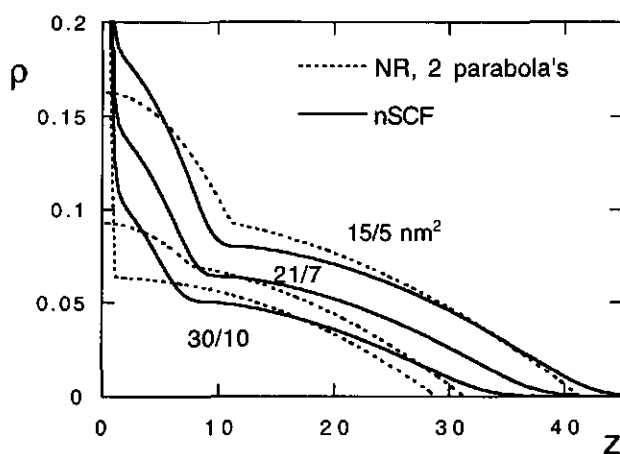


FIGURE 3.14. Same as Figure 3.12 for Bb3-series at three grafting densities.

In Figure 3.14 the same is done for the Bb3-series. The length ratio is the same as in the Bb1-series, but the mixing ratio is 1:3, whereas it is 1:5 in the Bb1-series. As a result, the contribution of the smaller chains in the Bb3-series to the density profile is significantly less than in the Bb1-series. This is clear from the nSCF profiles in Figure 3.14. At the lowest σ the contribution of the short chains to the nSCF density profile is small. This is reflected in the fitted value of H_1 in Table 3.4. No reasonable value for H_1 was found using a model consisting of two parabola's, two blocks or a combination of both. With increasing σ the contribution of the short chains increases, and the quality of the biparabolic fit subsequently increases. Thus, the layer structure, determined experimentally from NR, is consistent with a bimodal structure in the case that in the

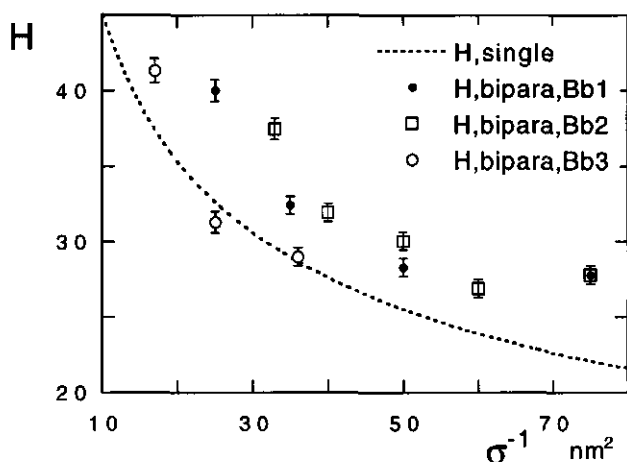


FIGURE 3.15. The additional stretching of the long PEO-chains ($N = 700$) in bimodal brushes as a function of the area per molecule of the long chains. The dotted curve is the fit through the height in a parabolic model of the monodisperse brushes for $N = 700$. The symbols denote the total brush height in the bimodal brushes at the same area per long chain. Error bars denote the estimated uncertainty in H .

nSCF density profile a proximal and distal regime can explicitly be distinguished. At the lowest σ the fit of a model consisting of a single and double parabola is roughly equivalent. In this case the (subtle) bimodal structure, as observed in the nSCF profile, is not obtained from the NR-data analysis.

It is interesting to examine to what extent the long block is additionally stretched due to the presence of the shorter chains. In other words, how far out is the longer chain pushed by the underlying layer. In Figure 3.15 the total height of the bimodal brushes, i.e. H_2 , is shown as a function of the area per long chain. The curve is the power law fit of the parabolic modelled thickness of the monodisperse brush as a function of the area per chain. It is clear that the total brush thickness in the Bb1- and Bb2-series is significantly larger than that of the monodisperse brush, whereas that of the Bb3-series is comparable to it. Moreover, the additional extension of the Bb1-series is less than that of the Bb2-series.

The results in Figure 3.15 can be understood by considering the mixing and chain length ratio's. The mixing ratio of the Bb1- and Bb2-series is equal, but the length of the short block is 148 and 250, respectively. This difference causes the height of the inner layer in the Bb2-series to be higher than that in Bb1 at a given grafting density, and the outer layer to be pushed further from the grafting plane. The length ratio's of the Bb1- and Bb3-series are equal, but the mixing ratio is 1:5 and 1:3, respectively. At a given area per long chain, the number of grafted short chains is much less in the Bb3-series, and therefore the additional stretching of the long chains is less. As follows from Figure 3.15 the number of short chains in the Bb3-series is not high enough to cause a significant

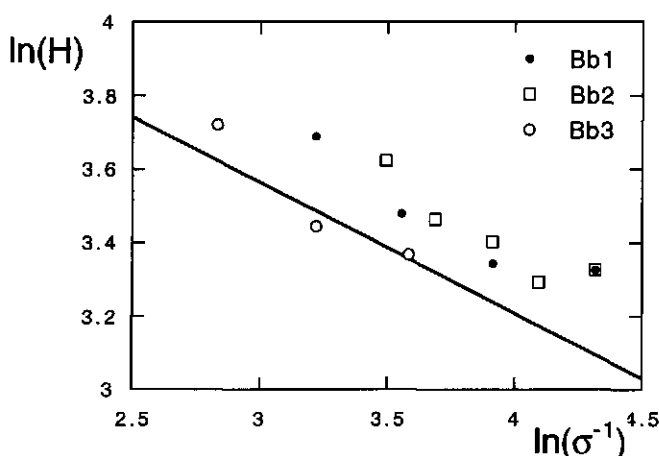


FIGURE 3.16. the results of Figure 3.15 plotted double-logarithmically. The solid line is the fit of results for the monodisperse PEO-brush, with an exponent 0.36. The symbols are the bimodal results.

increase in extension with respect to the monodisperse brush. Therefore, as expected, the thickness of the bimodal brush at a given grafting density of long chains increases with increasing length and increasing grafting density of the shorter chains.

Finally, as predicted by aSCF models for bimodal brushes, the same power law should hold for the overall height as a function of σ in a bimodal brush, at fixed length and mixing ratio, as the one applicable to a monodisperse brush, i.e. $H \sim \sigma^{1/3}$. [99, 100] In Figure 3.16 the overall brush height is plotted as a function of the area per long chain in a double-logarithmic plot. The solid line is the best fit of the data of the monodisperse PEO brush using a parabolic model, the symbols are the results for bimodal brushes. It is clear that the results of the Bb1- and Bb2-series roughly follow the aSCF power law, with the exception of the lowest grafting density. This 'exception', however, is not surprising: at this σ the surface pressure is not far above the saturated surface pressure of PEO and the PEO chains are only partially 'pushed' into the water phase. Thus, the condition of strong stretching of the chains is not met, and the power law for brushes is not obeyed.

3.5. DISCUSSION AND CONCLUSIONS

In this chapter we have investigated both monodisperse and bimodal PEO-brushes at the air/water interface with neutron reflectivity (NR). Analysis of the NR-data using various models and comparison of the resulting NR density profiles with theoretical predictions yields insight in the structure of such grafted layers and how the structure may be controlled.

Monodisperse PEO brushes, consisting of chains of uniform length, are investigated at several (high) grafting densities. Previous examination of the surface pressure isotherms in Chapter 2 demonstrated that at these grafting densities the grafted layer is expected

to assume a brush conformation. Analysis of the NR-data shows that at relatively low grafting densities the monomer density profile of the brush is rather flat and has an extended tail region, in which the monomer density smoothly decays to zero. As the grafting density increases, the gradient in monomer density increases, and at high grafting density the profile is predominantly parabolic. This parabolic profile has been predicted by aSCF models for brushes. The overall increase of the brush height with increasing grafting density is found to obey the aSCF scaling law, i.e. $H \sim \sigma^{1/3}$.

Our results for monodisperse brushes corroborate, and improve upon, the results for PEO brushes of Bijsterbosch *et al.* [69] They contradict, however, those of Richards *et al.*, who concluded that neutron reflectivity is not suitable for investigating the structure of a hydrogenated polymer layer on D₂O. [65] In this chapter we have demonstrated that not only can the height of a hydrogenated PEO brush on D₂O be examined with NR, but also the internal structure of the brush. The reason for the failure of Richards *et al.* to find a brush-like structure of polymethyl-methylacrylate polyethylene-oxide block copolymers spread at the air/water interface is simple: their NR-measurements were performed at surface pressures up to 6 mNm⁻¹, whereas our measurements were done at significantly higher surface pressures (see Table 3.1). Thus, in the study of Richards *et al.* the grafting densities are low, so that adsorption of PEO chains to the air/water interface results in flat structures, also known as 'pancakes'. [69] As shown in this chapter, a true parabolic density profile in the brush is only obtained at very high grafting densities, of order 10 mg m⁻². The grafting densities measured by Richards *et al.* were 0.6 and 1.2 mg m⁻². Clearly, a brush structure cannot be expected at such low densities for adsorbing polymers.

Bimodal brushes were made by mixing two PEO lengths at a given mixing ratio. Analysis of NR-data of such bimodal brushes clearly revealed the bimodal structure of the PEO layer. The small chains are found close to the surface, whereas the long chains protrude through this proximal layer into the bulk phase. It is shown that at a given area per long PEO chain the long chains in a bimodal brush are more strongly stretched than those in a monodisperse brush, due to the presence of the grafted short chains. This additional stretching increases with increasing number of short chains per long chain, and increasing length of the short chains.

The experimental monomer density profiles, obtained by fitting the NR-data to several models, are compared with the density profiles predicted by the numerical Scheutjens-Fleer self-consistent-field (nSCF) model. Good agreement between the surface pressure isotherms of monodisperse brushes in the nSCF model and the experimental isotherms demonstrates that thermodynamic variables, such as the surface pressure, are correctly modelled in the nSCF model. Good agreement between the nSCF model and the experimental results is also found for structural properties, i.e. the monomer density profiles. From analysis of the NR-data it is concluded that the density profile of a monodisperse brush at low grafting density is a relatively flat profile with an extended tail region. This experimental density profile corresponds quantitatively with the numerical profile. At high grafting density the best fit of the NR-data is a parabolic profile, which also agrees well with the numerical. At intermediate grafting densities the numerical profiles display both

a parabolic decay in monomer density and an extended tail region. This is mirrored by the equal fit quality of the NR-data of a parabolic model and a model consisting of a block with extended tail region.

In the case of bimodal brushes the agreement between the NR-data and nSCF profiles for the thickness of both the inner and outer layer is quite good. The quantitative agreement of the density profiles, however, is less good than that of monodisperse brushes. It is shown that in the case that two density regions can not be clearly discerned in the nSCF density profile, a bimodal density profile does not fit the NR-data well.

A small comment can be made with respect to lateral inhomogeneities in the bimodal brush layer. One may ask whether the long and short PEO chains can phase separate into regions relatively rich in short chains and regions relatively rich in long chains. Such phase separation was never observed in the surface pressure isotherms or with Brewster angle microscopy. It can be argued, however, that such phase separation does not occur in the PEO bimodal brushes. Phase separation generally originates from unfavourable energetic interactions, and is tempered by the mixing entropy. In the case of chemically different grafted chains (i.e. PS-PEO and PS-PVP), such unfavourable energetic interactions may be expected. However, as in our study the short and long chains are chemically equivalent, such unfavourable interactions are not present and the mixing entropy ensures a homogeneous monolayer.

We conclude that the combination of NR with nSCF models is an excellent technique for investigating the internal structure of grafted polymeric layers in contact with a solvent in detail. Experimental verification of the predicted layer structure using NR demonstrates the predictive power of nSCF models, whereas comparison of the numerical results with results obtained from fitting various models to the NR-data demonstrates the detail in structure that can be discerned with NR.

ACKNOWLEDGEMENTS

This study was supported by the Training and Mobility of Researchers Programme for Large-scale Facilities of the European Union. We thank J. Webster for his help with the preparation of the NR-data.

Annealed Brushes

ABSTRACT

Brushes consisting of polystyrene-polyacrylic acid (PS-PAA) diblock copolymers were investigated experimentally using three different techniques. The surface pressure π of the block copolymers at the air/water interface was measured as a function of σ for varying salt concentration, PAA chain length and pH. It is concluded that the scaling behaviour of $\pi(\sigma)$ of long PAA-chains in the SB-regime agrees with analytical mean-field models. The scaling behaviour of $\pi(\sigma)$ in the $\tilde{O}S$ B-regime was not observed, due to adsorption of the polyacid chains to the air/water interface. Comparison of the PS-PAA surface pressure isotherms at low pH and no salt with those of PS-PEO diblock copolymers suggests an adsorption/desorption transition in the PS-PAA layer, as the lateral fluctuations in monomer density in the PS-PAA and PS-PEO monolayer are similar. The titration of PAA-brushes in the $\tilde{O}S$ B-regime was followed with reflectometry. The titration curve is observed to shift towards higher pH-values with increasing σ , as predicted by scaling and aSCF models for annealed brushes. Finally, the thickness of PAA-brushes was measured with ellipsometry as a function of pH, ionic strength and grafting density. It is found that at a given pH the brush thickness depends non-monotonically on the ionic strength I , i.e. it initially increases and subsequently decreases with increasing ionic strength. This behaviour agrees with theoretical predictions for annealed brushes in the $\tilde{O}S$ B-regime. The experimental scaling exponent ν in the power law $H \sim I^\nu$ (± 0.1) is less than that predicted theoretically ($1/3$) for the $\tilde{O}S$ B-regime.

4.1. INTRODUCTION

In Chapter 2 and 3 the structural and thermodynamic properties of neutral, adsorbing polymers tethered to a surface or an interface and in contact with a good solvent have been examined in some detail. As briefly discussed in Chapter 1, the behaviour of *annealed* brushes is more complex than that of neutral polymers, as the intrinsic properties of the chains do not only depend on the solvent quality but also on the local environment. A good example of annealed brushes is the case of densely grafted, weak-acidic polymers. The (average) fraction of charged monomers α in such brushes is predicted to depend not only on the pH, but also on the grafting density σ and the salt concentration. [34–36] The result is that the strength of osmotic interactions between monomers, which depends on α , may become a function of σ . In contrast, the strength of osmotic interactions between monomers in a neutral brush solely depends on the solvent quality, and is independent of σ . Two brush regimes for grafted, weak-acidic chains are distinguished as a function of

the salt concentration: (i) the annealed osmotic brush regime ($\tilde{O}S_B$) at low salt concentrations, where the average degree of dissociation α in the brush is much less than the value α_b in the bulk, and (ii) the salted brush regime (S_B) at high salt concentrations, in which $\alpha \approx \alpha_b$.

As mentioned in Chapter 1, the scaling behaviour of $\pi(\sigma)$ and $H(\sigma)$ for polyelectrolyte brushes in the S_B -regime is predicted to be similar to that of neutral brushes, with the monomer-monomer virial coefficient v_0 replaced by an effective coefficient $v_0 \sim \alpha_b^2/\kappa^2$. [25,34,36] The thickness of NaPSS brushes was investigated experimentally by Guenoun *et al.* as a function of the ionic strength at constant grafting density. [71] They concluded that in the S_B -regime H decreases as a function of the ionic strength with the predicted scaling exponent $-1/3$. Surface pressure isotherms of block copolymers with a long hydrophobic (polyethylene) and hydrophilic (NaPSS) block were measured by Ahrens *et al.* [106] However, due to the combined contribution of the anchoring and bouy block to π , investigation of power law exponents of $\pi(\sigma)$ and subsequent identification of conformational regimes was not possible. The thickness of a polybase brush was investigated with NR by An *et al.* [107] The brush thickness at fixed grafting density was found to increase with increasing pH, i.e increasing fraction of charged monomers. However, the results were not compared to any scaling law for annealed brushes in the $\tilde{O}S_B$ -regime.

As we have seen in Chapter 2, valuable information concerning the conformation of grafted polymers may be obtained from analysis of surface pressure isotherms. To this end the $\pi(\sigma)$ -isotherms of PS-PAA block copolymers are analysed at various salt concentrations and pH for two different PAA-block lengths. As is the case for the PS-PEO block copolymers investigated in ref. 69 and Chapter 2, the PS anchor block is small compared to the PAA-block and does not contribute to π .

PAA-brushes are also examined using reflectometry. In general, reflectometry is applied for quantitative investigation of adsorption of polymers or proteins from a bulk solution on a substrate. [108] In section 4.3 we will demonstrate that reflectometry can also be used to obtain information on the (average) charge density in a layer adjacent to the substrate. This leads to titration isotherms of PAA brushes at various grafting densities and low ionic strength.

Finally, the thickness of a grafted PAA-brush at fixed grafting density and varying pH and ionic strength is measured with ellipsometry. Using this technique, we can experimentally check the theoretically predicted non-monotonic behaviour of the PAA brush thickness as a function of the grafting density, ionic strength and pH.

4.2. SURFACE PRESSURE ISOTHERMS

4.2.1. Materials & Method

The PS-PAA block copolymers were synthesised by Polymer Source Inc., Quebec. The investigated block copolymer samples are PS(33)-PAA(368) and PS(36)-PAA(122), and were used as received. The size of the blocks denotes the number of monomers. The reported polydispersities were 1.06 and 1.05. The block copolymer was first dissolved during two days at 60 °C in dioxane, after which toluene was added to obtain a solution

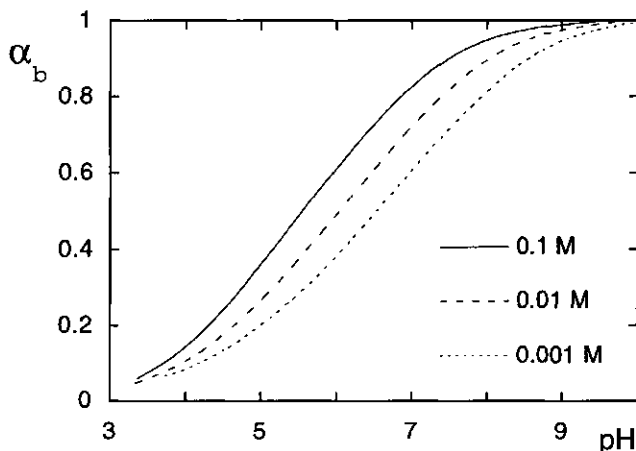


FIGURE 4.1. The bulk degree of dissociation α_b of PAA as a function of the pH for three salt concentrations.

of 1 gl^{-1} in a 60%/40% dioxane/toluene mixture. This mixing of solvents is necessary as PAA does not dissolve in the usual organic spreading solvents, such as pure chloroform or toluene, due to its polarity. With this mix of solvents the density of the spreading solution is lower than that of water, which facilitates deposition. Also, the solvent is sufficiently hydrophobic to prevent loss during spreading. It must be remarked that aged solutions showed hysteresis in the surface pressure isotherms, which is attributed to slow coagulation of the diblock copolymer. Therefore, only the reversible results of freshly prepared solutions are discussed.

Deposition of the polymer solution on the air/water interface in a Langmuir trough was done with a Hamilton precision microsyringe, after which the toluene was allowed to evaporate for approximately 1/2 hour. Typically, 50-100 μl of polymer solution was deposited on the trough interface (600-80 cm^2). The surface pressure measurements were performed with a teflon Langmuir film balance with a moving barrier. The (de)compression rate was standard $10 \text{ mm}^2\text{s}^{-1}$, the temperature $296 \pm 0.5^\circ\text{K}$. The surface pressure was measured continuously with a Wilhelmy platinum plate tensiometer. The sensitivity of the tensiometer is 0.02 mNm^{-1} . Several (de)compression isotherms were obtained during each measurement. The subphase consisted of deionized water to which HCl, NaOH and NaCl (Merck) were added in order to set the pH and salt concentration at the desired value. The deposited block copolymer layer was found to be stable up to surface pressures of order 45 mNm^{-1} . Above this limit, polymer was irreversibly lost in the bulk phase.

4.2.2. Results

For reference, a titration curve of PAA consisting of 7000 monomers in a bulk solution of 0.001, 0.01 and 0.1 M KNO_3 is given in Figure 4.1. KNO_3 is an inert electrolyte, similar to NaCl. The degree of dissociation in the bulk α_b is plotted as a function of

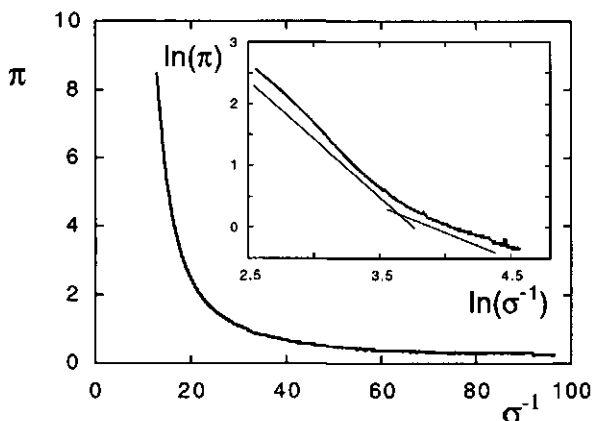


FIGURE 4.2. Surface pressure of PS(33)-PAA(368) (in unit mNm^{-1}) plotted linearly and double-logarithmically (inset) as a function of the area per chain σ^{-1} (nm^2) at pH 4.4 and 0.1 M NaCl. Lines with slopes 0.8 and 1.8 are drawn as an illustration in the inset.

the pH and it increases slightly with increasing salt concentration. The reason for this is the decreasing electrostatic cost of dissociation with increasing ionic strength. If we assume that the titration curve may be characterised by an intrinsic $\text{p}K_a$, then this value is approximately 5.5 for 0.1 M.

For the surface pressure isotherms of the PS-PAA diblock copolymers we start with the simplest system, i.e. relatively weakly charged tethered polyelectrolytes in a solution of high ionic strength. In Figure 4.2 the surface pressure isotherm of PS(33)-PAA(368) at pH 4.4 and 0.1 M NaCl is plotted as a function of σ^{-1} (area per molecule, in nm^2) on a linear scale. In the inset the same isotherm is plotted double-logarithmically. Figure 4.2 demonstrates that two density regimes can be distinguished in the isotherm. At low σ the surface pressure increases slowly, with a power law exponent between 0.7 and 0.9. At high σ the surface pressure increases more strongly, with a power law exponent 1.7 - 1.9. For clarity, two straight lines are drawn in the inset of Figure 4.2 with a slope 0.8 at low σ and 1.8 at high σ . Although it is difficult to pinpoint the grafting density at which the transition from the low density to the high density regime occurs, the cross-over density is estimated to be of the order 35 nm^2 per molecule.

Similar results for a smaller PAA-block, i.e. PS(35)-PAA(122), are shown in Figure 4.3 for pH 4.7 and 0.1 M NaCl. This isotherm has a low density regime with a weak increase in surface pressure, a cross-over to a second regime at higher densities with a high power law exponent (approximately 3) and a third regime at very high densities with again a lower exponent.

It must be noted that a slight hysteresis occurs in the isotherms at 0.1 M; the surface pressure *increases* slightly with increasing number of compression/expansion cycles. This increase in surface pressure excludes the usual cause of hysteresis in such systems,

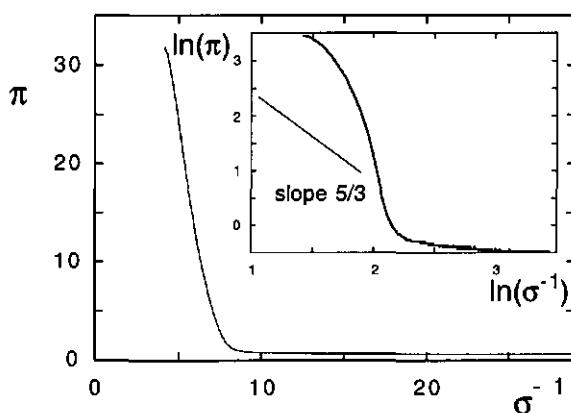


FIGURE 4.3. Surface pressure of PS(33)-PAA(122) plotted linearly and double-logarithmically (inset) as a function of σ^{-1} at pH 4.7 and 0.1 M NaCl.

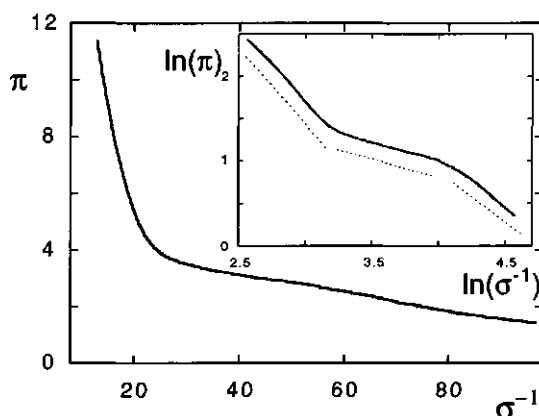


FIGURE 4.4. Surface pressure isotherms of PS(33)-PAA(368) plotted linearly and double-logarithmically (inset) as a function of σ^{-1} at pH 4.7 in the absence of salt. Dotted lines are drawn in the inset as a guide to the eye.

namely loss of material. Evidently, the surface pressure must drop during loss of adsorbed polymers. The hysteresis only affects the magnitude of the surface pressure; the value of the scaling exponents in the double-logarithmic plots and the cross-over densities are identical. This hysteresis is therefore believed to stem from a slow unfolding of the collapsed PAA-block in time after deposition on the air/water interface.

In the absence of salt and at low pH the surface pressure isotherms are markedly different. This is most evident for the long PAA-chains, as shown in Figure 4.4. Three

distinct regimes may be identified in the double-logarithmic plot; one at low density with a relatively high power law exponent (1.5-2.5), an intermediate regime with a low exponent (0.3-0.5), and at high densities again a regime with a high exponent (1.6-2). These regimes, indicated by dotted lines in the double-logarithmic plot in Figure 4.4, are observed in the case of no added salt or low salt concentration (10^{-3} M NaCl) in the pH-regime 3 to 5. The three distinct regimes are also observed in the case of short PAA-chains under similar conditions (not shown).

At pH-values above 5.5 the clear distinction between several scaling regimes in the isotherms is lost, both in the case of added salt (Figure 4.2) and in the absence of salt (Figure 4.4). For 0.1 M added salt the distinct difference of a low and high density regime gradually disappears as the pH exceeds 5.5. The surface pressure at high densities increases more strongly with increasing σ than at low pH, i.e. the exponents in the double-logarithmic plot are higher, but a single power law can not be fitted to the data. In the absence of salt the three distinct regimes in the isotherm disappear as the pH exceeds 5.5. The isotherm at pH 6.5 and no added salt for PS(33)-PAA(368) resembles the isotherm with added salt. There is no regime with a constant well-defined scaling exponent, and the (apparent) exponent increases gradually as the grafting density increases.

4.2.3. Discussion

Using Figure 4.1 the average degree of dissociation of the grafted PAA-chains in the pH-regime 3.5 - 5 with 0.1 M inert electrolyte is estimated to be of order 0.1 to 0.3. The Debye length of the bulk solution is of the order of 1 nm, so the effect of electrostatic screening is strong. The interactions between the dissociated monomers are therefore limited in range, and the value of α of the grafted chains is close to the bulk value α_b . This experimental regime should correspond with the SB-regime proposed in mean-field models. [34, 35] The degree of dissociation in the SB-regime is predicted to remain constant up to high grafting densities at constant pH, due to the excess of inert counterions. [34-36] At low grafting densities, i.e. $\sigma < \sigma^*$, mean-field theories predict the tethered PAA-chains to have a swollen coil conformation, whereas for $\sigma > \sigma^*$ a brush conformation is expected. The transition density σ^* is defined as $1/\sigma^* \approx 4\pi R_G^2$, where R_G is the radius of gyration of the grafted chain. The predicted scaling behaviour of π as a function of σ in the coil and SB-regimes is $\pi \sim \sigma$ and $\pi \sim \sigma^{5/3}$, respectively.

These predicted power laws for $\pi(\sigma)$ correlate roughly with the observed regimes in Figure 4.2. At low grafting densities the surface pressure is low and increases slowly. This corresponds to the regime of weakly interacting swollen coils. The fact that the surface pressure increases less than proportional with σ (the scaling exponent is 0.7 - 0.9) indicates that some conformational organisation may take place. At high grafting densities the tethered PAA-chains develop strong intermolecular excluded-volume interactions, which result in a strong increase in π with increasing σ . A power law exponent of 1.7 - 1.9 is found in this regime, which corresponds roughly with the predicted exponent 5/3 in the SB-regime of mean-field models.

The short PAA chains show a similar SB-regime, but the exponent at high σ is higher than that of the long chains. Moreover, the width of the scaling regimes with constant power law exponents is less. This may be due to the fact that end-effects, which are not taken into account in mean-field models, are relatively important in the case of short end-grafted chains. This agrees with the results for neutral PEO-brushes in Chapter 2, where solely long PEO-chains ($N = 445,700$) are found to obey the mean-field power laws of $H(\sigma)$ and $\pi(\sigma)$. Shorter PEO chains also show a stronger dependence of π on σ , see Figure 2.5.

We may conclude from Figure 4.2 that the transition of the PAA(368) chains from a coil to a brush conformation occurs at $1/\sigma^* \approx 35 \text{ nm}^2$. According to mean-field models, the transition density σ^* is given as $1/\sigma^* \approx 4\pi R_G^2 = cN^{6/5}$, where c is a numerical prefactor that contains, amongst others, the effective virial coefficient v_0 . Inserting the values for PAA(368) we find that c is approximately 0.175. If we use this value to determine the cross-over density of PAA(122) under the same conditions, $1/\sigma^*$ is equal to 9 nm^2 , which corresponds nicely with the apparent transition density in Figure 4.3. Such agreement would not be found if the scaling law for the coil size, i.e. $R_G \sim N^{3/5}$, is strongly disobeyed. Thus, the conformational transition is believed to be a coil to SB transition.

Following the above, it is tempting to also interpret Figure 4.4 using the mean-field theory for annealed brushes in the $\tilde{\text{OsB}}$ -regime, as the low pH (low α) and zero added salt correspond to the specified theoretical conditions. [34, 35] According to this mean-field theory, the polymeric monolayer at low σ (regime 1) consists of weakly interacting, charged chains ($\alpha \approx \alpha_b$). As σ increases (regime 2), the overall degree of dissociation in the brush decreases, see Eq.(1.11). In other words, the chains are effectively neutralised as σ increases. At high σ (regime 3) the brush effectively consists of neutral chains ($\alpha \approx 0$), and the scaling relationships for H and π are predicted to be those of neutral brushes. Regime 1 should correspond with the regime at small σ with the power law exponent of order 2 in Figure 4.4, regime 2 with the intermediate density regime with power law exponent 0.3, and regime 3 with the regime at high σ with an exponent of order 1.8. As we will demonstrate, this interpretation is too simple, due to the fact that it does not consider adsorption effects of grafted PAA to the air/water interface.

To start with, the saturated surface pressure of PAA homopolymer solutions (11K and 29K, 0.01 g l^{-1}) was measured with and without added salt. At pH 3 and no added salt a saturated surface pressure of approximately 3.8 mNm^{-1} was measured. In contrast, the saturated surface pressure in the pH-regime 3 - 5 and 0.1 M NaCl was approximately zero. At pH 5.5 and above the saturated surface pressure was close to zero, both for no added salt and 0.1 M .

At low pH and no added salt PAA is close to neutral, see Figure 4.1. As the structure of PAA is intrinsically amphipolar (apolar C-C backbone, polar $-\text{COOH}$ side-groups), neutral PAA is expected to adsorb at the air/water interface. At high pH or high ionic strength, however, the chain is (partially) charged. Adsorption of charged chains to an air/water interface is unfavourable, as (i) localisation of the counterions is entropically

unfavourable, and (ii) the gradient of the dielectric constant at the interface creates a repulsive electrostatic potential. This repulsive potential, which originates from the divergence of an electric field by a dielectric gradient, can be modelled by image charges. [110] The electrostatic cost ΔE of bringing a single charge from the bulk of phase a to a distance d from an interface between phases a and b (with corresponding dielectric constants ϵ_a and ϵ_b) is given by

$$(4.1) \quad \Delta E = e\Psi(d) - e\Psi(\infty) = \frac{\epsilon_a - \epsilon_b}{\epsilon_a + \epsilon_b} \frac{e^2}{8\pi\epsilon_a d}$$

where effects of neighbouring charges have been neglected. If we estimate the distance d of a monovalent ion adsorbed at the air/water interface to be of order 3 \AA , ΔE is of order $k_B T$. Thus, adsorption at the air/water interface is only expected to be significant in the case of PAA-chains with a low charge density, i.e. low pH. At high pH the charge on the PAA-chains prevents adsorption and the saturated surface pressure is close to zero. This agrees with the observed saturated surface pressure of PAA solutions as a function of the pH and ionic strength and with adsorption of PAA on PS-surfaces. [111]

Adsorption of grafted PAA chains can be demonstrated more rigorously by considering the 2D compressibility of the PS-PAA monolayer. [112] The compressibility of a monolayer is a measure for the density fluctuations, and is therefore coupled to the monomeric conformational susceptibility ξ , introduced in Chapter 2. Fluctuations in the overall particle density occur in any given system. The equilibrium fluctuation density in a 3D-system, denoted by Υ , is defined as [113]

$$(4.2) \quad \Upsilon = \sqrt{\Delta \rho^2} = \sqrt{\frac{-k_B T \bar{\rho}^2}{V \left(\frac{\partial p}{\partial V} \right)_T}}$$

where $\bar{\rho}$ denotes the average particle density and p is the pressure in the system. It is convenient to express the strength of these fluctuations relative to those in ideal systems. The latter are simply $\Upsilon_{id} = \sqrt{\bar{\rho}}$. [113] As we consider a monolayer, the 2D equivalent Υ_R of the normalised fluctuation density is

$$(4.3) \quad \Upsilon_R \equiv \frac{\Upsilon}{\Upsilon_{id}} = \sqrt{k_B T \left(\frac{\partial \pi}{\partial \sigma} \right)^{-1}}$$

where we have used the fact that $\pi_{id} = k_B T \sigma$. Inserting Eq.(2.12) it follows that $\Upsilon_R = (k_B T \sigma N^2 \xi)^{-1/2}$, which demonstrates that the fluctuation strength and the conformational susceptibility are coupled. Generally speaking, the strength of density fluctuations is the strongest in the proximity of a phase transition. In the case of a first-order phase transition in a monolayer, e.g. an expanded-liquid to condensed-liquid transition in surfactant monolayers, $(\partial \pi / \partial \sigma) = 0$. Eq.(4.3) shows that the strength of the density fluctuations diverges during such a first-order phase transition.

We now consider the strength of density fluctuations in the PS-PAA and PS-PEO monolayers. In Figure 4.5 Υ_R of PS(38)-PEO(445) and PS(34)-PAA(368) are shown

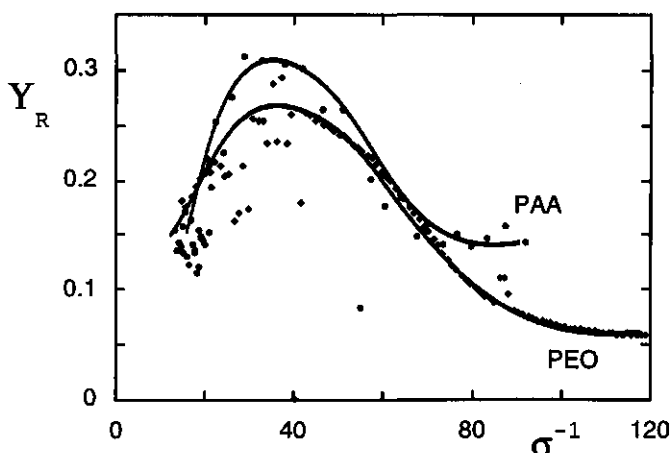


FIGURE 4.5. The renormalised fluctuation density Υ_R as a function of the area per chain σ^{-1} (nm^2) for PS-PEO(445) and PS-PAA(368) at pH 4.7 and no added salt. The curves are a guide to the eye.

as a function of the area per chain σ^{-1} . The lengths of both the anchoring PS-blocks and the hydrophilic PEO and PAA blocks are comparable. The PS-PAA isotherm was measured at pH 4.7 and no added salt (Figure 4.4). Evidently, the behaviour of $\Upsilon_R(\sigma^{-1})$ is qualitatively the same for both polymers; at low σ the density fluctuations are small, at higher σ the fluctuations increase and high σ again decrease with increasing σ . This is consistent with the picture of an adsorption/desorption transition of tethered chains, as discussed extensively in Chapter 2. If we introduce σ_c to denote the grafting density at which the maximum in $\Upsilon_R(\sigma)$ is found, then the chains are adsorbed at the interface in a pancake conformation for $\sigma \ll \sigma_c$. In this regime the density fluctuations in the monolayer are low, as the chains are completely adsorbed. As the adsorption strength is weaker for PAA as compared to PEO, the low surface pressures make the pancake regime of PAA experimentally less accessible than the pancake regime of PEO, which explains the small number of data points of PAA at low σ in Figure 4.5. If $\sigma \sim \sigma_c$ the adsorption/desorption transition of the grafted chains greatly enhances the fluctuations in the monolayer. For $\sigma \gg \sigma_c$ the chains are almost completely desorbed in a brush conformation, and the fluctuation strength is small again. As follows from Eq.(1.5) and Eq.(4.3), the fluctuation strength in the brush regime scales as $\Upsilon_R \sim \sigma^{-2/3}$, i.e. it decreases with increasing σ . This scaling exponent is roughly retrieved for the PEO brush.

When the maximum in Υ_R is indeed associated with the adsorption/desorption transition of tethered chains, this maximum should (approximately) occur at the saturated surface pressure of the adsorbing block. In the case of PEO homopolymer the saturated surface pressure for long chains is known to be 9.8 mNm^{-1} . [85] The surface pressure of the PS-PEO(445) diblock copolymer is found to be 9.6 mNm^{-1} at σ_c . The surface pressure of PS-PAA(368) at σ_c at pH 4.7 and no added salt is found to be 3.2 mNm^{-1} .

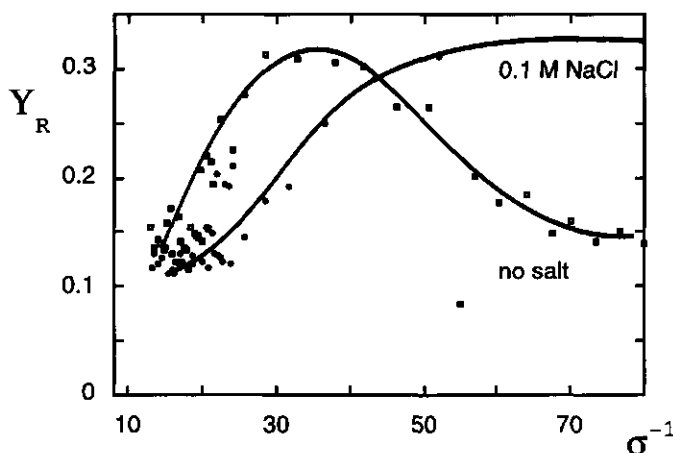


FIGURE 4.6. Υ_R as a function of the area per chain σ^{-1} (nm^2) for PS-PAA(368) at pH 4.4, 0.1 M NaCl and at pH 4.7 with no added salt. The latter curve is the same as in Figure 4.5. The curves through the data points are a guide to the eye.

We recall that the surface pressure of solutions of PAA-homopolymer at low pH and no added salt is also found to be of order 3 mNm^{-1} . Thus, a strong correlation is found between $\Upsilon_R(\sigma)$ and the adsorption properties of the grafted chains.

We can therefore conclude that at relatively low pH and no added salt grafted PAA-chains have a pancake conformation at low σ instead of the theoretically predicted osmotic brush in the ÖsB-regime. This pancake conformation is responsible for the high exponent in Figure 4.4 at low σ . The scaling exponent y in $\pi \sim \sigma^y$ in the pancake regime is given as $y = 2\nu/(2\nu - 1)$ in a 2D system, where the exponent ν characterises the relationship between the radius of gyration of a chain and its length, i.e. $R_G \sim N^\nu$. [114] For an ideal 2D self-avoiding walk ν equals $3/4$, i.e. the surface pressure of flat pancakes should increase as $\pi \sim \sigma^3$. [69, 114] Our exponent y is closer to 2 than to 3, so a completely flat pancake conformation is unlikely. The high value nevertheless indicates strongly interacting chains in a pancake-like conformation.

Naturally, the same analysis for lateral density fluctuations can be performed for PAA at different salt concentrations. In Figure 4.6 Υ_R is plotted for PS-PAA monolayers at pH 4.7 and no salt and at pH 4.4 and 0.1 M NaCl. Clearly, the form of $\Upsilon_R(\sigma)$ with and without added salt differs: at low σ the fluctuations are large in the case of added salt. This is attributed to the small increase of π as a function of σ in the coil regime, and the subsequent large density fluctuations. The strength of the fluctuations decreases with increasing σ , which corresponds to the increasing monomer density in the grafted layer as the brush regime is approached. There is no maximum in $\Upsilon_R(\sigma)$ in the case of added salt, which indicates that the adsorption/desorption transition is absent. We

again conclude that the adsorption of the PAA-chains, and thus the polymer conformation, depends strongly on the salt concentration in this pH-regime.

At high pH the $\pi(\sigma)$ -isotherms with and without added salt are observed not to obey a single power law. This indicates that the interaction between the grafted chains is not dominated by a single osmotic interaction. In NB- or SB-regime the scaling behaviour of $\pi(\sigma)$ stems from the dominance of binary monomer-monomer interactions. In the derivation of the scaling laws in the SB-regime the assumption is made that the osmotic pressure in the brush layer is proportional to the difference in total ion concentration in the brush and in the bulk solution. [34] This assumption is only valid in the limits of low ion densities; at high densities the complete virial expansion in terms of $\Delta\rho_{ion}$ must be taken into account. The result of these higher order terms in $\Delta\rho_{ion}$ is that no clear scaling regime for $\pi(\sigma)$ is found. Thus, the absence of scaling regimes in the $\pi(\sigma)$ -isotherms at high pH is the result of high charge densities in the brush.

4.3. REFLECTOMETRY

4.3.1. Materials & Method

The refractive index of PAA-solutions in the range from 0.006 g/ml to 0.125 g/ml was measured with an Abbe refractometer. The protonation-deprotonation of PAA was examined by potentiometric titrations using a fully automated titration system. [109]

The Si-wafers coated with PS were prepared as described in ref. 115. In short, a Si-wafer is etched in 5 % HF for a few minutes to remove the oxide layer. Subsequently, the wafer is placed for 2 hours in a 5% styrene solution in toluene at 150 °C, in a N₂-environment under reflux conditions. The result is a chemically and thermally stable, covalently bonded styrene monolayer on the Si-wafer. The thickness of this layer, measured with ellipsometry, is approximately 2 nm. A PS-layer of 80 nm was spincoated on the wafer at 3000 min⁻¹ from a 15 gl⁻¹ solution of PS (43K) in chloroform and dried with N₂. The result is a Si-wafer hydrophobised with PS, the reflected intensity of which is insensitive to pH-changes. This last feature is essential, as the change in optical reflectivity of PS-layers coated with PAA is measured as a function of the pH. We remark that during the radical reaction a few oligomers may form in the styrene monolayer. As a PS-layer of 80 nm is spincoated on top of the monolayer, these oligomers are of no importance, and may even serve to improve the stability of the spincoated PS-layer.

PS-PAA monolayers were prepared on a clean H₂O subphase in a Langmuir trough as described in the previous section. The PS-PAA block copolymers were transferred from the air/water interface to the coated PS-layers using the Schaeffer variant of the LB-technique. [116] The transfer ratio was close to one. Following this, the wafers were first dried in air to evaporate the water layer on the LB-layer, and subsequently heated at 150 °C for 10 minutes on a heating stage. Immediate heating above 100 °C after dipping resulted in layers that appeared to be damaged to the eye, probably due to the rapid retreat of the water layer. During heating above the glass temperature of PS (± 100 °C) the PS-blocks of the PS-PAA block copolymers diffuse into the spincoated PS-layer. [90]

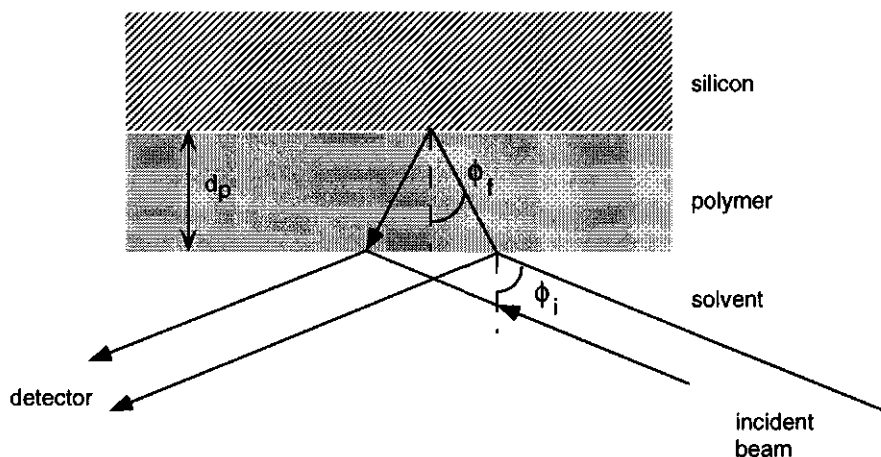


FIGURE 4.7. A schematic illustration of reflection at the wafer/solvent interface.

After cooling, the PS-layer becomes glassy again, and the PS blocks are firmly 'rooted' in the PS sublayer. In this manner the block copolymers are irreversibly fixed at the grafting density at which the LB-film was prepared. Without this thermal annealing the PAA-layer is instable in solutions of high pH, i.e. the PS-PAA chains are pulled from the wafer, as a result of the high electrostatic potential in the PAA-layer. Three wafers were prepared in this manner, with grafting densities 18, 12.3 and 8 nm² per PS-PAA molecule.

The wafers with grafted PAA were brought in contact with solutions of varying pH and constant ionic strength (10^{-3} M) in a reflectometer. A constant ionic strength is important, as the degree of dissociation in the brush is a function of the ionic strength, as well as of pH and grafting density. [34–36] It was found, however, that reflectometry was not successful using solutions with high concentrations of salt.

The technique of reflectometry has been discussed extensively in ref. 108. A polarised laser beam is reflected on a silicon surface with an adsorbed or grafted polymer layer and both the intensity of the normal and parallel polarisation directions with respect to the reflecting plane are measured, as shown in Figure 4.7. The output signal S is the ratio of the parallel and perpendicular polarised reflectivities R_p and R_s , respectively. In the appendix we discuss the reflectivity of a layer consisting of grafted annealed polyelectrolytes.

4.3.2. Results

We first demonstrate that the refractive index of a solution of PAA is proportional to the overall degree of dissociation α . In Figure 4.8 the dn/dc of a PAA-solution is shown as a function of α for 10^{-3} M KNO₃. The data points nicely fall onto a straight line. This is as expected, since the overall refractive index is determined by the highly localised electronic properties of the constituting particles. Each dissociated carboxylate group contributes a fixed amount to the overall refractive index, hence the linearity with

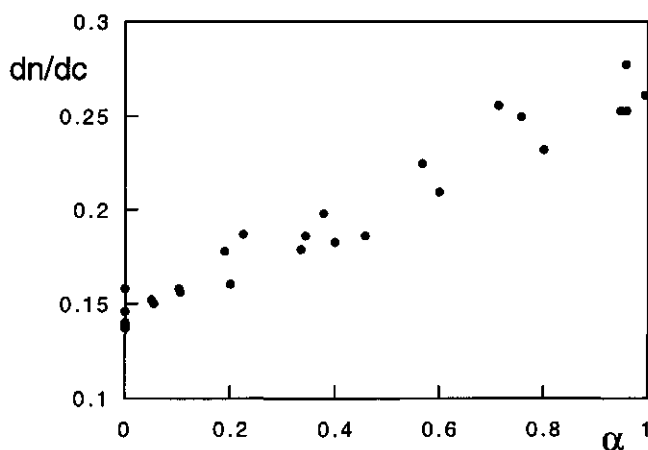


FIGURE 4.8. The change in dn/dc of PAA in 10^{-3} M KNO_3 with increasing α .

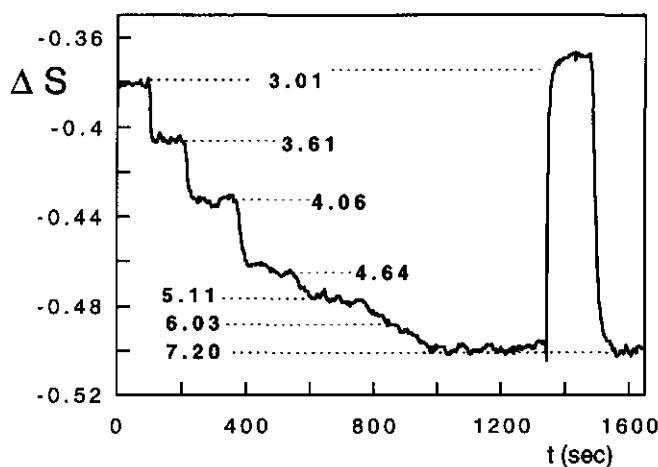


FIGURE 4.9. The reflection signal ΔS of grafted PAA, 18.3 nm^2 per molecule, for various pH-values (indicated in the figure) and 10^{-3} M ionic strength.

α . Thus, the reflectometry signal ΔS of grafted PAA-brushes at a given σ is proportional to the (average degree of) dissociation of the brush, as discussed in the appendix.¹

The reflectivity of the PAA-brushes is considered next. In Figure 4.9 the measured reflectivity signal ΔS is shown as the pH of the solvent varies at constant ionic strength (10^{-3} M). It is clear that the change in signal is reversible: at the end of the cycle in Figure 4.9 the pH changes from 7.2 to 3.0 and back, and no effective change in ΔS is

¹We remark that α is not a constant, but varies as a function of the distance to the grafting plane. [35,36] However, as the spatial distribution of α is small compared to the wavelength of the laser, reflectometry is insensitive to this dissociation gradient and an average value over the brush is measured. Therefore, with α the value averaged over the brush layer is implied.

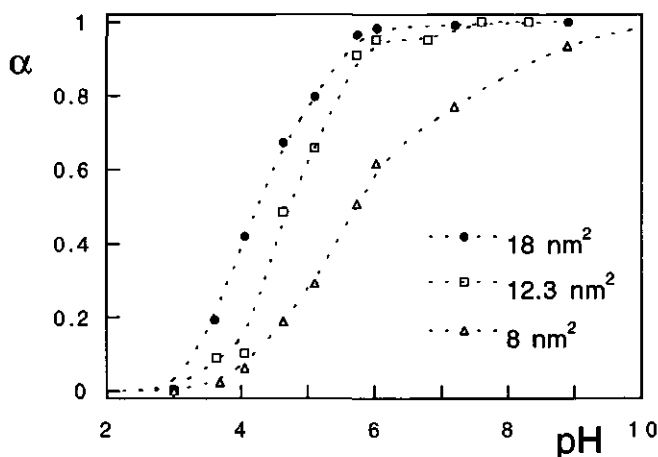


FIGURE 4.10. The titration curves of PAA-brushes for three areas per chain and 10^{-3} M ionic strength.

observed. This reversibility of ΔS in a pH-cycle is essential, as it indicates that the total amount Γ remains constant during the titration. The chains remain grafted despite the high charge density at high pH (and corresponding high electrostatic potential in the layer). Moreover, the reversibility of ΔS is a prerequisite for the determination of the overall degree of dissociation in the layer, as shown in the appendix.

The titration curves of PAA at the three grafting densities and 10^{-3} M are presented in Figure 4.10. All curves commence at pH 3, due to the requirement of constant ionic strength of 10^{-3} M.

4.3.3. Discussion

It is seen in Figure 4.10 that the titration curves of the grafted PAA-chains effectively shift to higher pH-values with increasing σ , as the theory of annealed brushes predicts. [35,36] The shift in effective pK_a value is approximately 1.5 units as σ^{-1} decreases from 18 to 8 nm^2 . We remark that the reflectivities at pH-values lower than 3 could not be measured, due to the requirement of constant ionic strength of 10^{-3} M. This is the reason that α increases stronger than expected at low pH, as the assumption is made that $\alpha = 0$ for pH values equal to 3. Also, the assumption is made that at pH 11 the chains are fully dissociated. Using this assumption, the full titration curve is calculated via Eq.(4.14) in the appendix. It is not possible to increase the pH to values much higher than 10, as the Si-wafer itself is hydrolysed at high pH values. Thus, the 'real' titration curves may differ somewhat from those presented in Figure 4.10. This is also concluded when the titration curves of Figure 4.10 are compared to those in Figure 4.1. If we consider $\alpha = 0.5$ as a measure of the pK_a of the grafted PAA-chains a lower value is obtained for 18 nm^2 per chain (± 4.5) from Figure 4.10 than for PAA in a bulk solution (± 6) in Figure 4.1.

Notwithstanding these inaccuracies, we can use the titration isotherms to roughly estimate the difference in electrostatic potential in the PAA-brush at two grafting densities. Using Donnan equilibrium concepts, the average value of α is given as [35]

$$(4.4) \quad \frac{\alpha}{1 - \alpha} = \frac{K_a}{\rho_{H^+} \exp(-\Psi e/k_B T)}$$

where ρ_{H^+} is the proton concentration in the bulk, K_a the dissociation constant of acrylic acid in dilute solutions and Ψ the average electrostatic potential in the layer.² If the pH-values at which $\alpha = 0.5$ in Figure 4.10 are inserted, it follows that as σ^{-1} decreases from 18 to 8 nm², Ψ increases by approximately 90 mV. This is a significant increase, which indicates that the close-grafting of polyelectrolyte chains greatly enhances the electrostatic potential in the layer. From the shape of the titration isotherms of 8 and 18 nm² per chain it can be also seen that this difference in Ψ increases significantly with increasing α .

This shift in apparent pK_a agrees qualitatively with theoretical models for annealed brushes, that predict the (overall) degree of dissociation α to decrease strongly with increasing grafting density σ at constant pH and ionic strength. [34] We note that scaling models for annealed brushes predict α to decrease as $\sigma^{-2/3}$, whereas in our measurements a more or less linear relationship is observed, i.e. $\alpha \sim \sigma^{-1}$. The number of densities measured is limited to three, however, and more measurements would be necessary to ascertain the power exponent more accurately.

4.4. ELLIPSOMETRY

4.4.1. Materials & Method

Si-wafers coated with PS and PS-PAA were prepared as described in section 4.3.1. A PS-layer of approximately 65 nm was spincoated from a 10 g l⁻¹ solution of PS with molar mass 43 K. These wafers were placed in an optical cell containing a known volume of pure, deionised H₂O at a certain pH. After measurement of the ellipsometric parameters Δ and Ψ (see below), an amount of a solution of 1 M NaCl at identical pH was added. In this manner a Δ , Ψ -curve was obtained for a PAA-brush at a given pH and varying ionic strength. Moreover, care was taken to maintain the laser beam on the same spot of the Si-wafer during measurement of the Δ , Ψ -curve to ensure that small lateral inhomogeneities in the spin-coated PS-layer would not influence the outcome.

The measurements were performed with a Multiskop ellipsometer from Optrel, Germany. The optical cell was obtained from Akzo Nobel and has two planar faces at 20° with respect to the normal. The arms of the ellipsometer were mounted to give an angle of incidence of 70° with respect to the normal. The laser used is a He-Ne laser with a wavelength of 632.8 nm. The measurements were done at room temperature.

The experimental set-up of an ellipsometer is similar to that of a reflectometer, see Figure 4.7. The electric field of a reflected laser beam may be divided into a component polarised parallel to the plane of reflection (p) and a component polarised perpendicular

²Actually a potential gradient $\Psi(z)$ is present in the brush, which is coupled to the dissociation gradient $\alpha(z)$. As is the case for α , an average value for Ψ is estimated. [35,36]

to this plane (s). When a beam in medium α encounters a single α, β -interface at an angle ϕ , part of the beam is reflected at the same angle and part is refracted at an angle ϕ' , given by Snell's law ($\sin \phi' = \sin \phi n_\alpha / n_\beta$).³ The reflection of both components is expressed by the Fresnel coefficients $r_{\alpha\beta}^{p,s}$ [117, 118]

$$(4.5) \quad r_{\alpha\beta}^p = \frac{n_\beta \cos \phi - n_\alpha \cos \phi'}{n_\beta \cos \phi + n_\alpha \cos \phi'} \quad r_{\alpha\beta}^s = \frac{n_\alpha \cos \phi - n_\beta \cos \phi'}{n_\alpha \cos \phi + n_\beta \cos \phi'}$$

In our case of a coated Si-wafer in contact with water at least two interfaces are to be considered: water-polymer ($\alpha\beta$) and polymer-Si ($\beta\gamma$). The overall reflection coefficients, taking internal reflection into account, are given as [117, 118]

$$(4.6) \quad R_p = \frac{r_{\alpha\beta}^p + r_{\beta\gamma}^p \exp(-2id_p)}{1 + r_{\alpha\beta}^p r_{\beta\gamma}^p \exp(-2id_p)} \quad R_s = \frac{r_{\alpha\beta}^s + r_{\beta\gamma}^s \exp(-2id_p)}{1 + r_{\alpha\beta}^s r_{\beta\gamma}^s \exp(-2id_p)}$$

where d_p denotes the thickness of the polymer layer, see Figure 4.7, and $i = \sqrt{-1}$. In the case that one or more of the media are non-dielectric, for instance Si, the complete refractive index $\tilde{n} = n - in'$ must be taken into account.

We now denote the initial phase difference between the parallel and perpendicular polarised components of the incident beam as δ_1 . If that of the outgoing, reflected beam is δ_2 , the overall phase difference that occurs upon reflection is

$$(4.7) \quad \Delta = \delta_1 - \delta_2$$

Furthermore, the ratio of the amplitudes of both reflected components is given as

$$(4.8) \quad \tan \Psi = \frac{|R_p|}{|R_s|}$$

The above equation can be combined to an overall equation for the reflection of a polarised beam on a surface,

$$(4.9) \quad \frac{R_p}{R_s} = \tan \Psi e^{i\Delta}$$

The quantities Δ and Ψ are measured and contain information on the optical properties of the reflecting surface. Using a suitable model to mimic the investigated system, Δ and Ψ may be transformed into physical quantities, such as the layer thickness and density. We return to this point in the following sections.

4.4.2. Results

As we consider the behaviour of grafted PAA chains in an aqueous solution of varying ionic strength, the variation of the refractive index of water containing added salt must be considered first. In Figure 4.11 the refractive index of a NaCl-solution is shown as a function of the salt concentration. It is clear that n increases slightly with increasing concentration (the fitted expression is $1.333 + 0.00987 c_s$, with c_s in M). This increase of n with increasing salt concentration must be taken into account when analysing the results.

³Here we have assumed that both medium α and β are dielectrics, i.e. the imaginary part of the refractive index is zero.

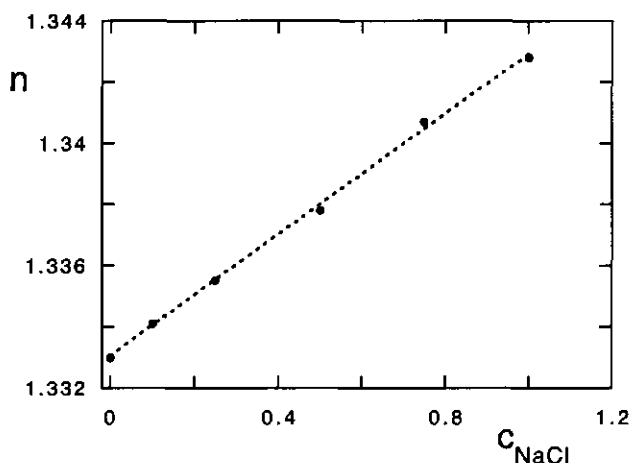


FIGURE 4.11. The refractive index n of a NaCl-solution as function of the concentration (in M).

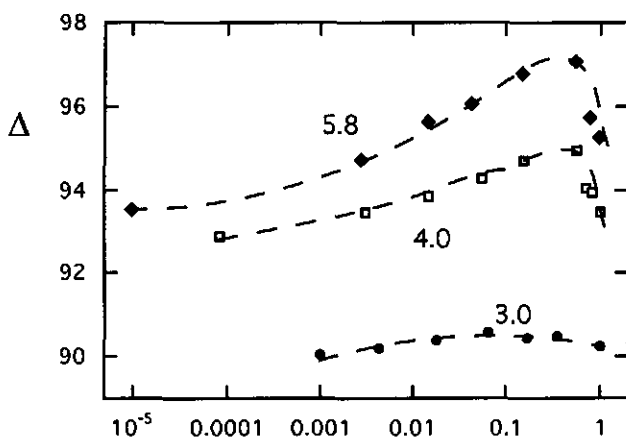


FIGURE 4.12. Δ (in degrees) as a function of the ionic strength I for 3.9 nm^2 per PAA-chain at three pH-values, plotted semi-logarithmically. The dashed curves are drawn as a guide for the eye.

In Figures 4.12 and 4.13 Δ and Ψ are shown as a function of the total ionic strength (this explicitly includes the proton contribution to I) at a relatively high grafting density (3.9 nm^2 per PAA chain). As is clear from Figure 4.12, Δ and Ψ are relatively insensitive to variations in I at pH 3.0. At higher pH, however, Δ and Ψ vary significantly and non-monotonically with increasing I . Evidently, the difference between the Δ , Ψ -curves at pH 3.0 and 5.8 reflects a difference in behaviour of the grafted PAA-layer with increasing ionic strength.

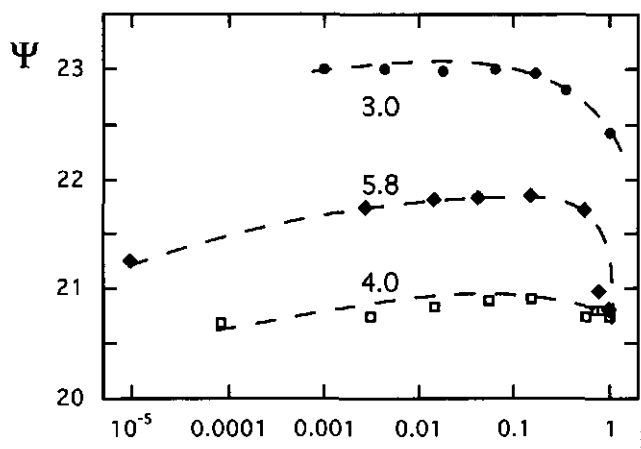


FIGURE 4.13. The same as Figure 4.12 for Ψ .

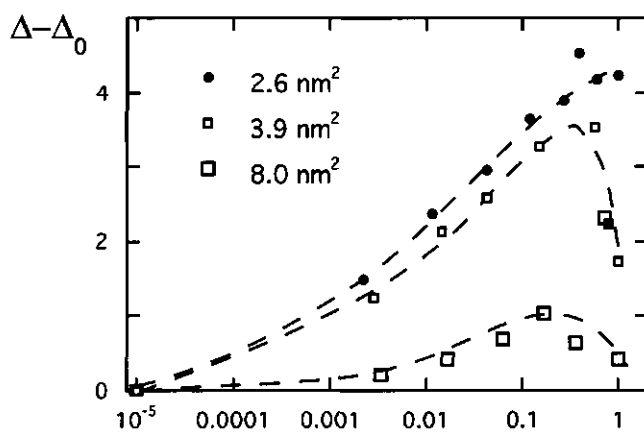


FIGURE 4.14. The increase in Δ with increasing I for three grafting densities and pH 5.9, plotted semi-logarithmically. The dashed curves are drawn as a guide for the eye.

In Figure 4.14 the increase in Δ , denoted as $\Delta - \Delta_0$, is shown as a function of the ionic strength for three grafting densities, at a fixed pH of 5.9. The quantity Δ_0 is the value of Δ at zero added salt, i.e. at $I \approx 10^{-\text{pH}}$. It is clear that the effect of increasing ionic strength on Δ increases with increasing grafting density. Also, the maximum in Δ appears to shift to higher ionic strengths with increasing grafting density.

To obtain values for the brush thickness and monomer density from the measured values of Δ and Ψ it is necessary to make use of a presupposed model that mimics the investigated system. We use a box-model to model the PAA-brush, i.e. the refractive index, which is coupled to the monomer density, is assumed to be uniform throughout

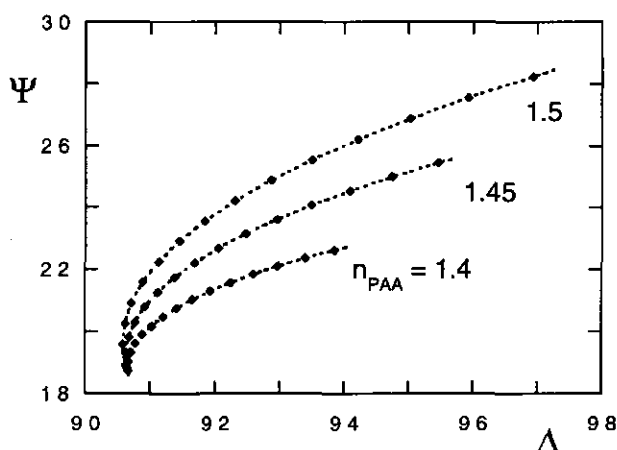


FIGURE 4.15. Δ, Ψ -curves calculated with the box-model for $n_{PS} = 1.56$, $d_{PS} = 60$ nm and three values for n_{PAA} . The modelled PAA thickness is 0 to 50 nm, with every 3 nm a marker.

n_{Si}	n_{PS}	d_{PS}	n_{PAA}
3.885 - 0.0185i	1.54-1.56	55 - 65 nm	1.35 - 1.59

TABLE 4.1. Parameters for modelling ellipsometry results. [118]

the layer. The values used for the refractive index and thickness of the Si and PS-layer are shown in Table 4.1. In Figure 4.15 the Δ, Ψ -curves, calculated numerically using the box-model, are shown as the thickness of the PAA-brush increases from 0 (low value of Δ and Ψ) to 50 nm (high value of Δ and Ψ). Experimentally, both the PAA thickness and overall refractive index are expected to vary with varying ionic strength. This entails that the experimental Δ, Ψ -curves with varying ionic strength are expected to cross the numerical Δ, Ψ -curves for constant n in Figure 4.15.

In Figure 4.16 we have plotted the fitted thickness from the data of Figure 4.12 and 4.13 as a function of the ionic strength at three pH values. Error bars denote the estimated uncertainty in the fitted value of H . At pH 3.0 the brush thickness is found to be independent of the ionic strength. At higher pH values the thickness initially increases and subsequently decreases with increasing ionic strength. This effect is most pronounced for pH 5.8.

In Figure 4.17 the brush thickness is plotted as a function of the ionic strength at pH 4.0 for four grafting densities. The brush thickness is found to be a non-monotonic function of the ionic strength for all grafting densities. The greatest (absolute) increase in thickness is observed at the highest grafting density, i.e. 2.6 nm^2 per PAA-molecule.

Using the box-model to fit the ellipsometry data, we obtain the thickness and the overall refractive index of the layer. Evidently, the latter is related to the monomer

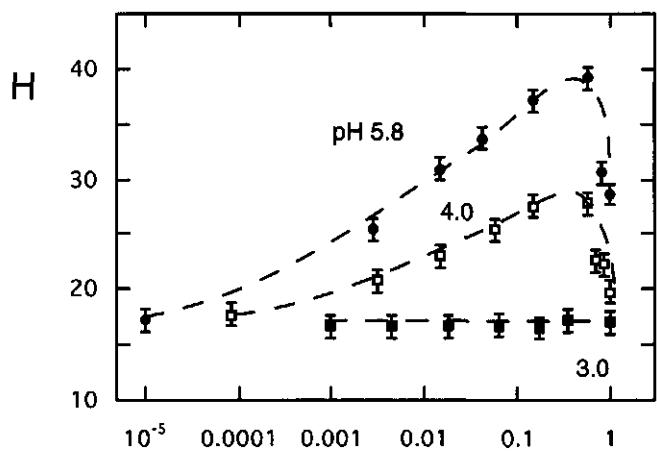


FIGURE 4.16. The thickness H of the PAA layer (in nm) plotted semi-logarithmically as a function of I for three pH values, σ^{-1} is 3.9 nm^2 . The dashed curves are a guide to the eye.

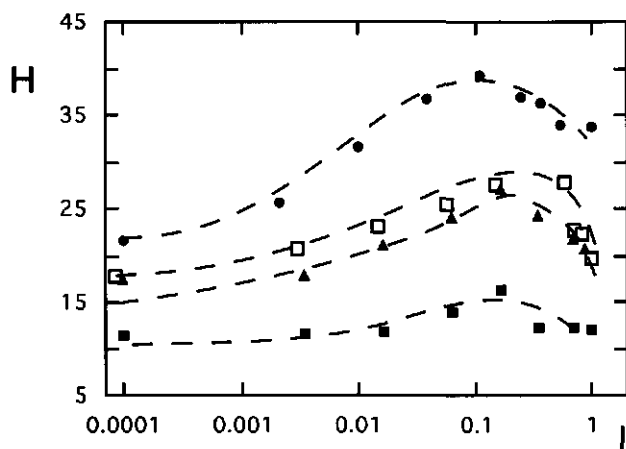


FIGURE 4.17. The thickness H of the PAA layer (in nm) plotted semi-logarithmically as a function of I at pH 4.0 for σ^{-1} 8 nm^2 (closed squares), 6.2 nm^2 (triangles), 3.9 nm^2 (open squares) and 2.6 nm^2 (circles). The dashed curves are a guide to the eye.

number density ρ . The overall refractive index in the box-model can be written as $n_{\text{PAA}} = (1 - \rho v)n_{\text{H}_2\text{O}} + \rho v((1 - \alpha)n_{\text{COOH}} + \alpha n_{\text{COO}^- \text{Na}^+})$. It depends on the density ρ , degree of dissociation α , refractive index of the non-dissociated monomer and that of the dissociated monomer plus counterion. The constant v denotes the ratio of the volume of a monomer and a water molecule, which formally is also a function of α . As this expression contains at least two unknown parameters (ρ and α), it is not possible to determine either ρ or α unambiguously from the fitted value of n_{PAA} .

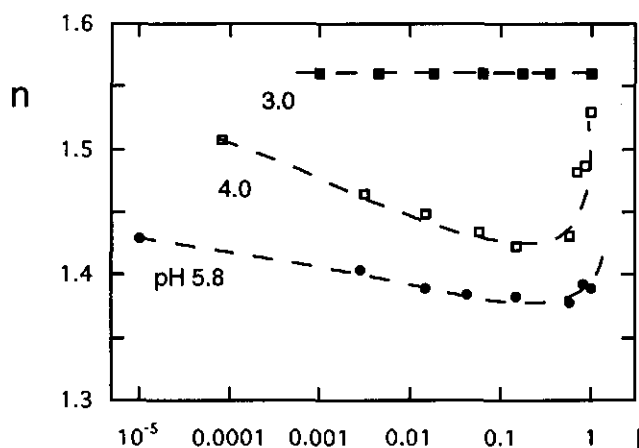


FIGURE 4.18. The refractive index n of the PAA layer plotted semi-logarithmically as a function of I for three pH-values, σ^{-1} is 3.9 nm^2 . The dashed curves are a guide to the eye.

Nevertheless, it is interesting to examine the overall value of n as a function of I and the pH. In Figure 4.18 the fitted value of n is shown for the same data as used in Figure 4.16. At pH 3.0 n is independent of I , which agrees with the constant value of H in Figure 4.16. The refractive index of the PAA-layer at pH 4.0 and 5.8 initially decreases with increasing pH at low ionic strength. This corresponds with an additional stretching of the PAA-brush, see Figure 4.16. At high ionic strength, however, both the decrease in brush thickness and the increasing co- and counterion density (Cl^- and Na^+) in the brush result in an increasing value of n with increasing I . Thus, the non-monotonic behaviour of the refractive index of the brush qualitatively mirrors that of the thickness.

4.4.3. Discussion

As mentioned in the previous section, a presupposed model is necessary to transform the measured values of Δ and Ψ into physical parameters. In this respect, the final results obtained by ellipsometry are not unambiguous and must be interpreted with care, as is the case with neutron reflectivity, see Chapter 3. To demonstrate that the variation of Δ and Ψ with varying ionic strength is significant we plotted the Δ and Ψ -data in Figures 4.12-14 and the model calculations in Figure 4.15. The non-monotonic trends in $H(I)$ and $n(I)$ do not depend on the values used for the thickness of the spin-coated PS-layer and its refractive index. The precise values of H and n , however, do depend on the refractive index and thickness of the spin-coated layer.

We have used the simplest possible model to mimic the PAA-brush, i.e. the box-model. Analytical and numerical SCF calculations predict density and counterion distributions throughout the brush. As only two parameters are measured with ellipsometry, it is not possible to deal with such density distributions. To determine either the counterion

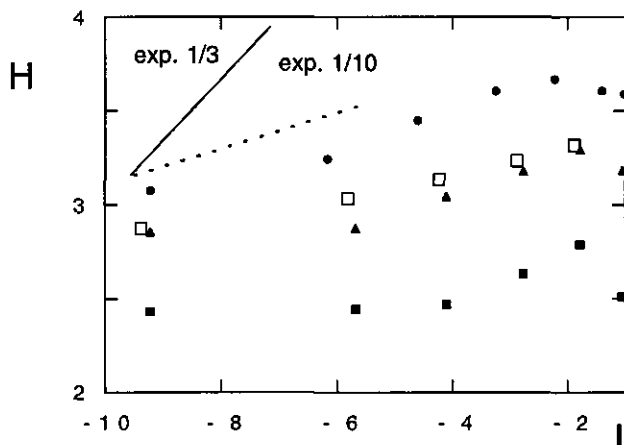


FIGURE 4.19. The data of Figure 4.17 plotted double-logarithmically. A line corresponding to a scaling exponent $1/3$ (solid line) and $1/10$ (dashed line) is plotted as well.

or monomer density distribution, one needs a scattering technique with a high spatial resolution, for instance neutron or X-ray scattering.

Evidently, the most interesting result is the non-monotonic behaviour of $H(I)$. This non-monotonic behaviour stems from the influence of the ionic strength on the electrostatic potential in the grafted layer. In pure deionised water the Debye length κ^{-1} , which characterises the range over which charged entities interact via electrostatic interactions, is of order 100 nm. Under such conditions the overall charge density of the grafted chains in the brush is significantly below α_b (see Figure 4.10). As the ionic strength increases the overall charge density on the grafted chains increases, and the brush thickness increases as a result of the enhanced electrostatic interactions. This corresponds to the $\tilde{\text{OsB}}$ -regime as proposed theoretically by Zhulina *et al.* [34] and Lyatskaya *et al.* [35] At high ionic strength α is close to α_b ; in this regime a subsequent increase in ionic strength merely decreases the strength of the electrostatic interactions and the brush thickness decreases. This decrease is characterised by a decrease in the monomeric excluded volume v_{eff} , see Eq.(1.6), and corresponds with the SB-regime.

Theoretically, the brush thickness in the $\tilde{\text{OsB}}$ -regime is predicted to scale as

$$(4.10) \quad H \sim N\sigma^{-1/3}(\alpha_b(1 - \alpha_b)^{-1})^{2/3}(\rho_{H^+} + \rho_s)^{1/3}$$

see Eq.(1.12). [34] In our experiments σ and N are fixed, and if α_b is assumed independent of I (Figure 4.1 shows this assumption to be not completely valid), this expression reduces to $H \sim I^{1/3}$ at a given pH. However, if we plot the experimental data of Figure 4.17 double-logarithmically, we obtain power laws with an exponent close to 0.1 instead of 0.33, shown in Figure 4.19. The same exponent is also found at pH 5.8 (not shown). Thus, the experimental dependence of the brush thickness on the ionic strength in the $\tilde{\text{OsB}}$ -regime is significantly less than predicted theoretically.

The difference between the experimentally observed power law exponent and the theoretical exponent is probably due to neglect of steric interactions in the theoretical analysis. Stated simply, in the case of charged brushes there are two forces that induce stretching (steric and electrostatic) and one force that opposes stretching (conformational). In order to obtain a scaling law, either the steric or electrostatic force must be neglected, as was done for the steric force by Zhulina *et al.* to obtain the scaling behaviour for $H(I)$ in the $\tilde{O}S$ B-regime. [34] However, this is not correct, as also follows from examination of Eq.(4.10). If we let the ionic strength decrease to zero, then the brush thickness is also predicted to approach zero. Evidently, if α approaches zero the PAA-brush resembles a neutral brush, the height of which is determined by steric interactions. If such steric interactions are taken into account, the increase in brush thickness with increasing ionic strength in the $\tilde{O}S$ B-regime is less than given by the above mean-field scaling law.

The analytical model of Zhulina *et al.* also predicts the brush thickness at low ionic strength and pH to decrease with increasing grafting density. The underlying reason for this decrease is the decrease in fraction of dissociated monomers with increasing grafting density (see Figure 4.10). However, in Figure 4.17 the thickness of the PAA brush increases with increasing grafting density at low ionic strength and pH. It is believed that the steric interactions result in an increase of the brush thickness with increasing grafting density.

4.5. CONCLUSIONS

In this chapter we have investigated the properties of grafted PAA chains using surface pressure measurements, reflectometry and ellipsometry. These results are compared to theoretical predictions for the behaviour of end-grafted weak-acidic polymers under various conditions.

Analysis of surface pressure isotherms of PS-PAA at the air/water interface yields information on the conformation of the grafted PAA chains. It is shown that at low pH and high salt concentration the power law of the surface pressure as a function of the grafting density corresponds with the mean-field power law for charged brushes in the salted brush regime, i.e. $\pi \sim \sigma^{5/3}$ in the case of long chains. Short chains do not obey this scaling law. This result is similar to that of neutral polymers in the brush regime, as discussed in Chapter 2. Analysis of the compressibility of the PS-PAA monolayer demonstrates that the PAA chains adsorb to the interface at low salt concentrations and low pH. This adsorption prevents the occurrence of an osmotic brush regime of annealed chains ($\tilde{O}S$ B regime).

The titration curves of grafted PAA chains were determined with reflectometry. As predicted by theoretical models, the titration curves are shifted to higher pH-values with increasing grafting density. This shift results from the enhanced electrostatic potential in the grafted layer with increasing grafting density.

Using ellipsometry the thickness of the grafted PAA layer was measured. The PAA brush thickness is found to be non-monotonic as a function of the ionic strength at a

given pH. The extent of (de)swelling increases with increasing pH and grafting density. At pH 3 (far below the pK_a of PAA) the brush height is independent of the ionic strength, as the fraction of dissociated monomers is close to zero. At higher pH the brush initially swells with increasing ionic strength, due to an increasing fraction of charged monomers. At an ionic strength of order 0.1 M the charge density is close to that of a PAA-chain in a dilute bulk solution. In this regime the thickness decreases with increasing ionic strength, due to increased screening of electrostatic interactions between charged monomers.

The non-monotonic behaviour agrees qualitatively with the predictions of Zhulina *et al.* [34], Lyatskaya *et al.* [35] and Israëls *et al.* [36]. The mean-field power law of Zhulina *et al.* for the $\tilde{O}SB$ -regime, $H \sim I^{1/3}$ at a given pH and σ , is not observed; the measured exponent is of the order of 0.1. The swelling is therefore less than predicted, which is probably due to steric interactions that are neglected in the analysis of Zhulina *et al.* Also, theoretically the brush thickness is predicted to decrease with increasing grafting density in the $\tilde{O}SB$ -regime, whereas experimentally it is found to increase. Again, the difference is believed to originate from the neglect of steric interactions in the theoretical analysis.

One may wonder under which conditions the $\tilde{O}SB$ -regime, as theoretically characterised in the analytical and numerical models, is experimentally accessible. The theoretical models assume the polymers to be grafted to an inert, neutral surface. Due to its chemical structure, the carbon backbone of a polymer is intrinsically hydrophobic. The solubility of polymers is generally due to charged or polar groups on the chain. As the dielectric constants of most organic compounds are low compared to that of water, the problems associated with the dielectric anisotropy of the water/air interface are also present for polyacids chemically or physically grafted to a fluid/fluid interface or solid/fluid surface. [111] Also, shielding of the carbon backbone from the water phase results in an additional affinity of grafted polyacids for such fluid/fluid or solid/fluid interfaces. Thus, the occurrence of the $\tilde{O}SB$ -regime for annealed polymers grafted to an apolar surface is, in general, unlikely at low grafting densities, due to adsorption effects.

At grafting densities above the pancake-brush transition the chains are relatively closely packed, and steric interactions, which are neglected in the analytical models for the $\tilde{O}SB$ -regime, are important. The non-monotonic dependence of the brush height as a function of the ionic strength, which is indicative for the $\tilde{O}SB$ -regime, is observed experimentally at high grafting densities. The quantitative agreement between the analytical models and experiments, however, is poor, as the chains are stretched by both steric and electrostatic interactions in this grafting regime.

ACKNOWLEDGEMENTS

We thank Ben Dijk for providing the data for the refractive index of NaCl-solutions and Marcelo Avena for the PAA titration isotherms.

APPENDIX

In this appendix we discuss the optical reflectivity of a layer consisting of grafted polyelectrolytes. The phase difference resulting from a given polymer layer is (see Figure 4.7)

$$(4.11) \quad \phi = \frac{4\pi d_p n_p \cos \theta_f}{\lambda_0}$$

where d_p and n_p are the thickness and refractive index of the polymeric layer, respectively, and λ_0 the wavelength of the beam in vacuum. Using optical models (i.e. Abeles' method [117]), a relationship between ϕ and the reflectivities R_p and R_s can be established. We now consider the case that polymer chains are grafted to a substrate. If, for the sake of simplicity, we assume the polymer layer to be homogeneous, then n_p can be written as

$$(4.12) \quad n_p = n_s + \left(\frac{dn}{dc} \right) \frac{\Gamma}{d_p}$$

where Γ is the total amount of grafted polymer and dn/dc the change in refractive index as a function of the polymer concentration.

During reflectometry the output signal S measures the ratio of the parallel and perpendicular polarised reflectivities R_p and R_s , respectively. During a (conventional) measurement of the adsorption of polymer or proteins, the change in signal changes is

$$(4.13) \quad \Delta S = f \left(\left(\frac{R_p}{R_s} \right)_{\Gamma} - \left(\frac{R_p}{R_s} \right)_0 \right)$$

where the subscript Γ denotes silicon with an adsorbed layer and 0 that of the bare silicon surface, and f is a sensitivity constant. From optical models Γ can be calculated for a given ratio R_p/R_s . It turns out that for most cases R_p/R_s is linear with Γ and insensitive to the exact distribution of material in the adsorbed layer. [108] If we combine this with Eqs.(4.11) and (4.12) it is clear that upon adsorption R_p/R_s is proportional to ϕ for a given dn/dc . However, if Γ is constant and the dn/dc of the layer varies with varying α , it follows that a similar proportionality of R_p/R_s is retrieved. This result is used in the titration of annealed brushes. Under the assumption that the dn/dc is proportional to α , which is demonstrated in Figure 4.8, it follows that

$$(4.14) \quad \alpha = \left(\frac{\Delta S_{\alpha} - \Delta S_{\alpha=0}}{\Delta S_{\alpha=1} - \Delta S_{\alpha=0}} \right)$$

provided that Γ is constant during the measurement.

Polymers with Surfactants

ABSTRACT

A mean-field analytical model is developed for polymers with annealed excluded-volume interactions. This may mimic the behaviour of polymers in solutions that contain amphiphilic molecules, e.g. globular proteins or surfactants, capable of co-operative association with the polymer chains. In this chapter we concentrate on the behaviour of single, complexed coils in a good solvent with a Flory-like model. It is concluded that the coverage of the polymer chain with complexed amphiphiles increases continuously with increasing adsorption strength, i.e. increasing bulk amphiphile concentration. The size of the coils can increase, decrease or have a maximum with increasing coverage, depending on the relative strength of the monomer-monomer, monomer-complex and complex-complex excluded-volume interactions. Comparison with experimental data for PEO/SDS-gels shows good agreement between the predicted coil volume and the experimental (de)swelling of PEO-gels upon complexation with SDS-surfactants.

5.1. INTRODUCTION

The interaction of polymers or polyelectrolytes with nanocolloids is a rich area of research with several practical applications, as explained in Chapter 1. Nanocolloids are defined here as colloidal particles whose size is an order of magnitude smaller than the overall size of the complexing polymer, but significantly larger than that of a monomer. A good example of polymer complexation with nanocolloids is the formation of complexes of neutral polymers with micelles of anionic surfactants. Other examples are complexation of hydrophobically modified polymers with proteins, or the electrostatically driven complexation of polyelectrolytes and oppositely charged proteins or dendrimers. In this chapter we develop an analytical model that mimics the complexation of single, hydrophilic coils in a dilute solution with surfactants. The results are equally valid for complexation with other amphiphiles, e.g. globular proteins.

It is well known that at concentrations below the critical micelle concentration (CMC) certain surfactants co-operatively form polymer-micelle complexes with neutral polymers. [119] Such complexes are predominantly formed by anionic surfactants; cationic and neutral surfactants show little affinity for the polymer chains. NMR studies suggest that the polymer monomers coat the micellar surface, and do not penetrate the micellar interior. [120] It is found by some authors that the size of the micelles adsorbed on the polymer is less than that of free micelles in the bulk, and does not depend on the degree of coverage, i.e. on the surfactant concentration. [121–123] Other studies suggest that the number of surfactants per adsorbed micelle does depend on the surfactant concentration.

[124] The micelles are found to be of spherical shape: subsequently, the complex of a polymer chain loaded with micelles has been coined a 'necklace', see Figure 1.4. [120-122]

The driving force for complex formation is suggested to be the shielding of hydrophobic areas on the micellar surface by the polymer chain. [125] Each surfactant molecule consists of a hydrophilic (usually ionic) "head group" and a hydrophobic (hydrocarbon) 'tail', which usually comprises 10-20 alkyl groups. Because of their amphiphilic nature, surfactant molecules self-assemble into aggregates of finite size (micelles) at concentrations exceeding a certain critical value, the CMC. [126,127]. In micelles the hydrophobic tails form the core, thus avoiding unfavourable contacts with water, while the hydrophilic heads straddle the core-water interface. However, as the core-water interface is only partially covered by the heads, hydrophobic patches are present on the interface. In the presence of hydrophilic polymer chains association of ionic surfactants may occur at a critical association concentration (CAC), which is generally below the CMC. This entails that only individual surfactants but no micelles are present in the solution. In this case the affinity between the hydrophobic tails of surfactants and the polymer units is not strong enough to bind individual surfactants to the chain. [120,128,129] However, weak attractive interactions may trigger self-assembly of surfactants into micellar-like aggregates complexed with the polymer chain.

A widely studied experimental model system for association in polymer-surfactant solutions is polyethyleneoxide (PEO) and sodium dodecyl sulfate (SDS). The CAC is 10^{-3} M in 0.1 M NaCl solutions, whereas the CMC under the same ionic conditions is approximately $1.5 \cdot 10^{-3}$ M. [121,123] The SDS-micelles bound to the PEO consist of approximately 50 surfactants at this ionic strength, which is significantly less than the aggregation number for non-complexed micelles. [130] Similar aggregation numbers are also obtained for SDS in combination with polyvinyl alcohol and polyvinyl pyrrolidone. [123] The number of PEO-monomers surrounding one micelle is estimated to be of the order 25-100. [121,123,130] The formation of polymer-micelle complexes strongly enhances the visco-elasticity of a bulk solution of PEO/SDS solutions. [129]

As mentioned, polymers or polyelectrolytes may form complexes with proteins or micellar-like aggregates. We stress, however, that there is an important distinction between association of proteins or surfactants with polymers. In the case of water-soluble, globular proteins the majority of the hydrophobic groups is usually found in the interior of the globule (their attraction leads to the formation of a dense globule with a well-defined spatial structure), whereas at the globule-water interface the hydrophilic groups are exposed to water, and thus provide the solubility of the globules. As is the case with micellar aggregates, hydrophobic patches occupy a certain fraction of the globule interface. The attractive (hydrophobic) interaction of such patches with polymeric monomers provides the driving force for polymer-protein association. Generally the spatial (ternary) structure of the protein globule remains unperturbed upon complexation, i.e. only the hydrophobic patches on the interface interact with the polymer. Hence, association of proteins occurs non-cooperatively (at low degree of loading). In contrast, due to the large number of surfactants that constitute a single micelle, polymer-surfactant complexation may occur highly co-operatively.

Several theoretical models are available that describe the behaviour of a single polymer chain in contact with a surfactant solution. Nagarajan [131, 132] and Ruckenstein *et al.* [133] proposed models that determine the CAC's and the aggregation number of the polymer-micelle complexes as a function of molecular parameters, i.e. the size of the head group, the length of the alkyl chain etc. Nagarajan assumes the polymer monomers to adsorb directly on the hydrophobic areas on the micellar surface. This results both in a decrease of the hydrophobic interactions and an increase in the steric repulsion between the charged heads. Ruckenstein *et al.* assume the polymer adsorption to make the area around the micelle less hydrophilic. This is advantageous for the apolar micellar core, but disadvantageous for the hydrophilic head groups. Recently, an elaborate molecular-thermodynamic model for polymer chains covered by spherical micelles was suggested by Nikas and Blankstein. [134] In this model the elasticity of the polymer, solvent quality, electrostatic forces and specific polymer-surfactant interactions are considered. This model calculates the CAC, amount of micelles adsorbed per polymer, aggregation number and size of the complex as a function of several molecular input parameters.

The above models all consider the formation of a single polymer-micellar complex in a reservoir of surfactants. None of them, however, takes intra- and intermolecular excluded-volume interactions between polymers covered by adsorbed micelles into account. At high polymer concentrations such intra- and intermolecular interactions are important, and may largely determine the properties of the solution. This is the case for semi-dilute polymer solutions, but also for collapsed polymer globules, in which the monomer density is (locally) high, and for brushes in contact with solutions containing surfactants. To resolve this, a simple theoretical model that mimics the behaviour of single polymer chains in a good solvent in the presence of associating surfactants is presented in this chapter. In the following chapters this model is extended to semi-dilute solutions, bad solvent conditions and brushes.

5.2. MODEL

We consider a system of neutral polymer chains consisting of N monomers immersed in a solution containing surfactants and added electrolyte. The chains are assumed to be flexible, i.e. the Kuhn length is equal to the monomer length l , which is the unit length in the system.¹ The solvent is erstwhile assumed to be good (athermal) for the chain. We assume that the surfactant concentration is above the CAC, but below the CMC. This entails that no free micelles are present in the solution. The chemical potential μ_S of the surfactant is constant throughout the system and equals (in unit $k_B T$)

$$(5.1) \quad \mu_S = \mu_S^0 + \ln f_S \rho_b$$

where ρ_b is the (dimensionless) bulk density of surfactants, f_S the activity coefficient and μ_S^0 is the standard chemical potential of the surfactant in the bulk solution.

Adsorption of micelles on the polymer chains effectively modifies both intramolecular and (in semi-dilute solutions or collapsed coils) intermolecular interactions, and thus

¹ We remark that in some papers in the field of surfactant science the term 'monomer' is used to refer to a single surfactant molecule. In this thesis this phrase explicitly refers to polymeric segments.

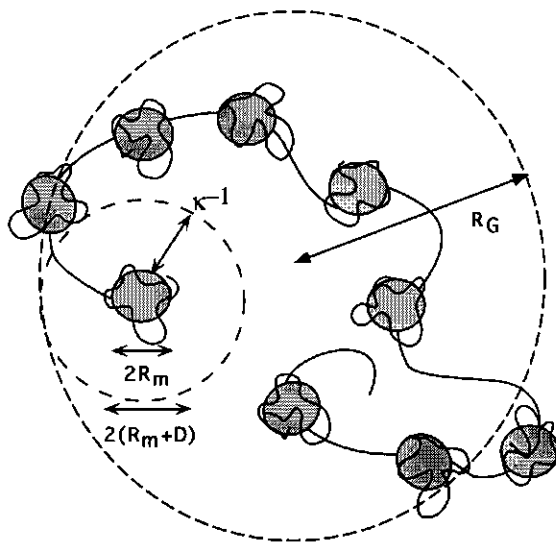


FIGURE 5.1. A schematic illustration of the length scales involved in a 'necklace'.

affects the conformation of the chains. An equilibrium adsorbed amount of surfactant per chain, as well as the equilibrium chain extension, can be obtained on the basis of an analysis of the grand canonical free energy F in a Flory-type approach (in units $k_B T$ per chain) [135]

$$(5.2) \quad F = F_{ad} + F_{mix} + F_{el} + F_{os}$$

which includes four main contributions, discussed separately below.

The first term describes the gain in free energy due to the adsorption of m micelles on the polymer chain. When surfactants aggregate on a polymer, a polymer strand of length N_{ad} associates with one micelle, consisting of p surfactants. We denote the energy of adsorption per unit chain length as u^0 . If there are m adsorbed micelles per chain, we thus have:

$$(5.3) \quad F_{ad} = mN_{ad}u^0 + mp\Delta\mu$$

where

$$(5.4) \quad \Delta\mu = \mathbb{C} - c \ln p_b$$

where \mathbb{C} is a constant that depends on the choice of system. Eq.(5.4) is derived in the appendix, and it is shown that the constant c varies between 1 and 2, depending on the ionic strength of the solution. We remark that both monomers that form 'trains' (sequences of monomers in direct contact with the micellar surface) as well as monomers that form 'loops' contribute to N_{ad} . [136]

We now turn towards the energy per adsorption per unit chain length u^0 . The micelles are assumed to be spherical of shape with a uniform radius R_m , which is large compared to the monomer length l . The aggregation number p and the number of monomers

associated with one micelle (the adsorbance capacity of a micelle) depend on the contact energy ϵ between monomers and the micellar surface. Our model of the polymer-micelle complex is based on existing theoretical models that describe the adsorption of a flexible polymer chain on small colloidal particles. [137–140] These models give the structure and the free energy of the complex (polymer chain and adsorbed spherical particle) in terms of the particle radius and the energy ϵ of the monomer attraction to the surface.

In our model we assume that the affinity of the monomers for the micellar surface is relatively strong, i.e. the thickness D of the adsorbed layer (i.e. the characteristic size of loops), given by $D \approx (|\epsilon - \epsilon_{cri}|)^{-1}$, is much smaller than the micellar size R_m . [137–139] The critical contact energy ϵ_{cri} , which corresponds to the onset of adsorption of a polymer onto a particle surface, is of order $k_B T$ and provides compensation for local steric restrictions imposed by localisation of a monomer at the surface. [136] The contact energy ϵ arises from the screening of hydrophobic areas on the micellar surface. In the framework of simple mean-field arguments the adsorbance capacity per micelle N_{ad} in good solvents is proportional to the area of the micellar surface, $N_{ad} \approx |\epsilon - \epsilon_{cri}| R_m^2$. [137] The free energy of adsorption of a polymer strand of length N_{ad} scales as $-N_{ad} (|\epsilon - \epsilon_{cri}|)^2$. We can write the area per surfactant as $a = 4\pi R_m^2/p \approx N_{ad}/(|\epsilon - \epsilon_{cri}|p)$. If we use this to eliminate p from Eq.(5.3), and omit numerical prefactors, we can write the free energy of adsorption per monomer in an adsorbed strand, F_{ad}/mN_{ad} , as

$$(5.5) \quad u \equiv \frac{F_{ad}}{mN_{ad}} \approx -(|\epsilon - \epsilon_{cri}|)^2 + \frac{\Delta\mu}{(|\epsilon - \epsilon_{cri}|a)}$$

Thus, u contains a constant contribution $u^0 = -(|\epsilon - \epsilon_{cri}|)^2$, that depends on the adsorption characteristics of the polymer on the micellar surface, and a term that depends explicitly on the work necessary for the formation of such a micelle. If we combine Eqs.(5.4) and (5.5), it follows that the (differential) monomeric free energy of adsorption can be expressed as $u = C' - c' \ln \rho_b$, where C' and c' are again constants that depend on the choice of system. Hence, the adsorption strength can be tuned by variation of the surfactant concentration: $N_{ad}u \gg 0$ at low ρ_b , and adsorption is unfavourable, whereas $N_{ad}u \ll 0$ at high ρ_b and adsorption is favourable. In the following it is convenient to define the fraction of adsorbed monomers (both in trains and loops) as

$$(5.6) \quad \theta = \frac{mN_{ad}}{N}$$

Therefore, $\theta = 0$ characterises a 'bare' chain, and $\theta = 1$ a fully complexed chain. If Eqs.(5.5) and (5.6) are combined, the total contribution of the micelle adsorption to the free energy of a polymer chain is simply

$$(5.7) \quad F_{ad} = N\theta u$$

The second term in the free energy of a polymer chain, F_{mix} , describes the translational, or mixing, entropy of m adsorbed micelles along the chain. In the most simple

approach the polymer contains NN_{ad}^{-1} 'adsorption sites' for the micelles, and thus

$$(5.8) \quad \begin{aligned} F_{mix} &\equiv -Ns(\theta) \\ &= \frac{N}{N_{ad}} \left(\theta \ln \frac{\theta}{N_{ad}(1-\theta) + \theta} + N_{ad}(1-\theta) \ln \frac{N_{ad}(1-\theta)}{N_{ad}(1-\theta) + \theta} \right) \end{aligned}$$

where $-s(\theta)$ denotes the average translational entropy per monomer corresponding to a degree of loading θ . In the appendix this expression for F_{mix} is derived.²

The third term F_{el} in Eq.(5.2) accounts for the elastic free energy of stretching, which stems from the loss of conformational entropy as the polymer stretches. As a simplest approximation we assume the elasticity of the chains to be Gaussian, regardless of the degree of coverage by micelles. The adsorption of micelles, however, modifies the unperturbed (Gaussian) size of the chain, and thus renormalises its elasticity. This is easily understood if we consider the case of total loading ($\theta = 1$). In this case a necklace consists of N/N_{ad} monomers of diameter $2R_m$ (as the thickness of the adsorbed layer is negligible), which generally has a different Gaussian radius than N monomers of unity length. At an intermediate value of θ a 'necklace' in our model consists of m micelles, connected by bridges formed by the $N(1-\theta)$ non-adsorbed monomers of the chain (of unit length). The length of such a bridge is $N(1-\theta)/(m-1) \approx N_{ad}(1-\theta)/\theta$. The Gaussian radius of the coil for a degree of loading θ is given by

$$(5.9) \quad R_0(\theta)^2 = N(1-\theta) + m(2R_m)^2 = N \left((1-\theta) + \frac{4\theta R_m^2}{N_{ad}} \right)$$

and depends explicitly on θ . If we introduce a parameter β to account for the renormalisation of the elastic modulus of a necklace, defined as

$$(5.10) \quad \beta = \frac{4R_m^2}{N_{ad}} - 1$$

then Eq.(5.9) simply reduces to $N(1+\beta\theta)$. The elastic free energy of the necklace is now given by

$$(5.11) \quad F_{el} = \frac{3R_G(\theta)^2}{2R_0(\theta)^2} = \frac{3R_G(\theta)^2}{2N(1+\beta\theta)}$$

where $R_G(\theta)$ denotes the equilibrium radius of gyration of the necklace at a coverage θ . As follows from its definition, β depends, generally speaking, on the contact energy ϵ of a monomer with the micellar surface and on the solvent quality for the polymer. It may vary between a large positive value (large nanocolloids, complexed with a relatively small number of monomers) and a value close to -1 (small nanocolloids, complexed with a relatively large number of monomers).

The last contribution to the free energy F_{os} is the osmotic contribution, originating from excluded-volume effects. In the framework of our mean-field model we characterise the chain by an average density of non-adsorbed monomers $N(1-\theta)R_G^{-3}$ and that of micelles mR_G^{-3} . Thus, F_{os} is written as a Taylor expansion in the monomer and micellar

²We remark that in our first paper on polymer-surfactant association a less accurate expression for F_{mix} is used, namely $NN_{ad}^{-1}(\theta \ln \theta + (1-\theta) \ln(1-\theta))$. [141]

densities, the prefactors of which are the virial coefficients, or excluded-volume parameters. Provided the solvent quality is good, the osmotic term F_{os} accounts for three types of binary, repulsive interactions: (i) between two non-adsorbed monomers, (ii) between two micelles covered by adsorbed polymer, and (iii) between non-adsorbed monomers and covered micelles. The excluded-volume parameters are denoted as \tilde{v}_0 , \tilde{v}_1 and \tilde{v}_2 , respectively. It is, however, convenient to write the osmotic free energy in terms of an effective excluded-volume parameter per monomer $v_{eff}(\theta)$, which is a function of the degree of coverage,

$$\begin{aligned}
 F_{os} &= \frac{(N(1-\theta))^2 \tilde{v}_0 + m^2 \tilde{v}_1 + Nm(1-\theta) \tilde{v}_2}{R_G^3} + \frac{N^3 w_{eff}(\theta)}{R_G^6} + \dots \\
 &= \frac{N^2 (v_0(1-\theta)^2 + v_1 \theta^2 + 2v_2 \theta(1-\theta))}{R_G^3} + \frac{N^3 w_{eff}(\theta)}{R_G^6} + \dots \\
 (5.12) \quad &= \frac{N^2 v_{eff}(\theta)}{R_G^3} + \frac{N^3 w_{eff}(\theta)}{R_G^6} + \dots
 \end{aligned}$$

Thus, if we define $v_0 = \tilde{v}_0$, $v_1 = \tilde{v}_1 N_{ad}^{-2}$ and $v_2 = \tilde{v}_2 (2N_{ad})^{-1}$, the effective excluded-volume parameter per monomer $v_{eff}(\theta)$ is defined as

$$(5.13) \quad v_{eff}(\theta) = v_0(1-\theta)^2 + v_1 \theta^2 + 2v_2 \theta(1-\theta)$$

The second term in Eq.(5.12) describes the ternary, or three-body, interactions between monomers and adsorbed micelles, where $w_{eff}(\theta)$ is the effective third-order virial coefficient which is generally positive. [142] Above the Θ -temperature all the contributions to $v_{eff}(\theta)$ are positive, i.e. the effective binary interactions in the system are repulsive. Under these conditions the third-order term in Eq.(5.12) can safely be neglected. In Chapter 6 the situation is considered where the temperature is below the Θ -temperature for the polymer chain, in which case the third-order term must be taken into account.

The equilibrium conformation for a certain set of parameters (N, v_i, u) is determined from the condition of minimal free energy per chain. For a bare coil (no adsorption of micelles) the free energy is dominated by two terms: the elastic energy and the excluded-volume interactions between the monomers. Minimisation of F with respect to R_G yields the mean-field scaling law $R_G \sim N^{3/5} v_0^{1/5}$. In the case of adsorbed micelles the free energy is minimised with respect to both the coil radius and the degree of coverage θ , i.e. the number of adsorbed micelles per chain.

$$(5.14) \quad \left(\frac{\partial F}{\partial R_G} \right)_\theta = \left(\frac{\partial F}{\partial \theta} \right)_{R_G} = 0$$

Minimisation with respect to R_G gives the coil radius as a function of θ :

$$(5.15) \quad R_G \approx N^{3/5} ((1 + \beta\theta)v_{eff}(\theta))^{1/5}$$

where $v_{eff}(\theta)$ is given by Eq.(5.13) and numerical prefactors are omitted. Note that Eq.(5.15) reduces to the expression for bare chains, $R_G \approx N^{3/5} v_0^{1/5}$, for $\theta = 0$. Combining

this with the second equilibrium condition yields

$$(5.16) \quad -s'(\theta) + N_{ad}u + N_{ad}N^{-4/5} \left(\frac{v'_{eff}(\theta)}{((1 + \beta\theta)v_{eff}(\theta))^{3/5}} - \frac{\beta v_{eff}(\theta)^{2/5}}{2(1 + \beta\theta)^{3/5}} \right) = 0$$

where we define $s'(\theta) = \frac{ds(\theta)}{d\theta}$ and $v'_{eff}(\theta) = \frac{dv_{eff}(\theta)}{d\theta}$.

From the above equation θ can be calculated for given set of excluded-volume parameters as a function of the effective adsorption energy u . In this way a binding isotherm is obtained, as the effective adsorption energy is a function of the surfactant concentration in the bulk (see Eq.(5.5)). For long chains, however, the third term in Eq.(5.16) is negligible compared to the first two terms, due to the denominator $N^{-4/5}$. If we neglect the last term in Eq.(5.16) the expression simplifies to

$$(5.17) \quad \begin{aligned} u &= \frac{s'(\theta)}{N_{ad}} \\ &= \ln \frac{N_{ad}(1 - \theta)}{N_{ad}(1 - \theta) + \theta} - \frac{1}{N_{ad}} \ln \frac{\theta}{N_{ad}(1 - \theta) + \theta} \end{aligned}$$

Note that in the case $N_{ad} = 1$ the above expression reduces to a Langmuir-like adsorption isotherm, i.e.

$$(5.18) \quad u = -\ln \left(\frac{\theta}{1 - \theta} \right)$$

5.3. ESTIMATION OF PARAMETERS

In order to proceed further and to make a basis for comparison between the predictions of the above model and experimental results, it is necessary to estimate the molecular parameters that appear in our model, namely the radius of a micelle R_m , the number of adsorbed monomers per micelle N_{ad} and the excluded-volume parameters v_0, v_1 and v_2 . Experimental data, available for several surfactant-polymer systems, are used as reference. [120–124, 130, 143] The system predominantly referred to is PEO and SDS.

The radius of an adsorbed micelle is typically between 2 and 5 nm, depending on the salt concentration. [120, 122, 143] Generally speaking, the number of surfactants and thus the micellar radius increases with increasing salt concentration. For a given salt concentration the number of surfactants per polymer-micelle complex is reported to be constant, i.e. independent of the degree of coverage. [120] We use a constant value for the micelle radius of order 10 times the monomer length l in our model. In the case of PEO the value for l is 0.35 nm [91]; the micellar radius in this case is approximately 3 nm.

As the micelle radius is large compared to the monomer length, and the affinity of the monomers to the micellar surface is sufficiently high, the curvature of the micellar surface plays no significant role in the adsorption of the polymer. [137] The number of adsorbed monomers per micelle N_{ad} is therefore proportional to the surface area of a micelle. Furthermore, it is independent of the degree of coverage, as the micelle radius is also assumed constant. The number of adsorbed PEO monomers per SDS micelle is reported by Gilanyi *et al.* to be of order of 120, Cabane gives a value 60 and Shirahama's

value is close to 100. [120,121,123] We use values for N_{ad} of order 10 -100, which are assumed to be constant for all values of θ .

We now turn towards the second-order virial coefficients v_0, v_1 and v_2 . Such coefficients can be estimated using an expression from the Baker-Henderson theory [144],

$$(5.19) \quad v_i = \frac{1}{2} \int_0^\infty \left(1 - e^{-U(\bar{r})/k_B T}\right) d\bar{r} = 2\pi \int_0^\infty \left(1 - e^{-U(r)/k_B T}\right) r^2 dr$$

where $U(\bar{r})$ is the interaction energy between the particles and r the center-to-center distance between the particles. The second expression for v_i is valid for interaction potentials $U(r)$ that do not depend on the orientation, i.e. are spherically symmetric, which is the case in our model.

As we restrict ourselves in this chapter to good solvent conditions, the bare monomers are treated as hard spheres without any long-range repulsion or attraction between themselves. The interaction potential can thus be given as $\Theta(r-1)U_{hwr}$, where $\Theta(\dots)$ is the Heavyside unit-function and U_{hwr} is a hard-wall repulsion (its value is close to infinity). The second virial coefficient of monomer-monomer interactions v_0 under athermal solvent conditions then equals

$$(5.20) \quad v_0 = \frac{4\pi}{6} \approx 1$$

as the monomer length l is unity. In Θ or poor solvent conditions the parameter v_0 becomes zero or negative, respectively. This is considered in the following chapter.

For the renormalised micelle-micelle v_1 and monomer-micelle v_2 virial coefficients we distinguish between micelles comprised of charged surfactants and non-charged micelles. In the case of neutral surfactants the micelle-micelle interactions are determined by the effective excluded volume of a micelle. This is larger than that of a bare micelle, because of the swollen corona of adsorbed polymer monomers. As a simplest approximation the interaction is treated as that between hard spheres, similar to monomer-monomer interactions. This gives

$$(5.21) \quad v_1 = \frac{2\pi}{3} \frac{(2(R_m + D))^3}{N_{ad}^2} \approx \frac{16\pi R_m^3}{N_{ad}^2} \sim R_m^{-1}$$

where D is again the thickness of the adsorbed layer, which is neglected. Note that, although the micelle-micelle virial coefficient \bar{v}_1 increases with R_m , the *renormalised* coefficient v_1 is predicted to decrease with R_m .

There is also a negative contribution to v_1 due to bridging attraction (i.e. loops in a corona adsorbing on another complexed micelle). Such attraction can be important at intermicellar distances between centers of micelles of order $2(R_m + D)$. Hence, in the absence of long-range Coulomb repulsion (uncharged complexed micelles) the necklace of micelles may collapse. We remark that, as formation of bridges is not instantaneous, the swollen necklace conformation may exist as a metastable state.

As stated in section 5.1, however, it is experimentally observed that surfactants that form polymer-micelle complexes are predominantly anionic. Several explanations have been suggested for this phenomenon, but, as the exact reason remains to be determined, the issue is not yet resolved. [130,131,133,134] It is therefore essential to include the

micellar charge in our model and to estimate its effect on the parameters. We again use the mean-field approximation and for simplicity write the intermicellar interaction potential as $U(r) = \Theta(r - 2(R_m + \kappa^{-1}))U_{hwr}$, where κ^{-1} is the Debye length. This expression is valid when κ^{-1} is large compared to D . The micelle-micelle interaction parameter v_1 is then given by

$$(5.22) \quad v_1 \approx \frac{16\pi (R_m + \kappa^{-1})^3}{3N_{ad}^2}$$

and may significantly exceed the 'geometrical' micelle-micelle excluded volume $\sim R_m^3$.

The renormalised second virial coefficient v_2 for monomer-micelle interactions is determined by the effective excluded volume of a micelle covered by adsorbed polymer for a monomeric unit. As R_m is large compared to l and to D , we approximate $U(r)$ as $U(r) \approx \Theta(r - R_m)U_{hwr}$, and it follows that

$$(5.23) \quad v_2 \approx \frac{2\pi R_m^3}{3N_{ad}}$$

This expression is valid in the limit of total coverage of the micellar surface by polymer. For partial coverage the above value is an overestimation, as there are attractive interactions between the uncovered hydrophobic patches on the micelle and the monomers. Because we restrict ourselves to neutral polymers, charges play no role in the monomer-micelle interactions. Therefore, v_2 is the same for neutral and charged micelles, and is independent of the salt concentration.

The last parameter which must be estimated is that of the mean adsorption energy per monomer u . Shirahama [121], Cabane [120] and Gilanyi *et al.* [123] report complexation of SDS with PEO in 0.1 M inert electrolyte (Cabane 0.4 M) to occur at approximately 1 mM SDS. The number of adsorbed monomers is of order 100. The free energy of adsorption is estimated to be $13 k_B T$ per micelle by Shirahama, 10 - $20 k_B T$ by Cabane and $16 k_B T$ by Gilanyi *et al.* This gives a value for u of approximately $0.15 k_B T$ at high degrees of loading. Naturally, this value depends on the surfactant concentration, as is evident from the definition of u (Eq.(5.5)). Therefore, u is a variable in our model, but its value should be of order $0.1 k_B T$. We finally note that when u is tuned by variation of the surfactant concentration, N_{ad} remains unaffected, which is assumed in our model. This is not the case if the temperature or solvent composition are varied, as this affects the 'bare' adsorption energy $|\epsilon - \epsilon_{cri}|$ (see the discussion concerning Eq.(5.5)).

5.4. RESULTS

In Figure 5.2 the degree of coverage θ , given by Eq.(5.16), is shown as a function of u for three different values of v_1 . We remind the reader that v_0 characterises the strength of osmotic interactions between bare monomers, v_1 that between complexed monomers and v_2 that between a bare and complexed monomer. The values for the chain length, v_0 , N_{ad} and R_m are constant for all following results. As shown in Figure 5.2 the adsorption of micelles on the polymer chain is continuous with increasing surfactant concentration (via u , see Eqs.(5.4) and (5.5)), and virtually independent of the excluded-volume parameters.

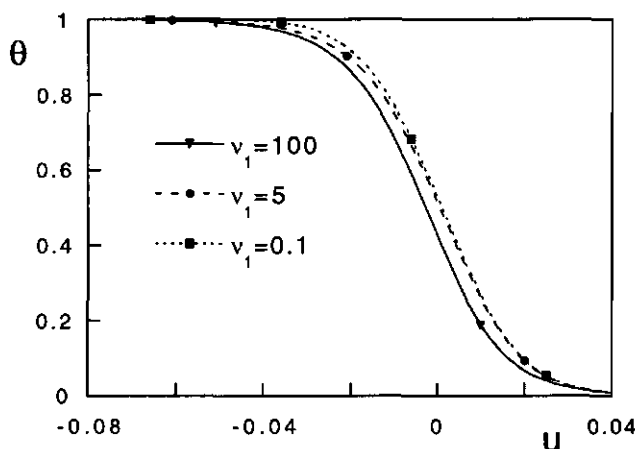


FIGURE 5.2. θ as a function of u for three values of v_1 , $N = 10000$, $N_{ad} = 100$, $R_m = 8$, $v_0 = 1$, $v_2 = 20$ and $\beta = 0$.

This demonstrates that the contribution of intramolecular excluded-volume interactions is negligible in comparison to the adsorption contribution for long chains. Thus, the degree of coverage of coils in a dilute solution depends only on the mean adsorption energy, i.e. the chemical potential of the surfactants.

Experimentally, the CAC is defined as the surfactant concentration at which an effect of a finite degree of loading is observed on physical quantities, such as the coil radius or the solution viscosity. Using Figure 5.2, we can roughly identify the CAC by the surfactant density in our model at which $u = 0$. Physically, this entails that there is no netto increase or decrease in free energy upon formation of a complex. If we insert $a \approx N_{ad}/|\epsilon - \epsilon_{cri}|p$ in Eq.(5.5), it follows that

$$\begin{aligned}
 \ln \rho_{CAC} &= \frac{C}{c} - \frac{(|\epsilon - \epsilon_{cri}|)^2 N_{ad}}{cp} \\
 (5.24) \qquad &\approx (\mu_p^0 - \mu_S^0) - \frac{(|\epsilon - \epsilon_{cri}|)^2 N_{ad}}{p}
 \end{aligned}$$

where in the second equation we have neglected the contribution of the counterions and set the activity coefficients equal to unity (see Eqs.(5.27) and (5.28)). The CAC in our model is therefore determined by a balance between the cost of transferring a surfactant molecule from the bulk solution to a micellar environment ($\mu_S^0 - \mu_p^0$), and the effective gain in free energy per surfactant from adsorption of a polymer strand on the micellar surface, $(|\epsilon - \epsilon_{cri}|)^2 N_{ad}/p$. It is clear from Eq.(5.24) that the difference between the CAC and CMC, the latter roughly defined by $\exp(\mu_p^0 - \mu_S^0)$, increases as $(|\epsilon - \epsilon_{cri}|)^2 N_{ad}/p$ increases, i.e. as adsorption of the polymer strand increasingly lowers the free energy of the micellar aggregate.

Whereas θ solely depends on u and is virtually independent of the excluded-volume parameters, the radius of the coil R_G is strongly affected by adsorption of micelles, and

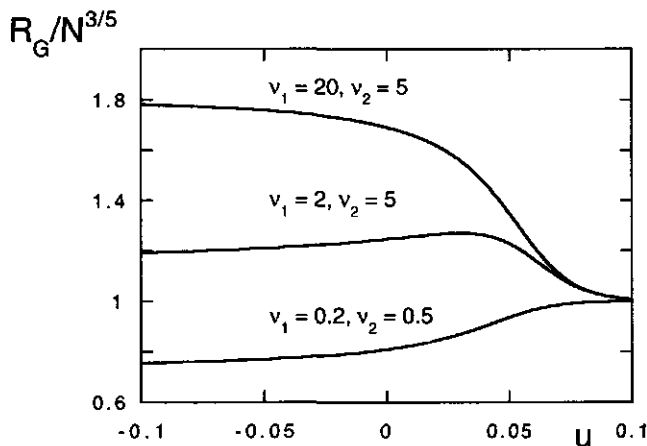


FIGURE 5.3. $R_G/N^{3/5}$ as a function of u for three sets of v_1 and v_2 . Other parameters are $N_{ad} = 100$ and $\beta = 0$.

depends on θ via the effective virial coefficient $v_{eff}(\theta)$. As v_0 is unity, the radius of gyration of a 'bare' chain is simply $N^{3/5}$ in our model (see Eq.(5.15)). In Figure 5.3 $R_G/N^{3/5}$, i.e. the ratio of the size of the complexed and bare chain, is plotted as a function of u for several values of v_1 and v_2 . When v_1 is much larger than v_0 and v_2 , the coil radius increases monotonically with increasing adsorption strength, as the excluded-volume interactions between the micelles are large compared to the monomer-monomer and monomer-micelle interactions. The strong micelle-micelle interactions provide strong swelling of the coil at large degrees of coverage. When both v_1 and v_2 are smaller than v_0 the opposite is the case. The coil wraps itself around the micelles and effectively shrinks with increasing adsorption strength. This behaviour may occur for adsorbing neutral micelles or charged micelles at high ionic strength.

An interesting case is found when v_2 is significantly larger than both v_0 and v_1 . Under such conditions, a maximum occurs in the coil radius at an intermediate coverage, as shown in Figure 5.3. At low coverage the polymer has wrapped itself around a few micelles. This has effectively shortened the chain but the osmotic interactions between the bare monomers and adsorbed micelles result in an overall swelling of the chain with increasing coverage. At high coverage the chain is nearly totally covered by micelles and the coil radius decreases with increasing coverage. As the v_2 -term dominates the osmotic interactions, the maximum in size occurs at $\theta \approx 1/2$, i.e. half coverage.

From Figure 5.3 one could conclude that at total loading (large negative u) the radius of the complexed chain is smaller than that of the bare chain when $v_1 < v_0$ and larger when $v_1 > v_0$. However, the effective number of monomers has decreased from N monomers of unit length to N/N_{ad} monomers of length $2R_m$. This renormalisation of the effective monomer length is characterised by β , defined in Eq.(5.10). A positive β denotes a system in which the effective monomer length increases upon loading (large complexed particles, small N_{ad}), a negative β a system in which the effective monomer

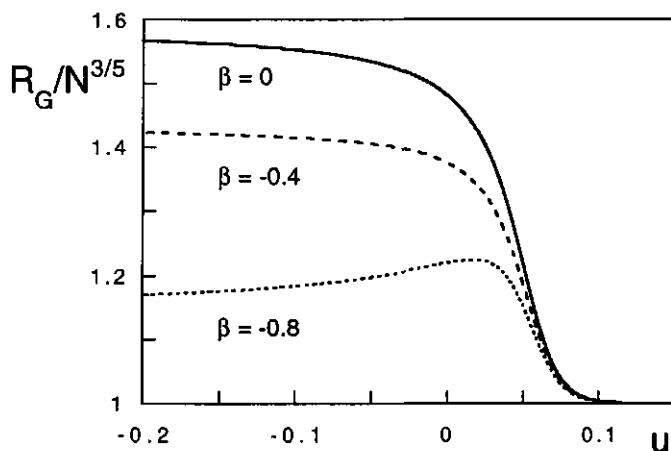


FIGURE 5.4. $R_G/N^{3/5}$ as a function of u for 3 values of β , $v_1 = 10$, $v_2 = 3$, $N_{ad} = 100$.

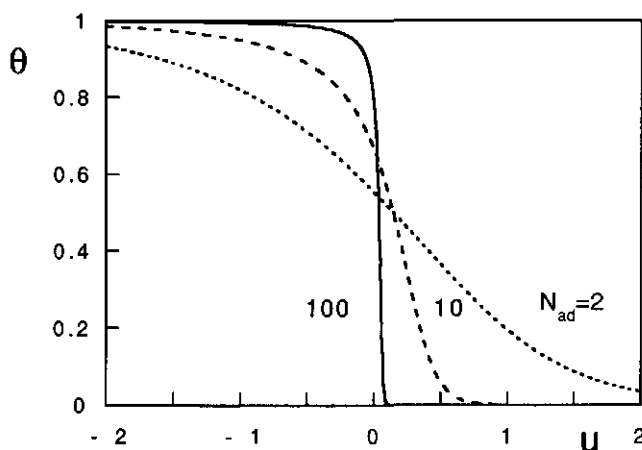


FIGURE 5.5. θ as a function of u for three values of N_{ad} .

length decreases (small complexed particles, large N_{ad}). In Figure 5.4 the ratio in coil size is shown for fixed excluded-volume interactions and varying β . In the case that $\beta = 0$ the coil monotonously swells with increasing θ , i.e. decreasing u , as the strength of the osmotic interactions effectively increases with loading ($v_1 > v_0$). However, as β becomes negative, the increase in coil size lessens and a maximum in R_G may even appear. This maximum is the overall result of an increase in strength of osmotic interactions and a decrease in effective chain length upon loading. We can thus conclude that the size of the complexed coil is a delicate balance between the strength of osmotic interactions in the complexed coils and the change in effective monomer length upon complexation.

An interesting parameter in our model is N_{ad} , which is the number of monomers complexed per micelle. In Figure 5.5 θ is plotted as a function of u for three values of N_{ad} . From Figure 5.5 or Eq.(5.17) it follows that the loading isotherm becomes 'steeper' with increasing N_{ad} . This entails that N_{ad} is a measure for the cooperativity of the complexation process. This is reasonable, as N_{ad} scales as $(|\epsilon - \epsilon_{cri}|) p^{2/3}$, where p is the number of surfactants in a complexed micelle. Thus, the 'steepness', or cooperativity, of the binding isotherm is both a measure for the number of surfactant molecules in a complex as for the number of monomers adsorbed per complex.

It is interesting to compare the above results with experimental data. In the literature several viscosity measurements of solutions of hydrophilic polymers in the presence of aggregating surfactants have been presented. At low polymer concentration the reduced viscosity of a polymer solution is a measure for the size of the polymer coils. Wang and Olofsson found that the reduced viscosity of EHEC, a hydrophilic cellulose polymer, at high SDS concentrations is lower than that of the bare polymer. [128] They conclude that adsorption leads to a more compact polymer complex, in spite of the electrostatic repulsion between the micelles. In contrast, various authors find the relative viscosity of PEO with SDS to have a maximum as a function of the SDS concentration at a constant high ionic strength. [143,145] Such a maximum in the viscosity corresponds to a maximum in the coil size. The effective decrease in coil size is ascribed to increasing electrostatic screening due to increasing surfactant concentration. However, Brown *et al.* found distinct maxima in the relative viscosity of PEO/SDS at constant high electrolyte concentrations. [143] Hence, the interpretation of such maxima in terms of modified electrostatic screening may be questioned. We suggest that such experimental maxima correspond to the maxima in coil size as predicted by our model, whereby a balance is present between an increase in osmotic repulsion and decrease in effective monomer length with increasing loading.

An interesting system consisting of a PAM-PEO gel in contact with an SDS-solution was recently investigated by Rosén *et al.* [146] The PAM-backbone (polyacrylamide) does not form complexes with SDS, and the change in gel volume is due to complex formation of the long PEO side-chains with SDS-micelles. In Figure 5.6 the results of Rosén *et al.* are shown. The relative increase in gel volume V/V_0 is given as a function of the SDS-concentration for several ionic strengths. The arrows in the figure denote the CAC's at the given ionic strengths. With increasing ionic strength the CAC drops to lower concentrations. The primary reason for the decrease in CAC is the decreasing electrostatic repulsion between the ionic head-groups with increasing ionic strength. At zero added salt the gel is found to swell strongly when c_{SDS} is above the CAC (approximately 6 mM). As the ionic strength increases, V/V_0 is found to decrease. This corresponds to the decrease of v_1 in our model with decreasing κ^{-1} . At high ionic strengths (1 M) the gel volume is found to decrease as the CAC is surpassed. This corresponds to $v_1 < v_0$ in our model, i.e. the renormalised osmotic interactions between complexed micelles are less than the monomer-monomer interactions.

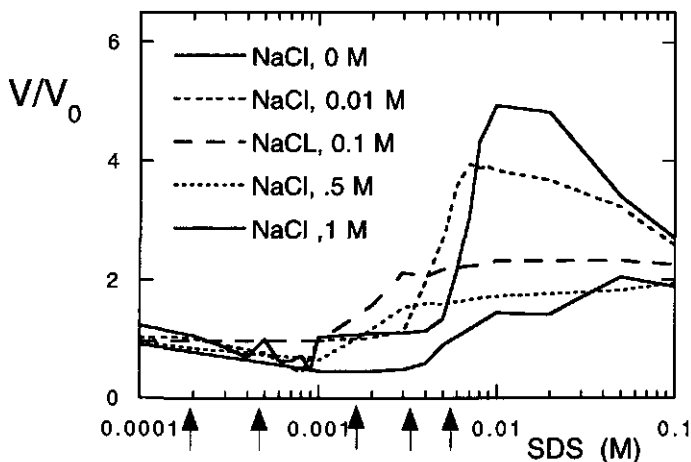


FIGURE 5.6. Relative swelling of a PAm-PEO gel, V/V_0 , as a function of SDS-concentrations at various ionic strengths, after Rosén et al. The arrows denote the CAC's for the various ionic strength's.

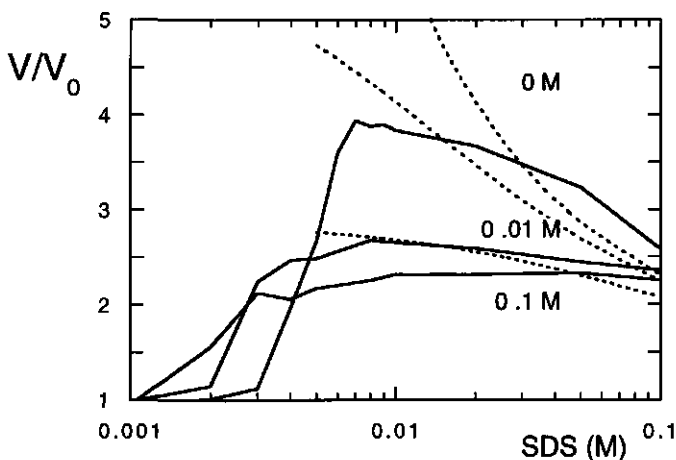


FIGURE 5.7. Decrease in V/V_0 with increasing c_{SDS} at low ionic strengths, both experimental (solid curves) and model predictions for $\theta = 1$ (dashed curves).

In Figure 5.6 a maximum in V/V_0 occurs at c_{max} for low concentrations of added electrolyte. As $c_{max} \gg c_{CAC}$, the maximum is believed to correspond to a total loading of the PEO-chains. The decrease in V/V_0 beyond this maximum is due to an effective increase in ionic strength of the solution as c_{SDS} increases. As the ionic strength of the system is known, we can compare the decrease in gel volume with that predicted by our model using the definition of v_1 . In Figure 5.7 the experimental data (solid curves) are plotted together with the results of our model (dashed curves). As the relative gel

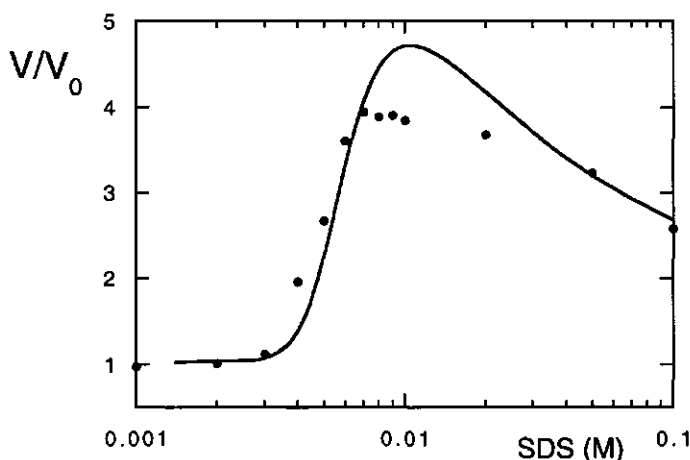


FIGURE 5.8. V/V_0 as a function of the surfactant concentration for zero added electrolyte, both model (solid curve) and exp. data (circles).

volume is considered, all numerical prefactors are cancelled. At total loading, the gel volume ratio in our model is given by (see Eq.(5.15))

$$(5.25) \quad \Delta V = \left(\frac{R_G(\theta = 1)}{R_G(\theta = 0)} \right)^3 = \left(\frac{(1 + \beta)v_1}{v_0} \right)^{3/5}$$

where v_1 is given by Eq.(5.22) and v_0 is approximately $4\pi l^3/3$. The κ^{-1} is determined by the combined contribution of the surfactant concentration and the added salt. According to Cabane [120], the radius of the micelles is of order 2.2 nm; according to Rosén *et al.* the number of adsorbed PEO-monomers is of order 60. [146] Using these results and setting $l = 3 \text{ \AA}$, the agreement between our simple model and the experimental data is quite reasonable.

Finally, we can combine all previous results in an isotherm for the gel volume as a function of the surfactant concentration. The only unknown parameters, which depend on the choice of system, are \mathbb{C}' and c' in the expression $u = \mathbb{C}' - c' \ln \rho_b$, see the discussion following Eq.(5.5). Inserting the values -0.5 and 0.11 for \mathbb{C}' and c' , respectively, the isotherm $V(c_{SDS})/V_0$ shown in Figure 5.8 is obtained for zero added electrolyte. It is clear that our model reproduces the swelling and subsequent deswelling of the gel reasonably well. We stress, however, that the values of \mathbb{C}' and c' have been fitted to obtain a good agreement between the model and experiments, and have no relationship to measurable parameters.

5.5. CONCLUSIONS

Using an analytical mean-field model we have investigated the behaviour of polymer chains in a dilute solution containing surfactants. The surfactants are assumed to adsorb on the polymer chain in micellar form. In our model the size of the micelles and number of adsorbed monomers are assumed to be independent of the degree of coverage

of the polymers. An average adsorption energy per adsorbed monomer is introduced to describe the overall polymer-micelle affinity. The monomer-monomer, monomer-micelle and micelle-micelle osmotic interactions are accounted for using mean-field excluded-volume parameters. The degree of coverage of the chains with micelles and the coil size is investigated as a function of the adsorption strength and excluded-volume parameters.

The coverage of single coils in a good solvent with micelles is found to be virtually independent of the excluded-volume interactions, and it increases monotonically with increasing adsorption strength (surfactant concentration). This result agrees qualitatively with experimental adsorption isotherms for hydrophilic polymers and associating surfactants. The coil radius depends strongly on the strength of the excluded-volume interactions. In the case of large micelle-micelle interactions (charged micelles at low electrolyte concentrations) the coil swells with increasing coverage. In the case of relatively large monomer-monomer and small micelle-micelle excluded-volume interactions the coil effectively shrinks. If the monomer-micelle interactions are dominant the coil radius has a maximum at a coverage around 50 %. This maximum may also occur if the unperturbed size of the coil (Gaussian radius) strongly decreases upon complexation. Experimentally, polymers in a surfactant solution are found to swell, shrink or have a maximum, depending on the choice of system.

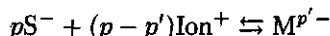
The results of our model are compared to experimental data for the swelling of a PAm-PEO gel with increasing SDS surfactant concentration. Reasonable agreement is found between the observed swelling of the gel and that predicted by our model at low ionic strengths. It can be concluded that the decrease in gel volume at surfactant concentrations far above the CAC is primarily the result of a decrease in strength of electrostatic repulsion between complexed micelles, due to the increase in ionic strength.

ACKNOWLEDGEMENTS

We thank Lennart Piculell for kindly making the PAm-PEO data available.

APPENDIX

We first consider the chemical potential of anionic surfactant molecules at the CAC and the corresponding expression for $\Delta\mu$ in Eq.(5.4). We can write the aggregation process as



i.e. p surfactant molecules and $(p - p')$ counterions combine to form a micellar aggregate of effective charge $p'-$. In the above expression counterion condensation on the micellar aggregate is explicitly taken into account. At the CAC the equilibrium of chemical potentials yields

$$(5.26) \quad \mu_p^0 = \mu_S + \left(1 - \frac{p'}{p}\right) \mu_{\text{Ion}}$$

where the left-hand side is the chemical potential of a surfactant and corresponding fraction of bound counterions in the micellar aggregate, and the right-hand side are the contributions of the single surfactant molecule and counterion in the bulk. If we insert the expressions for the surfactants and counterions (viz. $\mu_S = \mu_S^0 + \ln(f_S \rho_b)$, where f_S is the activity coefficient of the surfactant and ρ_b its density), the result is

$$(5.27) \quad \begin{aligned} \mu_p^0 &= \mu_S^0 + \ln f_S + \left(1 - \frac{p'}{p}\right) (\mu_{\text{Ion}}^0 + \ln f_{\text{Ion}}) + \ln \rho_b + \left(1 - \frac{p'}{p}\right) \ln \rho_{\text{Ion}} \\ &= C_1 + C_2 + \ln \rho_b + \left(1 - \frac{p'}{p}\right) \ln (\rho_{\text{salt}} + \rho_b) \end{aligned}$$

In the above equation all contributions that depend on the choice of system and are independent on the surfactant density are collected in the coefficients C_1 and C_2 . Also, the counterion density is a sum of the surfactant density and the density of added salt.

Using the above expression, we can distinguish two asymptotic regimes. In the first, *the density of added salt is high* compared to the surfactant density at the CAC, i.e. $\rho_{\text{salt}} \gg \rho_{b,\text{CAC}}$. If we then expand the second logarithm in Eq.(5.27) the result is

$$(5.28) \quad \begin{aligned} \Delta\mu &= \mu_p^0 - \left[C_1 + C_2 + \left(1 - \frac{p'}{p}\right) \ln \rho_{\text{salt}} + \left(1 - \frac{p'}{p}\right) \frac{\rho_b}{\rho_{\text{salt}}} + \ln \rho_b \right] \\ &\approx \mu_p^0 - \left[C_1 + C_2 + \left(1 - \frac{p'}{p}\right) \ln \rho_{\text{salt}} + \ln \rho_b \right] \end{aligned}$$

Thus, at high salt densities the electrolyte contribution is reduced to an additional constant contribution and $\Delta\mu$ is proportional to the logarithm of the surfactant density.

In the second asymptotic limit, *the density of added salt is low* compared to the surfactant density at the CAC, i.e. $\rho_{\text{salt}} \ll \rho_{b,\text{CAC}}$. In this case Eq.(5.27) reduces to

$$(5.29) \quad \Delta\mu = \mu_p^0 - \left[C_1 + C_2 + \left(2 - \frac{p'}{p}\right) \ln \rho_b \right]$$

and the contribution of $\ln \rho_b$ to $\Delta\mu$ depends explicitly on the degree of counterion condensation. Experimentally, it is found that $p'/p \sim 0.1 - 0.2$ for various micellar solutions. [147] Thus, in this regime $\Delta\mu$ is nearly proportional to $2 \ln \rho_b$. The underlying reason is that at low salt concentration the high electrostatic potential at the micellar

surface induces a large degree of counterion condensation. Thus, for every surfactant incorporated in an aggregate, both the translational entropy of the surfactant and of its counterion is lost, which results in the factor $2 \ln \rho_b$. We can therefore express $\Delta\mu$ in a general form as (i.e. Eq.(5.4))

$$(5.30) \quad \Delta\mu = \mathbb{C} - c \ln \rho_b$$

where c varies between unity (at high ionic strength) and 2 (at low ionic strength).

In this appendix we also consider the translational, or mixing, entropy of m amphiphiles, each bound to N_{ad} monomers on a chain of N monomers.

The total number of elements is clearly $N - mN_{ad} + m$. The total number of conformations Z is then

$$(5.31) \quad Z = \frac{(N - m(N_{ad} - 1))!}{m! (N - mN_{ad})!}$$

Inserting the definition of θ , given by Eq.(5.6), yields

$$(5.32) \quad Z = \frac{\left(N(1 - \theta) + \frac{N\theta}{N_{ad}} \right)!}{\left(\frac{N\theta}{N_{ad}} \right)! (N(1 - \theta))!}$$

The mixing entropy S_{mix} is defined by $-k_B \ln Z$. Using the Stirling approximation, $\ln N! \approx N \ln N - N$ which is valid for large N , the free energy of mixing per monomer is

$$(5.33) \quad \begin{aligned} \frac{F_{mix}}{Nk_B T} &\equiv -s(\theta) \\ &= \frac{1}{N_{ad}} \left(\theta \ln \frac{\theta}{N_{ad}(1 - \theta) + \theta} + N_{ad}(1 - \theta) \ln \frac{N_{ad}(1 - \theta)}{N_{ad}(1 - \theta) + \theta} \right) \end{aligned}$$

Phase Separation in Polymer-Surfactant Solutions

ABSTRACT

On the basis of an analytical mean-field model we consider phase separation and coil-globule transitions in solutions of polymer chains with annealed excluded-volume interactions. In our model the chain monomers can reversibly change from a hydrophobic state to a hydrophilic one, which mimics the formation of polymer/surfactant complexes. While the bare polymer chains are either hydrophobic or weakly hydrophilic, the formation of complexes may strongly enhance the solubility of the polymers in water. We predict different types of phase behaviour for solutions of originally hydrophilic or hydrophobic polymers mixed with amphiphiles. In the case of hydrophilic polymers the solution remains homogeneous at low concentrations of amphiphiles, whereas in the case of hydrophobic polymers it separates into a dilute and concentrated phase. The Θ -transition of the complexed, hydrophobic polymers may be induced either by variation of the concentration of amphiphiles or the temperature. At low ionic strength the collapse of an individual, complexed chain with decreasing solvent strength or decreasing amphiphile concentration acquires the character of a first-order phase transition. At high concentration of amphiphiles and high ionic strength we predict the possibility of co-existence of two semi-dilute polymer phases, both for hydrophilic and hydrophobic chains.

6.1. INTRODUCTION

In the previous chapter we presented a Flory-like mean-field model for the complexation of single hydrophilic chains with nanocolloids, viz. micellar aggregates. In this Flory-like approach, however, only intramolecular osmotic interactions are taken into account; interactions between various polymer-micelle complexes are not considered. As was demonstrated, the contribution of osmotic interactions on the loading isotherm in this dilute regime is negligible for long chains, as the overall monomer density is low. Evidently, this Flory-like approach is not valid in the semi-dilute regime above the Θ -temperature, or in solutions below the Θ -temperature. In both cases the (local) monomer density is high, and the annealing of excluded-volume interactions may strongly affect the polymer conformation.

The aim of this chapter is to generalise our approach to the domain of semi-dilute solutions and weakly hydrophobic polymers, using the insights gained in the previous chapter. The effect of complexation on the phase equilibrium and on the conformations of individual chains in solution is studied over a wide range of solvent qualities, including the region around the Θ -point. We again focus on the case where the polymer solution contains small amphiphilic molecules (surfactants) at a concentration below the CMC

but above the CAC. The main results of our analysis can be directly reformulated for polymer/protein mixtures.

The structure of this chapter is as follows. In section 6.2 our mean-field model is introduced, in which we use the so-called volume approximation. [148] In this approximation only the leading terms in the free energy of a collapsed globule are retained, i.e. terms $\sim N$, while lower order terms in N are neglected. Such terms are, for instance, the conformational entropy of the chain or the excess free energy of the globule/solvent interface. Thus, the volume approximation is correct in the limit of infinitely long chains. The collapsed (globular) state of the polymer chain in the volume approximation is characterised by the finite density $\rho_{glob} = -v_0/2w$, which is determined by the local balance of binary attraction and ternary repulsion between monomers, and is independent of N . Remarkably, the correlation length $\xi \sim |v_0|^{-1}$ of density fluctuations inside the globule is also independent of N , and coincides with that in a semi-dilute solution of concentration ρ_{glob} . In contrast, a polymer coil in a good solvent is characterized by strong density fluctuations on the scale of the coil as a whole, and the average density in the coil vanishes as $N \rightarrow \infty$. Therefore, in the framework of the volume approximation the coil conformation is associated with an infinitely dilute phase ($\rho = 0$), corresponding with zero osmotic pressure.

We start with a general formalism for polymers with annealed excluded-volume interactions in the volume approximation. In the following section the phase behaviour of polymer solutions containing surfactants capable of co-operative association with polymer chains is considered both for temperatures above and below the Θ -temperature. In section 6.4 the conformational transition in individual macromolecules upon complexation is examined in more detail. We also account for finite size effects and consider their effect on the conformational transition. Finally, in section 6.5 we discuss the results, compare them to available experimental observations, and draw some conclusions.

6.2. GENERAL FORMALISM

We consider a solution of polymer chains consisting of N monomers immersed in an aqueous phase. The dimensionless concentration (the volume fraction) of monomers in the solution is ρ . The chains are flexible, i.e. the Kuhn segment length is equal to the monomer length, which is taken as the unit length in the system.

The quality of the solvent for the monomer units is characterised by the second virial coefficient of monomer-monomer interactions v_0 , which, in a first approximation, is proportional to the relative deviation from the Θ -point, $v_0 \cong (T - \Theta)/T$. If the temperature T is above the Θ -point water is a good solvent for the polymer, whereas below the Θ -point the solvent is poor, and sufficiently long chains collapse and precipitate.¹

As is demonstrated in the following, the hydrophilic/hydrophobic properties of polymer chains can be tuned not only by varying the temperature, but also by addition of small amphiphilic molecules to the solution. The attraction between the hydrophobic

¹We remark that many hydrophilic polymers, such as PEO, EHEC and PNIPAM, exhibit an upper Θ -point, i.e. precipitate not with decreasing, but, with increasing temperature. The generalisation of our discussion for this case is, however, straightforward.

groups of the amphiphiles and the polymer chains provides the driving force for their complexation, whereas steric (or electrostatic) repulsion between complexed hydrophilic groups results in solubilisation of the polymer chains. As the binding energies involved are usually of order $k_B T$ the association is reversible.

Following the previous chapter, we assume that m surfactant aggregates are associated with one polymer chain, and each aggregate occupies a sequence of N_{ad} monomers. Once again the degree of loading of the chain by "adsorbed" aggregates can be defined as

$$(6.1) \quad \theta = mN_{ad}/N$$

This equation can be rewritten in terms of local number densities of adsorbed micelles ρ_m and monomer units ρ :

$$(6.2) \quad \rho_m = \rho\theta/N_{ad}$$

As the chains are either hydrophobic or weakly hydrophilic, it is reasonable to assume that an increase in the degree of loading of the chains enhances the repulsive osmotic interactions in the solution. Therefore, within our model θ is not an independent variable, but it is determined by the condition of minimal free energy of the polymer solution. This free energy (per unit volume, in unit $k_B T$) can be written as a function of ρ and θ as

$$(6.3) \quad f(\rho, \theta) = \frac{\rho}{N} \ln \rho - \rho s(\theta) + \rho\theta u + f_{os}(\rho, \theta)$$

The first term in Eq.(6.3) accounts for the translational entropy of the polymer chains as a whole and is negligible for large N . The second term in Eq.(6.3) is the mixing entropy which arises from the translational freedom of adsorbed micelles along the polymer chains, and is given by Eq.(5.8). The third term in Eq.(6.3) describes the free energy of formation of adsorbed micelles. This differential free energy, which can also be interpreted as "the adsorption strength", is given by Eq.(5.5).

Complexation of surfactant aggregates changes the osmotic interactions in the polymer solution. Following our earlier mean-field approach, we present the osmotic free energy density as a virial expansion in powers of average densities of all types of particles present in the solution

$$(6.4) \quad f_{os}(\{\rho_i\}) = \sum_{ij} \tilde{v}_{ij} \rho_i \rho_j + \sum_{ijl} \tilde{w}_{ijl} \rho_i \rho_j \rho_l + \dots$$

where ρ_i is the number density of particles of type i, j and l , which are either bare monomers or adsorbed aggregates. The second virial coefficient \tilde{v}_{ij} characterises binary interactions between the particle of type i and of type j , while the third virial coefficient \tilde{w}_{ijl} is the three-body interaction parameter. Fourth and higher order terms are neglected in further analysis. We again express Eq.(6.4) in terms of the monomer density ρ and renormalised virial coefficients

$$(6.5) \quad f_{osm}(\rho, \theta) \cong v_{eff}(\theta)\rho^2 + w(\theta)\rho^3$$

where $v_{eff}(\theta)$ is given by Eq.(5.13). It contains three parameters, i.e. v_0 (monomer-monomer), v_1 (renormalised micelle-micelle) and v_2 (renormalised monomer-micelle).

The effective averaged third virial coefficient $w(\theta)$ correspondingly comprises the normalised virial coefficients of ternary interactions between bare monomers and adsorbed micelles. An equation analogous to Eq.(5.13) can be formulated, but it is not presented here in an explicit form.

As discussed above, v_0 is either negative ($T < \Theta$), zero ($T = \Theta$) or positive ($T > \Theta$). The binary micelle-micelle virial coefficient v_1 does not depend explicitly on the solvent quality, and is given by Eq.(5.22). The cross-term v_2 in Eq.(5.13) describes the contribution of binary contacts between bare monomers and adsorbed micelles, and is of particular interest for solutions close to the Θ -temperature. We employ a coarse-grained description, in which we consider the interaction of a polymer-micelle complex, comprising the micelle itself and a strand of length N_{ad} adsorbed onto the micelle-water interface, with a bare monomer. The second virial coefficient of interaction of a monomer with a complexed micelle can now be written as

$$(6.6) \quad \tilde{v}_2 = \frac{2\pi R_m^3}{3} + 2\pi \int_{R_m}^{\infty} r^2 (1 - e^{-U(r)/k_B T}) dr$$

where the first term describes pure steric repulsion (impermeability of the micellar interior region for monomers, R_m is the micellar radius), while the second term describes the interaction of a bare monomer with the adsorbed layer around the micelle, formed by N_{ad} monomers. Thus, $U(r)$ is the average potential experienced by the monomer at a distance $r - R_m$ from the micellar surface. The range of the average molecular potential $U(r)$ is proportional to the so-called "adsorption length" and gives the effective cut-off length for the integral in Eq.(6.6). [149] As the N_{ad} monomers are strongly attracted to the surface in our system, the adsorption length is comparable to the monomer size. Note that Eq.(6.6) reduces to Eq.(5.23) under Θ -conditions, as the effective potential $U(r)$ is then zero by definition.

The sign of the second term in Eq.(6.6) depends on the character of the monomer-monomer interaction, which is repulsive ($U(r) > 0$) under good solvent conditions and attractive ($U(r) < 0$) under poor solvent conditions. To estimate $U(r)$ we use a mean-field shell approximation, assuming a

$$(6.7) \quad \frac{U(r)}{k_B T} = \begin{cases} v_0 N_{ad} / 4\pi R_m^2 & r \leq R_m + 1 \\ 0 & r \geq R_m + 1 \end{cases}$$

This leads to

$$(6.8) \quad v_2 \cong \frac{2\pi R_m^3}{3N_{ad}} + \frac{v_0}{2}$$

Hence, under good solvent conditions ($v_0 > 0$) the second virial coefficient of binary interaction between bare monomers and complexed micelles is positive, and the main term scales as R_m^3 , which is equivalent to Eq.(5.23). Under poor solvent conditions ($v_0 < 0$), however, the balance between steric repulsion (the first term in Eq.(6.6)) and short-range attraction (the second term in Eq.(6.6)) significantly reduces v_2 .

The third virial coefficients w_{ijk} are usually positive, even when the particles attract each other strongly. In a (bare) polymer solution below the Θ -point ternary repulsion

balances binary attraction, ensuring a finite density of the collapsed polymer phase. [19] As will be demonstrated in the following, the degree of loading of a collapsed coil is close to zero. Therefore, ternary interactions between bare monomers, for simplicity denoted by w , are the dominant ternary interactions in our system. We can safely ignore ternary contributions involving complexed micelles.

The equilibrium degree of loading of polymer chains by adsorbed micelles (at a given monomer concentration ρ and given adsorption strength u) can be obtained by minimising the free energy given by Eqs.(6.3), (6.5) and (5.8), with respect to θ , i.e.

$$(6.9) \quad \frac{\partial f(\rho, \theta)}{\partial \theta} = 0$$

This minimalisation leads to

$$(6.10) \quad \rho = \frac{1}{2w'(\theta)} [\sqrt{(v'_{eff}(\theta))^2 - 4w'(\theta)[s'(\theta_b) - s'(\theta)]} - v'_{eff}(\theta)]$$

where we have introduced the notation $w'(\theta) \equiv dw(\theta)/d\theta$, similar to $v'_{eff}(\theta)$ and $s'(\theta)$. We denote the maximum value of the degree of loading in an infinitely dilute solution ($\rho \approx 0$) as θ_b . This maximum depends solely on the adsorption strength $-u$ (i.e. the surfactant concentration) and N_{ad} as

$$(6.11) \quad \ln \frac{N_{ad}(1 - \theta_b)}{N_{ad}(1 - \theta_b) + \theta_b} - \frac{1}{N_{ad}} \ln \frac{\theta_b}{N_{ad}(1 - \theta_b) + \theta_b} = u$$

This bulk value θ_b is equivalent to the degree of loading of a single coil in an infinitely dilute solution above the Θ -temperature, as was discussed in the previous chapter (Eq.(5.17)).

Eqs.(6.3) and (6.10) describe parametrically the free energy per unit volume of the solution as a function of the monomer concentration and adsorption strength (via θ_b). One can easily check that the second term under the square root in Eq.(6.10) is usually small, so that Eq.(6.10) can be rewritten in a simplified form as

$$(6.12) \quad \rho(\theta) = -\frac{1}{v'_{eff}(\theta)} (s'(\theta_b) - s'(\theta))$$

Using Eq.(6.12), the equilibrium chemical potential of the monomer is given by (in unit $k_B T$)

$$(6.13) \quad \begin{aligned} \mu(\rho(\theta)) &= \frac{\partial f(\rho, \theta)/k_B T}{\partial \rho} \\ &= \theta s'(\theta) - s(\theta) + [2v_{eff}(\theta) - \theta v'_{eff}(\theta)]\rho(\theta) + [3w(\theta) - \theta w'(\theta)]\rho^2(\theta) \end{aligned}$$

In a good solvent all contributions to $v_{eff}(\theta)$ are positive, i.e. the effective binary interactions in the system are repulsive. Under these conditions the third-order osmotic interactions in Eqs.(6.5) and (6.13) can safely be neglected. Moreover, the condition $v'_{eff}(\theta) \geq 0$, which simply states that upon loading at a given density the strength of the osmotic interactions in solution increases, entails that $\theta \leq \theta_b$ for $\rho > 0$. The condition $d\rho/d\theta \leq 0$ ensures that the degree of loading, given by Eq.(6.12), corresponds to the

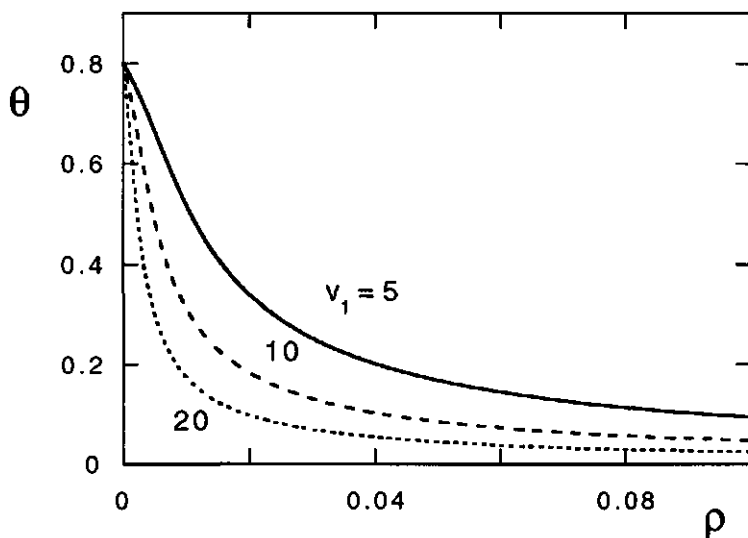


FIGURE 6.1. θ as a function of ρ for three values of v_1 (indicated in graph), $v_0 = v_2 = 1$, $N_{ad} = 100$, $\theta_b = 0.8$.

minimum of the free energy at a given ρ . Moreover, under this condition θ , defined by Eq.(6.12), is a single-valued function of ρ .

To illustrate this feature θ is plotted as a function of ρ for a fixed θ_b and three values of v_1 in Figure 6.1. As the monomer density in the solution increases, the degree of loading monotonically decreases due to the enhanced osmotic interactions. This decrease is the strongest for the strongest micelle-micelle interactions, i.e. the largest value of v_1 .

6.3. PHASE BEHAVIOUR

6.3.1. Good solvent

In order to describe phase equilibrium in a polymer-surfactant system at fixed chemical potential of the surfactants we have to analyse the behaviour of the free energy density f , or that of the monomeric chemical potential $\mu = \partial f / \partial \rho$, as a function of the monomer concentration ρ . The basic equations are Eqs.(6.3), (6.12) and (6.13). These equations contain 4 parameters, namely v_0, v_1, v_2 and θ_b , which depend on the temperature, on the ionic strength of the solution, and on the surfactant concentration. In our subsequent analysis we choose θ_b, v_1 and v_0 as three "independently tuned" parameters (by variation of the surfactant concentration, ionic strength of the solution and temperature, respectively).

We start the analysis of the behaviour of the chemical potential μ of a monomer as a function of the density ρ in the case that water is a good solvent for bare monomers, i.e. $v_0 > 0$. In Figure 6.2 μ is plotted as a function of ρ according to Eqs.(6.12) and (6.13) for three values of v_1 at constant v_0, v_2 and θ_b . For sufficiently large v_1 the chemical

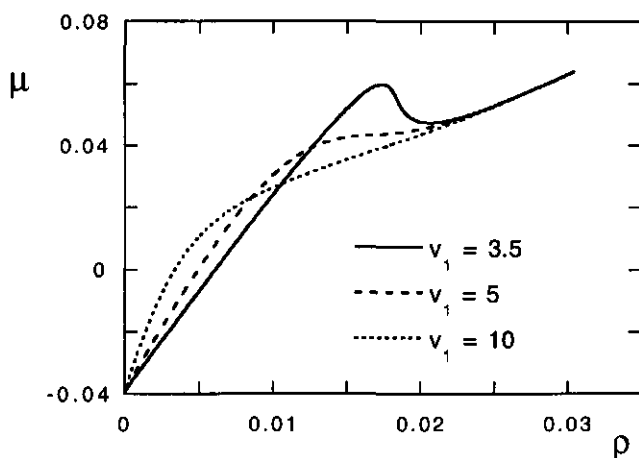


FIGURE 6.2. $\mu(\rho)$ (in unit $k_B T$) for three values of v_1 , $v_0 = 1$, $v_2 = 3$ and $N_{ad} = 100$.

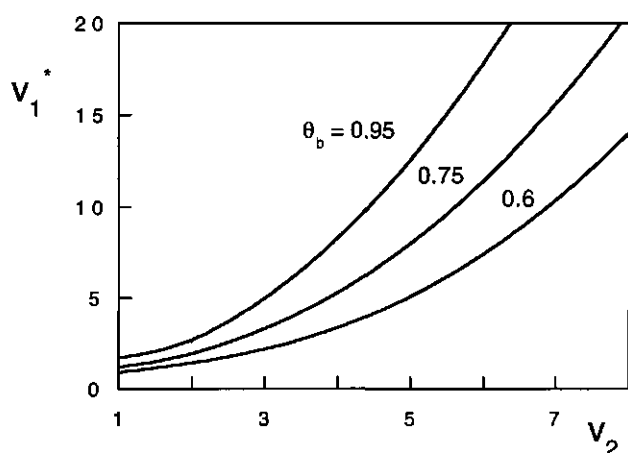


FIGURE 6.3. v_1^* as a function of v_2 for three values of θ_b , for $v_0 = 1$ and $N_{ad} = 100$.

potential increases monotonically with increasing density in the whole range of ρ . The osmotic interactions are dominated either by monomer-monomer repulsion at large ρ or by micelle-micelle repulsion at small ρ , or by their combination in the intermediate region. However, with decreasing v_1 the $\mu(\rho)$ -dependence flattens in the intermediate range of densities, as the monomer-micelle repulsion (characterised by the v_2 -term in Eq.(5.13)) becomes increasingly important. If v_1 is smaller than a certain critical value v_1^* , the chemical potential $\mu(\rho)$ is a non-monotonic function of ρ in the intermediate range of monomer concentrations. This non-monotonic behaviour of $\mu(\rho)$ suggests the possibility of phase separation into two co-existing phases, which differ with respect to both the polymer concentration and the degree of loading of the chains by adsorbed micelles.

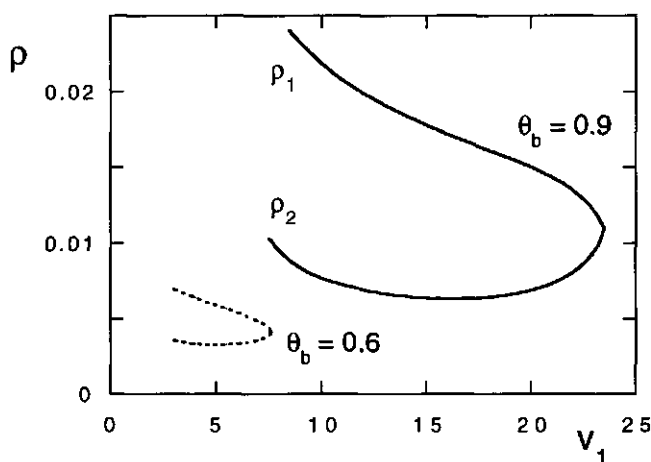


FIGURE 6.4. The coexisting densities ρ_1 and ρ_2 as a function of v_1 for $v_2 = 6$, $v_0 = 1$, $N_{ad} = 100$ and $\theta_b = 0.6$ (dashed curve) and $\theta_b = 0.9$ (solid curve).

This critical value v_1^* can be obtained by simultaneously solving the equations

$$(6.14) \quad \frac{d\mu}{d\rho} = \frac{d^2\mu}{d\rho^2} = 0$$

In Figure 6.3 v_1^* is shown as a function of v_2 for three values of θ_b . It appears to be a monotonically increasing function of v_2 and θ_b . This implies that the possibility of phase separation is enhanced by increasing the surfactant concentration and the ionic strength of the solution. (We remind the reader that salt reduces the repulsion between adsorbed micelles and thus results in a smaller value of v_1 .)

The polymer densities ρ_1 and ρ_2 in the co-existing phases are obtained using the standard Maxwell equal-area construction

$$(6.15) \quad \int_{\rho_1}^{\rho_2} (\mu(\rho) - \mu(\rho_1)) d\rho = 0$$

while the corresponding degrees of loading in both phases are obtained from Eq.(6.12). The phase diagram of the solution, i.e. the coexisting densities ρ_1 and ρ_2 , is shown as a function of v_1 in Figure 6.4. In the critical point, $v_1 = v_1^*$ we have $\rho_1 = \rho_2 = \rho^*$. With decreasing v_1 , corresponding with an increasing ionic strength of the solution, the two-phase region of the diagram widens. This suggests that the difference in density $\Delta\rho = \rho_2 - \rho_1$ and, correspondingly, the difference in the degrees of loading $\Delta\theta = \theta_1 - \theta_2$ in the co-existing phases increases with increasing ionic strength.

The appearance of the non-monotonic dependence of $\mu(\rho)$, which indicates the possibility of phase separation, is also evoked by an increase in the concentration of the surfactants (increasing θ_b) at constant v_1 and v_2 . The phase diagrams (binodal curves) in the (ρ, θ_b) -plane, shown in Figure 6.5, are qualitatively similar to those in the (ρ, v_1) -plane, shown in Figure 6.4. With decreasing v_1 (increasing ionic strength) the two-phase

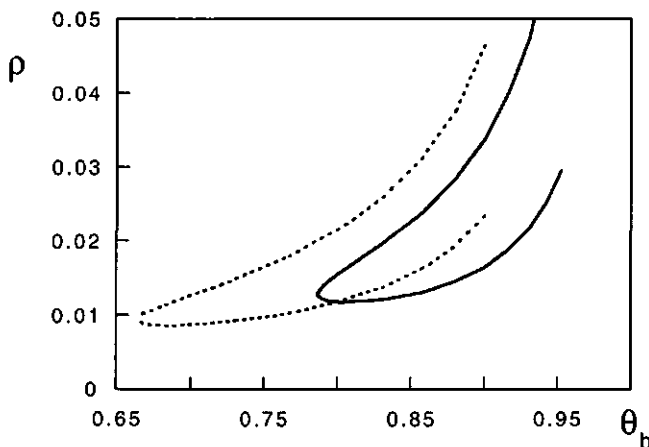


FIGURE 6.5. The coexisting densities ρ_1 and ρ_2 as a function of θ_b for $v_1 = 4$ (dashed curve) and $v_1 = 6$ (solid curve).

region in the (ρ, θ_b) -plane is extended to lower values of θ_b . Hence, a semi-dilute solution of hydrophilic polymers can be driven towards phase separation into two semi-dilute phases by an increase in the surfactant concentration and/or an increase in the ionic strength of the solution.

6.3.2. Bad solvent

We now focus on the case that $v_0 < 0$, i.e. poor solvent conditions, where the short-range attraction between monomers dominates the steric repulsion. In a *surfactant-free* solution this attraction results in the precipitation of polymers and formation of a dense (collapsed) phase coexisting with a dilute one. For infinitely long chains ($N \rightarrow \infty$) the concentration of the dilute phase approaches zero (for finite N it decreases exponentially with N). [148] This co-existence of a concentrated and (infinitely) dilute phase is reflected in the shape of the chemical potential $\mu(\rho)$, which exhibits a single minimum in the range $\rho > 0$. The equilibrium density of the collapsed phase is determined by the balance between attractive binary and repulsive ternary interactions between monomers. [19,135] It can be found using the same Maxwell construction, Eq.(6.15) with $\rho_1 = 0$, or by applying the condition of vanishing osmotic pressure in the dense phase

$$(6.16) \quad \frac{\partial}{\partial \rho} \frac{f(\rho, \theta)}{\rho} = 0$$

which leads to $\rho = -v_0/2w$.² Hence, with increasing T the density of the collapsed phase smoothly vanishes in the Θ -point, as $v_0 \sim (T - \Theta)/T$. As T approaches Θ the minimum in the $\mu(\rho)$ -curve progressively becomes more shallow and eventually it disappears at $T = \Theta$; at $T \geq \Theta$ the chemical potential is a monotonic increasing function of ρ .

²The validity of Eq.(6.16) is demonstrated by $\frac{\partial}{\partial \rho} \frac{f(\rho, \theta)}{\rho} = \frac{1}{\rho^2} \left(\rho \frac{\partial f(\rho, \theta)}{\partial \rho} - f(\rho, \theta) \right) = \frac{-p}{\rho^2}$, where p denotes the (osmotic) pressure in the system.

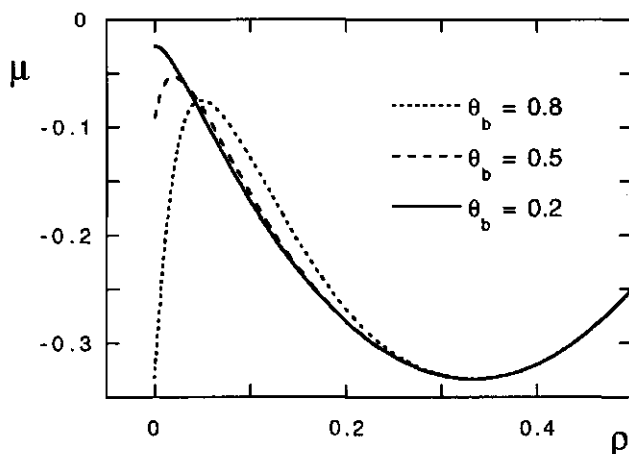


FIGURE 6.6. $\mu(\rho)$ for three values of θ_b , $v_0 = -1$ (far from the Θ -point), $v_1 = 10$, $N_{ad} = 10$, $v_2 = 1$ and $w = 1$.

The situation is markedly different when amphiphiles are present. Figure 6.6 illustrates the evolution of the $\mu(\rho)$ -curve with increasing surfactant concentration for $v_0 < 0$ at constant v_1 and v_2 . At small θ_b the shape of $\mu(\rho)$ -curves is qualitatively the same as in the surfactant-free solution, i.e. only one minimum corresponding to the collapsed phase is present. The shape and position of this minimum are roughly determined by the balance between binary attraction and ternary repulsion of bare monomers. At high θ_b (0.8 in Figure 6.6) the chemical potential in the dilute phase is lower than that of the globular phase, i.e. a necklace conformation is more favourable than the globular.

The density and the degree of loading in the collapsed phase co-existing with the (infinitely) dilute one at low values of θ_b can be found by either applying the Maxwell construction to $\mu(\rho)$, or, equivalently, by applying Eq.(6.16). This leads to $\rho = -v_{eff}(\theta)/2w$. In combination with Eq.(6.12) a closed equation is found for the degree of loading in the collapsed phase for a given set of v_0, v_1, v_2, w and θ_b

$$(6.17) \quad \frac{v_{eff}(\theta)v'_{eff}(\theta)}{2w} = s'(\theta_b) - s'(\theta)$$

As expected, an increase in θ_b mostly affects the shape of $\mu(\rho)$ in the range of small densities (when the degree of loading is close to θ_b , see Figure 6.1). As follows from Eq.(6.13), the chemical potential in the dilute phase is simply

$$(6.18) \quad \mu(0) \equiv \mu(\rho = 0) = \ln \left(\frac{N_{ad}(1 - \theta_b)}{N_{ad}(1 - \theta_b) + \theta_b} \right)$$

and an increase in θ_b results in a monotonic decrease in $\mu(0)$.

The initial slope of $\mu(\rho)$ -curve in Figure 6.6 is determined by the value of $v_{eff}(\theta_b)$ and increases monotonically with increasing θ_b . As $v_0 < 0$ and $v_1 > 0$ we can define the

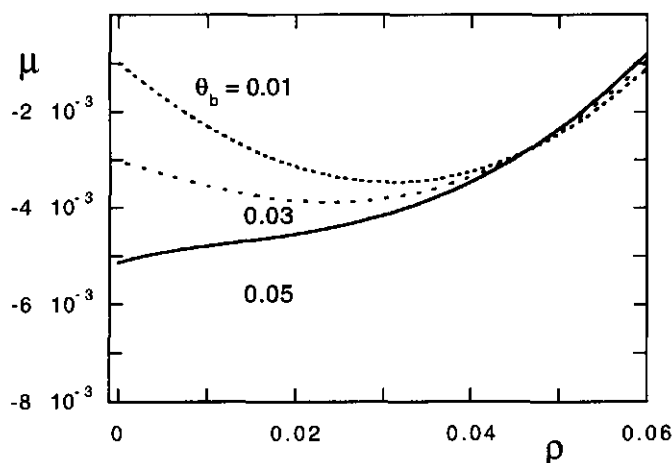


FIGURE 6.7. $\mu(\rho)$ for three small values of θ_b , $v_0 = -0.1$ (close to the Θ -point), $v_1 = 10$, $N_{ad} = 10$, $v_2 = 1$ and $w = 1$.

apparent Θ -point of the complexed chain by the condition $v_{eff}(\theta^*) = 0$, i.e. (Eq.(5.13))

$$(6.19) \quad \theta^* = \frac{v_0 - v_2 + \sqrt{v_2^2 - v_0 v_1}}{v_0 + v_1 - 2v_2}$$

Using this definition, it follows from Eq.(6.13) that $(d\mu/d\rho)_{\rho=0} \leq 0$ if $\theta_b \leq \theta^*$ and $(d\mu/d\rho)_{\rho=0} \geq 0$ if $\theta_b \geq \theta^*$.

Therefore, for $\theta_b \geq \theta^*$ in addition to the "globular" minimum an edge minimum at $\rho = 0$ appears in the $\mu(\rho)$ -curves, together with a maximum that separates both minima. The density ρ_{max} corresponding to this maximum shifts towards larger ρ with increasing θ_b , as seen in Figure 6.6. Simultaneously, the equilibrium concentration of the dense phase is found to decrease weakly. This decrease reflects a progressive but weak increase in the degree of loading in the dense phase with increasing surfactant concentration.

We now define a degree of coverage $\tilde{\theta}$ (with $\tilde{\theta} \geq \theta^*$) such that at $\theta_b \geq \tilde{\theta}$ we have $\mu(0) \leq \mu(\rho_{glob})$, where ρ_{glob} is the density of the collapsed phase. This density is found by solving Eqs.(6.12) and (6.17) simultaneously. For $\theta_b \leq \tilde{\theta}$ the dense (collapsed) phase co-exists with an infinitely dilute one, while for $\theta_b > \tilde{\theta}$ the highly loaded, dilute phase is thermodynamically more favourable than the collapsed one. Thus, for $\theta_b \leq \tilde{\theta}$ the polymer solution with amphiphiles resembles a pure polymer solution below the Θ -point, whereas for $\theta_b > \tilde{\theta}$ the co-existence of a collapsed (virtually unloaded) and a *semi-dilute* (loaded) phase may be expected, which is similar to the case for $v_0 > 0$ discussed in section 6.3.1.

The evolution of the $\mu(\rho)$ -curves with increasing surfactant concentration (increasing θ_b) in the vicinity of the Θ -point, $v_0^{crit} \leq v_0 \leq 0$, is different from that far from the Θ -point, as described previously (in section 6.4.1 we specify the condition $v_0^{crit} \leq v_0 \leq 0$ quantitatively). In this case $\tilde{\theta} = \theta^*$, i.e. the degree of loading at which the loaded phase

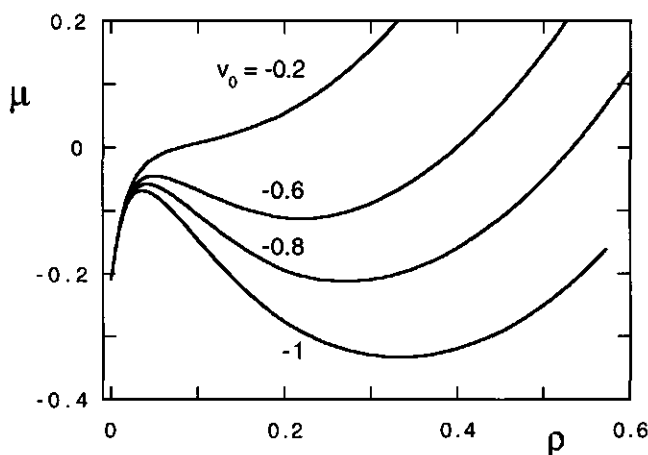


FIGURE 6.8. $\mu(\rho)$ for several values of v_0 for $\theta_b = 0.7$, $v_1 = 10$, $N_{ad} = 10$, $v_2 = 1$ and $w = 1$.

is thermodynamically as favourable as the collapsed phase is equal to the degree of loading at which the effective binary osmotic interactions are zero. As shown in Figure 6.7, the $\mu(\rho)$ -curves in this regime exhibit only one minimum at finite ρ in the whole range of $\theta_b < \theta^*$, and this minimum becomes an edge minimum at $\rho = 0$ for $\theta_b \geq \theta^*$. The value of ρ_{glob} progressively decreases with increasing θ_b in the regime $\theta_b < \theta^*$. This reflects an increasing degree of loading and decreasing polymer density in the collapsed phase. The minimum disappears continuously in the apparent Θ -point, i.e. at $\theta_b = \theta^*$. For $\theta_b \geq \theta^*$ μ is a monotonically increasing function of ρ . Hence, close to the Θ -temperature the Θ -transition induced by increasing surfactant concentration is continuous, and therefore resembles the conventional Θ -transition with increasing temperature in a 'bare' polymer solution. [150]

It is also instructive to analyse the $\mu(\rho)$ -curves at constant θ_b , v_1 and v_2 for varying v_0 , although, as we have discussed above, it is physically difficult to keep θ_b and v_2 unaffected by a change in solvent strength. We discuss two cases: (i) large values of θ_b and v_1 (Figure 6.8), and (ii) small values of θ_b and v_1 (Figure 6.9).

If v_1 and θ_b are sufficiently large (low ionic strength of the solution and high surfactant concentration) then even at large $-v_0$ we have $\theta^* \leq \theta_b$, so that the initial slope of the $\mu(\rho)$ curve is positive, $(d\mu/d\rho)_{\rho=0} \geq 0$. The $\mu(\rho)$ -curve exhibits a deep minimum corresponding to the globular phase (resulting from the large value of $-v_0$), a comparatively shallow edge minimum at $\rho = 0$, and a maximum separating both minima, as shown in Figure 6.8. This situation corresponds to the co-existence of a (infinitely) dilute and dense phase in the solution. The effect of increasing the solvent strength on the $\mu(\rho)$ -curves in the range of large ρ (corresponding to the collapsed phase) is similar to that described above for the case of a 'bare' polymer solution below the Θ -point. The edge minimum and the potential barrier, however, are almost not affected by the solvent strength. If we define a

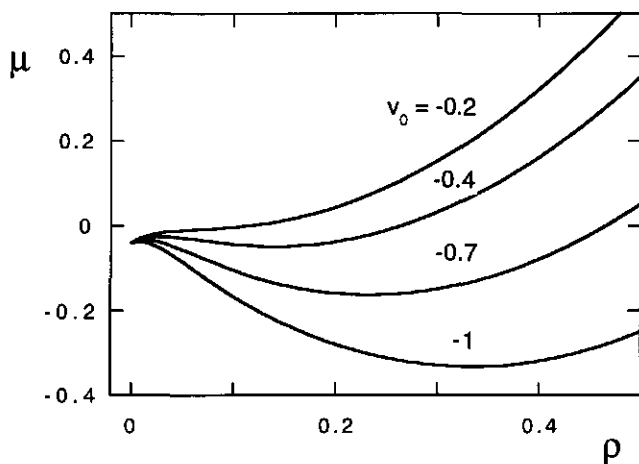


FIGURE 6.9. $\mu(\rho)$ for several values of v_0 for $\theta_b = 0.3$, $v_1 = 5$, $N_{ad} = 10$, $v_2 = 1$ and $w = 1$.

solvent strength \bar{v}_0 from the condition $\mu(0) \leq \mu(\rho_{glob})$ at $v_0 \geq \bar{v}_0$, then below \bar{v}_0 a dilute phase co-exists with a dense one. In a certain range above \bar{v}_0 the solution either consists of a single phase or two coexisting semi-dilute phases, provided the overall density is high enough. At even higher v_0 the function $\mu(\rho)$ becomes monotonic, i.e. the solution is homogeneous in the whole range of polymer concentrations. One finds that \bar{v}_0 is a decreasing function of v_1 (inverse ionic strength) and θ_b (surfactant concentration).

If, in contrast, v_1 and θ_b are sufficiently small (high ionic strength of the solution and low surfactant concentration), then at large $-v_0$ we have $\theta_b \leq \theta^*$, i.e. $(d\mu/d\rho)_{\rho=0} \leq 0$, and the $\mu(\rho)$ -curves exhibit only one minimum, as shown in Figure 6.9. This minimum corresponds to a collapsed bare phase co-existing with an (infinitely) dilute and loaded phase. With increasing v_0 the initial slope $(d\mu/d\rho)_{\rho=0} \leq 0$ gradually increases, while the depth of the minimum progressively decreases and its position is displaced to smaller ρ .

Therefore, close to the Θ -point the evolution of the $\mu(\rho)$ -curves with increasing v_0 is similar to that of the surfactant-free case with increasing v_0 : at any $v_0 \leq v_0^*$ the density of the collapsed phase is displaced to smaller values of ρ_{glob} with increasing v_0 (the definition of v_0^* for a given θ_b is similar to that of θ^* for a given v_0 , see Eq.(6.19)). The degree of loading θ_{glob} in the collapsed phase is determined by Eq.(6.17) and progressively increases with increasing v_0 . The minimum in the $\mu(\rho)$ -curve becomes an edge minimum at $\rho = 0$ as v_0 reaches the value v_0^* . Correspondingly, the density of the collapsed phase vanishes at $v_0 = v_0^*$ and θ_{glob} reaches the value θ_b , i.e. in the apparent Θ -point the collapsed and dilute phase are equivalent. We stress that the apparent Θ -point in polymer-surfactant systems at a finite θ_b and v_1 occurs for $v_0 < 0$. In the surfactant-free case the Θ -point by definition corresponds to $v_0 = 0$.

Following the above arguments, we can construct phase diagrams for the polymer solution below the Θ -point, similar to those above the Θ -point, see Figures 6.4 and 6.5.

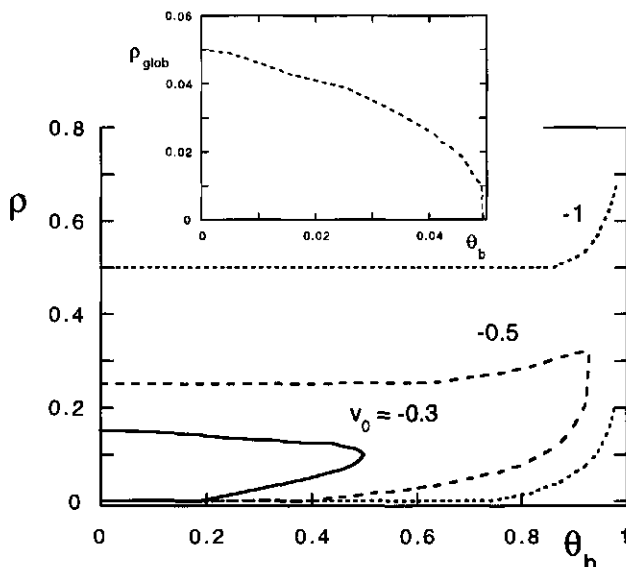


FIGURE 6.10. The bimodal densities ρ as a function of θ_b for four values of v_0 . In the inset $v_0 = -0.1$ and $v_1 = 2$ is shown, in the figure $v_0 = -0.3, -0.5$ and -1 , $v_1 = 5$. Other parameters are as in Figure 6.8.

In Figure 6.10 the phase diagram in the (θ_b, ρ) -plane is shown, i.e. the dependence of the densities of co-existing phases on θ_b , are presented for four different values of v_0 at given v_1 and v_2 . As follows from Figure 6.10, the phase diagrams may have very different shapes, depending on the deviation from the Θ -point, characterised by v_0 .

The values $v_0 = -0.1$ and $v_1 = 2$ correspond to the case $v_0 \geq v_0^{crit}$. In this case solely co-existence of a dilute and dense phase is possible at small values of θ_b , and ρ_{glob} decreases with increasing θ_b . As discussed, the density of the dense phase smoothly vanishes at $\theta_b = \theta^*$. This is shown in the inset of Figure 6.10. In contrast, the other values of v_0 in Figure 6.10 are below v_0^{crit} . In this case a dense phase ($\rho \approx -v_0/2w$) coexists with a dilute one ($\rho = 0$) for $\theta_b \leq \tilde{\theta}$, while for $\theta_b > \tilde{\theta}$ co-existence of two semi-dilute phases may occur. The particular shape of the phase diagram in the range $\theta_b > \tilde{\theta}$ depends on the solvent strength.

If v_0 is only slightly below v_0^{crit} ($v_0 = -0.3$ in Figure 6.10) then the density of the collapsed phase *decreases* with increasing θ_b , while the density of the co-existing loaded phase simultaneously *increases*. As a result, the phase lines merge at $\theta_b = \theta_b^{crit}$, which is a critical point of the phase diagram. For $\theta_b \geq \theta_b^{crit}$ the solution is homogeneous in the whole range of the polymer concentrations.

For lower v_0 ($v_0 = -0.5$ in Figure 6.10) the phase diagram still exhibits a critical point θ_b^{crit} but, in contrast to the previous case, the densities of both co-existing semi-dilute phases *increase* with increasing θ_b in the range $\tilde{\theta} \leq \theta_b \leq \theta_b^{crit}$.

At very low solvent strength ($v_0 = -1$ in Figure 6.10), the two-phase region occupies the whole range of θ_b without a critical point. Below $\tilde{\theta}$ (dense-dilute co-existence) the

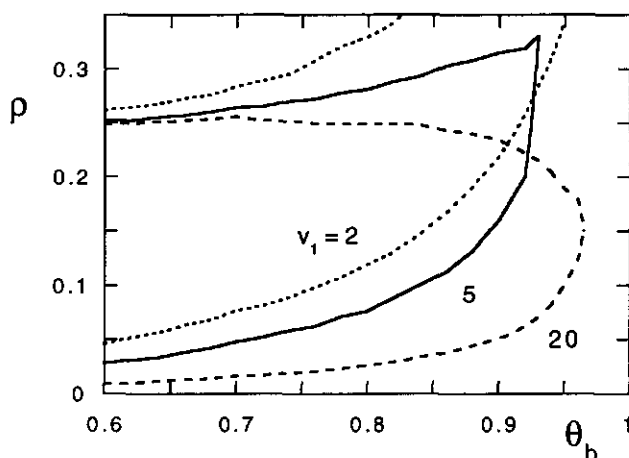


FIGURE 6.11. The bimodal densities ρ as a function of θ_b for three values of v_1 (indicated in the graph), and $v_0 = -0.5$. Other parameters are as in Figure 6.8.

density in the dense phase is weakly *decreasing* function of θ_b while above $\tilde{\theta}$ (co-existence of two semi-dilute phases) it is an *increasing* function of θ_b . This entails that, provided the polymer density in solution is high enough, phase separation into a bare, collapsed phase and a relatively loaded, semi-dilute phase may occur regardless of θ_b , i.e. the surfactant concentration.

The variation of the shape of phase diagrams in the (ρ, θ_b) -plane resulting from variation of v_1 (variation of the ionic strength) is illustrated in Figure 6.11 for $v_0 \approx -0.5$. As expected, $\tilde{\theta}$ in this regime is independent of v_1 (its value is 0.392), as it is roughly determined by the balance between the favourable monomer-monomer contacts (given by v_0) in the collapsed phase, and the free energy gain due to loading of the chain by micelles in the dilute phase (as $\rho = 0$ in the dilute phase there is no dependence of $\mu(0)$ on v_1 as well, see Eq.(6.18)).

Figure 6.11 demonstrates that the phase diagram varies with varying v_1 for $\theta_b > \tilde{\theta}$. If v_1 is small, the lower bimodal density is relatively high, and it increases strongly with increasing θ_b . This implies that at high surfactant concentrations the solution remains homogeneous up to relatively high monomer densities, as the osmotic cost of loading is low. At high values of v_1 , however, phase separation occurs at relatively low monomer densities, as the osmotic cost of loading is high in this regime. Also, at high values of v_1 phase separation persists up to values of θ_b close to unity. We therefore conclude that in semi-dilute solutions of hydrophobic polymers and associating ionic surfactants phase separation may be controlled via the ionic strength.

6.4. THE COIL-GLOBULE TRANSITION

6.4.1. The volume approximation

The arguments presented in the previous section concern the co-existence of collapsed and dilute phases in a solution of polymers associating with amphiphiles for poor solvent conditions. These arguments can also be applied to the analysis of the nature of the collapse-swelling transition induced by the variation of external parameters (solvent strength, concentration of surfactants or ionic strength of the solution) in an individual, infinitely long polymer chain, $N \rightarrow \infty$.

From our discussion in the previous section it follows that in the case $v_0 < 0$ the transition of an individual chain from a collapsed to a swollen conformation in a dilute solution can be induced by (i) increasing the concentration of surfactants, i.e. increasing θ_b , and (ii) increasing the solvent strength, i.e. increasing v_0 . Analysis of the $\mu(\rho)$ -curves allows us to localise the position of the collapse-swelling transition and to determine its character.

With increasing θ_b (at fixed v_1 and v_0 , far below the Θ -point) the chemical potential of a monomer in the dilute phase corresponding to the coil conformation ($\rho = 0$) decreases (see Eq.(6.18)), while that in the co-existing collapsed phase is virtually unaffected by θ_b . This trend reflects the increasing favourability of the dilute and highly loaded state with respect to the dense and unloaded state. The transition from a collapsed to a swollen conformation occurs when $\mu(0) = \mu(\rho_{glob})$. This transition may occur either as a continuous second-order phase transition at $\theta_b = \theta^*$, similar to the conventional Θ -transition in bare polymers, or with a finite jump in the monomer density between the collapsed and swollen phase at $\theta_b = \tilde{\theta}$. In the latter case the swelling transition acquires the character of a first-order phase transition. Experimentally, this should correspond to the co-existence of collapsed and swollen coils in solution within a narrow range of θ_b . Whether the transition is continuous or discontinuous is determined by the difference in free energy between the collapsed (unloaded) and swollen (loaded) state of the chain.

In Figure 6.12 the phase diagram for an infinitely long polymer chain is shown in the (θ_b, v_0) -plane for two values of v_1 . The solid curve depicts $\tilde{\theta}$ as a function of v_0 and virtually is independent of v_1 , the dashed curves correspond to θ^* for both values of v_1 . (We remind the reader that θ^* corresponds to the apparent Θ -point, i.e. $v_{eff}(\theta^*) = 0$, while $\tilde{\theta}$ corresponds to the surfactant concentration at which $\mu(0) = \mu_{glob}$, thus the surfactant concentration at which the coil-globule transition occurs).

At large $-v_0$ and v_1 we find $\tilde{\theta} > \theta^*$. As v_0 increases, the difference in $\tilde{\theta}$ and θ^* decreases and eventually it vanishes at $v_0 = v_0^{crit}$, when the curves $\tilde{\theta}(v_0)$ and $\theta^*(v_0)$ converge. This entails that, with increasing θ_b (i.e. transversing the phase diagram Figure 6.12 in the vertical direction), the swelling transition occurs abruptly as a first-order phase transition at $\theta_b = \tilde{\theta}$ if $v_0 < v_0^{crit}$, or continuously as a second-order phase transition at $\theta_b = \theta^*$ if $v_0 \geq v_0^{crit}$. Hence, v_0^{crit} is the critical point at which the curve of $\tilde{\theta}$ converges with that of θ^* , and at which the nature of the globule-coil phase transition changes from a first-order to a second-order phase transition.

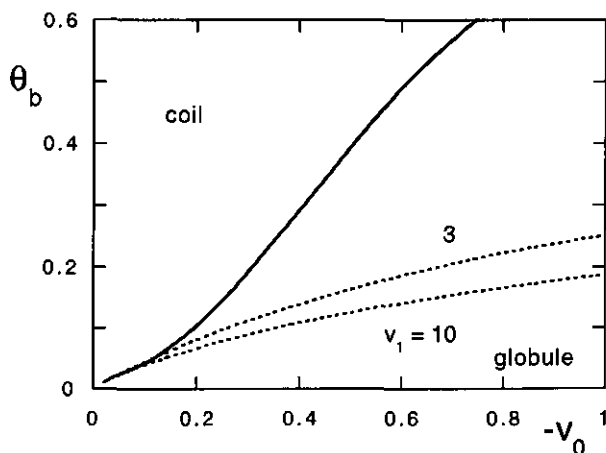


FIGURE 6.12. θ^* (dotted curve) and $\bar{\theta}$ (solid curve) as a function of v_0 for two values of v_1 . Other parameters as in Figure 6.8.

It is seen in Figure 6.12 that v_0^{crit} is shifted to slightly higher values of v_0 , i.e. to higher temperatures, with increasing v_1 . Thus, for temperatures close to the Θ -temperature our model predicts the coil-globule transition to be continuous at high ionic strengths and abrupt at low ionic strengths.

Figure 6.12 illustrates the nature of the globule-coil transition at a given v_0 with increasing θ_b . It also, however, depicts the nature of this transition induced by an increase in solvent strength, i.e. in v_0 , at fixed v_1, v_2 and θ_b (we have already discussed that these conditions are somewhat 'artificial'). An increasing solvent strength corresponds to the crossing of the boundaries between the collapsed and swollen state in Figure 6.12 with increasing v_0 , i.e. transversing the phase diagram along the horizontal axis. We may define two special values of v_0 . The first, denoted as v_0^* , is the solvent strength at which $v_{eff}(\theta_b) = 0$ (dashed curves in Figure 6.12). The second, denoted as \tilde{v}_0 , is the solvent strength at which the chemical potentials of a monomer in a globule and that in a coil are equal (solid curve in Figure 6.12). As follows from Figure 6.12 the transition is continuous at low values of θ_b and v_1 and occurs at $v_0 = v_0^*$, whereas at high values of θ_b it is abrupt and occurs at $\tilde{v}_0 > v_0^*$.

The transition from a globular to a swollen conformation of a long polymer chain is also reflected in the curves of $f(\rho)/\rho$ as a function of ρ , that is, in the dependence of the free energy per monomer on the density. From Eq.(6.16) it follows that the position of the minimum in these curves corresponds to the equilibrium density $\rho_{glob} = -v_{eff}(\theta)/2w$ of the globule. As shown in Figure 6.13, for $\theta_b \leq \theta^*$ this globular minimum is the only minimum in the $f(\rho)/\rho$ -curves; the collapsed state is then the equilibrium state of the chain. However, with increasing θ_b the free energy per monomer in the coil conformation, $(f(\rho)/\rho)_{\rho=0}$, decreases. If v_1 and $-v_0$ are large enough (i.e. $v_0 < v_0^{crit}$) a second (edge) minimum at $\rho = 0$ appears at $\theta_b = \theta^*$, i.e. at the loading for which $v(\theta^*) = 0$. The transition from a collapsed to a swollen conformation occurs (for infinitely long chains) at

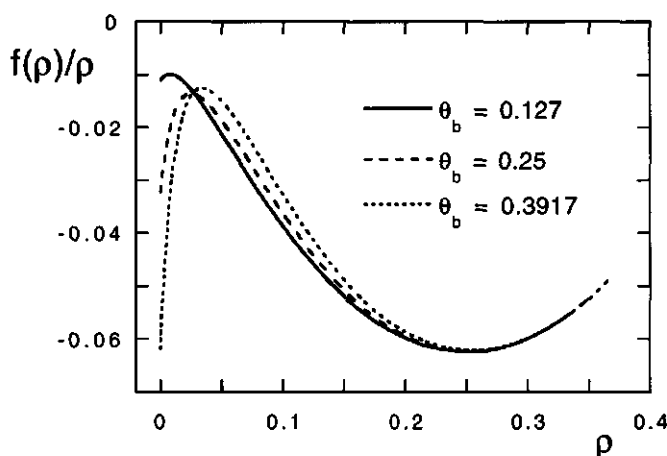


FIGURE 6.13. $f(\rho)/\rho$ as a function of ρ for three values of θ_b ($\theta_b < \theta^*$, $\theta_b = \theta^*$, $\theta_b = \bar{\theta}$) for $v_0 = -0.5$. Other parameters are $v_1 = 10$, $v_2 = 1$, $N_{ad} = 10$ and $w = 1$.

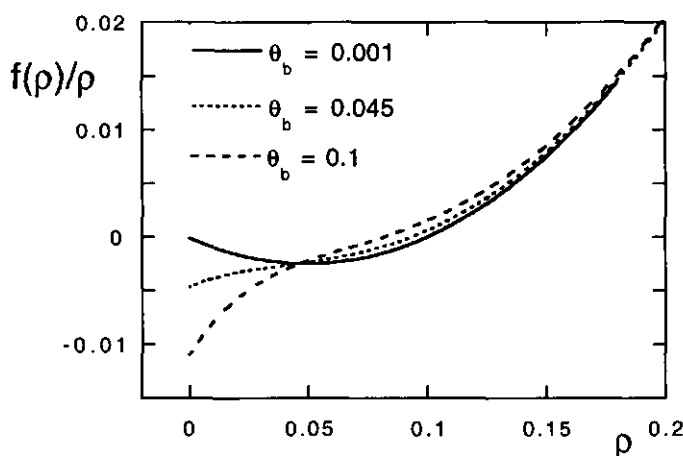


FIGURE 6.14. $f(\rho)/\rho$ as a function of ρ for three values of θ_b ($\theta_b < \theta^*$, $\theta_b = \theta^*$, $\theta_b > \bar{\theta}$) for $v_0 = -0.1$ and $v_1 = 3$, other parameters those of Figure 6.13.

$\theta_b = \bar{\theta}$ when $(f(\rho)/\rho)_{\rho=0}$ is equal to the depth of the globular minimum. The transition is a first-order phase transition with a finite jump in the polymer concentration $\Delta\rho \cong \rho_{glob}$.

In contrast, at small v_1 and $-v_0$ (i.e. $v_0 \geq v_0^{crit}$) an increase in θ_b results in progressive flattening of the $f(\rho)/\rho$ -curve and at $\theta_b = \theta^*$ the globular minimum disappears, i.e. $\rho_{glob}(\theta_b = \theta^*) = 0$. In this case the collapse-swelling transition occurs smoothly as a second-order transition: in the transition point $\theta_b = \theta^*$ the globule conformation has become equivalent to that of the coil (both have zero density). This scenario is illustrated in Figure 6.14.

6.4.2. Finite size corrections

The volume approximation is exact for the description of the coil-globule transition of infinitely long chains ($N \rightarrow \infty$). However, for the analysis of conformational transitions induced by variation of the solvent strength or concentration of amphiphiles in an individual chain of finite length we can extend our approach utilised in Chapter 5 for good solvents to poor solvent conditions. This approach is based on standard Flory-type arguments, and has been applied for the description of the collapse-swelling transition in polymer chains by several authors. [150,151] According to this approach, the free energy of a polymer-micelle complex can be presented as

$$(6.20) \quad F = F_{ad} + F_{tr} + F_{os} + F_{el}$$

Evidently, in poor solvents the adsorption contribution F_{ad} and the translational entropy F_{tr} are equivalent to the expressions used in Chapter 5 for good solvents.

The osmotic contribution F_{os} is obtained by integration of $f_{os}(\rho, \theta)$, given by Eq.(6.5), over the volume occupied by the chain, and equals

$$(6.21) \quad F_{os}/k_B T = N \rho v_{eff}(\theta) + N \rho^2 w$$

where $\rho \cong N/R_G^3$ is the average density of monomers inside the coil and R_G is its characteristic dimension (the radius of gyration).

The last contribution F_{el} to the free energy in Eq.(6.20) is the elastic or conformational entropy of a swollen or collapsed chain as a whole. We again estimate this entropy using a Gaussian approximation. Both swelling and collapse of the complexed chains with respect to its Gaussian size $R_0(\theta)$, given by Eq.(5.9), are entropically unfavourable. It is convenient to define an expansion parameter $\alpha \equiv R_G(\theta)/R_0(\theta)$, where R_G and R_0 are again functions of θ . Then, following ref. 151, we can present the conformational entropy penalty for swelling ($\alpha \geq 1$) and for collapse ($\alpha \leq 1$) as

$$(6.22) \quad F_{el}/k_B T = \begin{cases} \alpha^2 - \ln(\alpha^2) & \alpha \geq 1 \\ \alpha^{-2} + \ln(\alpha^2) & \alpha \leq 1 \end{cases}$$

Note that the elastic free energy, given by Eq.(6.22) reduces to $k_B T$ at $\alpha = 1$, and its derivative $\partial F_{el}/\partial \alpha$, which determines the restoring force in a deformed coil, vanishes at $\alpha = 1$. Thus, Eq.(6.22) describes the conformational free energy of a chain as a continuous and smooth function of α in the whole range of deformation.

As in the case of good solvent conditions, the equilibrium degree of loading of the chain by adsorbed micelles and the equilibrium chain dimension are found by minimising the total free energy F with respect to the coil size and the number of adsorbed micelles at constant temperature (solvent quality) and chemical potential of the surfactants. The first equilibrium condition, expressed in terms of α , yields

$$(6.23) \quad \frac{3}{2} N^{1/2} v_{eff}(\theta) (1 + \beta \theta)^{-3/2} + 3 w \alpha^{-3} (1 + \beta \theta)^{-3} = \begin{cases} \alpha^5 - \alpha^3 \\ \alpha^3 - \alpha \end{cases}$$

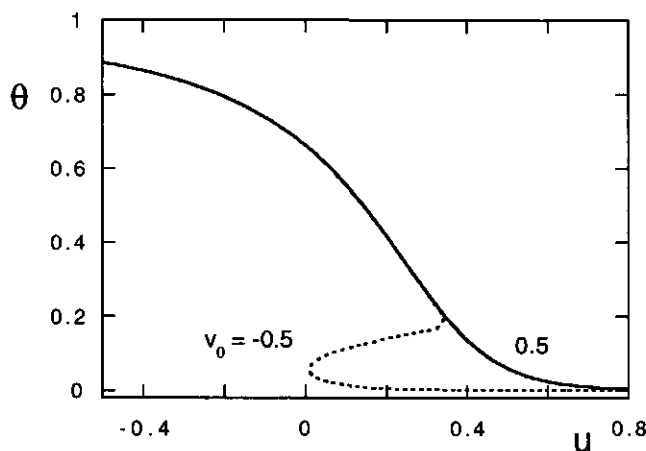


FIGURE 6.15. θ as a function of u for $v_0 = 0.5$ and $v_0 = -0.5$ (solid curve), $v_1 = 5$, $\beta = 0$, $N_{ad} = 5$ and $N = 10000$.

where the upper expression refers to swollen chains ($\alpha \geq 1$) and the lower expression refers to collapsed chains ($\alpha \leq 1$), respectively. We remark that Eq.(6.23) is similar to the expression for the swelling coefficient of the polymer chain in the usual theory of the coil-globule transition, and reduces to it if $v_{eff}(\theta) = \text{constant}$ and $\beta = 0$. [151] Furthermore, for large chains in good solvent conditions ($\alpha \gg 1$) Eq.(6.23) reduces to $R_G \approx N^{3/5}((1 + \beta\theta)v_{eff}(\theta))^{1/5}$, i.e. Eq.(5.15). The second condition gives

$$(6.24) \quad \frac{N^{1/2}v'_{eff}(\theta)}{\alpha^3(1 + \beta\theta)^{3/2}} + \frac{w'(\theta)}{\alpha^6(1 + \beta\theta)^3} + N[s'(\theta_b) - s'(\theta)] - \frac{\beta}{1 + \beta\theta} \left\{ \frac{\alpha^2 - 1}{1 - \alpha^2} \right\} = 0$$

where again the upper and the lower expressions refer to $\alpha \geq 1$ and $\alpha \leq 1$, respectively.

We start with the examination of the overall degree of loading of a long chain, $N = 10^4$, as a function of u , i.e. of the surfactant concentration. In Figure 6.15 θ is plotted against u both for good ($v_0 = 0.5$) and bad ($v_0 = -0.5$) solvent conditions. In the latter case v_0 is chosen smaller than the critical value for the corresponding set of v_1 and v_2 . Under good solvent conditions the degree of complexation increases continuously with decreasing u (increasing surfactant concentration), whereas in the poor solvent a van der Waals-loop in $\theta(u)$ is observed. Beyond the van der Waals-loop the results for good and bad solvency merge. This agrees with the result obtained in Chapter 5 that the dependence of θ on u for swollen coils is Langmuir-like, and in the coil regime θ does not depend significantly on excluded-volume interactions.

The same behaviour is observed for the radius of gyration of the coil. In Figure 6.16 the swelling ratio α is plotted for the same parameters as in Figure 6.15. In the good solvent case the renormalised micelle-micelle excluded-volume parameter is larger than the monomer-monomer, $v_1 > v_0$, so that the coil size at total coverage is larger than the bare coil size. Obviously, the results for α mimic those of θ ; in a good solvent the coil

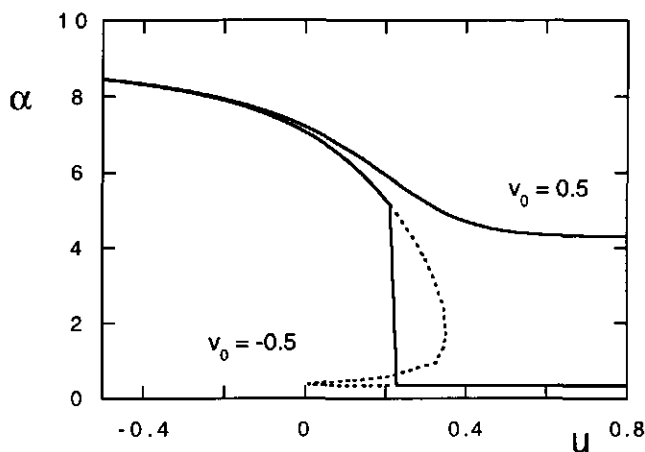


FIGURE 6.16. The expansion coefficient α as a function of u for the same values as Figure 6.15. The van der Waals-loop is shown by a dashed curve.

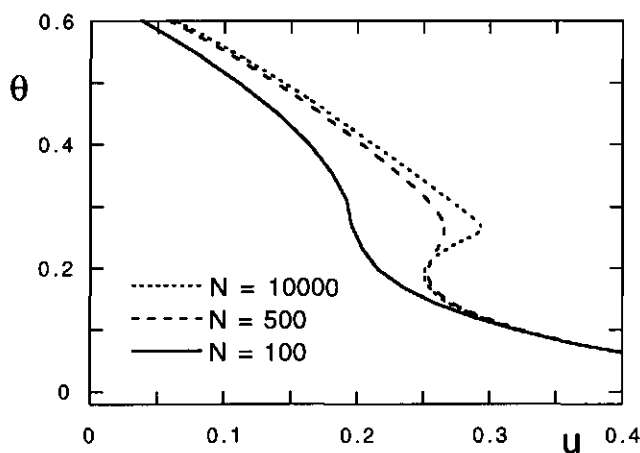


FIGURE 6.17. θ as a function of u for $N = 100, 500$ and 10000 , $v_0 = -0.35$, $v_1 = 3$, $v_2 = 0$, $w = 1$, $\beta = 0$ and $N_{ad} = 5$.

swells continuously, whereas in a bad solvent an abrupt jump from a collapsed globule to a swollen coil conformation is observed. The value of u at which this jump occurs is found by equating the total free energy of a collapsed globule with that of a swollen coil. The van der Waals-loop in Figure 6.16 for $v_0 = -0.5$ is shown as a dashed curve, the equilibrium conformation with a solid curve.

We thus find that the conformational changes occurring in a chain of considerable length upon complexation can be interpreted on the basis of the results obtained in section 6.4.1 for infinitely long chains using the volume approximation. However, in section 6.4.1 the contribution of the conformational entropy of the chain, which scales less than linearly

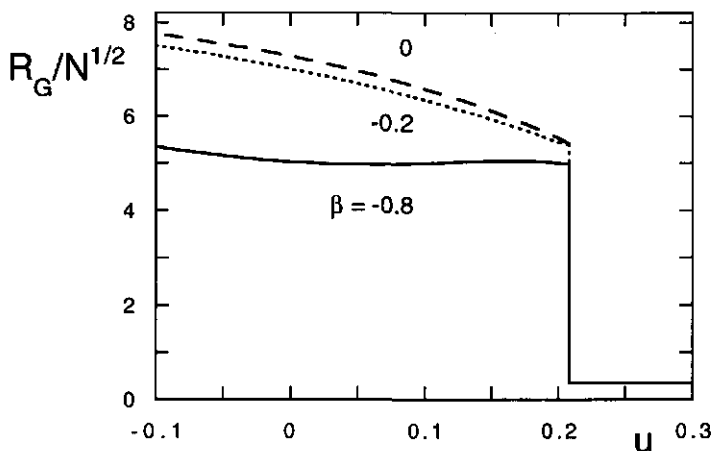


FIGURE 6.18. The ratio $R_G/N^{1/2}$ as a function of u for $\beta = 0$, -0.2 and -0.8 , $N = 10000$, $v_0 = -0.5$, $v_1 = 5$, $v_1 = 0$ and $N_{ad} = 10$

with N , is neglected. It is therefore interesting to examine how this conformational entropy affects the character of the collapse-swelling transition in a complexed chain of finite length under poor solvent conditions. In Figure 6.17 θ is plotted as a function of u for $v_0 < v_0^{crit}$ and three values of N (we keep in mind that $NN_{ad}^{-1} \gg 1$ in order to justify the mean-field approach). It is seen that the transition from a collapsed globule to a swollen coil is continuous for the shortest chain, whereas it is discontinuous for the longer chains. Moreover, the size of the van der Waals-loop increases with increasing N as the $\theta(u)$ -dependence approaches that of the infinitely long chain. The reason for the smoothening of the collapse-swelling transition of short chains with respect to that of long ones is evidently the conformational entropy penalty occurred in both the collapsed and swollen state, below and above the transition point, respectively.

We can thus conclude that the results obtained in the Flory-type model for large values of N approach those of the volume approximation, but the results for short chains differ with respect to the predicted nature of the globule-coil transition. This variation in the character of the globule-coil transition with varying chain length should also be observed experimentally.

Figure 6.18, finally, illustrates the effect of *local* conformational restrictions imposed by the wrapping of a strand of length N_{ad} around the micelles on the dimensions of the chain as a function of u . These conformational restrictions are characterised by β , defined in Eq.(5.10). A large value of β indicates that the Gaussian size of the complex increases with increasing θ , a negative value that the Gaussian size decreases with increasing θ , i.e. the chain wraps itself around the micelles. As one can see from Figure 6.18, a decrease in β leads to a progressive decrease in the size of the swollen coil. The effect gets stronger with increasing degree of loading. In contrast, the size of the chain in the collapsed (globular) state as well as the position of the globule-coil transition are virtually unaffected by the variation of β , as $\theta \approx 0$ in the collapsed state.

6.5. DISCUSSION AND CONCLUSIONS

We have presented a mean-field model for a polymer solution with annealed excluded-volume interactions that can be used to mimic the phase behaviour of polymers complexed with surfactants. As the degree of loading is an annealed degree of freedom and is coupled to the polymer conformation via the local polymer density, our approach leads to phase behaviour quite different from that of the conventional homopolymer solution.

Depending on the quality of the solvent for the bare polymer, i.e. depending on its hydrophilic or hydrophobic nature, we predict different types of phase separation to occur in a polymer solution with surfactants. If the polymer is *hydrophilic*, the solution is either homogeneous in the whole range of polymer concentrations at low ionic strength and low surfactant concentrations, or may phase separate into two semi-dilute phases at high ionic strength and high surfactant concentrations. This behaviour is reminiscent of phase separation in solutions of polymers capable of formation of stable clusters of more than 3 monomers, as predicted by de Gennes [152], although our model in the hydrophilic regime does not assume any attractive interactions between monomers.

If, in contrast, the polymer is *hydrophobic* the phase behaviour of the polymer/surfactant solution is greatly enriched. Depending on the solvent strength (degree of hydrophobicity of the polymer), ionic strength of the solution, overall monomer density and concentration of surfactants we expect stability or instability of the homogeneous solution with respect to separation into co-existing dilute and semi-dilute or two semi-dilute phases. The Θ -transition in the solution can be induced by the variation of (i) the solvent strength, and (ii) surfactant concentration, and may occur continuously or discontinuously. In the former case the concentrations of co-existing dilute and semi-dilute phases are equal in the Θ -point, while in the latter case the concentration of the semi-dilute (collapsed) phase remains finite in the Θ -point.

On the level of an individual chain the conformational transition from a collapsed (bare) to swollen (loaded) conformation may occur either continuously, as a second-order phase transition, or discontinuously, as a first-order phase transition. In the latter case there is a finite jump in the chain dimensions and in the degree of loading. If the globule-coil transition is induced by an increase in surfactant concentration at low ionic strength of the solution, a discontinuous transition occurs sufficiently far below the Θ -point of the bare polymer. If the transition is initiated by the variation of the solvent strength, then an abrupt transition occurs at high surfactant concentrations while a continuous transition takes place at low concentrations.

We remark that our conclusions concerning a change of character of the Θ -transition in a polymer with annealed excluded-volume interactions have been made earlier by Berikanov *et al.* [153] and Jeppesen and Kremer [154] in the context of conformational transitions in PEO. In ref.154 Monte Carlo simulations were performed using a model quite equivalent to that used in our analytical calculations; similar to our findings a jump-wise variation of the chain dimension was found as a function of the solvent strength. In general, the presence of an annealed degree of freedom (i.e. a parameter which adjusts

itself to local conditions to minimise the free energy) in a system capable of a second-order phase transition always enables a transition to become abrupt.

It is challenging to relate our theoretical predictions to experimental results of Pelton *et al.* [155, 156] and Lee and Cabane for mixtures of PNIPAM with SDS. [75] At temperatures above the LCST of PNIPAM and at intermediate surfactant concentrations, two populations of polymers, collapsed (unloaded) and swollen (polymers highly loaded with complexed SDS-micelles), were observed. Clearly, this co-existence reflects a competition between the gain in free energy of the chain resulting from collapse (minimising unfavourable monomer-water contacts) and the gain resulting from the adsorption of micellar aggregates. As two different conformational states may correspond to equally deep local minima in the free energy of the chain at a certain surfactant concentration, a first-order phase transition between these conformations, and their subsequent co-existence in solution may be expected. Also, in a recent paper the discontinuity in PNIPAM/SDS binding isotherms was found to increase as the temperature increasingly deviated from the Θ -temperature, as predicted by our model. [157]

Investigation of the structure of EHEC/SDS gels using SANS at varying temperatures yielded similar results. [158] At low temperatures a mesh of homogeneously distributed necklaces was observed. Upon heating, EHEC polymers are expelled from the mesh to form a polymer-rich phase. This microphase separation can finally result in a total collapse of the gel. This qualitatively agrees with the predicted phase behaviour of our model.

At this point we have discussed once again the limitations of the mean-field approach in our model. Only when the number of adsorbed micelles per correlation volume is sufficiently large may such a mean-field approach formally be applied, as the excluded-volume parameter needs to be averaged over loaded and unloaded monomers, taking the relative statistical weights into account. This condition imposes limitations on the local polymer densities which can be treated by our approach. The limitation becomes especially important in the range of poor solvent conditions, when the local polymer density $\rho \sim |v_0|^{-1}$ may be rather high and the correlation volume $\sim |v_0|^3$ correspondingly small. Therefore, in a formal sense our model is only applicable to polymer solutions in the vicinity of the Θ -point, and not to solutions far removed from the Θ -point. The insights gained from our model, however, may contribute to understanding the phase behaviour of the latter solutions, even if quantitative features are not correctly described.

Brushes with Annealed Excluded-volume Interactions

ABSTRACT

We present an analytical self-consistent-field (aSCF) theory for a neutral polymer brush with annealed excluded-volume interactions between the monomer units. This model mimics the reversible adsorption of solute molecules or aggregates, such as small globular proteins or surfactant micelles, on the grafted chains. The equilibrium structural properties of the brush (the brush thickness, the monomer density profile, the distribution of the end-monomers of the grafted chains) as well as the overall adsorbed amount and the adsorbate density profile are analysed as a function of the grafting density, the excluded-volume parameters and the chemical potential (the concentration) of the adsorbate in the solution. We demonstrate that with increasing grafting density the overall adsorbed amount always exhibits a maximum, whereas the root-mean-square brush thickness either increases monotonically or passes through a (local) maximum and minimum. At high grafting densities the chains are loaded with adsorbed aggregates in the distal region of the brush, whereas in the region proximal to the grafting surface depletion of aggregates occurs and the polymer brush retains an unperturbed structure. Depending on the relative strength of the excluded-volume interactions between unloaded and loaded monomers, both the degree of loading of the chains and the polymer density profile are either continuous or exhibit a discontinuity as a function of the distance from the grafting surface. In the latter case intrinsic phase separation occurs in the brush. The dense phase consists of unloaded and weakly extended chains and occupies the region proximal to the surface, whereas a more dilute phase consisting of highly loaded and strongly extended chains forms the periphery of the brush.

7.1. INTRODUCTION

Modification of solid-liquid or liquid-liquid interfaces using attached (irreversibly adsorbed or chemically anchored) polymer chains is an important tool for controlled manipulation of the physical properties of an interface. Steric stabilisation of colloidal particles against aggregation [136,159] and preservation of drug-delivery systems against lymphocytosis [160] by a protective layer formed by end-attached polymers are well-known examples. It is generally believed that the most effective protection is ensured by a relatively dense brush consisting of long chains.

One of the less understood but still very important problems in polymer science is the behaviour of polymer brushes in multi-component solutions. If the components in the bulk solution have different affinities for the grafted polymer chains one can expect enhancement of the concentration of particular components inside the brush. [161] This

problem has been addressed in terms of preferential solvation of the polymer brush in a binary solvent in refs.162–164. Small amounts of additives may have a strong effect on the conformation, and as a result, on the protective properties of brushes. Understanding such effects is important in order to predict the efficiency of protection obtained from grafted polymeric layers; in practical applications of grafted polymers (including biological ones) the solution always contains small organic molecules, proteins and/or surfactants, which may lead to specific interactions and association with polymer chains.

In the previous chapters we have presented a simple model to mimic the effect of co-operative association of surfactant molecules with polymer chains. In this chapter we extend our model to brushes interacting with nanocolloids by combining our phenomenological model of polymer-surfactant association with the aSCF approach for conventional polymer brushes, as briefly described in Chapter 1. [20–22, 25] The latter approach enables us to explicitly account for fluctuations in the chain extension and for the intrinsic inhomogeneity of the brush (non-uniform distributions of the polymer density and the concentration of adsorbed micelles) in the direction perpendicular to the grafting plane.

As a result of the non-uniform loading of grafted chains by adsorbed aggregates, the effective excluded-volume parameter of monomers is a function of the distance to the grafting surface. Moreover, this effective excluded volume adjusts itself to the local monomer density such that the overall free energy of the brush is minimised. In other words, the strength of the excluded-volume interactions depends on the degree of loading, which varies throughout the brush. In contrast, the strength of the excluded-volume interactions in a conventional neutral brush depends solely on the solvent quality. The situation is therefore similar to that of annealed brushes in the O \bar B-regime, in which the dissociation of the weak-acidic monomers adjusts itself to the local conditions, see Chapter 4. Thus, borrowing the terminology from the theory of polyelectrolytes, we can classify a brush with complexed nanocolloids as a polymer brush with annealed excluded-volume interactions. [34, 35, 165]

This chapter is organised as follows: in the next section we present an aSCF model for brushes with annealed excluded-volume interactions. In the following section we first consider the adsorption of micelles under the condition that the brush remains in the one-phase regime, afterwards intra-brush microphase separation, induced by adsorption of micelles onto the grafted chains, is discussed. This phase separation manifests itself as a discontinuity in the density profiles of monomers and adsorbed micelles. The large-scale properties of the brushes are examined in section 7.4. Finally, the results and implications of our model are discussed in section 7.5.

7.2. GENERAL ASCF FORMALISM

We consider a brush formed by long flexible polymer chains grafted at one end onto an impermeable and inert planar surface localised at $x = 0$ (x is the coordinate perpendicular to the grafting plane). The grafting density σ (expressed as the number of grafted chains per unit area) is assumed to be high enough to ensure strong overlap of the grafted chains. The number of monomer units per chain (equal to the number of Kuhn segments

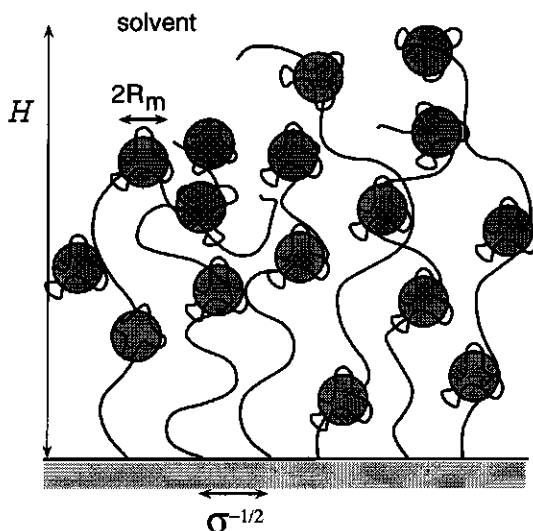


FIGURE 7.1. A schematic illustration of a brush with complexed nanocolloids.

for flexible polymers) is equal to N , and the monomer size is taken as the unit length. The brush is immersed in a solution containing surfactants at a concentration above the CAC but below the CMC. The surfactant molecules can co-operatively bind to the polymer chains in micellar-like aggregates and give rise to necklace-type polymer-micelle complexes. A schematic illustration of the system is shown in Figure 7.1.

In Chapters 5 and 6 we introduced an average degree of loading θ , which denoted the fraction of monomers on the chains in contact with complexed micelles, see Eq.(5.6). In a brush, however, the micelles are expected to be distributed non-uniformly along the grafted chains. We therefore introduce a local degree of loading $\theta(x)$, which is related to the local polymer density $\rho(x)$ and to the local number density of associated micelles $m(x)$ as

$$(7.1) \quad \theta(x) = m(x)N_{ad}/\rho(x)$$

Because of the free exchange of surfactants between adsorbed micelles and the bulk reservoir with fixed chemical potential of the surfactants, we use the free energy of the grafted layer in a grand canonical ensemble. Following the previous analysis, a free energy gain $-k_B T N_{ad} u$ (where k_B is the Boltzmann constant and T is the temperature) is ascribed to each micelle bound to a polymer chain, see Eq.(5.5). The corresponding contribution to the free energy of the brush (the 'adsorption' free energy per chain) is then given by

$$(7.2) \quad F_{ad}/k_B T = \sigma^{-1} u \int_0^H \rho(x) \theta(x) dx$$

The energy gain described by Eq.(7.2), favouring the formation of surfactant micelles bound to the chains, is complemented by the translational entropy of micelles along the chain, given by Eq.(5.8)

$$(7.3) \quad F_{mix}/k_B T = -\sigma^{-1} \int_0^H \rho(x) s(\theta(x)) dx$$

where the overall loading θ in Eq.(5.8) has been replaced by the local loading $\theta(x)$.

As discussed in Chapter 6, the equilibrium degree of loading of a polymer-micelle necklace-like complex of infinite length in a good solvent can be obtained by minimisation of the free energy $F_{ads} + F_{mix}$ with respect to $\theta(x)$, as the osmotic and elastic contributions to F scale less than linearly with N . As a result, one gets a uniform distribution of micelles along the chain (corresponding to maximal entropy) with an average degree of loading θ_b , defined by Eq.(6.11).

In the case of a brush, however, the osmotic contribution F_{os} and the conformational free energy F_{conf} also scale linearly with N . The former describes the contribution resulting from steric repulsion between crowded, grafted chains covered with micelles, the latter the loss of conformational entropy resulting from extension of the grafted chains in the direction perpendicular to the grafting surface. For the osmotic contribution to the free energy of the brush with adsorbed micelles we again use the excluded-volume approximation, i.e. only binary repulsive interactions between bare monomers and adsorbed micelles are taken into account. This gives

$$(7.4) \quad F_{os}/k_B T = \sigma^{-1} \int_0^H v_{eff}(x) \rho^2(x) dx$$

where the effective second virial coefficient $v_{eff}(x)$ is again given by $v_{eff}(\theta) = v_0(1-\theta)^2 + v_1\theta^2 + 2v_2\theta(1-\theta)$ (see Eq.(5.13)). This 'excluded-volume' approximation neglects higher order terms in the virial expansion of the osmotic free energy and is valid if all binary interactions are of repulsive character, as discussed in Chapter 6. Moreover, following Chapter 6 we assume that the second virial coefficients v_1 and v_2 are larger than v_0 . The osmotic interactions in the brush are thus enhanced by adsorption of aggregates. If v_0 is larger than v_1 and v_2 the adsorption of micelles may lead to the collapse of the brush. Such a situation is not considered in this chapter.

We now continue with the fourth contribution to the free energy, the conformational entropy of extended polymer chains. Because of osmotic repulsion the chains in the brush are extended in the direction perpendicular to the grafting surface, provided the grafting density is above the overlap threshold. The requirement of conservation of the finite monomer density in the brush formed by long chains results in an extension of the chains proportional to their contour length N . [17, 18] For long chains the relative extension (compared to their Gaussian dimensions) is high enough so that the strong stretching (or 'quasi-classical') approximation can be applied for calculation of the conformational entropy of non-uniformly extended chains in the brush. Following refs.21,22 and 25 we present the corresponding conformational contribution to the free energy of the brush F_{conf} as a functional of the normalised density $g(x)$ of the end monomers of the chains

and the distribution of local stretching $E(x, x') \equiv dx/ds$, where $s \in [0, N]$ is the distance along the chain contour. The latter quantity denotes the local stretching in the chain at distance x from the grafting surface under the constraint that the chain end is localised at a height x' , with $x < x'$. The conformational free energy is given by¹

$$(7.5) \quad F_{conf}/k_B T = \frac{3}{2} \int_0^H g(x') dx' \int_0^{x'} E(x, x') dx$$

We remark that Eq.(7.5) assumes that the chains retain Gaussian elasticity on all scales, irrespective of the degree of loading. Of course, adsorption of bulky micelles renormalises the local elasticity of the chain, but the effect is partially compensated by local steric restrictions imposed by micelles. We therefore effectively set β zero in the following analysis, which implies that the Gaussian size of the necklace is independent of the degree of complexation, see Eq.(5.10).

The monomer density profile $\rho(x)$ is related to the normalised density of the chain ends $g(x)$ and to the local chain stretching $E(x, x')$ via the conventional equation

$$(7.6) \quad \rho(x) = \sigma \int_x^H \frac{g(x') dx'}{E(x, x')}$$

Together with Eqs.(7.2), (7.3), (7.4) and (7.5) the latter equation defines the total free energy of the brush with annealed excluded-volume interactions

$$(7.7) \quad F = F_{conf} + F_{os} + F_{ad} + F_{mix}$$

as a functional of three independent functions: $g(x)$, $E(x, x')$ and $\theta(x)$.

The variation of the free energy defined by Eq.(7.7) with respect to $E(x, x')$, taking into account the appropriate normalisation conditions

$$(7.8) \quad \int_0^{x'} \frac{dx}{E(x, x')} = N$$

$$(7.9) \quad \int_0^H \rho(x) dx = N\sigma$$

results in a universal form of the distribution of local stretching in the chains

$$(7.10) \quad E(x, x') = \frac{\pi}{2N} \sqrt{x'^2 - x^2}$$

and in an equation which couples the polymer density $\rho(x)$ to the local degree of loading $\theta(x)$ and the distance x from the grafting surface.

$$(7.11) \quad 2v_{eff}(x)\rho(x) + u\theta(x) - s(\theta(x)) = \Lambda - \frac{3\pi^2 x^2}{8N^2}$$

¹We remark that, as we follow the convention of refs.21, 22 and 25, we use a prefactor 3/2 in Eq.(7.5) instead of the prefactor 1/2 used in Chapter 1 and in ref. 20.

The Lagrangian multiplier Λ is determined using the normalisation condition, Eq.(7.9), after minimisation of the total free energy with respect to the brush thickness H . We remark that in the case of a bare brush ($\theta(x) = 0$) only the first term on the left side of Eq.(7.11) remains, so that the equation then reproduces the well-known parabolic polymer density profile, given in Eq.(1.3). [20, 22, 25]

The variation of the total free energy, given by Eq.(7.7), with respect to the local degree of loading ($\delta F/\delta\theta(x) = 0$) provides the same relationship between the (local) polymer density $\rho(x)$ and the degree of loading $\theta(x)$ as is the case for the semi-dilute regime, discussed in the previous chapter (Eq.(6.12)), i.e.

$$(7.12) \quad \rho(x) = -\frac{s'(\theta_b) - s'(\theta(x))}{v'_{eff}(x)}$$

Combination of Eq.(7.11) and Eq.(7.12) yields two coupled equations for the monomer density distribution $\rho(x)$ and the profile of the degree of loading of chains by adsorbed micelles $\theta(x)$ as a function of the distance from the grafting surface.

As mentioned, Λ depends on H and must be determined via normalisation of the monomer density profile, as expressed in Eq.(7.9). However, we can obtain Λ directly by making use of the condition of vanishing polymer density at the brush edge, i.e. $\rho(H) = 0$. This is the case if the osmotic interactions in the brush have a purely repulsive character. [25] It follows from Eq.(7.12) that the degree of loading $\theta(x)$ at the brush edge, $x = H$, acquires its bulk value given by Eq.(6.11), i.e.

$$(7.13) \quad \theta(H) = \theta_b$$

Substitution of the above result in Eq.(7.11) yields for Λ

$$(7.14) \quad \Lambda = \frac{3\pi^2 H^2}{8N^2} + \ln \frac{N_{ad}(1 - \theta_b)}{N_{ad}(1 - \theta_b) + \theta_b}$$

The distribution of end-monomers of the chains can be obtained from the polymer density profile by inverting Eq.(7.6) which results in

$$(7.15) \quad g(x) = -\frac{x}{\sigma N} \int_x^H \frac{(d\rho(x)/dx)_x dx'}{\sqrt{x'^2 - x^2}}$$

provided that $\rho(H) = 0$. [25] At this point it is convenient to introduce reduced variables, renormalised with respect to the chain length,

$$(7.16) \quad h = \frac{H}{\sqrt{8N^2/3\pi^2}}$$

and

$$(7.17) \quad z = \frac{x}{\sqrt{8N^2/3\pi^2}}$$

As the height of the brush at maximal extension equals $H = N$, the reduced height h cannot exceed $\sqrt{3\pi^2/8}$.

Eqs.(7.11), (7.12) and (7.14), expressed in reduced variables, yield a closed equation for the profile of the degree of loading $\theta(z)$ as a function of z

$$(7.18) \quad h^2 - z^2 = - \frac{2v_{eff}(z)(s'(\theta_b) - s'(\theta(z))) + v'_{eff}(z)(\theta(z)s'(z) + s(z))}{v'_{eff}(z)} - \ln \left(\frac{N_{ad}(1 - \theta_b)}{N_{ad}(1 - \theta_b) + \theta_b} \right)$$

and for the monomer density profile

$$(7.19) \quad \rho(z) = \frac{1}{2v_{eff}(z) - \theta(z)v'_{eff}(z)} \left(h^2 - z^2 - \ln \left(\frac{1 - \theta(z)}{1 - \theta_b} \frac{N_{ad}(1 - \theta_b) + \theta_b}{N_{ad}(1 - \theta(z)) + \theta(z)} \right) \right)$$

In the limit $N_{ad}u \gg 1$ the adsorption of micelles is suppressed ($\theta(z) \cong 0$, $v_{eff}(z) \cong v_0$) and Eq.(7.19) reduces to the usual parabolic polymer density profile for a bare brush in a good solvent. [20,22] At high loading ($\theta_b \cong 1$) and $v_1, v_2 > v_0$, the polymer density in a brush loaded by micelles is always smaller (i.e. the chains are more extended) than in a bare brush.

The reduced overall brush thickness h can be obtained as a function of the grafting density σ by applying the normalisation condition, given by Eq.(7.9), to the density profile $\rho(z)$, defined by Eqs.(7.18) and (7.19). It defines the maximal span of grafted chains in the direction perpendicular to the grafting surface. We also introduce the root-mean-square brush thickness h_{rms} , defined as

$$(7.20) \quad h_{rms}^2 = \int_0^h z^2 \rho(z) dz / \int_0^h \rho(z) dz$$

which is the second moment of the polymer density distribution. In the case of a brush with a strongly inhomogeneous density distribution in the z -direction, the quantity h_{rms} gives the characteristic range of distribution of the majority of monomers of the grafted chains.

7.3. INTRINSIC STRUCTURE OF THE BRUSH

The remarkable feature of both profiles $\rho(z)$ and $\theta(z)$, as given by Eqs.(7.18) and (7.19), is their universality as a function of z^2 , irrespective of the grafting density. The origin of this universality is, of course, the parabolic profile of the monomer chemical potential in a brush formed by strongly extended monodisperse polymer chains with Gaussian elasticity. This universality holds irrespective of the particular form of osmotic interactions in the brush. [25] The grafting density σ only determines the cut-off length h of the density profiles via the corresponding normalisation condition, Eq.(7.9).

The condition of stability requires that $\rho(z)$ is a decreasing function of z , whereas $\theta(z)$ increases with z and reaches its maximum value θ_b at the brush edge, i.e. at $z = h$. In Figure 7.2 $\theta(z^2)$ is plotted according to Eq.(7.18) for three values of v_2 and fixed v_1 and θ_b . As follows from the figure, θ either increases monotonically as a function of z^2 or it acquires multiple values in a certain range of z^2 , depending on the relative magnitude of the excluded-volume parameters.

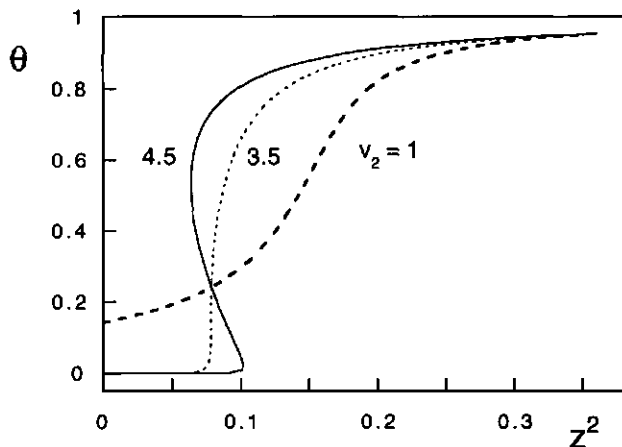


FIGURE 7.2. θ as a function of z^2 for $v_1 = 10$ and v_2 is varied in the range from 1 to 4.5. The monomeric adsorption energy is $u = -0.16$, $v_0 = 1$, and $N_{ad} = 100$ (default values).

According to Eq.(7.18) θ is a single-valued function of z^2 or, equivalently, z^2 is a monotonically increasing function of θ if $v_1 \geq v_1^*(v_2, \theta_b)$. However, when $v_1 \leq v_1^*(v_2, \theta_b)$, z^2 exhibits non-monotonic behaviour as a function of θ in the range $\theta \in [0, \theta_b]$. It must be emphasised that the monomeric chemical potential $\mu(z) \sim z^2$, see Eq.(7.11). As the occurrence of the van der Waals-loop in z^2 , or equivalently $\mu(\rho)$, is a generic feature of our model, the same diagrams for v_1^* as shown in Chapter 6 (Figure 6.3) also apply in the case of brushes complexed with micelles.

If $v_1 \geq v_1^*$, i.e. v_1 is above the critical line, the local properties of the brush are continuous and smooth functions of the distance from the grafting surface. For $v_1 < v_1^*$ the appearance of a van der Waals-type loop in the $\theta(z^2)$ -dependence suggests an abrupt variation in the equilibrium degree of loading and in the polymer density at some particular distance from the surface. This jump-wise variation in the local properties of the brush indicates internal micro-phase separation.

With increasing θ_b the region $v_1 \leq v_1^*(v_2, \theta_b)$ corresponding to the microphase separation in the brush extends and occupies a larger part of the phase diagram in the (v_1, v_2) -plane, as presented in Figure 6.3. This implies that microphase separation may be enhanced by increasing the bulk surfactant concentration.

7.3.1. Continuous distributions: one-phase brush

We first consider a system in which the excluded-volume interaction parameter between two adsorbed micelles is large compared to the corresponding parameters of monomer-monomer and monomer-micelle interactions, i.e. $v_1 \gg v_0, v_2$. This corresponds to the region $v_1 > v_1^*(v_2)$ in Figure 6.3. In this case θ is a single-valued function of z^2 and all the local properties of the brush are continuous and smooth functions of the distance z from the grafting surface. The brush is thus in a one-phase regime. Experimentally this

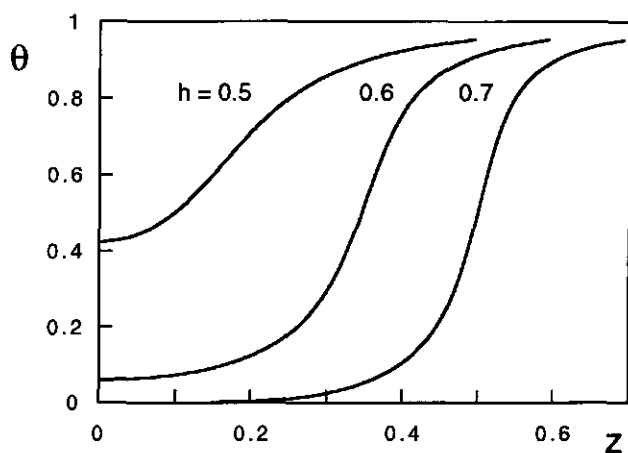


FIGURE 7.3. $\theta(z)$ as a function of z for $v_1 = 10$ and $v_2 = 2$. The values of σ and corresponding values of h are $\sigma = 6.60 \cdot 10^{-3}$ at $h = 0.5$, $\sigma = 2.39 \cdot 10^{-2}$ at $h = 0.6$ and $\sigma = 5.68 \cdot 10^{-2}$ at $h = 0.7$.

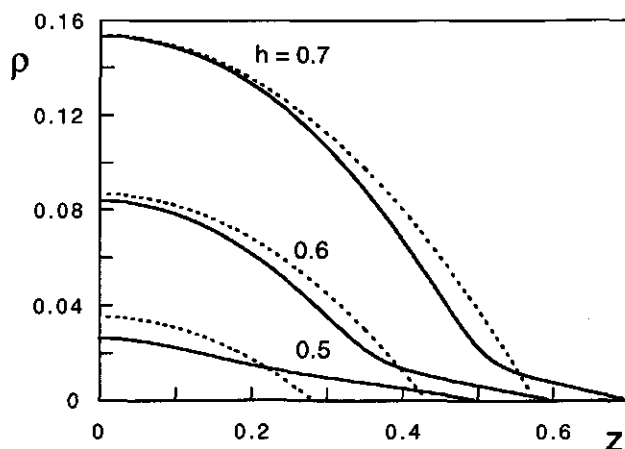


FIGURE 7.4. $\rho(z)$ for the same set of parameters as used in Figure 7.3. The dashed curves indicate the monomer density in a "bare" brush for the same values of σ .

situation corresponds to the adsorption of small, highly charged micellar aggregates at comparatively low ionic strength in the solution, i.e. when the long-range Coulomb repulsion provides the dominant contribution to the second virial coefficient of micelle-micelle interaction (see the discussion following Eq.(5.22)).

In Figures 7.3 and 7.4 the profiles of $\theta(z)$ and $\rho(z)$ are plotted for various values of h , i.e. for various values of σ . The excluded-volume parameters are $v_0 = 1$ (default value), $v_2 = 2$ and $v_1 = 10$. As can be seen in Figure 6.3, the value of v_1 lies well above

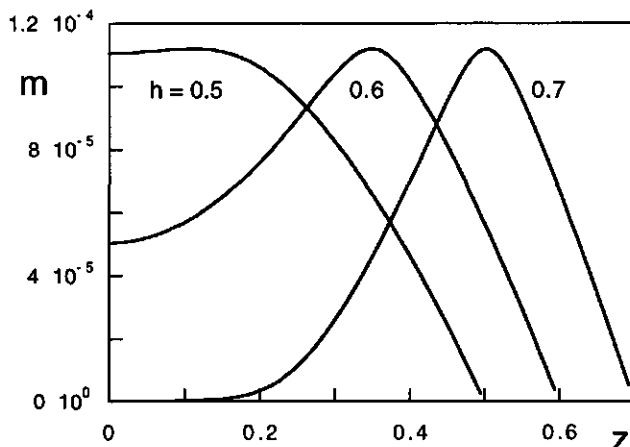


FIGURE 7.5. The number density $m(z)$ of adsorbed micelles for the same set of parameters as used in Figures 7.3 and 7.4.

the critical line. The value of the effective adsorption energy per monomer is set at $u = -0.15$, which for $N_{ad} = 100$ corresponds to a bulk coverage $\theta_b \cong 0.95$, see Eq.(6.11).

As illustrated in Figures 7.3 and 7.4, for a given grafting density the degree of loading decays monotonically from the bulk value θ_b at the brush edge ($z = h$) to its proximal value at $z = 0$. Simultaneously, the polymer density (which vanishes at $z = h$) monotonically increases as the grafting surface is approached. An increase in σ corresponds to a shift of the cut-off length h of the universal curves $\theta(z^2)$ and $\rho(z^2)$, defined by Eqs.(7.18) and (7.19). This results in a decrease in the proximal degree of loading $\theta(z = 0)$ and in a simultaneous increase in the proximal polymer density $\rho(z = 0)$.

At low grafting density (for example $h = 0.5$, $\sigma = 6.6 \cdot 10^{-3}$) the brush is highly loaded by adsorbed micelles and, as a result, strongly extended as compared to a bare brush. For comparison we also show in Figure 7.4 the parabolic polymer density profiles (dashed curves) for bare brushes at the same grafting densities and monomer-monomer excluded-volume parameter v_0 . The additional extension of grafted chains, due to enhanced osmotic interactions from the adsorbed micelles, is reflected in a much smaller average polymer density within a highly loaded brush. With increasing grafting density (and corresponding increase in h) the adsorbed micelles are squeezed from the interior regions where the polymer density is relatively high towards the more dilute periphery of the brush. This results in an increasing intrinsic inhomogeneity of the brush with increasing σ , as is shown in Figure 7.3. At sufficiently high σ the degree of loading drops to approximately zero in the region proximal to the grafting surface, due to the high local polymer density imposed by the dense grafting of the chains on the surface.

This depletion of micelles from the proximal region is illustrated in Figure 7.5, where the number density profiles of adsorbed micelles $m(z) = \rho(z)\theta(z)/N_{ad}$ are plotted for the same set of parameters as used in Figures 7.3 and 7.4. As can be seen from Figure 7.5, the density profiles of adsorbed micelles change dramatically with increasing grafting density.

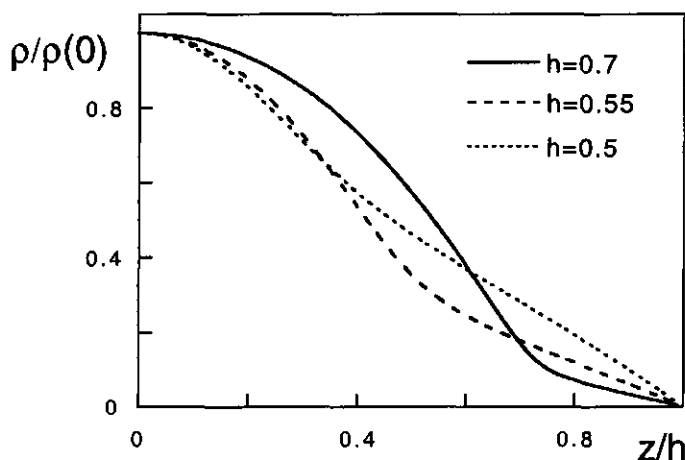


FIGURE 7.6. The monomer density distribution $\rho(z)/\rho(0)$ as a function of z/h for three values of the reduced brush thickness, $h = 0.5, 0.55$ and 0.7 , using the parameters of Figure 7.3, $\sigma = 1.32 \cdot 10^{-2}$ for $h = 0.55$.

At low σ , $m(z)$ decreases monotonically with the distance z from the grafting surface and is relatively high near the grafting plane. This decrease in $m(z)$ with increasing z reflects the decay of the polymer density at a fairly uniform loading of chains by adsorbed micelles, $\theta(z) \cong \theta_b$. With increasing σ the micelles are squeezed from the proximal region and a maximum in the $m(z)$ profiles appears. This maximum becomes more pronounced and shifts from the central region of the brush to the periphery as σ increases.

It must be emphasised that this depletion of micelles near the grafting plane differs from the depletion of polymer from a narrow proximal region, due to local steric restrictions imposed by the impermeability of the grafting plane for polymer chains. [22, 136] The latter depletion is not taken into account in our aSCF model.

The increasing inhomogeneity of the brush with increasing grafting density is also illustrated in Figure 7.6, where the monomer density normalised by the proximal value $\rho(0)$ is plotted as a function of the reduced distance z/h from the surface for different values of σ . At high grafting densities the brush consists, roughly speaking, of two regions: (i) a region proximal to the surface characterised by a low degree of loading and by a high monomer density, and (ii) a dilute distal region with a low monomer density and high degree of loading. In the proximal region the shape of the polymer density profile is close to the parabolic profile typical for a bare brush. [20, 22, 25] The terminal parts of the chains which reach the distal region are densely covered by adsorbed micelles and, as a result, are strongly extended in comparison to the chains at the periphery of the bare brush. This extension "smoothens" the polymer density profile near the brush edge in comparison to the parabolic decay of a bare brush. This effect should not be confused with the deviation from the parabolic density profile, caused by Gaussian fluctuations of the weakly stretched terminal parts of the chains. The latter effect has been observed

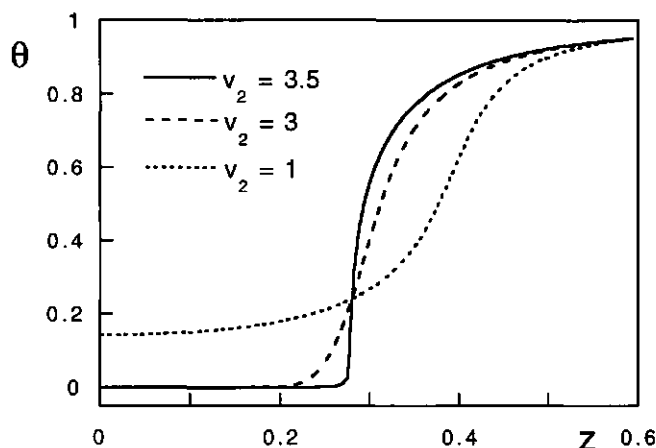


FIGURE 7.7. The effect of monomer-micelle excluded-volume interactions on $\theta(z)$. Three values of v_2 (1, 3 and 3.5) are considered with $v_1 = 10$.

experimentally in Chapter 3 and in nSCF calculations [26], but is not accounted for by the “quasi-classical” aSCF approximation used in our analysis.

The depletion of adsorbed micelles from the proximal region of the brush with increasing grafting density is primary caused by strong micelle-micelle repulsion. However, in the intermediate region separating the proximal depletion zone and the highly loaded periphery of the brush the repulsive interactions of bare monomers with adsorbed micelles play a dominant role. Therefore, the slope of the $\theta(z)$ curves in this region is sensitive to the value of the monomer-micelle excluded-volume parameter v_2 . With increasing v_2 an intermediate degree of loading is more unfavourable, and this results in a narrowing of the intermediate region. This effect is illustrated in Figure 7.7 where the profiles $\theta(z)$ of the degree of loading are plotted for a constant brush thickness ($h = 0.6$) and for three sets of excluded-volume parameters, corresponding to increasing v_2 at fixed v_1 . The width of the region over which the decay of the degree of loading occurs decreases progressively with increasing v_2 , as seen in Figure 7.7. The same effect occurs when v_1 decreases with respect to v_2 .

7.3.2. Microphase separation

In the previous section we have analysed the behaviour of grafted polymers with adsorbed micelles under the condition that the effective (renormalised) parameter of the micelle-micelle excluded-volume interactions v_1 is larger than $v_1^*(v_2)$, see Figure 6.3. Physically, this situation corresponds to the dominance of the screened Coulomb micelle-micelle repulsion in the intra-brush osmotic interactions. This is not necessarily the case if the ionic strength of the solution is increased.

As demonstrated in the previous section (Figure 7.7), an increase in the magnitude of the monomer-micelle repulsion v_2 results in a stronger inhomogeneity of the brush.

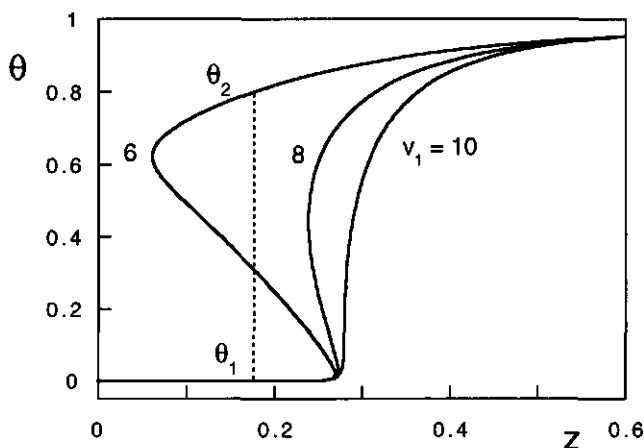


FIGURE 7.8. $\theta(z)$ for three values of v_1 and $v_2 = 3.5$. In the plot the values θ_1 and θ_2 of the degree of loading in two co-existing phases are indicated for $v_1 = 6$.

Simultaneously, the intermediate region where both the polymer density and the degree of loading experience major spatial variations narrows. This tendency indicates the possibility of microphase segregation, which leads to a co-existence of a dense (unloaded) phase in the proximal region, and a sparse (loaded) phase in the distal region of the brush. Such segregation occurs when the monomer-micelle interactions are dominant and intermediate degrees of loading are relatively unfavourable.

In Figure 7.8 $\theta(z)$ is plotted for constant $v_2 = 3.5$ and for three different values of v_1 . The set of parameters corresponds to decreasing micelle-micelle excluded volume and constant monomer-micelle excluded volume. As mentioned earlier, this variation may be realised experimentally by increasing the ionic strength.

At $v_1 = 10$ the coverage $\theta(z)$ still increases continuously with increasing z . This situation corresponds to $v_1 \geq v_1^*(v_2)$, and has been discussed in the previous section. On the contrary, at $v_1 = 8$ and 6 the dependence $\theta(z)$ demonstrates a van der Waals loop. This implies that the degree of loading changes abruptly at a certain distance from the grafting surface, denoted by z_0 . For $v_1 = 6$ this is illustrated by the vertical dashed line through the points θ_1 and θ_2 . The position z_0 of the boundary between the co-existing phases and the degree of loading at $z = z_0$ in the bare and highly loaded phase (which we denote as θ_1 and θ_2 , respectively) can be determined using the Maxwell equal-area construction

$$(7.21) \quad \int_{\theta_1}^{\theta_2} (z^2(\theta) - z_0^2) \frac{d\rho}{d\theta} d\theta = 0$$

This is equivalent to the requirement of equality of the osmotic pressure in the two co-existing phases. We stress that the above equation is not equivalent to an equal-area construction in a $\theta(z)$ -plane.

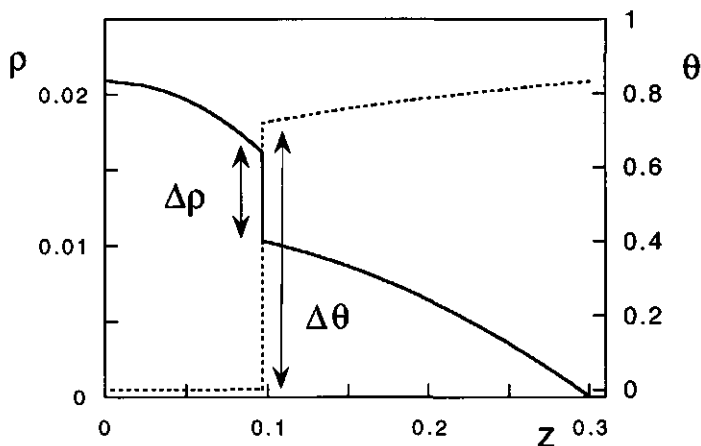


FIGURE 7.9. $\rho(z)$ (left axis, solid curve) and $\theta(z)$ (right axis, dashed curve) for $v_1 = 6$, $v_2 = 3.5$, $\theta_b = 0.831$ and $h = 0.3$. The magnitudes of the jumps in polymer density ($\Delta\rho$) and in the degree of loading ($\Delta\theta$) are indicated.

The discontinuity in $\theta(z)$ evidently concurs with a discontinuity in the polymer density profile $\rho(z)$, as these two quantities are coupled via Eq.(7.19). Hence, at $z = z_0$ the density jumps from a high value ρ_1 in the weakly loaded (dense) phase to a smaller value ρ_2 in the highly loaded (extended) phase. In Figure 7.9 the monomer density and the degree of loading are plotted as a function of z . The jumps in polymer density $\Delta\rho \equiv \rho_1 - \rho_2$ and in the degree of loading, $\Delta\theta \equiv \theta_2 - \theta_1$, are indicated by arrows.

The density profile of adsorbed micelles, $m(z) \sim \rho(z)\theta(z)$ also exhibits an upward jump, $\Delta m = m_2 - m_1$ at $z = z_0$. The relative magnitude $\Delta m/m_1$ of this jump is, however, smaller than that of the jump in the degree of loading, $\Delta\theta/\theta_1$ because $\rho_2 < \rho_1$. In particular, the difference Δm decreases strongly as the parameters approach the critical point for microphase separation.

The discontinuity in $\rho(z)$ has significant consequences for the distribution $g(z)$ of the end-monomers, as given by Eq.(7.15). As the polymer density exhibits a jump $\Delta\rho$ at $z = z_0$, we can formally split the density profile into two parts,

$$(7.22) \quad \rho(z) = \tilde{\rho}(z) + \Theta(z_0 - z)\Delta\rho$$

where $\tilde{\rho}(z) = \rho(z) - \Delta\rho$ at $z \in [0, z_0]$. The function $\tilde{\rho}(z) = \rho(z)$ at $z \in (z_0, h]$ is a continuous and smooth function of z and $\Theta(z)$ is the Heaviside step function. Substitution of this distribution into Eq.(7.15) gives the end-monomer distribution (in reduced variables) for $z < z_0$,

$$(7.23) \quad g(z) = -\frac{z}{\sigma} \int_z^h \frac{(d\tilde{\rho}(z)/dz)_{z'} dz'}{\sqrt{z'^2 - z^2}} + \frac{z}{\sigma} \frac{\Delta\rho}{\sqrt{z_0^2 - z^2}}$$

while at $z > z_0$ Eq.(7.15) holds.

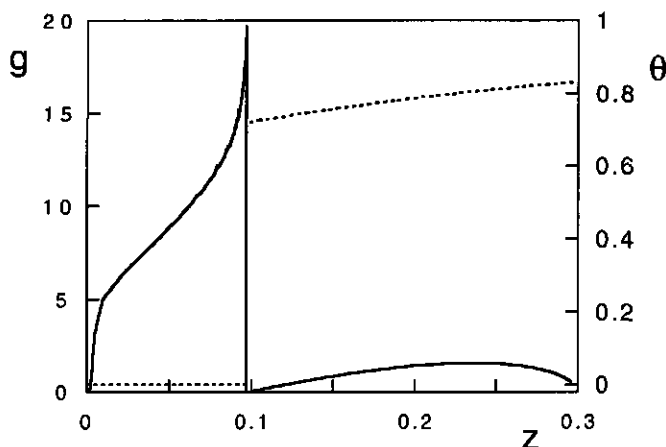


FIGURE 7.10. The end-point distribution function $g(z)$ (solid curve) for the same parameters as in Figure 7.9. The coverage $\theta(z)$ is also shown to illustrate the microphase separation (dashed curve).

As follows from Eq.(7.23), the density $g(z)$ of end-monomers diverges at $z \rightarrow z_0$ as $\sim (z_0^2 - z^2)^{-1/2}$. This behaviour of $g(z)$ indicates a bimodal distribution of chain ends in the brush. The 'proximal' maximum in $g(z)$ at $z = z_0$ corresponds to the population of weakly loaded and weakly extended chains which form the dense proximal phase in the brush. The remaining fraction of chains, whose ends are distributed in the range $z_0 \leq z \leq h$, contribute a small portion of their monomers to the dense phase, as they are strongly extended in the proximal region. The latter chains thus bring the majority of their monomers to the sparse and highly loaded peripheric region of the brush. The end-point distribution $g(z)$ is plotted in Figure 7.10, for the same parameters as in Figure 7.9. For comparison, the distribution of coverage $\theta(z)$ is shown in the same graph. The bimodal distribution of $g(z)$ and the discontinuity of $\theta(z)$ at z_0 are evident.

We remark that even if $v_1 \leq v_1^*(v_2, \theta_b)$, the two phases co-exist in the brush only when the grafting density is high enough, i.e. when the proximal value of the degree of loading $\theta_0 \equiv \theta(z = 0)$ is smaller than θ_1 . In the case that the chains in the brush are grafted rather sparsely, the degree of loading decays continuously from θ_b to θ_0 as z decreases from h to 0. The brush as a whole is then in the highly loaded and extended state. As σ increases, the proximal value of the degree of loading θ_0 decreases as micelles are squeezed out of the brush. When θ_0 reaches the value θ_2 , corresponding to the minimal degree of loading in the "loaded" phase, the proximal region with a high polymer density and low coverage $\theta(z) \leq \theta_1$ appears. Correspondingly, at larger grafting densities the brush is in a two-phase state with discontinuous profiles $\theta(z)$ and $\rho(z)$. Further increase in σ leads to an increase in the relative weight of the dense phase comprising the majority of the chains, whereas the relative weight of the extended phase decreases.

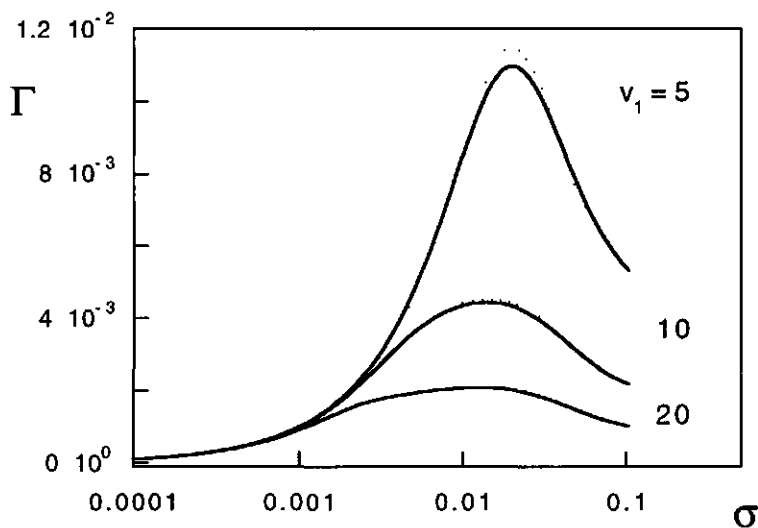


FIGURE 7.11. The adsorbance Γ plotted semi-logarithmically as a function of σ for three different values of v_1 , $\theta_b = 0.95$ and $v_2 = 2$.

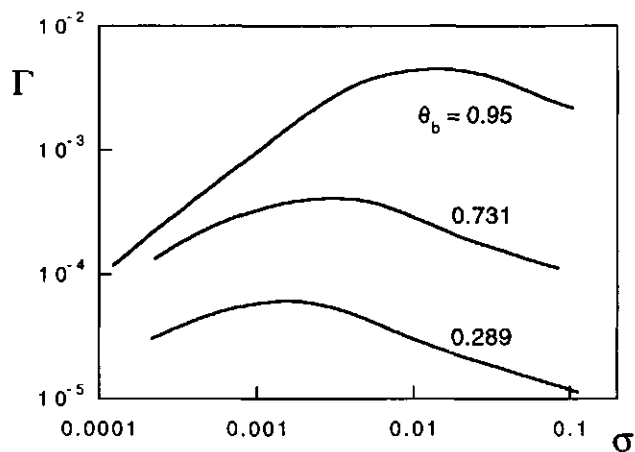


FIGURE 7.12. The adsorbance Γ plotted double-logarithmically for $v_1 = 10$, $v_2 = 2$ and three values of θ_b .

7.4. LARGE-SCALE PROPERTIES

We now turn to the overall (large-scale) properties of brush with adsorbed micelles. In Figure 7.11 and 7.12 the total number of micelles adsorbed per unit area of the brush,

$$(7.24) \quad \Gamma = N_{ad}^{-1} \int_0^h \rho(z) \theta(z) dz,$$

is plotted semi-logarithmically as a function of σ at fixed adsorption strength for three different values of the parameter v_1 (Figure 7.11) and double-logarithmically at fixed excluded-volume parameters and three different values of the adsorption energy per micelle (Figure 7.12). The adsorbed amount per unit area Γ exhibits a maximum as a function of the grafting density σ for all sets of parameters. The height and position of the maximum Γ_{max} depend on the strength of osmotic interactions and on the adsorption strength $-N_{ad}u$ per micelle.

The maximum in Γ in Figure 7.11 can be explained as follows. At low grafting densities the degree of loading is close to θ_b throughout the brush, and Γ is virtually independent of the micelle-micelle osmotic interactions. With increasing σ the overall adsorbed amount increases nearly proportional to σ until the osmotic repulsive interactions in the brush become comparable to the free energy gain resulting from the adsorption of micelles. A further increase in σ results in the formation of a proximal depletion zone and in a progressive decrease in the average degree of loading. The latter tendency is so pronounced that, in spite of the increasing number of grafted chains per unit area, the overall amount of adsorbed micelles decreases with increasing σ . The same reasoning holds for Figure 7.12. Obviously, the height Γ_{max} of the maximum decreases with decreasing adsorption strength $-N_{ad}u$. The position of the maximum depends only weakly on the micelle-micelle excluded-volume parameter v_1 (Figure 7.11) but it is shifted towards smaller values of σ with decreasing adsorption strength (Figure 7.12).

At fixed grafting density the adsorbed amount Γ is thus affected by variation of the adsorption strength or by variation of the micelle-micelle excluded-volume parameter v_1 . The latter parameter can be tuned by varying the ionic strength of the solution. With decreasing ionic strength the total adsorbed amount decreases significantly (Figure 7.11), provided all other parameters remain constant. Our model therefore predicts that an increase in ionic strength of a solution can strongly enhance the adsorption of charged aggregates on a grafted polymeric layer.

Another important question concerns the behaviour of the total height h and of the root-mean-square height h_{rms} of the brush as a function of σ . There is a remarkable difference in the behaviour of $h(\sigma)$ and $h_{rms}(\sigma)$ for a polymer brush with annealed excluded volume as compared to a conventional brush in a good solvent. We recall that h characterises the overall span of grafted chains in the z -direction, while h_{rms} characterises the average thickness of the brush. For a conventional polymer brush with a 'quenched' excluded-volume parameter, both h and h_{rms} monotonically increase with increasing σ , whereas the ratio h/h_{rms} remains constant.² [25] In other words, with increasing grafting density the structure of the brush changes in a self-similar way and the density distribution remains invariant in re-scaled variables.

²This is easily seen if we insert the expression for $\rho(z)$ in the aSCF model, Eq.(1.3), in the definition for H_{rms}^2 , Eq.(7.20). The value of H_{rms} in the aSCF model is then $H_{rms}^2 = \Lambda N^2 (\sigma v_0)^{2/3}$, where the constant Λ equals $\frac{1}{3} \left(\frac{\pi^2}{12} \right)^{2/3} - \frac{\pi^2}{90} \left(\frac{\pi^2}{12} \right)^{5/3}$. As $H_{rms}^2 \sim H^2$, the ratio $H_{rms}/H = \sqrt{\frac{1}{5}}$, and is thus independent of either N or σ , or *self-similar*.

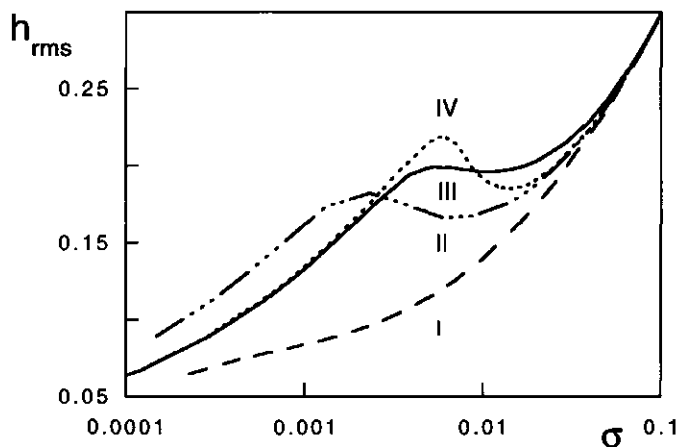


FIGURE 7.13. h_{rms} plotted semi-logarithmically as a function of σ for four sets of (v_1, v_2, θ_b) , I (10, 2, 0.731), II (20, 2, 0.95), III (10, 2, 0.95) and IV (10, 3.5, 0.95).

The situation is quite different for a brush formed by chains with annealed excluded volume. Here the total height h of the brush increases monotonically as a function of σ , whereas h_{rms} can exhibit non-monotonic behaviour, depending on the values of the excluded-volume parameters and θ_b . In Figure 7.13 h_{rms} is plotted semi-logarithmically as a function of σ for three values of v_2 and fixed v_1 . When the micelle-micelle osmotic interactions are dominant, i.e. $v_1 \gg v_1^*$, h_{rms} increases monotonously with increasing σ , just as the overall brush height h does. However, with increasing v_2 or θ_b the $h_{rms}(\sigma)$ curve progressively flattens in the intermediate range of σ and eventually a local maximum and a minimum appear when the boundary $v_1^*(v_2) = v_1$ is approached (see Figure 6.3). These local extremes become more pronounced as v_2 increases, i.e. as the brush becomes more inhomogeneous and eventually exhibits micro-phase separation.

The difference in behaviour of $h(\sigma)$ and $h_{rms}(\sigma)$ at large values of the monomer-micelle excluded-volume parameter v_2 can be rationalised as follows. At small grafting density the brush is relatively homogeneous, and the extension of the chains increases with increasing σ without significant changes in the distribution of loading inside the brush. As a result, both h and h_{rms} grow with increasing σ , as the strength of the osmotic interactions is constant in this regime. However, at larger σ depletion of micelles from the proximal region occurs, whereas the chains near the brush edge remain loaded and extended. In the one-phase regime the width of the intermediate region (between the depletion zone and the loaded periphery of the brush) decreases with increasing v_2 , i.e. upon approach of the boundary $v_1 = v_1^*(v_2)$. At $v_1 \leq v_1^*(v_2)$ the brush is in the two-phase regime, with a sharp boundary between proximal (dense) and peripheral (extended) regions. The major contribution to h_{rms} is provided by the region where the majority of polymer monomers is distributed, i.e. by the proximal region of the brush. In contrast, h is determined by the span of the most extended chains in the distal region.

With increasing grafting density the dominant effect is the enrichment of the proximal region by unloaded, weakly extended chains. This results in an effective decrease in h_{rms} , whereas the total thickness of the brush, determined by a minority of strongly extended and loaded chains, continuously grows as σ increases. At even higher grafting density the contribution of the distal region to h_{rms} is negligible. The increase in both h_{rms} and h is determined by the monomer-monomer repulsive interaction in the proximal region, just as in conventional bare brushes. This results in the convergence of the plots in Figure 7.13 for various sets of excluded-volume parameters at high values of σ .

7.5. DISCUSSION AND CONCLUSIONS

Grafted polymers in contact with a solution containing adsorbate particles (surfactants forming micellar aggregates, proteins, etc.) are described using a model for a polymer brush with annealed excluded-volume interactions. The overall structure of the grafted layer is determined by a balance between the gain in adsorption energy of aggregates on the one hand, and the osmotic interactions and the conformational entropy penalty for the stretching of loaded chains counteracting adsorption on the other.

The adsorption of aggregates enhances the repulsive osmotic interactions in the brush and therefore induces additional stretching of the grafted chains. Due to this adsorption the excluded-volume parameter becomes non-uniform (annealed) throughout the brush at high grafting densities. It follows from our analysis that the distribution of adsorbed aggregates (micelles) is inhomogeneous in dense brushes. Such brushes are therefore intrinsically more inhomogeneous than conventional ("bare") polymer brushes in a good solvent.

With increasing grafting density the steric repulsion between grafted chains loaded with adsorbed aggregates becomes stronger. As a result, the equilibrium degree of loading in the proximal region decreases strongly and the inhomogeneity of the brush is more pronounced. At high grafting densities the brush as a whole effectively consists of two regions. In the dilute periphery the chains are highly loaded by adsorbed micelles, whereas in the proximal interior of the brush depletion of micelles occurs and the unperturbed "parabolic" structure is retained. The boundary between the loaded periphery and the depletion region is diffuse if the micelle-micelle repulsion is strong ($v_1 \gg v_1^*(v_2)$, see Figure 6.3). For a lower value of v_1 the polymer density as well as the degree of loading and the density profile of adsorbed micelles may exhibit a discontinuity at a certain distance from the grafting surface, indicating phase separation inside the brush. This phase separation is also reflected in a bimodal distribution of the end-monomers. In the proximal region, which is depleted of micelles, a maximum in this distribution occurs, corresponding to weakly extended and "bare" chains. The distal maximum of the distribution of end-monomers represents the strongly extended and highly loaded chains that form a sparse and extended phase at the edge of the brush.

We remark that a similar microphase segregation into a proximal (dense) phase and strongly extended peripheric phase has been described earlier for a polymer brush formed by weakly charged polyelectrolyte chains under poor solvent conditions, where binary

short-range attractive interactions between non-charged monomers compete with the Coulomb repulsion between charged ones. [166] Another example of such internal segregation is a polymer brush in a good solvent with repulsive binary monomer-monomer interactions and attractive higher-order osmotic interactions between monomers. The latter case corresponds to the so-called "n-cluster" model of phase separation in the polymer solutions as introduced by de Gennes. [152] This model has been applied to polymer brushes in refs. 167 and 168. In both cases microphase separation is induced by an 'inverse' order of repulsive and attractive interactions between monomers (lower-order repulsion, higher-order attraction). In contrast to a polyelectrolyte brush in a poor solvent and a brush capable of n-cluster association, however, our model of a brush with annealed excluded-volume interactions demonstrates intrinsic phase separation in the absence of any attractive interactions between monomers.

It is instructive to compare the results of the present aSCF approach to our earlier analysis of a polymer brush with annealed excluded volume based on the Alexander-de Gennes box-model.³ [17, 18] In the framework of the latter model the chains in the brush are assumed to be stretched uniformly and equally: a delta-function for the end-monomer distribution is pre-assumed, and hence the brush as a whole is forced to be in a one-phase regime. If the monomer-micelle excluded-volume parameter v_2 is large enough the box-like model predicts an abrupt variation of the overall brush height and of the degree of loading with variation of the grafting density or adsorption strength. This behaviour is reminiscent of a first-order phase transition. The release of the constraint of equal stretching of the chains changes the situation qualitatively: instead of a first-order phase transition with an abrupt variation of the brush height and of the adsorbed amount, co-existence of a dense and sparse, extended phase within the brush is predicted. Correspondingly, the variation of the overall properties of the brush with increasing grafting density or adsorption energy occurs smoothly, due to gradual re-partitioning of the chains between the dense and extended phase.

Two large-scale (global) properties of the brush, viz. the overall adsorbed amount Γ of micelles per unit area and the root-mean-square brush thickness h_{rms} , are predicted to exhibit non-monotonic behaviour as a function of the grafting density σ . A maximum is found in $\Gamma(\sigma)$, whereas $h_{rms}(\sigma)$ is an increasing function of σ at low and high grafting density but may decrease in the intermediate range. The physical reason of such non-monotonic behaviour of both quantities is the expulsion of adsorbed aggregates from the brush with increasing grafting density. Because of the competition between adsorption energy and osmotic repulsion, the position and the height of the local maxima in $\Gamma(\sigma)$ and $h_{rms}(\sigma)$ depend on the adsorption strength and on the strength of the micelle-micelle and monomer-micelle osmotic interactions.

The major limitations of our aSCF model are related to its mean-field nature. The obvious requirement for the applicability of our arguments is $R_m \ll \sigma^{-1/2}$, i.e. the size of a micelle must be smaller than the average distance between grafted chains (the

³This box-like approach was applied in our first paper on polymer-surfactant association, but is not presented in this thesis. [141]

‘mesh’ size), as the correlation length of density fluctuations inside the brush is proportional to the mesh size. [17, 18] Moreover, an even stronger condition must be satisfied in order to justify the mean-field approach based on the renormalisation of the excluded-volume parameters, namely the number of micelles immobilised in a correlation volume $\sim \sigma^{-3/2}$ must be sufficiently large. As we have demonstrated in Chapter 5, the mean-field approximation works reasonably well in the coil regime, i.e. at low monomer densities. Also, the experiments in Chapter 2 and 3 demonstrate good agreement between the theoretical predictions of aSCF models for “bare” polymer brushes and experimental results for long PEO chains. Therefore, we expect that our mean-field approach utilised in the aSCF model for brushes with annealed excluded-volume interactions provides a qualitatively correct description both for the relatively sparse and fairly uniformly loaded distal region and the relatively bare and dense proximal region.

Interactions of PEO Brushes with BSA

ABSTRACT

The interaction between PEO brushes and nanocolloids (in this case BSA proteins) is investigated experimentally. The adsorption of BSA on a hydrophobic substrate with grafted PEO chains is measured with reflectometry. For short grafted chains the adsorbed amount Γ of BSA decreases continuously with increasing σ . In the case of long PEO chains, however, Γ is found to have a maximum as a function of σ . Qualitatively, the experimental dependence of Γ on σ agrees with the results of our analytical SCF model. PEO chains show no affinity for BSA in the bulk, whereas in a grafted conformation an effective attraction is observed. Some comments are made on the nature of this affinity, which is not yet fully understood.

8.1. INTRODUCTION

The prevention of protein adsorption on surfaces in contact with blood is a challenge, both from a medical and a chemical-physical point of view. Protein adsorption can result in coagulation of adsorbed blood proteins and subsequent surface-induced thrombosis. [169] Grafting or irreversible adsorption of water-soluble polymers onto the surface is a well-established method to reduce protein adsorption. [170–175] The decrease in the adsorbed amount is generally attributed to steric repulsion between the grafted hydrophilic polymer and the solvated proteins.

Due to its hydrophilicity PEO is widely used as stabilising agent; a review on the properties of PEO and its biomedical applications is given by Lee *et al.* [170] PEO is usually end-tethered to the surface through irreversible adsorption of diblock or triblock copolymers. When a hydrophilic block like PEO is chemically bound to a hydrophobic block, such as polypropylene-oxide (PPO) or an alkyl chain, the polymer density at the surface is enhanced, as the hydrophobic block is prone to adsorb strongly on a hydrophobic surface. Moreover, as desorption of the hydrophobic block from the hydrophobic surface is unfavourable, the surface density remains essentially constant, in contrast to hydrophilic homopolymer that can desorb.

In recent studies the adsorption of several proteins on a hydrophobic surface was measured as a function of PEO-PPO-PEO triblock copolymer surface density. [171,172] It was shown that an increase in surface density results in a continuous decrease in protein adsorption. It was concluded that the surface density predominantly determines the decrease in protein adsorption; the chain length was found to have little effect. [171] In a study of Prime *et al.* PEO was chemically bound to an alkyl chain and an increasing PEO length was found to strongly reduce the protein adsorption. [175] The PEO chain

length used by McPherson *et al.* [171] and by Schroën *et al.* [172] was 128 or less, and in the work of Prime *et al.* it was as low as 17 monomers. [175]

From a theoretical point of view the interaction between hydrophilic chains grafted onto a surface and nanocolloids, such as proteins, is extremely interesting. Jeon *et al.* suggested a simple model for the interaction between a substrate with terminally attached hydrophilic chains and solvated proteins. [176,177] In this model the proteins are assumed to compress the grafted layer, thus enhancing the excluded-volume interactions in the brush-like layer. The van der Waals attraction between proteins and the substrate is compared to the induced steric repulsion of the chains. An important conclusion of this model is that longer chains are more effective in suppressing the adsorption, as the van der Waals interactions between particles and the substrate decrease strongly with increasing separation distance (increasing brush height). McPherson *et al.* compared their experimental results for PEO-PPO-PEO triblock copolymers and various adsorbing proteins with results of a numerical SCF model. [171] In the nSCF model the particles are prone to adsorb on the surface and the excluded-volume interactions between the grafted chains and particles are repulsive. They conclude that the blocking of adsorption sites by grafted chains is the main mechanism for reducing protein adsorption, i.e. σ is the main parameter that controls the amount of adsorption. The influence of the chain length is reported to be marginal, in contrast to the model of Jeon *et al.* [176,177]

In the previous chapter an aSCF model for grafted chains with annealed excluded-volume interactions was presented. This model mimics the behaviour of long and densely grafted chains that can form complexes with nanocolloids. The overall adsorption per unit area in this model has a maximum as a function of σ and increases linearly with N . In contrast to the above mentioned models, our aSCF model explicitly assumes attractive interactions between the grafted chains and the complexing nanocolloids.

Although the reduction of the adsorbed amount per unit area Γ by grafting PEO chains was investigated experimentally in previous studies, the chains lengths used were relatively short. [171,175] In this chapter we investigate adsorption of bovine serum albumin (BSA), a blood protein, on PS substrates with grafted PEO chains of length 148, 445 and 700 monomers. According to the conclusions of Prime *et al.* and the model of Jeon *et al.*, the considerable length of the PEO chains should be a formidable barrier to protein adsorption. On the other hand, the work of McPherson *et al.* suggests σ to be the main factor in determining Γ . [171] Therefore, measurement of the adsorption of BSA on PS surfaces grafted with PEO chains of varying length and surface density is necessary to check the theoretical predictions of Jeon *et al.* and McPherson *et al.*

8.2. MATERIALS AND METHODS

The hydrophobic substrates were made from silicon wafers with a natural silica layer of approximately 2 nm, as determined by ellipsometry. On this surface a layer of polyvinylpyridine-polystyrene (PVP-PS) block copolymer (molar mass 21400/20700, Polymer Source Inc.) was adsorbed from a 100 ppm chloroform solution. After adsorption the wafers were rinsed for 10 sec. in chloroform to wash away excess polymer, and dried

under nitrogen. The PVP-PS layer thus formed was approximately 3 nm thick and acts as a stabiliser for the PS layer spincoated on top. The PS layer (molar mass 184K) was spincoated from a 0.1% solution in chloroform at 3000 min^{-1} . The thickness of the PS layer, including the PVP-PS layer, was approximately 8 nm. Reflectometry showed the bare PS layers to be stable in water.

For dynamic light-scattering experiments a PEO homopolymer (molar mass 445K, Pol.Lab.LTD, UK) was used. The protein used for adsorption measurements is Bovine Serum Albumin (BSA), from Sigma Chem.Co. The molar mass of BSA is approximately 66K, its iso-electric point 4.8. BSA is reported to be sigar shaped, with a radius of 3 nm and a length of 14 nm. [178]

Monolayers of PS-PEO block copolymers were prepared in a Langmuir trough in the same fashion as described in Chapter 4 and ref. 69. The Si-PS wafers were dipped through the interface (air \rightarrow water) in the usual fashion of LB-preparation. [116] The deposition on the wafer proceeded readily, a transfer ratio of 1 was usually obtained. After retraction, the LB sample was washed with water in order to remove any PEO polymer not taken up in the brush. In this manner we obtained a single PS-PEO layer adsorbed on PS. Continuous washing with water did not desorb the PS-PEO monolayer, as indicated by the stable base line in the reflectometer.

8.3. RESULTS

The interaction between PEO and BSA in the bulk has been extensively studied. [170, 179] The current opinion is that no attractive interactions between PEO and proteins are present, which facilitates, for instance, the use of PEO as a protein excluder. Abbott *et al.* concluded that the effective interaction between PEO and BSA is repulsive, although the repulsion is less than expected. [179] The hydrodynamic radius of PEO homopolymer in salt-free BSA solutions ranging from 0 to 500 ppm was measured with dynamic light scattering. No significant change in the PEO radius of gyration with respect to that in pure water was observed, indicating that in a dilute bulk solution the interactions between PEO and BSA are either repulsive or very weakly attractive of nature.

In Figure 8.1 the adsorbed amount of BSA is shown as a function of σ , for the three PEO block lengths. Curves are drawn through the data points to guide the eye. The amount of BSA adsorbed on bare PS is approximately 0.5 mg/m^2 . In the case of grafted PEO chains of 148 monomers, the adsorbed amount drops continuously with increasing grafting density. However, if long PEO chains (445 and 700 monomers) are grafted, the adsorbed amount first increases at low σ , and then it decreases again at high σ . The maximum adsorbed amount Γ_{max} seems to increase with increasing chain length. Note that for all chain lengths Γ remains finite at very high σ .

It is instructive to renormalise the results for the BSA adsorption on LB-films of short PEO chains (148 monomers) with respect to the adsorbed amount on bare PS, Γ/Γ_0 . These data are plotted in Figure 8.2 together with same renormalised amount as found for the adsorption of lysosome on PEO-PPO-PEO triblock copolymers by McPherson *et al.* [171] The PEO chain length of the triblock copolymer of McPherson is 128 monomers,

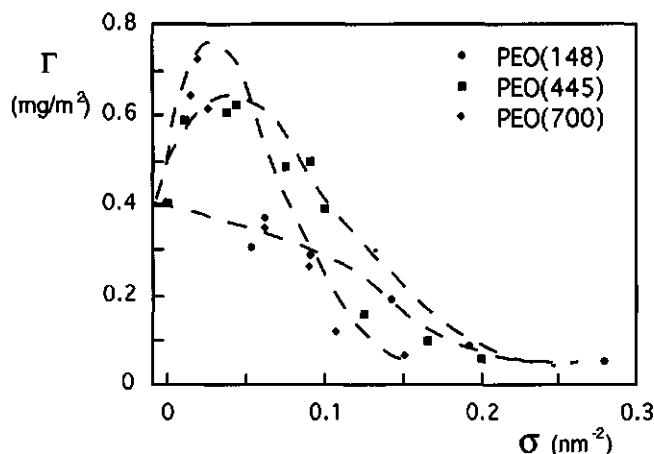


FIGURE 8.1. The adsorbed amount Γ of BSA protein as a function of the grafting density σ for three PEO lengths.

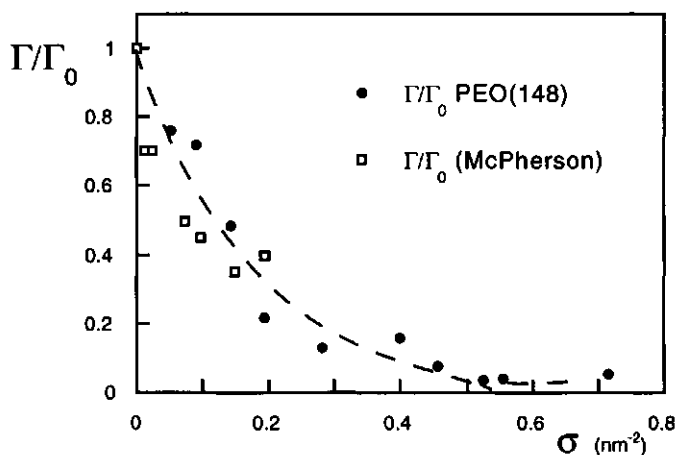


FIGURE 8.2. The ratio Γ/Γ_0 , of our results and PEO(128) from McPherson *et al.* [171]

thus comparable to our short block. A dashed curve is drawn through the data points to guide the eye. It is clear that the decrease in protein adsorption with increasing σ is approximately equivalent in both studies. Our results for the short chains thus agree with previously reported results. The results with long chains are qualitatively different though, and at variance with currently held opinions.

It is interesting to compare the maximum in the adsorbed amount of BSA (Figure 8.1) with the maximum predicted by our model for grafted chains interacting with nanocolloidal particles (see Figures 7.12 and 7.13). (We refer the reader to Chapters 5, 6 and 7 for details on the model parameters.) Qualitatively, the adsorption isotherms show the same

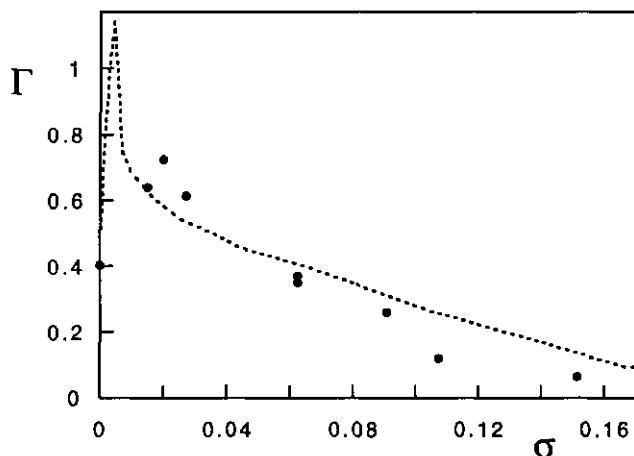


FIGURE 8.3. Total adsorbed amount Γ (in mg/m^2) as a function of σ (nm^{-2}) of BSA on a PEO brush ($N = 700$, circles) and model calculations (dashed curve). The used parameters are $\theta_b = 0.2$, $v_1 = 40$, $N_{ad} = 70$, $\Gamma_0 = 0.4$, $l = 0.25$ nm and $a = 6$ nm^2 .

trend. One feature present in the experimental PEO-BSA system but not considered in our aSCF model, however, is adsorption of particles on the hydrophobic substrate. As argued by McPherson *et al.*, the main mechanism for the decrease of adsorption with increasing σ is the decrease of accessible substrate surface. We can implement this in a crude way in our model by assuming a linear relationship between adsorption on the substrate Γ_s and the grafting density.

$$(8.1) \quad \Gamma_s = \begin{cases} \Gamma_0(1 - a\sigma) & \text{for } a\sigma \leq 1 \\ 0 & \text{for } a\sigma \geq 1 \end{cases}$$

where Γ_0 is the amount adsorbed on the bare hydrophobic substrate and the prefactor a is a measure for the size of the adsorbing particles. If the area σ^{-1} per grafted chain is equal to a then no adsorption takes place on the substrate. The total adsorption Γ now is the sum of the substrate adsorption Γ_s and adsorption Γ_b within the brush. In Figure 8.3 the experimental data for BSA adsorption for the longest PEO chains (dots) are plotted together with $\Gamma_s + \Gamma_b$ as calculated theoretically (dashed curve). We stress that the inserted values of the excluded-volume parameters and adsorption strength have no direct quantitative meaning. It is evident, however, that both the experimental and the calculated adsorption follow the same trend.

8.4. DISCUSSION AND CONCLUSIONS

In this chapter we have investigated the adsorption of BSA on a hydrophobic substrate with grafted PEO chains. It is observed that there is a continuous decrease in Γ with increasing σ for short chains, but a distinct maximum in Γ for long chains. The latter feature is a novel result: so far, all experimental studies of protein adsorption on

surfaces with grafted PEO have used chain lengths of at most 128 monomers, and only a continuous decrease of Γ with increasing σ is reported. Theoretical models for such systems have emphasised the repulsive nature of protein-PEO interactions, so that they cannot cope with the maximum as found in this study.

Our aSCF model for brushes with annealed excluded-volume interactions, presented in Chapter 7, provides an interpretation for the maximum in Γ as experimentally found for long, grafted PEO chains. Our model explicitly accounts for an effective attraction between the grafted chains and the adsorbing nanocolloid. The fact that experimentally such a maximum also occurs, brings us to the conclusion that there is indeed some attraction between grafted PEO and BSA.

The idea that grafted PEO chains may have affinity for proteins is confirmed by analysing the results for the short grafted chains, both ours and those of McPherson *et al.* (see Figure 8.2). In the case that the PEO-protein interaction is solely repulsive, the net protein adsorption is expected to be zero at high σ , as the steric hindrance of the grafted chains is too high a barrier for the proteins to reach the substrate. This conclusion is validated by Single-Chain Mean-Field-Theory calculations. [171] Experimentally, however, a considerable residual adsorption is found at high σ . McPherson *et al.* attribute the adsorption at high grafting densities to inhomogeneities in the coverage of the substrate by polymer, and dismiss any attractive interactions between PEO and the proteins. [171] However, the existence of such inhomogeneities is not substantiated. In addition, the maximum in Γ in the case of long chains clearly contradicts the notion that the interaction between the grafted chains and proteins solely consists of steric repulsion.

One may wonder what the nature is of these attractive interactions between grafted PEO and BSA. Dynamic light-scattering experiments suggest that there are no attractive interactions between PEO and BSA in a dilute solution of free chains, but grafted chains appear to bind BSA. The surface of BSA consists of hydrophobic and hydrophilic (charged) areas, similar to that of a micelle. [178] It is therefore reasonable to suggest that the same enthalpic interactions are present between PEO and BSA as in the case of PEO-SDS complexes, stemming from a (weak) attractive hydrophobic interaction between PEO and the micellar surface. In a bulk solution this attractive interaction must be compared to the loss in conformational entropy of the polymer upon adsorption: this loss could be too large for appreciable adsorption to occur. However, if the PEO chains are grafted the conformational entropy of a chain is significantly reduced by the presence of the grafting substrate and neighbouring chains. Therefore, complex formation might be favourable for such restricted chains, resulting in a maximum in Γ as a function of σ .

This hypothesis is supported by recent force-distance profiles of (short) PEO-brushes and proteins. [180] In these measurements attractive interactions between PEO and proteins are observed under high compression. In another study BSA proteins were found to diffuse spontaneously into a close-packed bilayer of C₁₂EO₈. [181] Again, this suggests that confined PEO-chains exhibit attractive interactions with BSA.

A different explanation for the maximum in Γ , without assuming attractive interactions between PEO and BSA, is that the proteins are kinetically 'trapped' in the grafted PEO chains. Such entrapment may occur in the case of long grafted PEO chains, but

is unlikely to occur in short PEO chains. This would explain the length dependence in Figure 8.1. Also, since the proteins are less prone to diffuse into a densely grafted layer this argument also explains the maximum in $\Gamma(\sigma)$. However, it is improbable that the BSA proteins should spontaneously diffuse into a grafted PEO layer when the PEO-BSA interactions are purely repulsive. Moreover, if the proteins are kinetically trapped within the layer, then the adsorbed amount should decrease in time during washing with pure solvent. This was checked by adsorbing BSA at a grafting density near the maximum and washing the cell with pure water. The reflectivity signal, and thus adsorbed amount, remained constant during washing for several hours. This suggests that the interactions between grafted PEO and BSA are indeed attractive in nature, and that the proteins are not kinetically trapped in the PEO brush.

ACKNOWLEDGEMENTS

We thank Dick Gage and Willem Norde for the many useful discussions on polymer-protein interactions.

Complexation of Polyelectrolytes with Nanocolloids

ABSTRACT

In this chapter our analysis of polymers complexing with several particles is extended to complexation of quenched polyelectrolytes with oppositely charged nanocolloids. In our model complexation is determined by a balance between the loss of conformational entropy of the adsorbed strand and a decrease in electrostatic energy, both of the particle and the chain. Generally speaking, complexation is induced by a decrease in ionic strength. The nature of the transition from a bare to a fully complexed chain (first-order or continuous) and the conformation of the latter (globular or swollen) depends mainly on the ratio of the charge density σ_0 of the particle and the charge density α of the polyelectrolyte (defined as charge per unit area or unit length, respectively). If $\alpha/\sigma_0 \sim 1$, a first-order phase transition with decreasing ionic strength from a bare and swollen coil to an insoluble globule is predicted. In contrast, if $\alpha/\sigma_0 \gg 1$, the transition from a swollen coil to a soluble complex is predicted to be continuous. Experimental data, in which both kinds of transitions are reported, support our numerical results.

9.1. INTRODUCTION

Complexation of solvated polyelectrolytes with charged nanocolloids, such as proteins, micelles or liposomes, can have serious consequences for the stability of such solutions. If the interactions between two polyelectrolyte chains or between a polyelectrolyte chain and particle are attractive, coacervation can result in insoluble complexes and subsequent phase separation. [182] Solutions containing polyelectrolytes and charged particles are widely used in food products, drugs [183] and applied for isolation of specific proteins from solution via coacervation. [16] Insight in the physics underlying complex coacervation is therefore not only valuable from an academic point of view, but is also of interest for various practical applications.

Complex coacervation of a strongly charged polycation (PDMDAAC) with mixed micelles (consisting of anionic SDS and a neutral triton surfactant) was investigated experimentally by Dubin *et al.* [187, 188] Phase separation of complexed polyelectrolytes and micelles was observed in certain regimes of micellar charge density and ionic strength of the solution, whereas in other charge density regimes the coacervate remained soluble. [187] The results suggested that; as the micellar charge density approaches a value critical for complex coacervation, the polyelectrolyte is continuously loaded with micelles, and the coil radius decreases. In a recent paper, however, Miura *et al.* report an abrupt transition from a bare chain to a non-soluble coacervate. [204] The charge density σ of the mixed micelle at which complexation occurred was found to scale with the square root of

the ionic strength I by several authors. [187,188,204] Such a dependence is characteristic for coacervation processes in which electrostatic interactions are the driving force.

Complex coacervation is a powerful tool to separate specific proteins from a solution containing various protein species in a controlled manner via precipitation. In a recent paper Mattison *et al.* investigated complexation of PDMDAAC and bovine serum albumine (BSA) as a function of the pH and ionic strength. [16] As BSA is amphoteric, its charge density is pH dependent. A phase diagram was obtained in which the ionic strength at which soluble and non-soluble complexes form is plotted as a function of pH, or equivalently, of the overall charge density on BSA. A remarkable result is that complexation may occur when the overall net charge on the BSA is positive, that is, has the same sign as that of PDMDAAC. In the regime of like (overall) charges the $I^{1/2}$ dependence for the onset of complexation was also observed. This power dependence suggests that, although complexation seems to be predominantly determined by electrostatic interactions, it is not necessarily the net charge on the particle that determines the outcome; local charge effects may also play an important role.

The formation of polyelectrolyte-particle complexes has been investigated theoretically with several models. One of the earliest theoretical studies is that of Tainaka, who presented a model for the complexation of a polycation and polyanion with identical charge densities, with or without counterions. [189,190] It was concluded that in the absence of counterions coacervation readily takes place, but the presence of counterions strongly suppresses coacervation. It must be remarked that Tainaka's model is valid for two flexible polyions and does not consider the complexation of a polyion with several small particles. The binding of a flexible, weakly charged polycation to a rodlike, highly charged polyanion was examined analytically by Odijk. [191] Collapse of the polycation onto the polyanion was found to depend strongly on the ionic strength: a slight decrease in ionic strength results in a strong decrease in thickness of the adsorbed layer, which indicates complexation. Although elegant, Odijk's model has the disadvantage that it does not predict the onset of complexation of a long polyelectrolyte with small spherical particles, nor the overall conformation of such a complex.

Recently Haronska *et al.* considered the adsorption of a polyelectrolyte on an oppositely charged spherical particle using a nSCF model. [192] In their model the monomer density distribution as a function of the distance to the particle surface is determined for a given ionic strength. Comparison of the predicted results with experimental data shows that the dependence of the ionic strength at complexation on the charge density of the chain is too weak. As the adsorption of chains on a single particle is examined, this model is not suitable to predict the conformation of a polyelectrolyte with several complexed particles. Moreover, the numerical calculations do not facilitate a clear and intuitive understanding of the process of complexation. The same holds for Monte Carlo studies on the interactions between polyelectrolytes and micelles. [193-195]

In the previous chapters we presented a mean-field model for neutral polymers subject to annealed excluded-volume interactions. At low monomer densities our model mimics the behaviour of single polymer chains complexed with charged nanocolloids in a dilute

bulk phase, at (locally) high monomer densities it mimics the interactions between polymers and nanocolloids in semi-dilute solutions, bad solvents or in polymer brushes. In this chapter we extend our model to polyelectrolyte chains with annealed excluded-volume interactions. This models the complexation of polyelectrolytes and oppositely charged particles. We analyse the phase behaviour of such solutions as a function of the charge density of the particle, that of the chain, and the ionic strength. The validity of our approach is evaluated by comparing our numerical predictions for the predicted onset of complexation and overall conformation with experimental data for polyelectrolyte-protein, polyelectrolyte-micelle and polyelectrolyte-dendrimer coacervation found in the literature.

9.2. MODEL

We consider a solution of quasi-infinitely long and flexible polyelectrolyte chains consisting of N monomers of length l , which is again taken as the unit length, and density ρ . The polyelectrolyte is quenched; the charge density α is constant and defined as the fraction of dissociated monomers, distributed uniformly along the chain. All energies are expressed in unit $k_B T$, all charge densities in the number of unit charges e per unit length (for a chain) or unit area (for a particle). The solvent is considered to be good for both charged and neutral monomers. We again employ the volume approximation as described in section 6.2, in which the coil conformation under good solvent conditions is characterised by $\rho \approx 0$. The chains are immersed in a solution of ionic strength I , characterised by the Debye length κ^{-1} . As the ionic strength in most experimental applications is moderate to high, we limit ourselves to the regime in which the bare polyelectrolyte has a coil conformation. This prerequisite implies that the electrostatic interactions between charged monomers may effectively be modelled by osmotic interactions, similar to the SB-regime discussed in Chapter 4. The rod-like limit for vanishing ionic strength and high charge density is therefore not considered. [196, 197] This entails that the average distance between two adjacent charges on the chain α^{-1} is at least of order of the screening length κ^{-1} . Consequently, it must be checked whether $\alpha/\kappa \lesssim 1$ in the regime in which complexation occurs. We remark that the charge density on the chain cannot increase indefinitely, but is limited by the process of charge condensation. [198, 199] Accordingly, it follows that $\alpha^{-1} \geq l_B/l$, where l_B denotes the Bjerrum length (7 Å in water at 298 °K).

Besides polyelectrolyte chains and inert salt, the solution also contains nanocolloids that are oppositely charged to the polyelectrolytes. As in previous chapters, we use a grand canonical approach; the polyelectrolyte chains are in contact with an infinite reservoir of particles. Effects resulting from bridging or incomplete coverage, due to unfavourable mixing ratio's, are therefore not considered. The equilibrium conformation of a particle, be it a protein, micelle or liposome, is spherical and its charge density is quenched. The size of a particle is small compared to the overall coil size and large compared to that of a monomer. We stress that the spherical conformation of the particle is stable; we do not consider the possibility of denaturation of a protein or collapse of a

liposome as a result of interactions with polyelectrolytes. [183] Experimental data relating to the conservation of enzymatic activity of proteins upon complexation show this to be a reasonable assumption. [184–186]

When complexation between a long polyelectrolyte chain and oppositely charged particles occurs, a necklace-like structure is the result, in which the intrinsic properties of the “beads” (complexes) differ from those of the chain (monomers). In the volume approximation the same expression for the free energy density can be used as in Chapter 6, i.e. Eq.(6.3). We express Eq.(6.3), however, in terms of $\tau \equiv 1 - \theta$, instead of θ . In other words, we consider the fraction of *uncomplexed* monomers τ instead of the fraction of complexed monomers θ . The reason for this is clarified further in this section. The equivalent expression in terms of τ is

$$(9.1) \quad f(\rho, \tau) = \frac{\rho}{N} \ln \rho - \rho s(\tau) + \rho \tau u + f_{os}(\rho, \tau)$$

where u now denotes the effective change in free energy upon ‘unloading’ of a monomer. We again neglect the first term, which accounts for the translational entropy of the polyelectrolyte as a whole. The second term, the translational entropy $s(\tau)$, given by to Eq.(5.8), provided $1 - \tau$ is inserted for θ .

The third term is the effective gain in free energy as a monomer changes its conformation from loaded to bare. In the case of complexation of a polyelectrolyte strand with an oppositely charged particle this term is assumed to consist effectively of three contributions: (i) the change in the (mean-field) electrostatic energy as a strand of length N_{ad} with $N_{ad}\alpha$ charges adsorbs on a particle of radius R_p with q charges; (ii) the loss of translational entropy of a complexed particle; and (iii) the loss of conformational entropy of N_{ad} adsorbed monomers. We do not take any other possible interactions into account, such as hydrophobic interactions between the adsorbed monomers and the particle.

We start with the first contribution to u . The complexation process effectively amounts to the loss of $N_{ad}\alpha$ charges on a flexible strand of length N_{ad} and the loss of q charges on a sphere of radius R_p . However, depending on the charge density ratio, the resulting complex is either neutral or has an excess charge. Therefore, the cost of placing $q_{ex} = N_{ad}\alpha - q$ charges on a sphere of radius R_p must also be taken into account.¹ Furthermore, when two charged particles form a complex with an effectively lower charge density, the counterions in the double layers are (partially) released into the bulk solution. This counterion release, however, does not change the free energy of the system. This can be understood if we imagine that two charged particles with equal charge densities of opposite sign are formed from two identical neutral particles in a bulk solution of constant ionic strength. According to the Poisson-Boltzmann expression, the loss in entropy due to localisation of counterions in both double layers is balanced by the gain in electrostatic energy. [201] The effective change in electrostatic free energy in the system is entirely due to formation of the charge densities on both particles. Therefore, if we want to evaluate

¹We neglect the effective increase in the radius of a complexed particle, i.e. $\Delta r \approx (N_{ad}/4\pi R_p^2)$.

the overall electrostatic contribution to u , only the effective changes in surface charge densities have to be considered.

To simplify matters, we assume that the charging of a polyelectrolyte strand is similar to the charging of a rod of length N_{ad} , with a diameter equal to unity and charge density α/π . As the overall monomer density in the volume approximation is approximately zero in the coil conformation, intramolecular overlap of double layers is negligible. We also neglect any dependence of the electrostatic energy on the curvature of the chain; this is reasonable, provided the Debye length κ^{-1} does not significantly exceed the distance α^{-1} between charges on the chain.

The simple Gouy-Chapman model is used for the dependence between surface charge and potential.

$$(9.2) \quad F_e = \pi N_{ad} \int_0^{\sigma_0} \Psi_0(\sigma'_0) d\sigma'_0 = \frac{N_{ad} \alpha^2}{2\pi\epsilon\kappa}$$

where we have used the Debye-Huckel expression for planar surfaces for the surface potential, i.e. $\Psi_0(\sigma_0) = \sigma_0/\epsilon\kappa$. We remark that the exact solution of the Poisson-Boltzmann expression for cylindrical symmetry results in a numerical correction of the above expression, which lowers F_e . [201] As expected, in this simple approach the energy involved in charging a polyelectrolyte strand scales linearly with its length, quadratically with the charge density and inversely with κ .

The surface charge density of solvated particles of charge q and radius R_p is simply $\sigma_0 = q/4\pi R_p^2$. We estimate the electrostatic energy necessary for formation of this charge density using the same approach. This gives us

$$(9.3) \quad F_e = 4\pi R_p^2 \int_0^{\sigma_0} \Psi_0(\sigma'_0) d\sigma'_0 = \frac{q^2}{8\pi\epsilon R_p^2 \kappa}$$

where again the Debye-Huckel expression is applied. Upon complex formation charges on the particle are (partially) neutralised by charges on the polyelectrolyte. The total change in electrostatic energy upon complexation per monomer is therefore

$$(9.4) \quad \Delta f_e = \left(\frac{q_{ex}^2 - q^2}{8\pi\epsilon R_p^2 \kappa N_{ad}} - \frac{\alpha^2}{2\pi\epsilon\kappa} \right)$$

Upon unloading, the change in electrostatic energy is evidently $-\Delta f_e$.

The second contribution to u is the gain in translational entropy of the complexed particles upon unloading. We express the chemical potential of the particles in the bulk as $\mu_p = \mu_p^0 + \ln \rho_p$, as counterion condensation is not taken into account. As μ_p^0 is expected to remain constant upon complexation, the gain in translational entropy, expressed per monomer, is simply $N_{ad}^{-1} \ln \rho_p$.

The third contribution to u is the entropic cost involved in localisation of N_{ad} monomers on a particle surface. Provided the particle is large compared to a monomer, this cost is similar to the cost of adsorption of a polymer on a planar surface. It is well known

that adsorption of a strand of length N_{ad} requires a critical adsorption energy of order $N_{ad}k_B T$.² We thus find for the effective change in free energy per monomer upon *unloading*

$$(9.5) \quad u = \left(\frac{q^2 - q_{ex}^2}{8\pi\epsilon R_p^2 N_{ad}\kappa} + \frac{\alpha^2}{2\pi\epsilon\kappa} \right) + \frac{\ln \rho_p}{N_{ad}} - \epsilon_{cri}$$

where the critical adsorption energy per monomer is denoted by ϵ_{cri} , introduced in Eq.(5.5) in Chapter 5. According to Eq.(9.5), the adsorption energy per monomer is a balance between the entropic cost of localising a polyelectrolyte strand on a particle, and the electrostatic gain of such a localisation. Roughly speaking, for a given polyelectrolyte such a localisation is favourable in the case of small and highly charged particles at low ionic strength and high particle density, whereas it is unfavourable for lowly charged, large particles at high ionic strength and low particle density.

We remark that the above expression for u is only valid in the regime of $\alpha \sim 1$. If $\alpha \ll 1$, the formation of a complex may result in a corona of loops around the particle, formed by neutral monomers. The repulsive steric interactions between such loops may significantly alter Eq.(9.5). As such interactions are not taken into account, we restrict ourselves to $\alpha \sim 1$.

We now turn towards the last term in Eq.(9.1), $f_{os}(\rho, \tau)$. This osmotic contribution is again a sum over the particle densities and the concurrent virial coefficients, as expressed in Eq.(6.5). As was shown in the previous chapters, the interplay of the osmotic and the adsorption term in Eq.(9.1) determines the phase behaviour of the system in the case that the monomer density is (locally) high. Therefore, care must be taken to ensure that the osmotic interactions are treated correctly in the case of complexes of polyelectrolytes and charged particles.

We must first realise that the effective charge density of the polyelectrolytes decreases upon complexation, or equivalently, increases with increasing τ , as

$$(9.6) \quad \begin{aligned} \alpha_{eff}(\tau) &= \alpha\tau + \frac{q_{ex}(1-\tau)}{N_{ad}} \\ &= \alpha - \frac{q(1-\tau)}{N_{ad}} \\ &< \alpha \end{aligned} \quad \text{for } 0 \leq \tau < 1$$

where we use the definition $q_{ex} \equiv N_{ad}\alpha - q$. As electrostatic interactions between monomers of like charge strongly enhance the osmotic interactions, the effective strength of osmotic interactions at a given ionic strength is expected to decrease with increasing

²The critical adsorption energy of an ideal chain in a mean-field lattice model is given by $-\ln(1 - \lambda_1)$, where λ_1^{-1} is the coordination number of the lattice. For a cubic lattice the critical adsorption energy is approximately $0.2 k_B T$, for a tetrahedral lattice $0.3 k_B T$. There are, however, no exact analytical expressions for the critical adsorption energy in a 3D continuum model. [136] We remark that additional interactions to u , such as hydrophobic interactions or chain stiffness, may result in an effective shift in

loading. This is the reason that Eq.(9.1) is expressed in terms of τ , the fraction of unloaded monomers, instead of θ , the fraction of loaded monomers. As it can be expected that $v'_{eff}(\tau) > 0$ for $0 < \tau < 1$, the same approach may be employed as in Chapter 6, where $v'_{eff}(\theta) > 0$ for $0 < \theta < 1$.

To keep notation simple, we maintain the convention that v_0 denotes the second virial coefficient of two monomers, v_1 denotes the renormalised virial coefficient of two complexes and v_2 denotes the renormalised cross-term. Thus, the effective excluded-volume parameter in terms of τ is (compare with Eq.(5.13))

$$(9.7) \quad v_{eff}(\tau) = v_1(1 - \tau)^2 + v_0\tau^2 + 2v_2\tau(1 - \tau)$$

The monomer-monomer virial coefficient consists of two contributions: a bare steric contribution and an electrostatic contribution. In a first approximation we can set the average electrostatic potential between two monomers equal to zero at distances larger than κ^{-1} , and consider the interaction to be unscreened at distances shorter than κ^{-1} . Inserting the hard-wall repulsion U_{hwr} and the unscreened electrostatic potential $U(r) = \alpha^2/\epsilon r$ in Eq.(5.19) and expanding the exponent, we can write the mean monomeric virial coefficient as

$$(9.8) \quad v_0 \approx \frac{4\pi}{3} \left(1 + \frac{\alpha^2}{\epsilon \kappa^2} \right)$$

where the first term is the bare steric contribution and the second the electrostatic repulsion. If we set α zero in the above expression, we retrieve the definition for v_0 used in Chapter 5, i.e. the monomeric virial coefficient for a neutral polymer in a good solvent. Thus, the solvent is good for both neutral and charged monomers.

The renormalised complex-complex virial coefficient v_1 is determined by a sum of interactions. Naturally, at center-to-center distances smaller than $2(R_p + \delta)$ a hard-wall, or Born repulsion is found. The parameter δ characterises the range of the Born repulsion, and is of atomic length scale. [200] At larger distances the interaction potential is a sum of two contributions: an attractive van der Waals contribution and a repulsive electrostatic potential resulting from the excess charge on the complexes.

$$(9.9) \quad U(r) = \begin{cases} U_{hwr} & \text{if } r \leq R_p + \delta \\ U_{vdW}(r) + U_{el}(r) & \text{if } r > R_p + \delta \end{cases}$$

To proceed, we first consider the van der Waals interactions for $r > R_p + \delta$. The Hamaker expression for two spheres is [202]

$$(9.10) \quad U_{vdW}(r) = -\frac{A_H}{6} \left(\frac{R_p^2}{r^2 - R_p^2} + \frac{R_p^2}{r^2} + 2 \ln \left(1 - \frac{R_p^2}{r^2} \right) \right)$$

where A_H is the Hamaker constant for the particles (in units of $k_B T$), which characterises the strength of the van der Waals interactions between the particles. Note that if $\delta = 0$ $U_{vdW}(R_p) = -\infty$, which is physically unrealistic. This is the reason for introducing of a small but finite value of δ .

In the regime $\kappa R_p \lesssim 5$ an approximate expression of Verweij and Overbeek for the electrostatic interaction between the complexes with an excess charge q_{ex} is used. [203]

$$(9.11) \quad U_{el}(r) = \frac{q_{ex}^2}{8\pi\epsilon\kappa^2 R_p^2} e^{-\kappa(r-R_p)}$$

Insertion of Eqs.(9.10) and (9.11) into (5.19) and multiplication by N_{ad}^{-2} gives v_1 for a given set of R_p, A_H, q_{ex} and κ . It is convenient to define $r' \equiv r - R_p$. The resulting expression for v_1 is

$$(9.12) \quad v_1 = \frac{8\pi(R_p + \delta)^3}{3N_{ad}^2} + \frac{2\pi}{N_{ad}^2} \int_{\delta}^{\infty} (R_p + r')^2 \left(1 - \left(\frac{2R_p r' + r'^2}{(R_p + r')^2} \right)^{\frac{A_H}{3}} \right) \exp \left(\frac{A_H R_p^2}{6} \left(\frac{1}{2R_p r' + r'^2} + \frac{1}{(r' + R_p)^2} \right) - \mathbb{D} e^{-\kappa r'} \right) dr'$$

where we have defined $\mathbb{D} \equiv q_{ex}^2/8\pi\epsilon\kappa^2 R_p^2$. It is useful further to renormalise r' with respect to R_p , i.e. $\tilde{r} \equiv r' R_p^{-1}$. If the limit of small \tilde{r} is taken, the integrand reduces to

$$(9.13) \quad v_1 \approx \frac{V_p}{N_{ad}^2} \left[2(1 + \delta)^3 + \frac{1}{2} \int_{\delta/R_p}^{\infty} \left(1 - 2\tilde{r}^{\frac{A_H}{3}} e^{\frac{A_H}{12} - \mathbb{D}} \right) d\tilde{r} \right]$$

It is clear that if $\delta/R_p \rightarrow 0$ this term becomes highly negative for any value of \mathbb{D} , due to the non-zero value of A_H .³ This implies that, irrespective of the excess charge on the particles and the ionic strength of the solution, the second virial coefficient would be negative, i.e. the particles always attract each other. This contradicts the general experience that colloidal solutions of charged particles are stable with respect to aggregation, provided the charge density of the particles is relatively high and the ionic strength relatively low.

This paradoxal situation has been resolved around 1940 by Deryagin, Landau, Verwey and Overbeek, and forms the heart of the classic DLVO-theory. In Figure 9.1 the potential $U(r')$, given by Eq.(9.9), is plotted for a given set of parameters and two ionic strengths. We remind the reader that the distance between the surfaces of the particles is $2r' = 2(r - R_p)$. It is clear that, as r' approaches zero, the potential $U(r')$ becomes highly negative. However, a maximum U_{max} is present at a certain distance r'_{max} . This maximum determines whether the thermodynamically stable conformation of aggregated particles ($r' \approx 0$) is reached within a reasonable time-limit, which is the case at high ionic strength where u_{max} is small or the maximum is absent (e.g. $\kappa = 0.3$ in Figure 9.1). In this case the binary virial coefficient is indeed negative. In the case of low ionic strength ($\kappa = 0.1$ in Figure 9.1) or higher charge densities (not shown) the particles are kinetically stabilised against aggregation by the maximum U_{max} in the interaction potential, provided the height of this barrier is high enough. The effective interactions between the

³The negative value of v_1 is obvious when the identity $e^x = \sum_{n=0}^{\infty} \frac{x^n}{n!}$ is used. The integrand in Eq.(9.12) then becomes $1 - \sum_{n=0}^{\infty} \frac{2e^{-\mathbb{D}}}{n!} \left(\frac{A_H}{12} \right)^n \tilde{r}^{\frac{A_H}{3}-n}$, which diverges as $\tilde{r} \rightarrow 0$.

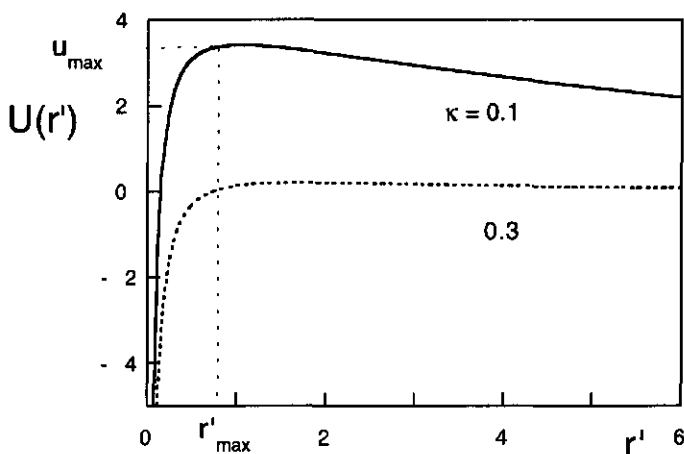


FIGURE 9.1. The interaction potential $U(r')$ between two nanocolloids according to Eq.(9.9) for two ionic strengths. Parameters: $q_{ex} = 5$, $A_H = 2$, $\epsilon = 1$, $\delta = 0$ and $R_p = 5$.

particles in this regime are repulsive and an effective positive binary virial coefficient is the result. A negative value for v_1 is found if $U_{max} \lesssim 1$, a positive value if $U_{max} \gg 1$. The position and the value of U_{max} are determined by setting the derivative of U with respect to r' zero. At small distances between the particles we can approximate U_{vdW} in Eq.(9.10) as $-A_H R_p / 12r'$. It follows that

$$(9.14) \quad r'^2_{max} e^{-\kappa r'_{max}} = \frac{A_H R_p}{12\kappa D}$$

If we insert this into the expression for the potential energy, Eq.(9.9), we find

$$(9.15) \quad U_{max} \equiv U(r'_{max}) = \frac{A_H R_p}{12r'_{max}} \left(\frac{1}{r'_{max}\kappa} - 1 \right)$$

It is clear that if $\kappa^{-1} = r'_{max}$ the height of the barrier is zero, and aggregation of complexes can occur readily. When $\kappa^{-1} \gg r'_{max}$, U_{max} is of the order of several $k_B T$, and the complexes are stabilised kinetically. Following the DLVO theory, a 'critical' ionic strength κ_c is defined for a given q_{ex} , R_p and A_H at which U_{max} equals zero. Above this ionic strength the complexes are considered not to be stabilised kinetically. [203] Inserting $\kappa_c r'_{max} = 1$ into Eq.(9.14), this critical ionic strength is given as

$$(9.16) \quad \kappa_c = \left(\frac{3q_{ex}^2}{2\pi\epsilon\epsilon_0 R_p^3 A_H} \right)^{1/3} \approx \frac{\sigma_{ex}^{2/3}}{A_H^{1/3} R_p^{1/3}}$$

It is determined by a balance of the excess charge density, the particle size and the Hamaker constant. In our model we now define v_1 as

$$(9.17) \quad v_1 = \begin{cases} \frac{2\pi}{N_{ad}^2} \int_{R_p+r'_{max}}^{\infty} r^2 (1 - e^{-U(r)}) dr & \text{if } \kappa < \kappa_c \\ \sim \frac{-R_p^3}{N_{ad}^2} & \text{if } \kappa \geq \kappa_c \end{cases}$$

where $U(r)$ is given by Eqs.(9.10) and (9.11). Using this approximation v_1 jumps from a positive to a negative value at κ_c , which is also illustrated in Figure 9.2. This may appear physically unrealistic, but the root of the problem lies in the definition of colloidal stability, i.e. the relationship between U_{max} and the effective virial coefficients. For colloidal solutions with an ionic strength close to κ_c , the second virial coefficient of the particles depends on the time-scale of the performed measurements. On short time-scales a solution may appear stable against aggregation, corresponding to a positive virial coefficient. On long time-scales, however, aggregation takes place, which implies a negative virial coefficient. Thus, the jump in v_1 may be identified with the experimental regime in which the virial coefficient is time-dependent.

We also remark that in Chapters 5, 6 and 7 we have implicitly assumed that $U_{max} \gg 1$, i.e. the thermodynamically stable state (aggregated complexes) is not considered. This is reasonable as the complexes are stabilised by their charge, and complexation with neutral polymers under influence of hydrophobic interactions does not significantly alter the charge density on the particles. Roughly speaking, if the particles are stable in solution, they should also be stable when complexed with a neutral chain. In this chapter, however, complexation explicitly changes the charge density on the complexed particle, and the overall contribution of both electrostatic and van der Waals interactions to the effective virial coefficients must be taken into account.

Finally, we consider the interaction between a monomer and a complex. Again the interaction potential at $r \geq R_p$ consists of an attractive van der Waals term, an electrostatic part and a hard-wall contribution. The van der Waals attraction between a single monomer and a complex, however, is small and can be neglected. We linearise the electrostatic contribution, and the result is

$$(9.18) \quad \begin{aligned} v_2 &= \frac{4\pi R_p^3}{3N_{ad}} + \frac{2\pi}{N_{ad}} \int_{R_p}^{\infty} r^2 \left(\frac{\alpha q_{ex} R_p}{4\pi\epsilon r} \right) e^{-\kappa(r-R_p)} dr \\ &= \frac{4\pi R_p^3}{3N_{ad}} + \mathbb{E} (R_p^2 \kappa^{-1} + R_p \kappa^{-2}) \end{aligned}$$

where $\mathbb{E} \equiv \alpha q_{ex} / \epsilon R_p^2 N_{ad}$. If the excess and monomer charge are of opposite sign, $\mathbb{E} < 0$ and the virial coefficient may change from a positive to negative value with decreasing κ or increasing q_{ex} . The ionic strength below which the interaction changes from repulsive to attractive is $\kappa \lesssim \alpha q_{ex} / \epsilon R_p^3$ in the regime $R_p \gg \kappa^{-1}$. If the excess and monomer charge are of the same sign then the virial coefficient increases with decreasing κ or increasing q_{ex} , as expected.

From the above discussion, it can be deduced that the osmotic interactions in a bare polyelectrolyte chain are repulsive ($v_0 > 0$, see Eq.(9.8)) and can decrease strongly in

strength with increasing loading. The value of v_1 can even become negative at high ionic strengths and low excess charge densities, which implies that the binary interactions between complexes are attractive (see Eq.(9.17)). At total loading, therefore, the polyelectrolyte complex may have a globular conformation. As we have seen in Chapter 6, the density in a globule is determined by a balance between attractive binary and repulsive ternary interactions. As ternary interactions are only of importance at high degrees of loading, the only relevant third-order osmotic interaction is that of complexed monomers. Following Chapter 6 we again denote the third-order virial coefficient by w , which is set unity by default. All other ternary interactions are neglected.

We have now discussed all relevant parameters in our model except N_{ad} . In previous chapters N_{ad} was assumed to be a constant and independent of other parameters. This does not appear to be a reasonable assumption in the case of polyelectrolytes complexing with oppositely charged, nanocolloidal particles. In this case q_{ex} depends explicitly on N_{ad} , and (partially) determines the strength of the osmotic interactions. We therefore assume that the number of monomers complexed with a particle is determined by a minimum in the free energy of formation of a single complex.⁴ Thus, we estimate N_{ad} by minimising $N_{ad}u$ with respect to N_{ad} . This results in

$$(9.19) \quad \frac{N_{ad}\alpha^2}{4\pi\epsilon R_p^2\kappa} - \frac{\alpha q}{4\pi\epsilon R_p^2\kappa} - \frac{2\alpha^2}{\pi\epsilon\kappa} + \epsilon_{cri} = 0$$

or,

$$(9.20) \quad N_{ad} = 4\pi R_p^2 \left(\frac{\sigma_0}{\alpha} + \frac{2}{\pi} - \frac{\epsilon_{cri}\epsilon\kappa}{\alpha^2} \right)$$

Using this approach, two asymptotic regimes for N_{ad} appear: if the charge density on the particle is low, i.e. $\sigma_0/\alpha \ll 1$, then N_{ad} is independent of σ_0 and scales proportional to R_p^2 . This entails that for a given α the number of complexed monomers is proportional to the area of the particle. The excess charge density σ_{ex} in this regime, $\sigma_{ex} \approx 2\alpha/\pi - \epsilon_{cri}\epsilon\kappa/\alpha$, is predominantly determined by α . If, however, $\sigma_0/\alpha \gg 1$, then N_{ad} approximately equals q/α and all charges on the particle are effectively neutralised ($\sigma_{ex} \approx 0$).

As in our model $v_{eff}(\tau) > 0$ and $\frac{\partial \rho}{\partial \tau} < 0$ for $0 < \tau < 1$, the same conditions are obeyed as in Chapter 6, that is, τ is a single-valued function of ρ and its equilibrium value is obtained by minimising f in Eq.(9.1) with respect to τ . Using Eq.(6.12) the monomer density is given as

⁴A formally more correct approach would be by minimising $f(\rho, \tau)$, i.e. Eq.(9.1), with respect to both τ and N_{ad} . This, however, yields several terms proportional to N_{ad}^{-2} and N_{ad}^{-3} . If such terms are neglected, Eq.(9.19) is obtained.

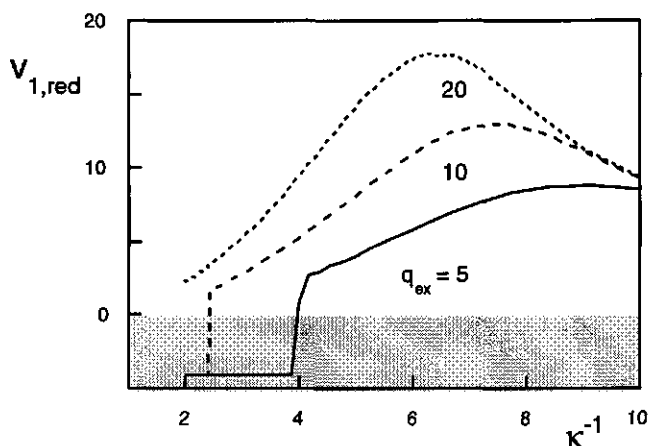


FIGURE 9.2. The reduced v_1 as a function of κ^{-1} for three values of q_{ex} , other values are $A_H = 2$, $\epsilon = 1$ and $R_p = 5$. The shaded area denotes the regime in which $v_1 < 0$.

$$(9.21) \quad \rho = -\frac{(s'(\tau_b) - s'(\tau))}{v'_{eff}(\tau)}$$

where $s'(\tau) \equiv ds(\tau)/d\tau$ and $s'(\tau_b)$ is the value of $s'(\tau)$ in τ_b . Here, τ_b is defined as

$$(9.22) \quad u = \frac{s'(\tau_b)}{N_{ad}} = -\ln \frac{N_{ad}\tau_b}{N_{ad}\tau_b + (1 - \tau_b)} + \frac{1}{N_{ad}} \ln \frac{1 - \tau_b}{N_{ad}\tau_b + (1 - \tau_b)}$$

9.3. RESULTS

9.3.1. Separate parameters

We start by examining the behaviour of v_1 , given by Eq.(9.17), for a fixed excess charge q_{ex} as a function of the ionic strength. We define a reduced parameter $v_{1,red}$ by dividing v_1 , given by Eq.(9.17), by either $8\pi(R_p + \kappa^{-1})^3/3N_{ad}^2$ for $v_1 > 0$ or by $8\pi R_p^3/3N_{ad}^2$ for $v_1 < 0$. In Figure 9.2 $v_{1,red}$ is shown as a function of κ^{-1} for three values of q_{ex} . If $v_{1,red} \sim 1$ for $v_1 > 0$, the value calculated by Eq.(9.17) corresponds roughly to the definition used previously, i.e. Eq.(5.22). If $v_{1,red} \sim -1$ for $v_1 < 0$, the value of the negative virial coefficient is of order of the particle volume. As is clear from Figure 9.2, the value of q_{ex} greatly determines the value of v_1 at high ionic strengths, i.e. low κ^{-1} . For low values of q_{ex} the effective value of v_1 is negative (shaded area): in this case the electrostatic repulsion between two complexed particles is not sufficient to stabilise the particles kinetically. At lower ionic strengths, or higher excess charges, this electrostatic repulsion dominates the attractive van der Waals interactions and the effective binary virial coefficient is positive. We remark that the maximum in $v_{1,red}$ results from the renormalisation, i.e. for fixed q_{ex} , R_p and A_H v_1 increases continuously with increasing κ^{-1} .

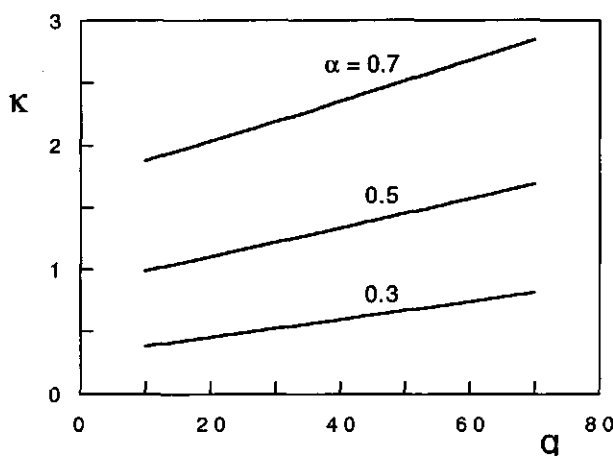


FIGURE 9.3. The value of $\kappa(q)$ for which $u(\kappa, q, \alpha) = 0$ as a function of q for three values of α , see Eq.(9.5). Other parameters are $R_p = 5$, $\epsilon = 0.35$, $\rho_p = 10^{-4}$ and $\epsilon_{cri} = 0.3$.

It is interesting to see in Figure 9.2 that the value of $v_{1,red}$ converges for the three values of q_{ex} at low ionic strengths. At low ionic strength the range of the electrostatic interactions, characterised by κ^{-1} , is relatively large. As a result, a small value of q_{ex} is sufficient to stabilise the particles. The electrostatic repulsion in this regime is mainly governed by the range of the interactions, the value of the surface charge is relatively unimportant. Thus, $v_{1,red}$ converges to a single curve for different values of q_{ex} .

In the previous chapters, it was concluded that a good estimation of the onset of complexation is obtained by setting u zero. For polymer-micelle complexation, where u is determined by the surfactant concentration, $u = 0$ defines a certain surfactant concentration. In a similar manner, for a given solution of polyelectrolytes and oppositely charged nanocolloids, the ionic strength may be identified as the variable which controls the value of u . In Figure 9.3 the value of κ which corresponds to $u = 0$ is plotted as a function of q for three values of α . It is clear that with increasing q or α $\kappa(u = 0)$ increases, i.e. the ionic strength at which complexation is estimated to occur increases with increasing charge densities. This is not surprising, as the decrease in electrostatic free energy upon complexation increases with increasing charge densities, as follows from Eq.(9.4). Since this decrease is proportional to q/κ , $\kappa(u = 0)$ increases proportional with q , provided all other terms in Eq.(9.5) remain constant.

Using the results from Figure 9.3, we can check whether the condition $\alpha/\kappa \lesssim 1$ is obeyed. As discussed in the beginning of section 9.2, this condition entails that the average distance between two adjacent charges, α^{-1} , is at least of the same order as the Debye length κ^{-1} and therefore the polyelectrolyte has a coil conformation. It follows from Figure 9.3 that this condition is indeed obeyed in the regime in which complexation is expected to take place, i.e. the assumption that prior to complexation a bare polyelectrolyte has a coil conformation is reasonable.

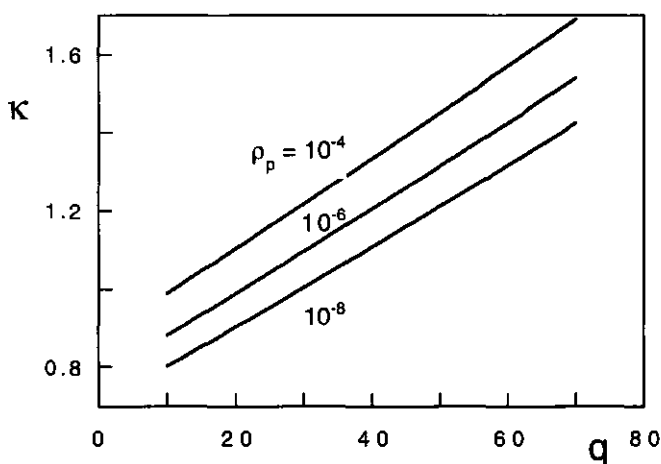


FIGURE 9.4. The value of $\kappa(q)$ for which $u(\kappa, q, \rho_p) = 0$ for three values of ρ_p , other parameters $R_p = 5$, $\epsilon = 0.35$, $\alpha = 0.5$ and $\epsilon_{cri} = 0.3$.

In Figure 9.4 $\kappa(u = 0)$ is shown as a function of q for three values of the bulk density of particles ρ_p at constant α . It is clear that the onset of complexation is considerably less sensitive to a change in ρ_p than to a change in q or α . This can be related to the co-operativity of the complexation process. As discussed in Chapter 5, in the case of polymer-micelle complexation the loss of translational entropy of surfactants upon formation of a complex is given by $pN_{ad}^{-1} \ln \rho_p$, where p is the number of surfactants in a complex. As $p \sim N_{ad}$ this loss of entropy is a decisive factor in the formation of complexes. In the case of polyelectrolyte-particle complexation, however, p equals 1. Therefore, the shift in u with varying ρ_p is small in the case of polyelectrolyte-particle complexation, due to the denominator N_{ad} . Hence, the onset of complexation in a given polyelectrolyte-particle solution is predominantly determined by α , q and κ .

We now turn towards the behaviour of N_{ad} and the excess charge density σ_{ex} . As N_{ad} in our model is also determined by κ (see Eq.(9.20)), it is necessary to examine N_{ad} in the regime where complexation is expected to occur, i.e. at $\kappa(u = 0)$. In Figure 9.5 N_{ad} and σ_{ex} at this ionic strength are shown as a function of q for three values of α . As expected, N_{ad} increases with decreasing α ; as complexation generally results in a (nearly) neutral complex, the charge on the complexed strand $N_{ad}\alpha$ is roughly proportional to the charge on the particle q . A more interesting quantity is the excess charge on the complex and the colloidal stabilisation resulting from this charge. For a given q the excess charge increases with increasing α . However, this does not necessarily imply that the colloidal stability is also enhanced with increasing α . As shown in Figure 9.3, $\kappa(u = 0)$ increases strongly with increasing α . The colloidal stability gained from the excess charge decreases strongly with increasing κ (see Figure 9.2 and Eq.(9.16)). The regime in which $v_1 < 0$ is shown with bold dashes in Figure 9.5, and it is clear that this regime is wider for $\alpha = 0.7$ than for $\alpha = 0.3$. Thus, the interesting result is found that for a given initial charge density on the particle the resultant excess charge density is significantly higher for a

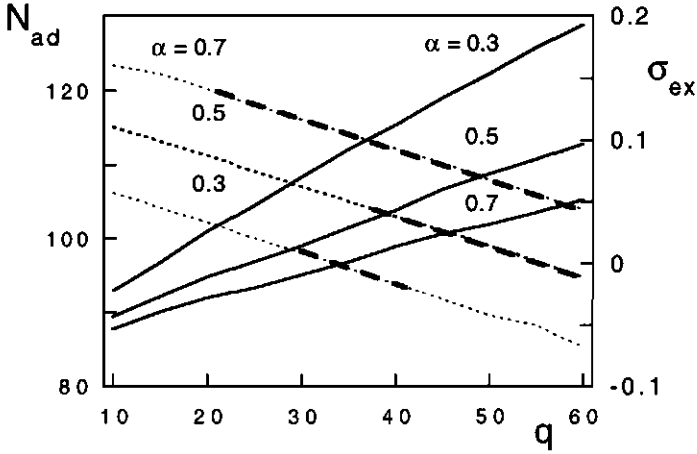


FIGURE 9.5. The parameters N_{ad} (solid curves) and σ_{ex} (dashed curves) as a function of q for three values of α at $\kappa(u = 0)$. In the dashed curves the q -regime in which $v_1 < 0$ is shown with bold dashes. Other parameters as in Figure 9.4, $A_H = 2$.

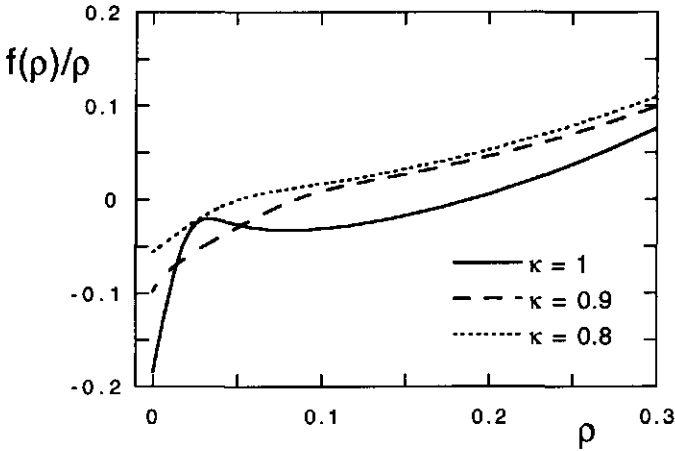


FIGURE 9.6. The free energy per monomer $f(\rho)/\rho$ as a function of ρ for $\alpha = 1$, $R_p = 3$, $q = 10$, $A_H = 2$, $\epsilon = 0.7$ and $\epsilon_{cri} = 0.6$ ($\alpha/\sigma_0 = 11.4$). The values of τ_b are 0.195, 0.535 and 0.994 with increasing κ .

large value of α than for a small one. However, as the ionic strength at which complexes form increases strongly with increasing α , the colloidal stability gained from the excess charge density is generally not sufficient for the high values of α , whereas it may suffice for low α .

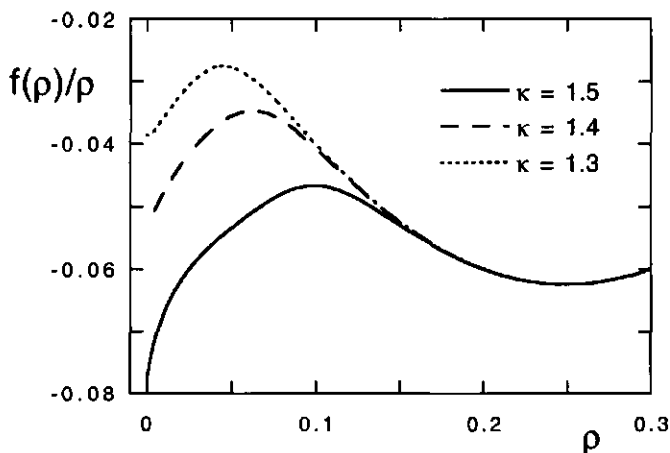


FIGURE 9.7. The free energy per monomer $f(\rho)/\rho$ as a function of ρ for the same parameters as Figure 9.6, with $q = 50$ ($\alpha/\sigma_0 \approx 2.5$). The values of τ_b are 0.134, 0.242 and 0.497 with increasing κ .

9.3.2. Phase behaviour

In the previous paragraph various parameters that play a role in the complexation of polyelectrolytes and particles were discussed separately. In the following we consider the overall conformation of the complexed chain as a function of α , q and κ . We remind the reader that we use the volume approximation, i.e. the chain length is considered to be large. As discussed in Chapter 6, a useful quantity to investigate the phase behaviour in the volume approximation is the free energy per monomer, $f(\rho)/\rho$. In Figures 9.6 and 9.7 $f(\rho)/\rho$ is plotted as a function of ρ at various ionic strengths for the charge density ratio's $\alpha/\sigma_0 \gg 1$ (Figure 9.6) and $\alpha/\sigma_0 \sim 1$ (Figure 9.7).

In the case that the ratio $\alpha/\sigma_0 \gg 1$, shown in Figure 9.6, the minimum value of $f(\rho)/\rho$ is consistently found at $\rho = 0$, irrespective of the value of κ (and thus τ_b). In the volume approximation zero monomer density corresponds to a swollen coil conformation. Thus, during the *continuous* loading of the polyelectrolyte with *decreasing* ionic strength, the polyelectrolyte retains its coil conformation. The continuity of the transition from a bare polyelectrolyte to a fully loaded complex stems from the colloidal stability gained from the excess charge of the complexes, shown in Figure 9.5. Even though $v_1 < v_0$, v_1 and v_2 are positive. As all binary osmotic interactions are repulsive, collapse of the necklace upon complexation does not occur. Thus, the complexation process at high α/σ_0 is similar to that of the polymer-micelle loading in a good solvent, as discussed in Chapter 6.

However, in the regime $\alpha/\sigma_0 \sim 1$, the excess charge is not sufficient to stabilise the complexed particles and $v_1 < 0$, see Figures 9.2 and 9.5. In this case the minimum of $f(\rho)/\rho$ is located either at ρ equals zero (at the high value of κ in Figure 9.7) or at a finite value of ρ (at the low value of κ in Figure 9.7). The state of zero density corresponds with a bare, soluble coil conformation, and the state of finite density with a collapsed

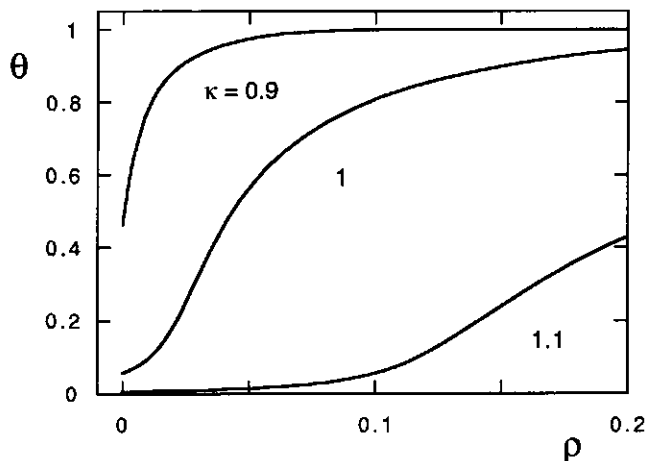


FIGURE 9.8. The degree of loading θ as a function of ρ for the same parameters as Figure 9.6 and κ 0.9, 1 and 1.1.

insoluble globule conformation, see Chapter 6. The transition from the coil conformation to the globule conformation occurs when $f(\rho)/\rho|_{\rho=0} = f(\rho_{glob})/\rho_{glob}$ (ρ_{glob} equals 0.25 in Figure 9.7). The transition from a bare, swollen polyelectrolyte to a loaded, insoluble complex is therefore discontinuous for $\alpha/\sigma_0 \sim 1$.

An interesting feature of our model is the fact that τ is predicted to decrease with increasing ρ , i.e. complexation is *enhanced* in semi-dilute solutions. This in contrast to polymer-micelle solutions, in which the degree of complexation was found to decrease with increasing monomer density. Evidently, the same physical mechanism that reduces complexation in semi-dilute polymer-micelle solutions enhances it in semi-dilute polyelectrolyte-particle solutions, namely the reduction of osmotic interactions. This is illustrated in Figure 9.8, where θ (the fraction of *loaded* monomers, equal to $1 - \tau$) is plotted as a function of ρ for various values of κ in the regime $\alpha/\sigma_0 \gg 1$. In Figure 9.8 θ is seen to increase with increasing ρ . We thus reach the general conclusion that the complexation behaviour of polymers or polyelectrolytes with nanocolloids in semi-dilute solutions is strongly determined by the relative strength of the osmotic interactions. If $v'_{eff}(\theta) > 0$ complexation is reduced with increasing ρ , whereas if $v'_{eff}(\theta) < 0$ it is enhanced.

Finally, it has been shown in Figure 9.6 that in dilute solutions the transition from a bare to a loaded conformation with decreasing ionic strength is continuous in the case that $\alpha/\sigma_0 \gg 1$. In semi-dilute solutions, however, phase separation may occur, due to the large differences in osmotic interactions of bare and complexed chains. This is demonstrated in Figure 9.9, where with an increasing value of κ a van der Waals-loop is observed in the chemical potential μ per monomer as a function of ρ (μ is defined as the derivative of $f(\tau, \rho)$ with respect to ρ , see Eq.(6.13)). This van der Waals-loop is the same as the van der Waals loop observed in our model for semi-dilute polymer-micelle solutions, see section 6.3.1. Clearly, when the overall monomer density ρ in the solution is high, the solution may phase separate into a relatively dilute phase consisting of almost

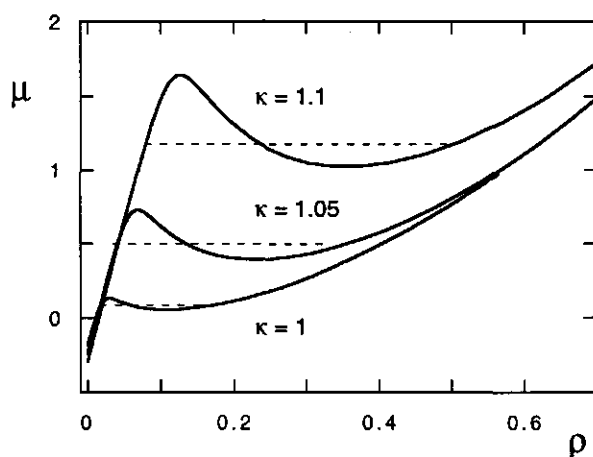


FIGURE 9.9. The chemical potential per monomer μ as a function of ρ for the same parameters as Figure 9.6 and three values of κ . The dashed lines denote the transition from a coil to a globule conformation.

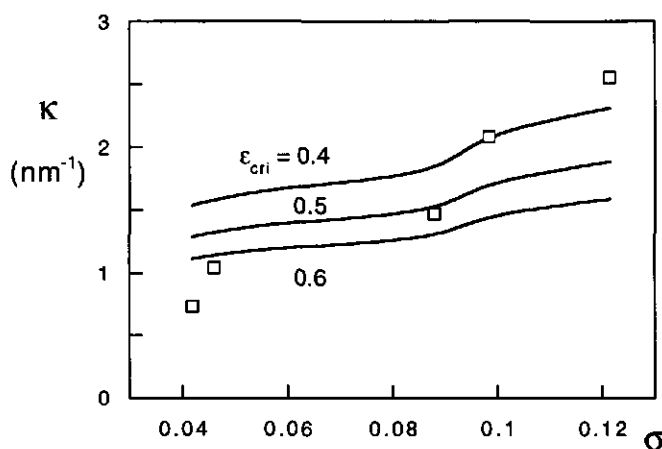


FIGURE 9.10. Comparison of experimental data for the onset of complexation of SDS-micelles and PDMAAC from McQuigg et al. [188] (open squares) and our model (solid curves) for three values of ϵ_{cri} , $l = 1$ nm, $\alpha = 1$ and $\rho_p = 10^{-6}$.

bare chains and a relatively concentrated phase consisting of highly loaded but soluble complexes, similar to the phase separation of semi-dilute polymer-micelle solutions into a loaded and a bare phase, see section 6.3.1.

9.3.3. Comparison with experiments

Although there exists a considerable amount of literature concerning complexation of polyelectrolytes and oppositely charged nanocolloids, the number of papers in which

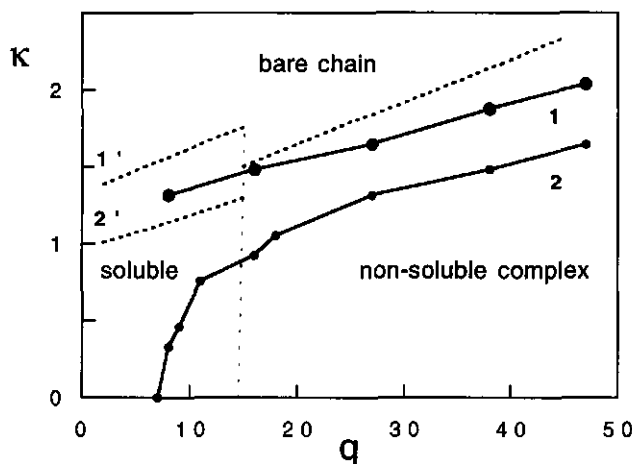


FIGURE 9.11. Comparison of the phase diagram of BSA and PDMAAC from Mattison *et al.* [16] (solid curves) and our model (dashed curves) for $\epsilon_{cri} = 0.6$, $l = 1$ nm, $\alpha = 0.9$, $\rho_p = 10^{-6}$ and $A_H = 2$.

the phase diagrams of such solutions are investigated quantitatively is limited. We compare our numerical results with the experimental data of three such papers: the first is by McQuigg *et al.*, and concerns the complexation of poly(dimethylammoniumchloride) (PDMAAC, a polycation), and mixed micelles consisting of SDS and non-ionic surfactants ($C_{12}E_6$). [188] The second paper, by Mattison *et al.*, investigates the complexation of PDMAAC and BSA. [16] Finally, Miura *et al.* examined the complexation of PDMAAC with oppositely charged dendrimers. [204]

By mixing anionic SDS and non-ionic $C_{12}E_6$ surfactants McQuigg *et al.* obtained micelles with a varying surface charge density and radius. The ionic strength at which the onset of complexation of such micelles with highly charged PDMAAC occurred was determined via turbidimetric titration. In Figure 9.10 the experimental results are shown, together with the ionic strength of complexation of our model $\kappa(u = 0)$. The monomer length of PDMAAC is estimated to be 1 nm and α is set unity. Three curves are drawn in Figure 9.10, corresponding to three values of ϵ_{cri} . The experimental increase of κ with increasing σ_0 is found to be larger than that of the model. It must be remarked that the experimental determination of σ_0 and R_p is difficult and to some extent ambiguous. [188] Nevertheless, insertion of the estimated physical parameters in our model yields a reasonable agreement between the observed critical ionic strength and that predicted by our model.

The complexation of BSA and PDMAAC was studied as a function of the pH and ionic strength by Mattison *et al.* [16] BSA is an ampholyte, the surface charge density therefore varies with varying pH. As is the case for PDMAAC and mixed micelles, at a certain pH, i.e. certain charge density on the protein, PDMAAC and BSA form complexes below a critical ionic strength. Mattison *et al.* distinguish two critical ionic strengths for a given charge density of the BSA: the first characterises the onset of complexation, the second

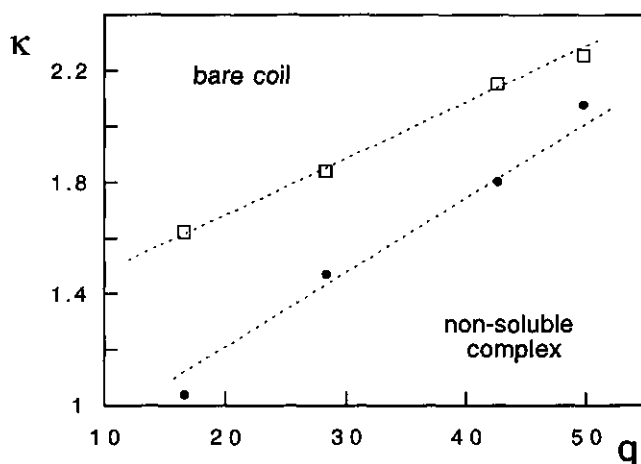


FIGURE 9.12. Comparison of the phase diagram of Miura *et al.* [204] (filled circles) and our model (open squares) for $\epsilon_{\text{cri}} = 0.7$, $l = 1$ nm, $\alpha = 1.4$, $\rho_p = 10^{-6}$, $R_p = 4$ and $A_H = 2$.

the formation of non-soluble complexes. In Figure 9.11 these critical ionic strengths are shown as a function of q . The upper solid curve, denoted by 1, is the experimental value of κ at the onset of complexation, the lower, denoted by 2, the formation of the non-soluble complex. Experimentally, it is observed that for $q \lesssim 7$ the resultant complexes are soluble.

The phase behaviour predicted by our model is also shown in Figure 9.11 with dashed curves. At low values of q the complexation is predicted to be continuous and we find two phase lines: the first, denoted by 1', gives the onset of complexation (defined as $\theta = 0.1$); the second, denoted by 2', gives the ionic strength at which a soluble, fully loaded complex is formed (defined as $\theta = 0.9$). At a critical value of q , however, the loading transition changes from continuous to abrupt. Above this value of q , only one phase line is predicted, namely the ionic strength $\kappa(q)$ at which the coil-globule transition abruptly occurs. At ionic strengths below this critical ionic strength our model predicts finite values of ρ , i.e. non-soluble globules, above it ρ equals zero, i.e. soluble, bare chains. This critical ionic strength depends, amongst others, on the value of the Hamaker constant of the complexed particles.

It must be remarked that the upper phase line of Mattison *et al.* extends to over-all negative values of q , i.e. complexation between similar charged polyelectrolytes and proteins (not shown in Figure 9.11). As our model has a mean-field character, it cannot cope with local electrostatic interactions, and it predicts that no complexation occurs. Therefore, comparison of the experimental BSA/PDMAAC phase lines and the theoretical ones demonstrates not only the applicability of our model but also some of its limitations.

In a recent paper Miura *et al.* presented data for complexation of PDADMAC (poly(diallyldimethylammoniumchloride)) with an oppositely charged dendrimer, whose

charge density is pH-dependent. [204] In this paper an abrupt transition from a bare coil to a non-soluble complex is reported. In Figure 9.12 some of the experimental data are presented in a phase diagram, together with the calculated phase diagram. According to Miura *et al.*, the PDADMAC is highly charged. We have therefore inserted a charge density equal to the inverse Bjerrum length. The radius of the dendrimer is not reported by Miura *et al.*, an estimated value of 4 nm was used in the calculations. A higher or lower value merely shifts the phase line somewhat. In Figure 9.12 both the experimental (filled circles) and the numerical phase lines (open squares), corresponding to the ionic strength at which the swollen coils abruptly form globular complexes, are shown. Although the excess charge density is non-zero in our model, due to the high initial surface charge densities the complexation takes place at high values of κ . The stabilisation gained from electrostatic repulsion of the excess charge on the complexes is insufficient to overcome the attractive van der Waals interactions between the same complexes. An insoluble, globular conformation is the result.

9.4. DISCUSSION AND CONCLUSIONS

In this chapter complexation of quenched polyelectrolytes and oppositely charged nanocolloids has been examined using an analytical mean-field model for polyelectrolytes with annealed excluded-volume interactions. We apply the so-called volume approximation, in which the chain length is close to infinity. In our model an effective adsorption energy per complexing monomer is calculated, which is the sum of the decrease in electrostatic free energy upon complexation and the entropic cost of localising the complexing monomers upon the particle surface. The complex-complex virial coefficient is shown to reflect a balance of attractive van der Waals interactions and repulsive electrostatic interactions, arising from an excess charge density on the complex. Its value is determined using a DLVO-like approach. Effectively, this excess charge density is low when the charge densities of the polyelectrolyte and the particle are of the same order of magnitude, and relatively high when the charge densities differ greatly. Therefore, the conformation of the complexed chain is either globular (dominant van der Waals interactions) or a swollen coil (dominant electrostatic interactions), depending on the ratio of the initial charge densities. The transition from a bare coil to a soluble complex is predicted to be continuous, whereas the transition from a bare coil to a globular conformation is predicted to be abrupt.

Several objections can be raised against the mean-field approach utilised in this chapter. To start with, the use of the Debye-Huckel expressions for planar charged systems for the surface potential on a sphere or, especially, a polyelectrolyte chain is questionable. Moreover, the stiffness of the polyelectrolyte chain is not taken into account. In our model, the entropic penalty of complexation per monomer is set equal to ϵ_{cri} , irrespective of the size of the nanocolloid. As is clear from Figure 9.9 and 9.10, inserting the literature value for ϵ_{cri} ($\pm 0.3 k_B T$) in our model yields higher values for the ionic strength at complexation than are experimentally found. This could result from either

an overestimation of the decrease in electrostatic free energy or an underestimation the entropic penalty, or both. [201]

Also, the problem remains of how the combined effect of attractive van der Waals interactions and repulsive electrostatic interactions should be translated into an overall virial coefficient. It is well known that the DLVO theory predicts two regimes for interacting particles with an excess charge density: the first is at low ionic strengths, in which strong electrostatic interactions result in a relatively high potential barrier. As the particles cannot surpass this barrier within a reasonable time-span, the particles are kinetically stable, although the aggregated state is the thermodynamic stable one. At high ionic strength this potential barrier is insufficient to stabilise the particles and, under the influence of van der Waals interactions, an aggregated phase forms. We introduce an effective complex-complex virial coefficient which, in the spirit of the DLVO theory, is positive when the potential barrier is relatively high and negative when the barrier is low. This approach has one major disadvantage: in a formal sense a virial coefficient is a thermodynamic parameter and according to its definition it has a negative value when a sum of van der Waals interactions and electrostatic interactions are considered, regardless of the ionic strength. The complex-complex virial coefficient in our model should therefore be interpreted as a 'kinetic' virial coefficient.

Nevertheless, the above simplifications have one clear advantage: the insight in the qualitative effects of the interactions underlying complexation is enhanced by the simple approach of our model, and it is this insight that may be lost in numerical models that are formally more correct. Moreover, to our knowledge our model is the first analytical theoretical approach that examines both the microscopic parameters that control complexation, and the overall phase behaviour of a solution of flexible polyelectrolyte chains and oppositely charged nanocolloids.

There are both similarities and differences between experimental data in the literature and the predictions of our model. At low values of σ_0 a continuous loading of the polyelectrolyte with particles with decreasing ionic strength is predicted by our model, resulting in a soluble complex at total loading. This continuous transition from a bare coil to a soluble complex is found experimentally by Mattison *et al.* [16] The ionic strength at which the onset of complexation occurs is predicted to depend linearly on the charge density on the particle for a given α . This is corroborated experimentally. Also, a critical charge density σ_0 on the particle, below which the resultant complex is soluble and above which it is non-soluble, is predicted and found experimentally. Above this critical charge density the transition from a bare coil to a non-soluble complex with decreasing ionic strength is predicted to be abrupt in our model. Such an abrupt transition is indeed found in the case of PDMAC and oppositely charged dendrimers. [204] A continuous transition, however, is reported in the case of PDMAAC and BSA. [16] This difference in loading mechanism can possibly be ascribed to experimental conditions. Mattison *et al.* state that the titration of the solution containing BSA from pH 3.5 to 8 took place in approximately one hour. It could be that in the intermittent pH regime, where complexation occurs, meta-stable conformations of partially loaded complexes are formed. These meta-stable complexes could remain soluble, and a further increase of the pH

leads to an increased charge density on the BSA and increased loading. As our model is based upon equilibrium conformations, such meta-stable conformations are not considered. Therefore, our model suggests that titration of PDMAAC-BSA solutions over a prolonged period of time could result in a different loading mechanism.

Finally, our model suggests that the complexation of polyelectrolytes and nanocolloids is enhanced in semi-dilute solutions. In such cases, the character of the transition can change from continuous to abrupt. This may have implications for the complexation behaviour of polyelectrolyte brushes and nanocolloids. These conclusions await theoretical and experimental verification.

Summary & Outlook

Layers of polymer chains end-attached to a grafting plane at high densities, so-called brushes, are a curious state of matter. The (average) monomer density within the brush is as high as in a semi-dilute polymer solution, resulting in a high osmotic pressure in the brush. Due to the grafting, however, this isotropic osmotic pressure results in an anisotropic stretching of the chains normal to the surface. This degree of stretching can be quite extensive; in this thesis PEO-chains of 700 monomers are considered which are stretched up to 20 % of their total contour length, i.e. form a brush with a thickness of 50 nm, merely by the presence of similar grafted chains. It is evident that such highly extended polymer layers may strongly modify the properties of the grafting surface. To this end brushes are applied as, for instance, adsorption inhibitors or colloidal stabilisers.

In this thesis we first focus on the thermodynamic and structural properties of polymer brushes, both neutral and charged. Following this, a mean-field model is developed that describes the effect of complexes formed by polymer (or polyelectrolyte) chains and nanocolloids on the polymer conformation, and the phase behaviour of such systems. These two modes of investigation converge in the theoretical and experimental investigation of the interactions between neutral brushes and nanocolloids which may form complexes with the polymer chains in a bulk solution.

A general introduction to brushes and polymer-nanocolloid complexes is presented in *Chapter 1*. The concepts underlying scaling and analytical self-consistent-field (aSCF) models of brushes are briefly discussed, as are a number of technological applications of grafted polymers. The difficulties encountered in the experimental preparation of a brush of controlled chain length and grafting density are also considered.

In *Chapter 2* surface pressure isotherms of neutral, end-grafted chains that can adsorb to the grafting plane are modelled with the numerical Scheutjens-Fleer self-consistent-field (nSCF) model. These numerical results are compared to experimental isotherms of PS-PEO diblock copolymers irreversibly adsorbed at the air/water interface. Semi-quantitative agreement between the numerical and experimental isotherms is found. It is shown that in the case of long chains the experimental and numerical isotherms obey the aSCF power law for the brush surface pressure π as a function of the grafting density σ , i.e. $\pi \sim \sigma^{5/3}$. The corresponding power law for the brush thickness H ($H \sim \sigma^{1/3}$) is only obeyed when the experimental surface pressure isotherms also follow the aSCF power law. The adsorption/desorption transition of grafted polymers upon increasing grafting density is investigated numerically by considering the chemical potential of the

grafted chains and its derivative with respect to the grafting density. It is shown that this adsorption/desorption transition is continuous, irrespective of the chain length and adsorption strength. The behaviour of the chemical potential of the grafted chains at large adsorption energies is reminiscent to that of a (mean-field) magnetic system approaching its critical point.

The monomer density profiles of monodisperse and bimodal PEO brushes are determined with neutron reflectivity and compared to profiles predicted by the nSCF model in *Chapter 3*. The monomer density distribution predicted by aSCF models, namely a parabolic profile, is only found at a relatively high grafting density. At lower densities the contribution of a 'tail' region at the edge of the brush to the reflectivity spectra is considerable. In this distal region, which originates from fluctuations of the extended chains, the density smoothly drops to zero. Good agreement is found between the experimental and nSCF density profiles. When short and long PEO chains are mixed at relatively high grafting densities a bimodal brush is formed. This bimodal structure is retrieved from the neutron reflectivity spectra. The bimodal density distribution is enhanced by unequal chain length ratio's and mixing ratio's at high grafting densities of such mixed layers. As expected on the basis of theoretical predictions, the long chains in the bimodal brush are additionally stretched by the presence of the shorter ones.

In *Chapter 4* the properties of annealed polyelectrolyte brushes, consisting of grafted polyacrylic-acid (PAA) chains in contact with an aqueous solution, are examined with surface pressure measurements, optical reflectivity and ellipsometry. When the ionic strength of the subphase is high and the pH relatively low, the predicted power law for the surface pressure as a function of the grafting density in the salted brush (SB) regime is found. At low ionic strength and pH, however, the PAA chains are found to adsorb at the air/water interface. Due to such adsorption the predicted osmotic brush regime is not observed. A novel manner to prepare brushes on a solid substrate is developed, namely Langmuir-Blodgett deposition of PS-PAA block copolymers from an air/water interface on a hydrophobic modified silicon wafer, followed by thermal annealing. Using this technique the average degree of dissociation of grafted PAA chains as a function of pH can be measured with reflectometry. It is shown that the dense grafting of the PAA chains shifts the titration curves significantly to higher pH, as predicted by scaling models and numerical studies. The thickness of the PAA brushes on hydrophobic modified silicon wafers is measured with ellipsometry as a function of pH, ionic strength and grafting density. At a pH not far from the monomeric pK_a , the brush thickness is theoretically predicted to initially increase with increasing ionic strength and to decrease again at high ionic strength. This non-monotonic behaviour of the brush thickness is indeed observed experimentally. The initial increase in brush thickness with increasing ionic strength is, however, experimentally less pronounced than that predicted by theory.

An analytical mean-field theory for long polymer chains that form complexes with nanocolloids is developed in the following chapters. In *Chapter 5* the complexation of

single polymer chains in a good solvent with surfactants in micellar aggregates is considered, using a Flory-like approach. It is shown that the number of complexed micelles on a polymer chain continuously increases with increasing surfactant concentration, in agreement with experimental evidence. The size of the coil can monotonously increase, decrease, or have a maximum as a function of the surfactant concentration. Comparison with experimental data for PEO-gels complexed with SDS shows a reasonable agreement between the predicted dependence of the gel volume on the overall ionic strength and experimental results.

In *Chapter 6* semi-dilute solutions of complexed chains are considered. Osmotic interactions are found to strongly influence the degree of complexation in a semi-dilute solution. The degree of loading of the chains by nanocolloids decreases with increasing monomer density when the osmotic interactions between complexed particles are strong compared to those between bare monomers. If, however, the complex-monomer osmotic interactions are strong compared to both the complex-complex and monomer-monomer, phase separation into a relatively dilute phase consisting of highly loaded chains and a relatively dense phase of bare chains may occur. Such phase separation is enhanced as the solvent quality decreases. If the solution is below the Θ -temperature of the bare polymer, a first-order phase transition from a bare, collapsed globule to a swollen coil with increasing particle density is predicted.

An analytical self-consistent-field theory for polymer brushes in the presence of particles capable of complexation is presented in *Chapter 7*. As a monomer density gradient is present, the density of complexed particles is also predicted to vary across the brush. The complexes are predominantly located in the distal region of the brush, where the average monomer density is low. In the proximal region of the brush, close to the grafting plane, the density of complexed particles is predicted to be low. Microphase separation may occur in the brush under the same conditions at which macroscopic phase separation occurs in a bulk solution. The overall number of complexed particles per unit area is predicted to have a maximum as a function of the grafting density. The height of the brush is found to either increase monotonously with increasing grafting density, or have a local maximum and minimum.

The adsorption of the protein BSA on hydrophobised silica wafers covered with grafted PEO chains is experimentally examined in *Chapter 8*. The amount of adsorbed BSA is measured with reflectometry at several grafting densities for different PEO chain lengths. Conventional models for the interaction between a brush and adsorbing proteins predict the adsorbed amount to decrease with increasing grafting density and chain length. However, it is observed that the adsorbed amount has a maximum as a function of the grafting density for long chains, whereas it decreases monotonously in the case of short chains. This maximum is qualitatively understood with our aSCF model presented in *Chapter 7*, and indicates that some attraction between grafted PEO chains and BSA may exist.

Finally, in *Chapter 9* our analytical model is extended to complexation of polyelectrolyte chains with oppositely charged nanocolloids. In a given system (fixed particle size and charge densities of the chain and particle) the ionic strength is the main parameter which controls complexation. At high ionic strength the attractive electrostatic interactions are suppressed and the degree of complexation is negligible. As the ionic strength decreases the attractive electrostatic interactions induce complexation. The transition from a bare polyelectrolyte to a complexed chain is predicted to be either continuous or abrupt, depending on the ratio of the charge densities and the Hamaker constant of the particles. In the former case the complex remains soluble, in the latter a non-soluble coacervate is formed. Both kinds of loading processes have been reported in the literature.

Recently, the view has been expressed that all great questions in natural sciences have been answered. [205] Others, however, maintain that several fundamental issues remain to be resolved. [206] Regardless of the validity of either claim, a large number of issues in the science of brush interfaces remain to be investigated. Chapters 2, 3 and 4 of this thesis concern the 'classical' features of brushes, i.e. the thickness and surface pressure of brushes, the monomer density distribution and the charge density of annealed brushes. One could say that these quantities are rather well understood by now, both experimentally and theoretically. Chapters 5 to 9, however, concern a novel area of investigation, namely the interactions of brushes with various kinds of adsorbing or complexing particles. As shown in Chapter 8, the (conventional) notion that the interactions of a PEO brush with proteins are similar to those of PEO chains in a bulk solution, i.e. consist solely of repulsive osmotic interactions, is too simple. The nature of polymer-particle interactions in a confined geometry may differ from that in a bulk solution. We predict that complexation of nanocolloids in brushes may have interesting consequences for the brush structure; experimental verification of such behaviour is not yet given. Another novel area of research is the wetting behaviour of liquids interacting with a brush surface. Whereas theoretical analyses have resulted in several theoretical wetting scenarios [207,208], experimental evidence of the various scenarios is scarce. [209] In Chapter 9 we considered the interactions of polyelectrolytes and oppositely charged particles in a bulk solution. It was shown that the phase behaviour of such solutions strongly depends on the initial charge densities of the polyelectrolyte and particle. A charged brush may exhibit even more pronounced phase behaviour, due to the high monomer densities and electrostatic potential within the brush; the collapse of a charged brush as it complexes with oppositely charged nanocolloids has not been investigated either experimentally or theoretically. Evidently, the use of polyelectrolyte brushes in various biotechnological applications greatly depends on such phase behaviour.

In all, one may say that it is time to focus on the real purpose of a brush, namely its interactions with soap and dirt.

Samenvatting

Borstels roepen bij de meeste mensen associaties op van poetsen, schrobben en boenen. Een borstel is inderdaad een nuttig huishoudelijk gebruiksapparaat, maar in de ogen van velen zeker niet interessant genoeg voor een wetenschappelijk onderzoek van vier jaar. Echter, borstels beslaan vele maten en vormen. In dit boekje is onderzoek naar *polymere nanoborstels* met een dikte van tientallen nanometers beschreven. De haren van dergelijke borstels bestaan uit polymeren die met hun uiteinden aan een oppervlak zijn verankerd.

De haren van dergelijke nanoborstels zijn ongeveer 10 000 000x kleiner dan de haren van een bezem. Toch hebben nanoborstels in veel toepassingen grofweg eenzelfde functie als een tandenborstel of bezem, namelijk een oppervlak schoonhouden van allerlei 'viezigheid'. In het geval van nanoborstels is er echter geen mechanische energie ('schrobben') voorhanden om het vuil te verwijderen. Het vermogen van een nanoborstel om een oppervlak schoon te houden hangt daarom af van zijn structuur en de moleculaire interacties met 'vuil'deeltjes. Het is om deze reden dat fysisch onderzoek nodig is om inzicht te krijgen in de grootheden en processen die bepalend zijn voor de structuur van een polymere borstel en zijn interacties met de omgeving. Het resultaat van dergelijk onderzoek over de afgelopen vier jaar is in dit boekje gepresenteerd. In de volgende alinea's worden de verschillende hoofdstukken kort besproken.

In *Hoofdstuk 2* wordt de experimentele oppervlaktedruk van neutrale blok copolymeren bestaande uit polystyreen-polyethyleenoxide (PS-PEO) vergeleken met numerieke berekeningen met het model van Scheutjens en Fler. Het blijkt dat er heel wat informatie over de structuur van verankerde polymeren uit dergelijke isothermen voor de oppervlaktedruk te verkrijgen is. Met behulp van deze isothermen wordt aangetoond dat een 'echte' borstel, namelijk een borstel die aan theoretisch voorspelde schalingswetten voldoet, pas verkregen wordt wanneer het aantal monomeren in de PEO-ketens meer dan enkele honderden beslaat. In dit hoofdstuk wordt ook de overgang van platte, geadsorbeerde ketens naar gestrekte ketens met toenemende verankeringsdichtheid numeriek onderzocht. Er wordt geconcludeerd dat deze overgang altijd gelijkmatig verloopt (2^e-orde fase-overgang) en niet abrupt (1^e-orde fase-overgang), zoals in de literatuur is voorspeld.

De structuur van ongeladen PEO-borstels is onderzocht met neutronen reflectometrie en de resultaten zijn gepresenteerd in *Hoofdstuk 3*. Bij een lage verankeringsdichtheid hebben monodisperse borstels (borstels bestaande uit polymeren van identieke lengte) een blokachtig dichtheidsprofiel met aan het uiteinde een overgangsgebied ('staart') waarin

de dichtheid geleidelijk afneemt naar nul. Bij een hoge verankeringsdichtheid heeft het dichtheidsprofiel een parabolische vorm. De experimentele profielen komen goed overeen met die berekend met het Scheutjens-Fleer model. Bimodale borstels (borstels met twee verschillende keten lengtes) vertonen een duidelijke bimodale structuur, namelijk een compacte laag met een relatief hoge monomeerdichtheid vlak bij het verankeringsoppervlak en een meer gestrekte laag met een lage monomeerdichtheid naar buiten toe. Zoals verwacht heeft de aanwezigheid van de kleinere ketens een sterkere strekking van de lange ketens tot gevolg.

In *Hoofdstuk 4* is het gedrag van verankerde geladen ketens bestaande uit polystyreen-polyacrylzuur (PS-PAA), onderzocht met oppervlaktedrukisothermen, optische reflectometrie en ellipsometrie, beschreven. Net als bij neutrale ketens blijken de oppervlaktedrukisothermen informatie te bevatten over de structuur van de verankerde laag. In aanwezigheid van veel zout in de waterfase is de schalingswet voor de oppervlaktedruk van een PAA-borstel als functie van de verankeringsdichtheid vergelijkbaar met die voor ongeladen ketens. Bij afwezigheid van zout en niet te hoge pH adsorbeert PAA aan het water/lucht oppervlak. Deze adsorptie hindert de vorming van de theoretisch voorspelde 'osmotisch' borstel. De fractie geladen monomeren in een PAA-borstel is onderzocht met reflectometrie. Bij een gegeven pH neemt deze fractie af met toenemende verankeringsdichtheid, in overeenstemming met theoretische voorspellingen. De dikte van de PAA-borstel is gemeten met behulp van ellipsometrie. Zoals theoretisch voorspeld neemt met toenemende zoutconcentratie en constante pH de dikte eerst toe en vervolgens bij hoge zoutconcentraties weer af. De initiële toename is echter minder sterk dan de theoretisch voorspelde.

Lange, water-oplosbare polymeren kunnen complexen vormen met verscheidene kleine deeltjes, zoals micellen of eiwitten. Een dergelijk complex wordt ook wel aangeduid als een 'kralensnoer'. Een theoretisch model voor het gedrag van een enkele lange keten met gecomplexeerde deeltjes is beschreven in *Hoofdstuk 5*. Een gecomplexeerde keten wordt in dit model gekarakteriseerd door de fractie gecomplexeerde monomeren, een gemiddelde energiewinst per monomeer bij complexatie, en de verschillende osmotische interacties tussen gecomplexeerde en ongecomplexeerde monomeren. Dit model geeft een kwalitatief correcte beschrijving van het gedrag van een PEO-gel in contact met een zeepoplossing.

In *Hoofdstuk 6* wordt het kralensnoermodel uitgewerkt voor semi-verdunde polymeeroplossingen. Er wordt voorspeld dat onder bepaalde omstandigheden scheiding in twee fasen kan optreden, bestaande uit een relatief ijle fase van gecomplexeerde ketens en een relatief geconcentreerde fase van kale ketens. In het geval van een slecht oplosmiddel bestaat deze geconcentreerde fase uit 'globules', ofwel zeer compacte polymeerkluwens. In het geval van globules in een zeepoplossing wordt met toenemende zeepconcentratie een abrupte (1^e-orde fase-) overgang voorspeld van een compacte kluwen naar een sterk gezwollen, gecomplexeerde keten. Een dergelijke 1^e-orde fase-overgang is in de literatuur experimenteel bevestigd.

Polymeerborstels kunnen opgebouwd zijn uit polymeerketens die in oplossing complexen vormen met bijvoorbeeld eiwitten of zeepmicellen. Daarom is in *Hoofdstuk 7* een analytische zelf-consistent-veld theorie voor complexerende polymeerborstels ontwikkeld, die stoelt op concepten die geïntroduceerd zijn in Hoofdstukken 5 en 6. Dit model voorspelt een dichtheidsverdeling van gecomplexeerde deeltjes in de borstel. Wanneer de osmotische interacties tussen deze deeltjes sterk zijn, zijn de deeltjes voornamelijk aan het uiteinde van de borstel te vinden en is de deeltjesdichtheid bij het verankeringsoppervlak gering. Deze dichtheidsverdeling heeft tot gevolg dat het totaal aantal deeltjes per oppervlakte-eenheid een maximum vertoont als functie van de verankeringsdichtheid. De dikte van de borstel kan volgens dit model ofwel toenemen met toenemende verankeringsdichtheid, ofwel een lokaal maximum en minimum hebben.

De resultaten voor de experimenteel bepaalde adsorptie van eiwitten (BSA) op een hydrofoob oppervlak bekleed met PEO-borstels zijn gepresenteerd in *Hoofdstuk 8*. Voor korte PEO-ketens neemt de adsorptie continu af met toenemende verankeringsdichtheid, zoals voorspeld door bestaande modellen voor interacties tussen verankerde polymeren en deeltjes. In het geval van lange ketens echter vertoont de adsorptie een maximum als functie van de verankeringsdichtheid. Dit maximum wordt kwalitatief verklaard met onze zelf-consistent-veld theorie, gepresenteerd in Hoofdstuk 7, en impliceert de aanwezigheid van attractieve interacties tussen de PEO-ketens en BSA. Zulke wisselwerkingen kunnen van belang zijn bij het ontwerpen van oppervlakken die eiwit adsorptie reduceren.

In *Hoofdstuk 9* tenslotte wordt het model uitgewerkt voor complexen van tegengesteld geladen deeltjes en polyelectrolyten. Voor een gegeven systeem blijkt de zoutconcentratie de grootte te zijn die complexvorming bepaalt, aangezien de attractieve electrostatische wisselwerkingen onderdrukt worden door een hoge zoutconcentratie. Volgens ons model kan complexvorming zowel geleidelijk als abrupt plaatsvinden met afnemende zoutconcentratie, afhankelijk van de relatieve ladingsdichtheden op de keten en het deeltje. In het eerste geval is het uiteindelijke complex oplosbaar, in het tweede geval is het onoplosbaar en scheidt zich af in een aparte fase. De theoretische resultaten kunnen experimentele waarnemingen uit de literatuur kwalitatief verklaren.

Glossary

Roman:

A_H	Hamaker constant
AdG	Alexander-de Gennes box model
aSCF	analytical self-consistent field model
CAC	critical association concentration
CMC	critical micelle concentration
D, d	thickness polymer layer
$G(z)$	monomer weighting factor
$G(z, z'; s)$	Green's function, probability of $s' = 1$ in z and $s' = s$ in z'
H, h	brush height, absolute and renormalised, respectively
H_{rms}, h_{rms}	root-mean-square thickness, absolute and renormalised, respectively
I	total ionic strength
l	length of a monomeric unit
l_B	Bjerrum length
$m, m(z)$	number of complexed micelles per chain, per unit volume
n	refractive index
N	chain length
N_{ad}	number of complexed monomers per nanocolloid
NR	neutron reflectivity
nSCF	numerical self-consistent field model
OsB, $\tilde{\text{OsB}}$	osmotic brush, quenched and annealed, respectively
q	component of the wavevector perpendicular to the reflection plane (Chapter 3)
q	bare charge on nanocolloid (Chapter 9)
q_{ex}	excess charge on polyelectrolyte-particle complex
$2r'$	distance between surfaces of nanocolloids
$R(q)$	reflectivity of neutrons at wavevector q
R_0	Gaussian radius of a polymer coil
R_G	radius of gyration of a polymer coil
R_m, R_p	radius of micelle or protein
s	monomer number
$s(\theta)$	translational entropy per monomer
$s'(\theta)$	derivative of $s(\theta)$ with respect to θ
SANS	small angle neutron scattering

SB	salted brush
SLD	scattering length density
SSAL	self-similar adsorbed layer
u	effective change in free energy upon complexation of a monomer
u^0	energy gain upon complexation of a monomer
$u_0(z)$	potential energy of the solvent at $z' = z$
$u'(z)$	potential energy of a monomer at $z' = z$
U_{hwr}	hard wall repulsion potential
v_0	monomer-monomer second virial coefficient
v_0^{crit}	critical monomer-monomer coefficient at which coil-globule transition becomes 1 st -order
v_1	(renormalised) micelle-micelle second virial coefficient
v_2	(renormalised) monomer-micelle second virial coefficient
$v_{eff}(\theta)$	effective second virial coefficient
$v'_{eff}(\theta)$	derivative of $v_{eff}(\theta)$ with respect to θ
v_1^*	critical v_1 for non-monotonic $\mu(\rho)$
x	distance to grafting plane
w	third virial coefficient
z	distance to grafting plane, in monomer length units
z_0	distance to grafting plane at which microphase separation occurs

Greek:

α	fraction of charged monomers (Chapter 4 and 9)
α	expansion coefficient, R_G/R_0 (Chapter 6)
α_b	bulk dissociation fraction
β	renormalisation coefficient of coil elasticity
Γ	total adsorbed amount per unit area
$\Gamma(z)$	scattering length density profile
δ	Born length
Δ	excess free energy per unit area (Chapter 2)
Δ	phase difference upon reflection (Chapter 4)
ϵ	contact energy monomer-micellar surface (Chapter 5 and 6)
ϵ	dielectric constant (Chapter 9)
ϵ_{cri}	critical monomeric adsorption energy
θ	fraction of complexed monomers
$\theta_{1,2}$	co-existing fractions of complexed monomers
θ_b	bulk value of θ
θ_b^{cri}	θ_b above which no phase separation occurs
θ^*	degree of loading for which $v_{eff}(\theta) = 0$
$\tilde{\theta}$	degree of loading at which $\mu_{glob} = \mu(0)$

$\theta(0)$	value of θ at the grafting plane, $\theta(z = 0)$
κ^{-1}	Debye length
κ_c	critical inverse Debye length
λ_i	probability of contact of layer z with layer $z + i$
μ	chemical potential
μ_b^0	chemical potential of a surfactant in the bulk
μ_p^0	chemical potential of a surfactant in an aggregate of size p
μ_{glob}	chemical potential monomer in a collapsed globule
$\mu(0)$	chemical potential monomer in infinitely dilute phase
ξ	monomeric conformational susceptibility
π	surface pressure
π_b	surface pressure of the brush
π_{pta}	surface pressure in adsorption-desorption plateau
$\rho(z)$	(dimensionless) monomer density at $z' = z$
$\rho_{1,2}$	co-existing monomer densities
ρ_{H^+}	bulk proton concentration
ρ_p	particle density in solution
ρ_s	bulk salt concentration
σ	number of grafted chains per unit area or lattice cell
σ^*	relative grafting density, $\sigma/4\pi R_G^2$
σ_0	charge density on nanocolloid
σ_{ex}	excess charge density on nanocolloid-polymer complex
Σ	total grafted amount, σN
ς_b	block roughness
ς_{int}	interface roughness
τ	fraction of uncomplexed monomers
χ	Flory-Huggins parameter
χ_{sur}	monomer-surface interaction parameter
χ^2	quality of NR-fit, relative to that of D ₂ O
Υ_R	relative strength of 2D fluctuations
Ψ	ratio of parallel and perpendicular polarised reflectivities

Bibliography

- [1] Stryer, L. *Biochemistry*, 3rd ed., W.H. Freeman: New York, 1988.
- [2] Allen, J.A. *An Outline of Polymer Chemistry*, Oliver & Boyd: Edinburgh, 1968.
- [3] Evans, D.F.; Wennerström, H. *The Colloidal Domain*, VCH: New York, 1994.
- [4] Kruyt, H.R. *Colloid Science*, Vol.I, Elsevier: Amsterdam, 1952.
- [5] de Kruif, C.G.; Zhulina, E.B. *Colloids & Surfaces A* **1996**, 117, 151.
- [6] Mellema, M.; Leermakers, F.A.M.; de Kruif, C.G. *Langmuir* **1999**, 15, 6304.
- [7] Walstra, P.; Jenness, R. *Dairy Chemistry & Physics*, Wiley: New York, 1984.
- [8] Holt, C.; Horne, D.S. *Neth. Milk Dairy J.* **1996**, 50, 85.
- [9] See Van Loosrecht, M.C.M.; Lyklema, J.; Norde, W.; Zehnder, A.J.B. *Microbio. Rev.* **1990**, 54, 75 and references therein.
- [10] Halperin, A. *Langmuir* **1999**, 15, 2525.
- [11] Gage, D.; Currie, E.P.K.; Norde, W. *in preparation*.
- [12] Lasic, D.D.; Martin, F.J.; Gabizon, A.; Huang, S.K.; Papahadjopoulos, D. *Biochim. et Biophys. Acta* **1991**, 1070, 187.
- [13] Allen, T.M. *Adv. Drug Delivery Rev.* **1994**, 13, 285.
- [14] Imanishi, N. *NAMS Membrane Q.* **1990**, 5, 2.
- [15] Dulong, L. *Angew. Macrom. Chem.* **1984**, 124, 437.
- [16] Mattison, K.W.; Brittain, I.J.; Dubin, P.L. *Biotech. Prog.* **1995**, 11, 632.
- [17] Alexander, S. *J. de Phys. Fr.* **1977**, 38, 983.
- [18] de Gennes, P-G. *Macromolecules* **1980**, 13, 1069.
- [19] de Gennes, P-G. *Scaling Concepts in Polymer Physics*, Cornell Univ. Press: Ithaca NY, 1979.
- [20] Milner, S.T.; Witten, T.A.; Cates, M.E. *Macromolecules* **1988**, 21, 2610.
- [21] Semenov, A.N. *Sov. Phys. JETP* **1985**, 61, 733.
- [22] Skvortsov, A.M.; Pavlushkov, I.V.; Gorbunov, A.A.; Zhulina, E.B.; Borisov, O.V.; Priamitsyn, V.A. *Pol. Sci. USSR* **1988**, 30, 1706.
- [23] Zhulina, E.B.; Borisov, O.V.; Priamitsyn, V.A. *J. of Coll. Int. Sci.* **1990**, 137, 495.
- [24] Feynman, R.P. *Lectures on Physics, Vol.I*, Addison-Wesley: Tokyo, 1970.
- [25] Zhulina, E.B.; Borisov, O.V.; Priamitsyn, V.A.; Birshtein, T.M. *Macromolecules* **1991**, 24, 140.
- [26] Wijmans, C.M.; Scheutjens, J.M.H.M.; Zhulina, E.B. *Macromolecules* **1992**, 25, 2657.
- [27] Milner, S.T. *J. Chem. Soc. Faraday Trans.* **1990**, 86, 1349.
- [28] Martin, J.I.; Wang, Z.G. *J. Phys. Chem.* **1995**, 99, 2833.
- [29] Carignano, M.A.; Szeifler, I. *J. Chem. Phys.* **1994**, 100, 3210.
- [30] Carignano, M.A.; Szeifler, I. *Macromolecules* **1995**, 28, 3197.
- [31] Borisov, O.V.; Birshtein, T.M.; Zhulina, E.B. *J. Phys. II Fr.* **1991**, 1, 521.
- [32] Pincus, P. *Macromolecules* **1991**, 24, 2912.
- [33] Borisov, O.V.; Zhulina, E.B.; Birshtein, T.M. *Macromolecules* **1994**, 27, 4795.

- [34] Zhulina, E.B.; Birshtein, T.M.; Borisov, O.V. *Macromolecules* **1995**, *28*, 1491.
- [35] Lyatskaya, Y.V.; Leermakers, F.A.M.; Fleer, G.J.; Zhulina, E.B.; Birshtein, T.M. *Macromolecules* **1995**, *28*, 3562.
- [36] Israëls, R.; Leermakers, F.A.M.; Fleer, G.J. *Macromolecules* **1994**, *27*, 3087.
- [37] Lai, P.-Y.; Binder, K. *J. Chem. Phys.* **1992**, *97*, 586.
- [38] Yeung, C.; Balazs, A.C.; Jasnow, D. *Macromolecules* **1993**, *26*, 1914.
- [39] Wagner, M.; Brochard-Wyart, F.; Hervet, H.; de Gennes, P-G. *Coll. Pol. Sci.* **1993**, *271*, 621.
- [40] Tang, H.; Szleifer, I. *Europhys. Lett.* **1994**, *28*, 19.
- [41] Tang, H. *Macromolecules* **1995**, *28*, 6258.
- [42] Zhulina, E.B.; Birshtein, T.M.; Priamitsyn, V.A.; Klushin, L.I. *Macromolecules* **1995**, *28*, 14.
- [43] Seveck, E.M. *Macromolecules* **1998**, *31*, 3361.
- [44] Doyle, P.S.; Shaqfeh, E.S.G.; Gast, A.P. *Phys. Rev. Lett.* **1997**, *78*, 1182.
- [45] Neelov, I.M.; Borisov, O.V.; Binder, K. *Macrom. Theory Simul.* **1998**, *7*, 141.
- [46] Amoskov, V.M.; Birshtein, T.M.; Pryamitsyn, V.A. *Macromolecules* **1996**, *29*, 7240.
- [47] Birshtein, T.M.; Mercurieva, A.A.; Pryamitsyn, V.A.; Polotzkiy, A. *Macromol. Chem., Theory Simul.* **1996**, *5*, 215.
- [48] Zhulina, E.B.; Borisov, O.V.; Birshtein, T.M. *J. de Phys. Fr.* **1992**, *2*, 63.
- [49] Ross, R.S.; Pincus, P. *Macromolecules* **1992**, *25*, 2177.
- [50] Misra, S.; Mattice, W.L.; Napper, D.H. *Macromolecules* **1994**, *27*, 7090.
- [51] Von Goeler, F.; Muthukumar, M. *J. Chem. Phys.* **1996**, *105*, 11335.
- [52] Auroy, P.A.; Auvray, L.; Lèger, L. *Macromolecules* **1991**, *24*, 2523.
- [53] Auroy, P.; Auvray, L.; Lèger, L. *Phys. Rev. Lett.* **1991**, *66*, 719.
- [54] Zhao, W.; Krausch, G.; Rafailovich, M.H.; Sokolov, J. *Macromolecules* **1994**, *27*, 2933.
- [55] Zeghal, M.; Auroy, P.; Deloche, B. *Phys. Rev. Lett.* **1995**, *75*, 2140.
- [56] Karim, A.; Tsukruk, V.V.; Douglas, J.F. *J. Phys. II Fr.* **1995**, *5*, 1441.
- [57] Ansarifar, M.A.; Luckham, P.F. *Polymer* **1988**, *29*, 329.
- [58] Marra, J.; Hair, M.L. *Colloids & Surfaces* **1988**, *34*, 215.
- [59] Watanabe, H.; Tirrell, M. *Macromolecules* **1993**, *26*, 6455.
- [60] Taunton, H.J.; Toprakcioglu, C.; Fetters, L.J.; Klein, J. *Macromolecules* **1990**, *23*, 571.
- [61] Norton, L.J.; Kramer, E.J.; Bates, F.S.; Gehlsen, M.D. *Macromolecules* **1995**, *28*, 8621.
- [62] Iwata, H.; Hirata, I.; Ikada, Y. *Langmuir* **1997**, *13*, 3063.
- [63] Granick, S.; Herz, J. *Macromolecules* **1985**, *18*, 460.
- [64] Richards, R.W.; Rochford, B.R.; Webster, J.R.P. *Faraday Discuss.* **1994**, *98*, 263.
- [65] Richards, R.W.; Rochford, B.R.; Webster, J.R.P. *Polymer* **1997**, *38*, 1169.
- [66] Kent, M.S.; Lee, L.T.; Farnoux, B.; Rondelz, F. *Macromolecules* **1992**, *25*, 6240.
- [67] Factor, B.J.; Lee, L.T.; Kent, M.S.; Rondelez, F. *Phys. Rev. E* **1993**, *48*, 2354.
- [68] Kent, M.S.; Lee, L.T.; Factor, B.J.; Rondelez, F.; Smith, G.H. *J. Chem. Phys.* **1995**, *103*, 2320.
- [69] Bijsterbosch, H.D.; de Haan, V.O.; de Graaf, A.W.; Leermakers, F.A.M.; Mellema, M.; Cohen Stuart, M.A.; van Well, A.A. *Langmuir* **1995**, *11*, 4467.
- [70] Barentin, C.; Muller, P.; Joanny, J.F. *Macromolecules* **1998**, *31*, 2198.

- [71] Guenoun, P.; Schlachli, A.; Sentenac, D.; Mays, J.W.; Benattar, J.J. *Phys. Rev. Lett.* **1995**, 74, 3628.
- [72] Amiel, C.; Sikka, M.; Schneider, J.W.; Tsao, Y.; Tirrell, M.; Mays, J.W. *Macromolecules* **1995**, 28, 3125.
- [73] Mir, Y.; Auroy, P.; Auvray, L. *Phys. Rev. Lett.* **1995**, 75, 2863.
- [74] Wang, G.; Olofsson, G. *J. Phys. Chem.* **1995**, 99, 5588.
- [75] Lee, L-T; Cabane, B. *Macromolecules* **1997**, 30, 6559.
- [76] Grest, G. *Macromolecules* **1994**, 27, 418.
- [77] Patel, S.; Tirrell, M. *Colloids & Surfaces* **1988**, 31, 157.
- [78] Whitmore, M.D.; Noolandi, J. *Macromolecules* **1990**, 23, 3321.
- [79] Murat, M.; Grest, G.S. *Macromolecules* **1989**, 22, 4054.
- [80] Field, J.B.; Toprakcioglu, C.; Ball, R.C.; Stanley, H.B.; Dai, L.; Barford, W.; Penfold, J.; Smith, G.; Hamilton, W. *Macromolecules* **1992**, 25, 434.
- [81] Baranowski, R.; Whitmore, M.D. *J. Chem. Phys.* **1995**, 103, 2343.
- [82] Ligoure, C. *J. de Phys. Fr.* **1993**, 3, 1607.
- [83] Aubouy, M.; Guiselin, O.; Rapaël, E. *Macromolecules* **1996**, 29, 7261.
- [84] Ou-Yang, D.; Gao, Z. *J. de Phys. Fr.* **1991**, 1, 1375.
- [85] Cao, B.H.; Kim, M.W. *Faraday Discuss.* **1994**, 98, 245.
- [86] Scheutjens, J.M.H.M.; Fleer, G.J. *J. Phys. Chem.* **1979**, 83, 1619.
- [87] Scheutjens, J.M.H.M.; Fleer, G.J. *J. Phys. Chem.* **1980**, 84, 178.
- [88] Silberberg, A. *J. Chem. Phys.* **1968**, 48, 2835.
- [89] Evers, O.A.; Scheutjens, J.M.H.M.; Fleer, G.J. *Macromolecules* **1990**, 23, 5221.
- [90] Brandrup, J.; Immergut, E.H. *Polymer Handbook*, 3rd ed.; Wiley: New York, 1989.
- [91] Molyneux, P. *Water-soluble Synthetic Polymers: Properties and Behaviour*; CRC-Press: New York, 1983.
- [92] Faraone, A.; Magazu, S.; Maisano, G.; Migliardo, P.; Tettamanti, E.; Villari, V. *J. Chem. Phys.* **1999**, 110, 1801.
- [93] Kent, M.S.; Lee, L.T.; Farnoux, B.; Rondelez, F. *Macromolecules* **1992**, 25, 6240.
- [94] Goldenfeld, N. *Lectures on Phase Transitions and the Renormalization Group*, Addison-Wesley: New York, 1993.
- [95] Cardy, J. *Scaling and Renormalization in Statistical Physics*, Cambridge Un. Press: Cambridge, 1996.
- [96] Davis, T.D. *Statistical Mechanics of Phases, Interfaces and Thin Films*, VCH: New York, 1996.
- [97] Lekner, J. *Theory of Reflection*, Martinus Nijhof Publishers: Dordrecht, 1987.
- [98] Richards, R.W.; Rochford, B.R.; Taylor, M.R. *Macromolecules* **1996**, 29, 1980.
- [99] Milner, S.T.; Witten, T.A.; Cates, M. *Macromolecules* **1989**, 22, 853.
- [100] Birshtein, T.M.; Lyatskya, Y.V.; Zhulina, E.B. *Polymer* **1990**, 31, 2185.
- [101] Dan, N.; Tirrell, M. *Macromolecules* **1993**, 26, 6467.
- [102] Kent, M.S.; Factor, B.J.; Satija, S.; Gallagher, P.; Smith, G.S. *Macromolecules* **1996**, 29, 2843.
- [103] Haruska, Z.; Hurtrez, G.; Walter, S.; Riess, G. *Polymer* **1992**, 33, 2447.
- [104] Abramowitz, M.; Stegun, I.A. (Eds.) *Handbook of Mathematical Functions*, Dover: New York, 1972.
- [105] Penfold, J. et al. *J. Chem. Soc. Faraday Trans.* **1997**, 93, 3899.
- [106] Ahrens, H.; Förster, S.; Helm, C.A. *Macromolecules* **1997**, 30, 8447.

- [107] An, S.W.; Thirtle, P.N.; Thomas, R.K.; Baines, F.L.; Billingham, N.C.; Armes, S.P.; Penfold, J. *Macromolecules* **1999**, 32, 2731.
- [108] Dijt, J.C.; Cohen Stuart, M.A.; Hofman, J.E.; Fleer, G.J. *J. of Coll. Int. Sci.* **1990**, 51, 141.
- [109] Kinniburgh, D.G.; Milne, C.J.; Venema, P. *Soil Sci. Soc. Am. J.* **1995**, 59, 417.
- [110] See Bèrard, D.R.; Patey, G.N. *J. Chem. Phys.* **1992**, 97, 4372, and references therein.
- [111] Göbel, J.G.; Besseling, N.A.M.; Cohen Stuart, M.A.; Poncet, C. *J. of Coll. Int. Sci.* **1999**, 209, 129.
- [112] Fornés, J.A. *Langmuir* **1997**, 13, 2779.
- [113] Landau, E.M.; Lifshitz, L.P. *Statistical Physics*, 3rd ed., Part 1, Pergamon Press: New York, 1980.
- [114] Vilanove, R.; Poupinet, D.; Rondelez, F. *Macromolecules* **1988**, 21, 2880.
- [115] Sieval, A.B.; Vleeming, V.; Zuilhof, H.; Sudhölter, E.J.R. *accepted by Langmuir*.
- [116] Roberts, G. (Ed.) *Langmuir-Blodgett Films*, Plenum Press: New York, 1990.
- [117] Born, M.; Wolf, E. *Principles of Optics*, 5th ed., Pergamon Press: Oxford, 1975.
- [118] Tompkins, H.G. *A User's Guide to Ellipsometry*, Academic Press: San Diego, 1993.
- [119] Hansson, P.; Lindman, B. *Current Opinion in Coll. and Int. Sci.* **1996**, 1, 604.
- [120] Cabane, B. *J. Phys. Chem.* **1977**, 81, 1639.
- [121] Shirahama, K. *Coll. Pol. Sci.* **1974**, 252, 978.
- [122] Cabane, B.; Duplessix, R. *Colloids & Surfaces* **1985**, 13, 19.
- [123] Gilanyi, T.; Wolfram, E. *Colloids & Surfaces* **1981**, 3, 181.
- [124] Van Stam, J.; Almgren, M.; Lindman, C. *Prog. Coll. Pol. Sci.* **1991**, 84, 13.
- [125] P. Linse; L. Piculell; P. Hansson in *Polymer-Surfactant Systems*, Vol.77 of the Surfactant Science Series, Ed: J. C. T. Kwak, Marcel Dekker: New York, 1998.
- [126] Tanford, C. *The Hydrophobic Effect*, Wiley: New York, 1980.
- [127] Israelachvili, J.N., *Intermolecular and Surface Forces*, Academic Press: London, 1985.
- [128] Wang, G.; Olofsson, G. *J. Phys. Chem.* **1995**, 99, 5588.
- [129] Brackman, J.C. *Langmuir* **1991**, 7, 469.
- [130] Witte, F.M.; Engberts, J.B.F.N. *Colloids and Surfaces* **1989**, 36, 417.
- [131] Nagarajan, R. *Colloids & Surfaces* **1985**, 13, 1.
- [132] Nagarajan, R. *J. Chem. Phys.* **1989**, 90, 1980.
- [133] Ruckenstein, E.; Huber, G.; Hoffman, H. *Langmuir* **1987**, 3, 382.
- [134] Nikas, Y.J.; Blankschtein, D. *Langmuir* **1994**, 10, 3512.
- [135] Flory, P.J. *Principles of Polymer Chemistry*, Cornell Univ. Press: Ithaca NY, 1953.
- [136] Fleer, G.J.; Cohen Stuart, M.A.; Scheutjens, J.M.H.M.; Cosgrove, T.; Vincent, B. *Polymers at Interfaces*, Chapman & Hall, London, 1993.
- [137] Pincus, P.A.; Sandroff, C.J.; Witten, T.A. *J. Phys. de Fr.* **1984**, 45, 725.
- [138] Birshtein, T.M.; Borisov, O.V. *Pol. Sci. USSR* **1986**, 28, 2265.
- [139] Pincus, P.A. *Lectures on Thermodynamics and Statistical Mechanics XVII*; Gonzalez, A.C., Varea, C., Eds.; World Publishing: Singapore, 1988.
- [140] Birshtein, T.M.; Borisov, O.V. *Polymer* **1991**, 32, 916.
- [141] Currie, E.P.K.; Van der Gucht, J.; Borisov, O.V.; Cohen Stuart, M.A. *Langmuir* **1998**, 14, 5740.
- [142] Hill, T.L. *An Introduction to Statistical Thermodynamics*, Dover: New York, 1960.
- [143] Brown, W.; Fundin, J.; da Graca Miguel, M. *Macromolecules* **1992**, 25, 7192.

- [144] McQuarrie, D.A. *Statistical Mechanics*, Addison-Wesley: New York, 1976.
- [145] Chari, K.; Antalek, B.; Lin, M.Y.; Sinha, S.K. *J. Chem. Phys.* **1994**, 100, 5294.
- [146] Rosén, O.; Picullell, L.; Hourdet, D. *Langmuir* **1998**, 14, 777.
- [147] Hunter, R.J. *Foundations of Colloid Science*, Clarendon Press: Oxford, 1986.
- [148] Lifshitz, I.M.; Grosberg, A.Yu.; Khokhlov, A.R. *Rev. Mod. Phys.*, **1978**, 50, 68
- [149] See Fleer, G.J.; van Male, J.; Johner, A. *Macromolecules* **1999**, 32, 825 and references therein.
- [150] (a) Stockmayer, W.H. *Macromol.Chem.*, **1960**, 50, 54; (b) Ptitsyn, O.B.; Eisner, J.E. *Biofizika*, **1965**, 10, 3; (c) de Gennes, P-G. *J. Phys. Lett.*, **1975**, 36, 55; (d) Post, C.B.; Zimm, B.H. *Biopolymers*, **1979**, 18, 1487; (e) Sanchez, I.C. *Macromolecules*, **1979**, 12, 980; (f) DiMarzio, E.A. *J. Chem. Phys.*, **1984**, 81, 969; (g) Muthukumar, M. *J. Chem. Phys.*, **1984**, 81, 6272.
- [151] Birshtein, T.M.; Pryamitsyn, V.A. *Macromolecules* **1991**, 24, 1554.
- [152] de Gennes, P-G. *Acad. Sci. Paris* **1991**, 313, 1117.
- [153] Berikanov S.; Bruinsma R.; Pincus, P. *Europhys. Lett.*, **1993**, 24, 183.
- [154] Jeppesen C.; Kremer K. *Europhys. Lett.*, **1996**, 34, 563.
- [155] Wu, X.Y.; Pelton, R.H.; Tam, K.C.; Woods, D.R.; Hamielec, A.E. *J. Pol. Sci., Part A: Pol.Chem.*, **1993**, 31, 957.
- [156] Tam, K.C.; Wu, X.Y.; Pelton, R.H. *J. Pol. Sci., Part A: Pol.Chem.*, **1993**, 31, 963.
- [157] Murase, Y.; Onda, T.; Tsujii, K.; Tanaka, T. *Macromolecules* **1999**, 32, 8589.
- [158] Lindell, K.; Cabane, B. *Langmuir* **1998**, 14, 6361.
- [159] Napper, D.H., *Polymeric Stabilization of Colloidal Dispersions*, Academic Press: London, 1985.
- [160] *Stealth Liposomes*, edited by D. Lasic and F. Martin, CRC Press: Boca Raton-London-Tokyo, 1995.
- [161] Auroy, P.; Auvray, L. *Macromolecules* **1992**, 25, 4134.
- [162] Lai, P.-Y.; Halperin, A. *Macromolecules* **1992**, 25, 6693.
- [163] Marko, J.F. *Macromolecules* **1993**, 26, 313.
- [164] Birshtein, T.M.; Lyatskaya, Y.V. *Macromolecules* **1994**, 27, 1256.
- [165] Raphaël, E.; Joanny, J-F. *Europhys.Lett.* **1990**, 13, 623.
- [166] Misra, S.; Tirrell, M.; Mattice, W. *Macromolecules* **1996**, 29, 6056.
- [167] Wagner, M.; Brochard-Wyart, F.; Hervet, H.; de Gennes, P-G. *Coll. Pol. Sci.* **1993**, 271, 621.
- [168] Halperin, A., *Europ. Phys. J. B*, **1998**, 3, 359.
- [169] See for instance Courtney, J.M.; Lambda, N.M.K.; Sundaram, S.; Forbes, C.D. *Biomaterials* **1994**, 15, 737 and references therein.
- [170] Lee, J.H.; Lee, H.B.; Andrade, J.H. *Prog. Pol. Sci.* **1995**, 20, 1043.
- [171] McPherson, T.; Kidane, A.; Szleifer, I.; Park, K. *Langmuir* **1998**, 14, 176.
- [172] Schoën, C.G.P.H.; Cohen Stuart, M.A.; van der Voort Maarschalk, K.; van der Padt, A.; van 't Riet, K. *Langmuir* **1995**, 11, 3068.
- [173] Lee, J.; Martic, P.A.; Tan, J.S. *J. of Coll. Int. Sci.* **1989**, 131, 252.
- [174] Tan, J.S.; Martic, P.A. *J. of Coll. Int. Sci.* **1990**, 136, 415.
- [175] Prime, K.L.; Whitesides, G.M. *J. Am. Chem. Soc.* **1993**, 115, 10714.
- [176] Jeon, S.I.; Lee, J.H.; Andrade, J.D.; de Gennes, P-G. *J. Coll. Int. Sci.* **1991**, 142, 149.
- [177] Jeon, S.I.; Andrade, J.D. *J. Coll.Int.Sci.* **1991**, 142, 159.

- [178] Carter, D.C.; Ho, J.X. *Adv. in Protein Chem.* **1994**, 45, 153.
- [179] Abbott, N.L.; Blankschtein, D.; Hatton, T.A. *Macromolecules* **1992**, 25, 3932.
- [180] Steth, S.R.; Leckband, D. *Proc. Natl. Acad. Sci.* **1997**, 94, 8399.
- [181] Benattar, J.J.; Nedyalkov, M.; Prost, J.; Tiss, A.; Verger, R.; Guilbert, C. *Phys. Rev. Lett.* **1999**, 82, 5297.
- [182] See Piculell, L.; Lindman, B. *Adv. Coll. Int. Sci.* **1992**, 41, 149 and references therein.
- [183] See Yaraslavov, A.A.; Kiseliova, E.A.; Udalykh, O.U.; Kabanov, V.A. *Langmuir* **1998**, 14, 5160 and references therein.
- [184] Kokufuta, E.; Takahashi, K. *Polymer* **1990**, 31, 1177.
- [185] Kokufuta, E. in *Macromolecular Complexes in Chemistry and Biology*, Dubin, P.L. et al Eds., Springer-Verlag: Heidelberg, 1993.
- [186] Izumi, T.; Hirata, M.; Takahashi, K.; Kokufuta, E. *Macromol. Sci., Pure Appl. Chem.* **1994**, A31, 39.
- [187] Dubin, P.L.; Oteri, R. *J. of Coll. Int. Sci.* **1983**, 95, 453.
- [188] McQuigg, D.W.; Kaplan, J.L.; Dubin, P.L. *J. Phys. Chem* **1992**, 96, 1973.
- [189] Tainaka, K. *J. Phys. Soc. Jpn.* **46**, 1979, 1899.
- [190] Tainaka, K. *J. Biopolymers* **19**, 1980, 1289.
- [191] Odijk, T. *Macromolecules* **1980**, 13, 1542.
- [192] Haronska, P.; Vilgis, T.A.; Grottenmüller, R.; Schmidt, M. *Macromol. Theory Simul.* **1998**, 7, 241.
- [193] Wallin, T.; Linse, P. *Langmuir* **1996**, 12, 305.
- [194] Wallin, T.; Linse, P. *J. Phys. Chem.* **1996**, 100, 17873.
- [195] Wallin, T.; Linse, P. *J. Phys. Chem.* **1997**, 101, 5506.
- [196] Odijk, T. *J. Pol. Sci. Pol. Phys.* **1977**, 15, 477.
- [197] Skolnick, J.; Fixman, M. *Macromolecules* **1977**, 10, 944.
- [198] Manning, G.S. *J. of Chem. Phys.* **1969**, 51, 924.
- [199] Oosawa, F. *Polyelectrolytes*, Marcel Dekker: 1971, New York.
- [200] Lyklema, J. *Fundamentals of Interface and Colloid Science, Vol.I*, Academic Press: London, 1991.
- [201] See Lyklema, J. *Fundamentals of Interface and Colloid Science, Vol.II*, Academic Press: London, 1995, and references therein.
- [202] Hamaker, H.C. *Physics* **1937**, 4, 1058.
- [203] Verweij, E.J.W.; Overbeek, J.Th.G. *Theory of Stability of Lyophobic Colloids*, Elsevier: Amsterdam, 1948.
- [204] Miura, N.; Dubin, P.L.; Moorefield, C.N.; Newkome, G.R. *Langmuir* **1999**, 15, 4245.
- [205] Horgan, J., *The End of Science*, Broadway Books: New York, 1997.
- [206] Maddox, J., *What remains to be discovered*, Simon & Schuster Trade: New York, 1996.
- [207] Mercurieva, A.A.; Leermakers, F.A.M.; Birshtein, T.M.; Fleer, G.J.; Zhulina, E.B. *accepted by Macromolecules*.
- [208] Leermakers, F.A.M.; Mercurieva, A.A.; van Male, J.; Zhulina, E.B.; Besseling, N.A.M.; Birshtein, T.M. *submitted to Langmuir*.
- [209] Maas, J.; Fleer, G.J.; Cohen Stuart, M.A. *accepted by Langmuir*.

Dankwoord

Een proefschrift kent één auteur maar komt tot stand met hulp van vele mensen. Zonder al deze bijdragen zou een OIO-schap nooit in enkele jaren geklaard kunnen worden. Op deze plaats wil ik de verschillende personen bedanken die in meer of mindere mate aan dit boekje hebben bijgedragen.

Ten eerste de geestelijke vaders van mijn project, Martien en Gerard. Zonder de creatieve ideeën van Martien waren verschillende experimentele problemen zeker niet opgelost. Gerard's zorgvuldigheid en kritische blik heeft de kwaliteit van het onderzoek en de presentatie daarvan sterk verbeterd. Van beiden heb ik bovendien de ruimte gekregen om mijn eigen wetenschappelijke pad te zoeken. Dit waardeer ik ten zeerste en ik hoop dat de uiteindelijke route niet teveel afwijkt van de geplande.

Frans Leermakers heeft aan het begin van mijn OIO-schap veel energie gestoken in Hoofdstuk 2, ook al was hij, volgens eigen zeggen, 'prettig overwerkt'. Frans, bedankt voor de hulp bij de eerste stapjes.

Hoofdstuk 3 is tot stand gekomen met de hulp van Marnix Wagemaker en Ad van Well van het IRI, TU Delft. Zonder hen waren de metingen en analyses van de neutronen reflectie data niet gelukt. Ik hoop dat dit hoofdstuk een voorbeeld is hoe het samenwerken van zachte, groene kolloïdchemici met harde neutronenfysici succesvol kan zijn.

Chapters 5, 6 and 7 are the result of a very fruitful cooperation with Oleg Borisov. Oleg, your ideas, criticisms, and comments were absolutely necessary for the development of our model. Many thanks for the fun during the past two years, and I hope we'll be able to work together again in the future.

Twee studenten heb ik mogen begeleiden in mijn OIO-schap, Jasper van der Gucht en Michel Venema. Dit waren zeer leerzame perioden voor mij. Ik wil hierbij Jasper geluk wensen met zijn OIO-schap op Fysko: gezien de indrukwekkende resultaten van zijn afstudeervak (gepresenteerd in Hoofdstuk 5 en 8) moet dit een mooi project worden.

Bij Organische Chemie zijn de Si-plaatjes met PS-coating, beschreven in Hoofdstuk 4, door Alex Sieval bereid. Waar vrijdagmiddag-experimenten al niet toe kunnen leiden ... Alex, bedankt voor de hulp en veel succes met je eigen aanstaande promotie.

Kamergenoten zijn heel belangrijk in een OIO-bestaan; iemand moet de dagelijkse verhalen aanhoren, humeuren doorstaan en de talloze telefoontjes voor de Veluweeloop aannemen. Ronald, Werner, Clara en Sonja, de gezelligheid in kamer 015 kende geen grenzen.

'Gedeelde smart is halve smart' luidt het gezegde en dit is zeker waar bij wetenschappelijk onderzoek. Gelukkig is er op Fysko een grote groep mede-AIO's/OIO's om je een

hart onder de riem te steken, een wild ideetje mee te bespreken of gewoon een babbel mee te maken. Ik wens eenieder veel succes en plezier bij zijn/haar eigen onderzoek.

Naast de verschillende individuen is Fysko als groep heel bijzonder. Er is altijd wel een Ben, Ronald, Gert, Rob, Peter, Josie, Wil, Bert of anderen beschikbaar om je welwillend terzijde te staan bij technische, financiële of grafische problemen. Ook waren de volleybalavonden, wandelweekends, Veluweloop, labuitjes en dergelijke hele gezellige afleidingen. Iedereen op Fysko, bedankt voor de geweldige tijd!

Tenslotte wordt het wel en wee van het onderzoek immer gedeeld met het thuisfront. Brechtje, jij hebt net zo goed de stress van het laatste jaar moeten voelen als ikzelf. Het is niet altijd leuk als je vriend in het weekend nog wat experimenten moet uitvoeren of aan het boekje moet werken. Daarom is jouw steun en warmte de afgelopen tijd zo belangrijk geweest. Het karwei is af, laten we nu gaan feesten!

Curriculum Vitae

Edwin Currie was born on the 5th August 1970 in Burnaby, Canada. After some wandering he arrived in The Netherlands where he obtained his VWO diploma at the Gymnasium Haganum in the Hague in 1988. He subsequently studied Chemistry at the University of Leiden, where he specialised in Physical Chemistry. He graduated in 1994 on the subject of optical properties of oil/water microemulsions.

After traveling and working for a year in Canada and the USA, he started in October 1995 as a Ph-D student at the Laboratory for Colloid Science and Physical Chemistry at Wageningen University. Presentations of the results of this project were given in St.Petersburg, Santa Barbara and Stockholm, besides several conferences in The Netherlands. Since January 2000 he is employed at DSM Research in Geleen, The Netherlands.

